THÈSE POUR OBTENIR LE GRADE DE DOCTEUR DE L'UNIVERSITÉ DE MONTPELLIER

En Physique et Astrophysique

École doctorale : Information, Structures, Systèmes

Unité de recherche : CEA Marcoule, DES/ISEC/DPME/SEME/LEMC

Origin of the Glass Corrosion Residual Rate: Monte Carlo, Molecular Dynamics, and Experiments

Présentée par : Sumit TIWARI

Le : 11 Décembre 2025

Sous la direction de Stéphane GIN, Jean-Marc DELAYE et Paul FOSSATI

Devant le jury composé de

Damien DAVAL, Chargé de recherche, Univ. Grenoble Alpes	Rapporteur
Matthieu MICOULAUT, Professeur, Sorbonne Université	Rapporteur
Lucyna FIRLEJ, Professeur, Univ. Montpellier	Président du jury
Romain DUPUIS, Chargé de recherche, Univ. Montpellier	Examinateur
Takahiro OHKUBO, Professeur, Chiba University	Examinateur
Jean-Marc DELAYE, Directeur de recherche, CEA Marcoule	Co-directeur de thèse
Stéphane GIN, Directeur de recherche, CEA Marcoule	Directeur de thèse
Paul FOSSATI, Ingénieur, CEA Saclay	Co-encadrant de thèse
Thibault CHARPENTIER, Directeur de recherche, CEA Saclay	Invité

UNIVERSITÉ DE MONTPELLIER

cea isec

Résumé

L'altération par l'eau du verre est un sujet d'importance centrale, avec des applications en microélectronique, dans le domaine de la santé (verres bioactifs), pour l'isolation des bâtiments (laines de verre ou laines de roches) ou encore pour le conditionnement des déchets nucléaires à vie longue. Pour ces derniers, des verres borosilicatés contenant plus de 30 oxydes sont développés et produits depuis plus d'une trentaine d'années en France. La durabilité chimique de ces verres peut être étudiée à l'aide de verres modèles simplifiés. Comprendre les processus qui gouvernent leur altération, et en particulier la transition vers le régime de vitesse résiduelle, est essentiel pour prédire les performances de ces matériaux à long terme.

Dans cette thèse, l'altération du verre est étudiée en suivant trois axes complémentaires : des expériences, la modélisation de type Monte Carlo et des simulations de dynamique moléculaire. Les expériences conduites sur trois verres de type SBNA (SiO_2 – B_2O_3 – Na_2O – Al_2O_3), présentant des teneurs variables en Al_2O_3, montrent que l'aluminium contrôle la vitesse de réorganisation du gel, laquelle détermine l'efficacité de la passivation et donc la vitesse résiduelle.

Des simulations Monte Carlo ont été utilisées pour décrire la maturation du gel et établir comment l'évolution temporelle de la morphologie de ces couches est corrélée à la diminution de la diffusivité des ions observée expérimentalement. Cette corrélation fournit une explication mécanistique de la formation de couches d'altération à faible diffusivité et de leur contribution à la passivation à long terme.

À l'échelle atomique, des simulations de dynamique moléculaire ont permis d'examiner la diffusion du bore au sein de gels modèles. Un champ de force dédié, basé sur des potentiels réactifs à charges diffuses, a été développé pour le bore en solution dans des pores de silice au moyen d'une procédure d'ajustement des forces à partir de données *ab initio*. Ces calculs montrent que les environnements locaux et la structure des pores gouvernent la mobilité du bore, fournissant ainsi une explication microscopique à la rétention variable de cet élément dans les gels d'altération.

Pris dans leur ensemble, les trois approches convergent vers une vision unifiée : la concentration en aluminium gouverne la dynamique de restructuration du gel, la maturation du gel est directement liée à la diminution de la diffusivité des ions au cours du temps, et les interactions à l'échelle atomique déterminent la mobilité d'espèces clés telles que le bore. Cette approche multi-échelles fait progresser notre compréhension de l'altération du verre dans le régime résiduel et offre une base pré-

dictive plus solide pour décrire la stabilité à long terme des verres de confinement des déchets nucléaires.

Abstract

Glass alteration by water is a subject of central importance, with applications ranging from the packaging of microelectronic materials and biomedical devices to the long-term immobilization of nuclear waste. Among these, the use of borosilicate glasses for the conditioning of high-level radioactive waste is particularly critical. Although industrial glasses such as R7T7 contain more than thirty oxides, their structural and chemical durability can be explored using simplified model glasses. Understanding the processes that govern alteration, and in particular the transition to the residual rate regime, is essential for predicting long-term performance in geological disposal.

In this thesis, glass alteration is investigated along three complementary axes: experiments, Monte Carlo modeling, and molecular dynamics simulations. Experiments performed on three SBNA (SiO_2 – B_2O_3 – Na_2O – Al_2O_3) glasses with varying Al_2O_3 content show that aluminum controls the rate of gel reorganization, which in turn governs passivation behavior.

Monte Carlo simulations have been used to describe gel maturation and to establish how the time-dependent evolution of morphology correlates with decreasing diffusivity in the gel observed experimentally. This correlation provides a mechanistic explanation for the emergence of low-diffusivity alteration layers.

At the atomic scale, molecular dynamics simulations have been used to investigate the diffusion of boron within model gels. A dedicated force field, based on diffuse-charge reactive potentials, was developed for boron in solution in nanoconfined silica through a force-matching procedure against *ab initio* data, enabling reliable classical simulations. These calculations show that local bonding environments and pore structures govern the mobility of boron, providing a microscopic explanation for its variable retention during alteration.

Taken together, the three approaches converge toward a unified view: aluminum content in glass governs the pace of gel restructuring, gel maturation is directly linked to the reduction of diffusivity with time, and atomic-scale interactions determine the mobility of key species such as boron. This multi-scale framework advances our understanding of glass alteration in the residual regime and provides a stronger predictive basis for the long-term stability of nuclear waste glasses.

To my family, for their endless support.

Acknowledgments

This thesis marks the culmination of an enriching and demanding journey that would not have been possible without the support and encouragement of many people. I wish to express my sincere gratitude to all those who accompanied me, directly or indirectly, throughout these years.

I would first like to express my deepest gratitude to the members of the jury — **Damien Daval**, **Matthieu Micoulaut**, **Lucyna Firlej**, **Romain Dupuis**, **Takahiro Ohkubo**, and **Thibault Charpentier** — for accepting to evaluate my work. Their time, expertise, and thoughtful comments are greatly appreciated. Their feedback and questions will continue to guide my scientific thinking well beyond this PhD.

I would also like to thank the **Doctoral School I2S** of the University of Montpellier for its continuous support and guidance throughout these years. Its training programs, events, and advice have been invaluable components of my doctoral experience.

My deepest appreciation goes to my supervisors — **Jean-Marc Delaye**, **Stéphane Gin**, and **Paul Fossati** — for their guidance, trust, and scientific insight. Their complementary expertise and constant encouragement shaped my approach to research and played a decisive role in the completion of this work. I am especially thankful to Jean-Marc for his patience, precision, and intellectual generosity; to Stéphane for his scientific clarity and inspiring discussions; and to Paul for his advice and constructive feedback throughout the project.

My warmest thanks go to all my colleagues at the **LEMC** and other laboratories in the CD building for their support, help, and friendship. In particular, I would like to thank **Sarah, Maxime (both Maximes), Abdelhak, Harouna, Sophie, Sathya, Manon, Pierre, Lionel, Nicole, Trilce, Camille, Clémentine, Faijan, Géraldine, Emmanuel, Cloé, Lamiae, Charles,** and **Hodroj** for their assistance, discussions, and kindness. Working with you made this experience both productive and enjoyable. I also wish to thank everyone I could not mention individually but who, in one way or another, contributed to the completion of this work.

Also, I would like to express my heartfelt gratitude to my friends in **Avignon** — **Rajesh, Rakesh, Laxmi, Inderdip, Prateek, Sai Ram, Sergio,** and many others — whose friendship, warmth, and humour made my stay truly memorable and turned Avignon into a home away from home.

Finally, I am deeply grateful to my **family** — my brother **Charit**, my sister **Chetna**,

and above all, my **parents**, for their continuous encouragement, values, and strength that have guided and supported me throughout my life.

Contents

List of Figures

List of Tables

Abbreviations

BET	Brunauer–Emmett–Teller surface area analysis
BO	Bridging Oxygen
COMB	Charge Optimized Many–Body potential
CP–MAS	Cross–Polarization Magic Angle Spinning (NMR technique)
DBX model	Dell–Bray–Xiao model (borosilicate glass structure)
DCRP	Diffuse Charge Reactive Potential
DFT	Density Functional Theory
D&S model	Du–Stebbins model (extended DBX including $\mathrm{Al_2O_3}$)
EDS	Energy Dispersive X–ray Spectroscopy
ETH (ETh)	Equivalent Thickness
FIB/SEM	Focused Ion Beam / Scanning Electron Microscopy
HLW	High–Level Waste
ICP	Inductively Coupled Plasma
ICP–MS	Inductively Coupled Plasma Mass Spectrometry
ICP–OES	Inductively Coupled Plasma Optical Emission Spectroscopy
IRO	Intermediate–Range Order
K	Molar ratio of $\mathrm{SiO_2/B_2O_3}$
KMC	Kinetic Monte Carlo
MC	Monte Carlo
MD	Molecular Dynamics
MSD	Mean Square Displacement
NBO	Non–Bridging Oxygen
NL(B)	Normalized Loss of Boron
NNBO	Number of Non–Bridging Oxygens
N_4	Fraction of tetrahedrally coordinated boron ($\mathrm{BO_4}$ units)
PIM	Polarizable Ion Model
Q^n	Tetrahedral species with n bridging oxygens
r_0	Initial dissolution rate
R	Molar ratio of $\mathrm{Na_2O/B_2O_3}$
RDF	Radial Distribution Function
ReaxFF	Reactive Force Field
r_r	Residual rate
$R_{\max}$	Critical modifier–to–boron ratio
SAXS	Small Angle X–ray Scattering
SBET	Specific Surface Area determined by the BET (Brunauer–Emmett–Teller) method
SGeo	Geometric Surface Area
SRO	Short–Range Order

TEM	Transmission Electron Microscopy
TGA	Thermogravimetric Analysis
ToF–SIMS	Time–of–Flight Secondary Ion Mass Spectrometry
T^n	Trigonal species with n bridging oxygens
B(III)	Three–coordinated boron (trigonal, BO_3)
B(IV)	Four–coordinated boron (tetrahedral, BO_4)

Introduction

Glass alteration is a critical process with far-reaching implications across multiple domains, including the packaging of microelectronic materials, biomedical applications, and the safe disposal of nuclear waste. Borosilicate glasses, in particular, are widely adopted for the immobilization and storage of high-level nuclear waste due to their chemical durability and structural stability. However, the long-term performance of these glasses under environmental conditions remains a complex challenge, as nuclear waste glasses, such as the French SON68 glass with over 30 components, exhibit intricate dissolution behaviors. Simplified glass models, however, allow researchers to systematically explore the structural and chemical factors governing glass alteration, providing insights into the long-term stability required for nuclear waste storage.

Among the elements influencing glass alteration, boron plays a pivotal role. Its potential retention within the alteration gel under specific conditions and its hypothesized connection to the slowing of alteration rates have opened new avenues for investigation. Understanding the dynamics of gel formation and maturation, particularly in the residual rate regime, is essential for predicting the long-term behavior of nuclear waste glasses. This regime, characterized by a significantly reduced dissolution rate, is influenced by the formation of a passivating gel layer, yet the underlying mechanisms remain poorly understood due to limitations in earlier models.

To address these challenges, computational and experimental approaches have been employed. Monte Carlo (MC) methods have proven effective for modeling complex systems like glass dissolution. Early MC models developed by Aertsens, Van Iseghem, and Devreux in the late 20th century, followed by more recent efforts by Kerisit, Jan and coworkers, laid the groundwork for studying glass-water interactions. However, these models struggled to capture the residual rate and gel maturation processes. A novel MC code, developed by J.-M. Delaye and coworkers, introduces significant advancements by accounting for water diffusion within the solid through two interlinked networks representing the glass and the solution. This code enables the exploration of the glass-solution interface and gel maturation dynamics, revealing distinct gel formation behaviors influenced by hydrolysis rates, which are linked to aluminum (Al) concentrations in the glass.

In parallel, molecular dynamics (MD) simulations provide atomic-scale insights into boron diffusion within the alteration gel. The development of accurate force

fields is crucial for reliable MD simulations. Two promising force fields, the Polarizable Ion Model (PIM) by Madden and the Diffuse Charge Reactive Potential (DCRP) by Mahadevan and Garofalini, were identified following an extensive literature review. The DCRP model, which employs fixed and diffuse charges and can simulate water in contact with silicate systems, was selected for further development through a force-matching procedure to derive parameters for simulating boron diffusion in a simplified gel model.

Experimental studies complement these computational efforts by providing data to validate and refine the MC and MD models. Glasses with varying Al_2O_3 content were synthesized and subjected to dissolution experiments, with solution analysis (ICP) and ToF-SIMS data revealing the impact of Al on gel morphology and passivation. Lower Al content glasses exhibited more passivating gels, potentially due to higher reorganization rates, highlighting the interplay between glass composition and alteration dynamics.

This thesis aims to advance the understanding of glass alteration, with a focus on the role of boron and aluminium and the dynamics of gel maturation in the residual rate regime. By integrating MC simulations, MD simulations, and experimental studies, the research seeks to address fundamental questions:

1. **How does the glass composition, particularly the aluminum and boron content, affect the formation and reorganization of the passivating gel layer during glass alteration?**
2. **Can the maturation dynamics of the gel layer be correlated with the residual rate?**

To answer the research question, the thesis is structured as follows:

Chapter 1: Background and Literature Review
This chapter provides an overview of glass alteration, emphasizing its significance for nuclear waste storage. It reviews the role of boron, and the limitations of existing models.

Chapter 2: Experimental Studies on Glass Alteration
This chapter presents the experimental approach, including long term glass dissolution experiments with glasses of varying Al_2O_3 content.This chapter specially focuses on the evolution of gel morphology with time and it's role on the passivation of glass.

Chapter 3: Monte Carlo Modeling of Glass Alteration
This chapter details the limitations of the previous Monte-Carlo models and the new Monte-Carlo code developed by J.-M. Delaye and cowork-

ers. The Monte-Carlo code is used to study the glass solution interface linking it to kinetics of alteration. This code has been modified to be used to study gel maturation and it's role in passivation.

Chapter 4: Molecular Dynamics Simulations of Boron Diffusion

This chapter describes the development of the DCRP force field for Molecular Dynamics simulations of boron diffusion in a model alteration gel. It outlines the force-matching procedure and the application of the force field to investigate free solution boron transport and it's diffusion in confined silica nanopores.

Chapter 5: Discussion

This chapter synthesizes findings from Monte Carlo simulations, Molecular Dynamics simulations, and experimental studies to address the research questions. It explores how multi-scale modeling can elucidate gel maturation dynamics and their link to alteration rates, proposing a hybrid explanation for gel passivation.

1 Literature Review

Contents

1.1 Scientific context

Radioactive substances, integral to energy production, medical applications, research, and defense, generate materials and waste that require meticulous management to safeguard human health and the environment. The International Atomic Energy Agency's radioactive waste classification and French Environment Code (Article L542-1-1) categorizes these substances into radioactive materials, intended for future use (e.g., nuclear fuels like uranium and plutonium), and radioactive waste, which lacks planned applications and necessitates safe disposal [1], [2]. Radioactive waste originates from five key sectors: nuclear power generation, research, defense, non-nuclear industries (such as rare earth mining, the manufacture of sealed sources, weld inspection, medical equipment sterilization, food sterilization and preservation), and the medical sector [2]. The contributions from these sectors are

shown in Figure 1.1. Effective waste management hinges on understanding the types of waste generated and implementing tailored disposal strategies, particularly for high-level waste (HLW), which poses significant challenges due to its intense radioactivity and long-lived radionuclides [1].

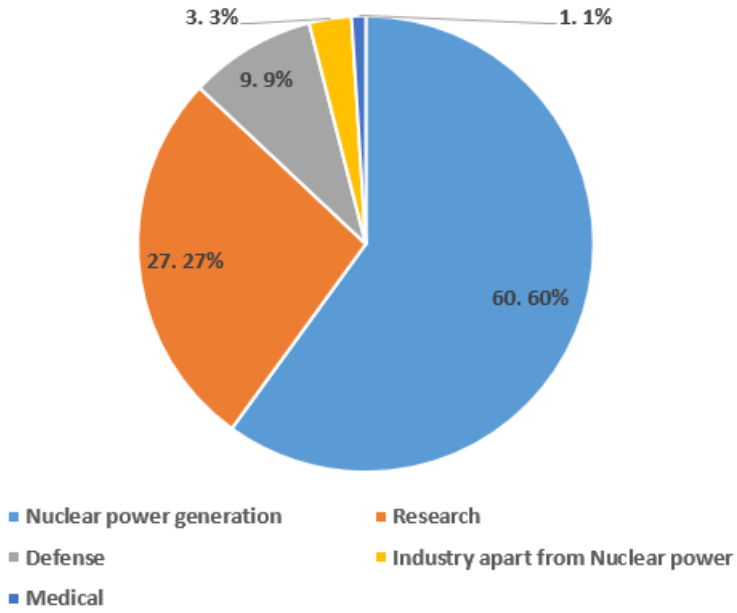

Figure 1.1: *Percentage Contribution to the radioactive waste from various sectors [2]*

High-level nuclear waste (HLW) is a byproduct of nuclear power generation and the reprocessing of spent nuclear fuel, posing one of the most formidable challenges in modern waste management [1]. This type of waste contains highly radioactive elements—such as plutonium, uranium, and fission products that emit ionizing radiation capable of damaging living tissues and contaminating ecosystems if not adequately contained. The danger of HLW stems from its persistent radioactivity, intense radiation from short-lived radionuclides, and long-term toxicity, with some isotopes remaining hazardous for thousands to millions of years. This extraordinary longevity necessitates isolating HLW from the biosphere over geological time scales, far exceeding the span of recorded human history. For nations relying on nuclear energy, safely disposing of HLW is a critical priority, driving the development of advanced technologies and scientific models to contain the waste and mitigate its risks. The complexity of this task lies not only in achieving initial containment but also in ensuring that it endures for millennia, protecting both current and future generations from its harmful effects [3].

The process of vitrification offers a robust solution for immobilizing HLW, transforming it into a stable, solid form suitable for long-term storage [3], [4], [5], [6]. Before vitrification, liquid or sludge-like waste is first subjected to a calcination

step, where water and volatile components are removed to produce a dry, granular residue [7]. This calcined product is then mixed with glass-forming materials, typically borosilicate glass frit, and heated to form a durable glass matrix. This matrix encapsulates the radioactive isotopes, preventing their release into the environment. Borosilicate glass is favored for its exceptional properties: it resists thermal shock, withstands chemical attack, and can incorporate a wide variety of waste compositions [8]. Once cooled, the vitrified waste is sealed in steel canisters, ready for disposal. This method significantly reduces the immediate risk of radionuclide dispersal, making it a cornerstone of nuclear waste management worldwide [7].

In context of the application of glass for the disposal of nuclear waste there are few possibilities for the treatment of spent nuclear fuel either directly storing the waste or incorporating fission products and minor actinides into the nuclear glass matrix. These nuclear glasses are designed to be stored in deep underground repositories, isolating the radioactive waste from the ecosystem. It has been accepted as a common solution in several countries for the disposal of radioactive waste [3].

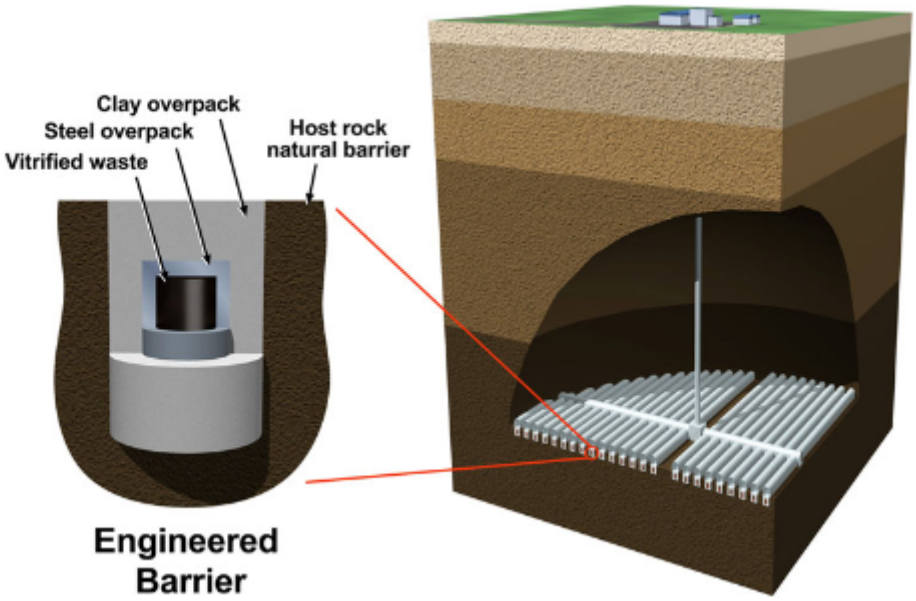

Figure 1.2: *Schematic of a generic geological disposal facility for vitrified radioactive waste, illustrating the multi-layered engineered barrier system [3].*

For a glass matrix to be suitable for nuclear waste disposal, it should meet a variety of requirements, including the minimization of manufacturing costs. The fine-tuning between the elaboration temperature (which should be sufficiently low) and viscosity must be appropriate when the molten glass is poured into the steel containers for storage. It is of the utmost importance to maintain a balance between the

glass former elements and the glass modifier elements.

At microscopic scales, the nuclear glass matrix is often assumed to be homogeneous, yet in practice it may contain numerous nanoscale precipitates that disrupt complete uniformity [4]. In some cases, such as UMo-based materials, the product is better described as a glass–ceramic, where crystalline phases are deliberately or unavoidably present within the amorphous network [4], [9]. Despite these microstructural complexities, the matrix retains the crucial ability to incorporate a wide variety of radioactive elements while minimizing uncontrolled crystallization. Moreover, the design of the waste form must ensure that the containment matrix remains suitable for safe handling and transport to disposal sites.

Last but not least, this glass must be able to endure internal radiation effects while also showing high resistance to environmental corrosion and ensuring the containment of radioactive elements over geological timescales.

It is a widely accepted method to use borosilicate glass for the disposal and treatment of nuclear wastes. There are several efforts to study glass dissolution and to understand the long-term stability of the glass for its use in the storage of nuclear wastes. Although the nuclear waste glasses used for storage are much more complex, for example, the R7T7 glass (composition is given in Table 1.1), which has more than 30 components, the main components being SiO_2, B_2O_3, Na_2O, Al_2O_3, and CaO, accounting for around 80% of the glass composition, the structural and chemical durability can be explored using much simpler models [10]. This methodological choice is part of what has been termed long-term behaviour (LTB) science: the recognition that in order to build reliable predictive models [7], the system must be simplified to its essential components. By focusing on binary or ternary aluminoborosilicate compositions, it becomes possible to disentangle the role of individual elements (e.g., boron as a network former or modifier, aluminum as a network stabiliser, alkali as charge balancers) in the alteration process. These mechanistic insights, once validated experimentally, can then be progressively re-introduced into more complex formulations such as SON68 or R7T7. In this way, the study of simplified glasses does not aim to reproduce repository conditions directly, but rather to isolate the fundamental mechanisms that ultimately govern the alteration kinetics of complex nuclear glasses. This tiered approach is a cornerstone of the LTB methodology and ensures that the models used in performance assessment rest on a solid scientific foundation rather than empirical extrapolation.

However, in the presence of water, the glass can degrade through a process known as corrosion, raising concerns about its long-term effectiveness in isolating HLW.

Deep geological repositories provide the next layer of defense, designed to isolate vitrified HLW from the biosphere for geological timescales. These repositories are

Table 1.1: *Chemical composition range of French R7T7 glass (wt%) [11].*

Oxide	Range (wt%)	Avg. (wt%)
SiO_2	42.4–51.7	45.6
B_2O_3	12.4–16.5	14.1
Al_2O_3	3.6–6.6	4.7
Na_2O	8.1–11.0	9.3
CaO	3.5–4.8	4.0
Fe_2O_3	< 4.5	1.1
NiO	< 0.5	0.1
Cr_2O_3	< 0.5	0.1
P_2O_5	< 1.0	0.2
Li_2O	1.6–2.4	2.0
ZnO	2.2–2.8	2.5
Oxides (FP+Zr+act.)	7.5–18.5	17.0
Actinide oxides	–	0.6
SiO_2+B_2O_3+Al_2O_3	> 60	64.4

constructed hundreds of meters underground in stable geological formations, such as clay, salt, or crystalline rock, that act as natural barriers to radionuclide migration. Engineered to withstand tectonic shifts, groundwater infiltration, and other environmental pressures, these facilities are intended to ensure containment for hundreds of thousands of years. A leading example is the CIGEO project in France, located 500 meters beneath the surface in the Callovo-Oxfordian claystone formation. This site is designed for the permanent disposal of both high-level and intermediate-level long-lived radioactive waste, with safety demonstrated over at least 100,000 years. The durability of the vitrified matrices is therefore crucial: their performance must guarantee that radionuclide release into the geosphere remains below thresholds harmful to human health. The claystone's low permeability and strong retention capacity further enhance long-term safety, while the vitrified waste—encased in steel canisters and concrete overpacks—is emplaced in underground tunnels. Nevertheless, the long-term stability of the glass waste forms remains a pivotal factor, as any degradation could compromise the repository's integrity over time [12], [13]. A schematic representation of a geological disposal facility for vitrified radioactive waste is shown in Figure 1.2 [3].

Glass corrosion emerges as a critical challenge in this context, as it describes the chemical degradation of the glass matrix when exposed to water—an inevitable occurrence in deep geological repositories. The process begins with ion exchange, where alkali ions like sodium (Na^+) in the glass are swapped with hydronium ions (H_3O^+) from water, weakening the glass structure . This is followed by hydrolysis,

which breaks the silicate network's Si-O-Si bonds, releasing silica and other constituents into the solution. As corrosion advances, a gel-like alteration layer forms on the glass surface, composed of hydrated glass and secondary precipitates. This layer can act as a protective barrier, slowing further degradation. Initially, the glass dissolves rapidly, but over time, this transitions to a slower, steady-state process known as the residual corrosion rate. Understanding this rate is essential for predicting how long the glass will contain radionuclides, as it determines the material's longevity under repository conditions [14], [15].

Several factors influence the residual corrosion rate, complicating efforts to predict glass behavior over millennia. These include the glass's composition, the chemistry of the surrounding water, temperature, and the properties of the alteration layer. Laboratory studies, often using simplified nuclear glasses with fewer components, have measured residual rates as low as 10^{-4} to 10^{-5} grams per square meter per day, suggesting high durability. However, these experiments, lasting months or years, cannot directly replicate the thousands to millions of years required for geological disposal. This temporal mismatch necessitates predictive models to extrapolate short-term data into long-term forecasts. Such models must account for the dynamic interactions between the glass, the alteration layer, and the repository environment, ensuring that safety assessments remain reliable over vast time scales [16].

This chapter is organised as follows. Section 1.2 introduces the structural aspects of glass, covering the fundamentals, structural parameters, and the coordination of key elements such as silicon, aluminum, sodium, calcium, and boron. Section 1.3 then addresses the alteration of glass, beginning with the initial dissolution rate, followed by the residual rate, and the possible resumption of alteration. It further discusses the experimental characterisation of glass alteration and the dynamics of gel formation, morphology, transport, and maturation, as well as the role of boron and aluminum in alumino-borosilicate glass alteration. Section 1.4 reviews modelling approaches, including density functional theory, classical molecular dynamics, and related methods. The chapter concludes with an overview of how these insights collectively advance the understanding of glass corrosion processes.

Conclusion

Glass alteration by water is a subject of central importance, with applications ranging from the protection of microelectronic components and biomedical devices to the long-term immobilization of nuclear waste. Among these cases, the use of borosilicate glasses for conditioning high-level radioactive waste is particularly critical. Industrial reference glasses such as R7T7 contain more than thirty different oxides, yet their structural and chemical durability can be explored through the study of simplified model systems. These model glasses make it possible to isolate the influence of specific components and to identify the mechanisms that drive reactivity. Understanding the mechanisms governing the residual rate is essential for reliable predictions of long-term performance under geological disposal conditions.

1.2 Glass structure

Glasses are materials characterized by their amorphous, non-crystalline structure, which lacks the long-range atomic order typical of crystalline solids [17]. This unique structural arrangement imparts glasses with distinctive physical, chemical, and mechanical properties, making them critical in applications ranging from everyday objects to advanced technological uses, such as the vitrification of HLW. Understanding the structure of glass at the atomic and molecular levels is essential for tailoring its properties to meet specific requirements, particularly in the context of nuclear waste management, where borosilicate glasses are widely employed for their chemical durability and ability to incorporate radionuclides. This section provides a comprehensive overview of glass structure, focusing on the roles of network formers, modifiers, and intermediate species, the structural parameters that define glass organization, and a detailed examination of the coordination environments of key elements, with a particular emphasis on boron due to its critical role in nuclear waste glasses.

1.2.1 Fundamentals of Glass Structure

Glass is formed through the rapid cooling of a molten material, a process known as supercooling, which prevents the atoms from arranging into a crystalline lattice. This rapid quenching traps the material in a metastable, disordered state, retaining the structural characteristics of the liquid phase. Unlike crystalline solids, which exhibit a sharp transition at their melting point accompanied by a distinct volume change, glass undergoes a gradual transformation over a temperature range known

as the glass transition region. This region is characterized by a continuous change in properties such as viscosity and specific volume, reflecting the dynamic nature of the glass structure.

The atomic structure of glass can be described in terms of three primary types of species based on their roles within the glass composition:

- **Network Formers**: These are high-valence elements, such as silicon (Si), phosphorus (P), and boron (B), that form the backbone of the glass network through covalent bonds with oxygen. Network formers create a three-dimensional framework of interconnected polyhedra, typically tetrahedra or trigonal units, linked by bridging oxygen (BO) atoms. For example, in silicate glasses, silicon forms SiO_4 tetrahedra, where each silicon atom is bonded to four oxygen atoms, and adjacent tetrahedra share oxygen atoms to form a continuous network.
- **Network Modifiers**: These are low-valence elements, such as alkali metals (e.g., sodium, Na; lithium, Li; potassium, K) and alkaline earth metals (e.g., calcium, Ca; magnesium, Mg), that disrupt the glass network. Network modifiers introduce ionic bonds, breaking bridging oxygen bonds to form non-bridging oxygen (NBO) atoms. NBOs are oxygen atoms bonded to only one network former, with their negative charge balanced by the positive charge of the modifier cation. This depolymerization reduces the connectivity of the network, lowering the glass's viscosity and melting temperature.
- **Intermediates**: Elements such as aluminum (Al), molybdenum (Mo), and zirconium (Zr) can function as either network formers or modifiers, depending on the glass composition and local chemical environment. For instance, aluminum can form AlO_4 tetrahedra, acting as a network former when charge-balanced by alkali or alkaline earth cations, or it can adopt higher coordination numbers, behaving as a modifier in certain contexts.

The interplay between these species determines the glass's structural and functional properties. The degree of network connectivity, governed by the balance between bridging and non-bridging oxygens, strongly affects chemical durability, thermal stability, and mechanical strength. The fraction of non-bridging oxygens (N_{NBO}) can be expressed in terms of oxide mole fractions as:

$$N_{\mathrm{NBO}} = \frac{2 \times \left(x_{\mathrm{modifiers}} - x_{\mathrm{charge\,compensators}}\right)}{N(O)}, \tag{1.1}$$

with

$$N(O) = \sum_i n_{O,i}\, x_i, \tag{1.2}$$

where $x_{\text{modifiers}}$ represents the total mole fraction of modifier oxides (e.g., Na_2O, K_2O, CaO, MgO), and $x_{\text{charge compensators}}$ is the mole fraction of network-former oxides requiring charge compensation (e.g., Al_2O_3, tetrahedral B_2O_3). In Eq. (1.2), $n_{O,i}$ is the number of oxygen atoms in one molecule of oxide i and x_i is its mole fraction. Equations (1.1)–(1.2) yield the fraction of non-bridging oxygens, which can be multiplied by 100 to obtain the percentage [18].

1.2.2 Structural Parameters of Glass

The structure of glass is characterized at multiple scales, from local atomic arrangements to intermediate-range connectivity. Three primary parameters are used to describe these structural features:

- **Short-Range Order (SRO)**: SRO (short-range order) refers to the local coordination environment of atoms, typically extending over distances of a few angstroms. It is analyzed through coordination numbers, which indicate the number of nearest-neighbor atoms, and radial distribution functions, which describe the probability of finding an atom at a given distance from another atom. For example, in silicate glasses, silicon typically adopts a tetrahedral coordination SiO_4, with a coordination number of 4. In contrast, boron may exist in either trigonal BO_3 or tetrahedral BO_4 configurations, depending on the glass composition.

- **Intermediate-Range Order (IRO)**: IRO encompasses the connectivity of structural units, such as the formation of rings, chains, or clusters, over distances of 5–20 Å. Unlike crystalline materials, where IRO extends over long distances, glass exhibits limited IRO due to its amorphous nature. Techniques such as radial and angular distribution functions provide insights into the arrangement of polyhedra and the presence of structural motifs, such as six-membered rings in silicate glasses.

- **Network Connectivity**: This parameter quantifies the degree of polymerization within the glass network, primarily through the distribution of bridging and non-bridging oxygens. The connectivity is often described using the Q_n and T_n notation, where Q_n refers to tetrahedral species (e.g., SiO_4 or AlO_4) with n bridging oxygens, and T_n refers to trigonal species (e.g., BO_3) with n bridging oxygens. For example, a Q_4 unit represents a silicon tetrahedron connected to four other tetrahedra via BOs, indicating high connectivity, while a

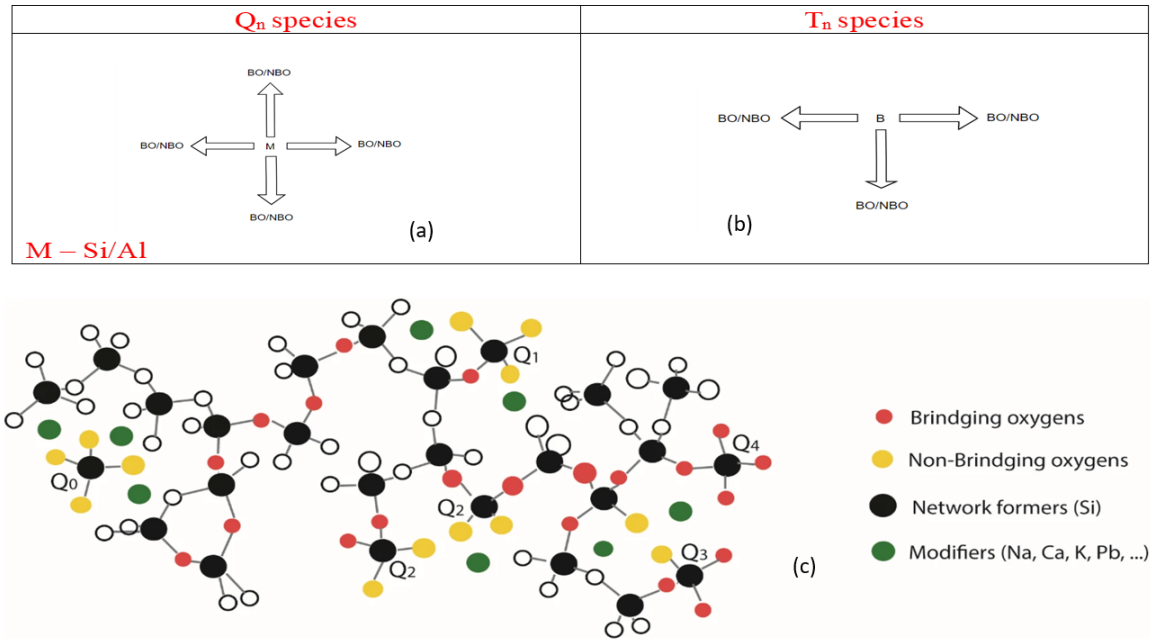

Figure 1.3: *(a) and (b) Q_n species (tetrahedral species connected to number of bridging oxygen) and T_n species (trigonal species connected to n number of bridging oxygen) and (c) Representation of Q_n based on Zachariasen representation [19]*

Q_2 unit has two BOs and two NBOs, indicating lower connectivity. A visual representation is shown in Figure 1.3.

These parameters collectively define the glass's structural framework and influence its behavior under various conditions, such as exposure to aqueous environments in nuclear waste disposal scenarios.

1.2.3 Coordination of Elements in Glass

The coordination environment of elements within the glass network is a critical determinant of its structural and chemical properties. Each element's coordination state—defined by the number and type of atoms to which it is bonded—depends on factors such as its valence, ionic radius, and the surrounding chemical environment. Below, we discuss the coordination of key elements commonly found in borosilicate glasses used for nuclear waste immobilization, including silicon, aluminum, sodium, and calcium, before delving into a detailed analysis of boron coordination.

Silicon Coordination

Silicon is the primary network former in silicate and borosilicate glasses, typically adopting a tetrahedral coordination SiO_4 [17]. Each silicon atom is covalently bonded to four oxygen atoms, forming a tetrahedron with Si–O bond lengths of approximately 1.6 Å [17]. In a fully polymerized network, these tetrahedra are connected via bridging oxygens, forming a Q_4 structure. The introduction of network modifiers,

such as sodium or calcium, breaks Si–O–Si bonds, creating non-bridging oxygens and reducing the connectivity to Q_3, Q_2, or lower species [17]. The distribution of Q_n species can be quantified using techniques such as nuclear magnetic resonance (NMR) spectroscopy, particularly $^{29}\mathrm{Si}$ NMR, which provides insights into the local environment and network connectivity.

Aluminum Coordination

Aluminum's coordination in oxide glasses is more complex due to its ability to act as both a network former and a modifier [17]. In borosilicate glasses, aluminum predominantly forms AlO_4 tetrahedra, acting as a network former when charge-balanced by alkali or alkaline earth cations [17]. The Al–O bond length is slightly longer than the Si–O bond (approximately 1.75 Å), reflecting aluminum's larger ionic radius [17]. The tetrahedral coordination requires a nearby cation (e.g., Na^+ or Ca^{2+}) to compensate for the negative charge of the $\mathrm{AlO_4}$ unit. However, it has been shown that Na^+ ions are the predominant charge compensators for AlO_4 units, while Ca^{2+} plays a more limited role [20]. In some compositions, particularly those with high aluminum content or low modifier concentrations, aluminum can adopt higher coordination states, such as five- or six-fold coordination (AlO_5 or AlO_6), behaving as a network modifier [17]. These higher coordination states are less common in nuclear waste glasses but can influence properties such as viscosity and chemical durability.

Sodium and Calcium Coordination

Sodium and calcium, as network modifiers, do not form part of the covalent network but instead occupy interstitial sites, balancing the charge of non-bridging oxygens or tetrahedral units like AlO_4 or BO_4 [17]. Sodium typically has a coordination number of 5–6, with Na–O distances ranging from 2.3 to 2.6 Å, forming irregular polyhedra. Calcium, with a higher charge and smaller ionic radius, has a coordination number of 6–8, with Ca–O distances of approximately 2.3–2.5 Å [17]. The coordination environments of these modifiers are highly disordered, reflecting the amorphous nature of the glass. Their presence disrupts the network, increasing the number of NBOs and reducing the glass's viscosity, which is advantageous for processing but can compromise chemical durability if not carefully balanced [17].

Boron coordination

Boron plays a structurally versatile and chemically significant role in borosilicate glasses. Unlike silicon, which predominantly adopts a tetrahedral configuration in glasses, boron is capable of existing in both trigonal $\mathrm{BO_3}$ and tetrahedral $\mathrm{BO_4}$ coordination states [17]. This dual behavior makes boron uniquely sensitive to changes in glass composition, particularly the ratio of network modifiers like sodium oxide

Na_2O to glass formers such as boron oxide B_2O_3 and silicon dioxide SiO_2 [17].

Importantly, boron also plays a vital role during vitrification by lowering the melting temperature and improving the processability of glass melts, making it easier to incorporate a wide range of waste elements [17]. This compositional dependence has a profound impact on the connectivity of the glass network and is especially important for designing glasses used in high-performance applications such as nuclear waste immobilization [17].

One of the most well-known phenomena associated with boron in glasses is the "boron anomaly." [17] In borate and borosilicate glasses, the addition of Na_2O initially results in an *increase* in network connectivity. This is because sodium ions help convert BO_3 units into BO_4 units, which form strong, three-dimensional connections similar to those of SiO_4 tetrahedra. This behavior leads to non-linear trends in glass properties, such as an initial increase in density, glass transition temperature, and elastic modulus with increasing alkali content—an effect referred to as the boron anomaly. To quantify the proportion of tetrahedrally coordinated boron in glass, the parameter N_4 is commonly used, defined as

$$N_4 = \frac{[BO_4]}{[BO_3] + [BO_4]} \tag{1.3}$$

The value of N_4 ranges from 0 (all boron in trigonal coordination) to 1 (all boron in tetrahedral coordination). To predict how N_4 changes with composition, Yun and Bray, followed by Dell et al., proposed a structural model based on experimental NMR data for ternary glasses containing SiO_2, B_2O_3, and Na_2O [21], [22]. They introduced two compositional ratios:

- $R = {}^{[Na_2O]}/_{[B_2O_3]}$: the molar ratio of boron oxide to sodium oxide,
- $K = {}^{[SiO_2]}/_{[B_2O_3]}$: the molar ratio of silica to boron oxide.

The maximum proportion of tetrahedral boron ($N_4 = 1$) is reached at a critical modifier-to-boron ratio, R_{max}, defined by

$$R_{max} = \frac{K}{16} + \frac{1}{2} \tag{1.4}$$

For compositions where $K \geq 8$, the system follows:

- If $R \leq R_{max}$, then $N_4 = R$;
- If $R > R_{max}$, then $N_4 = 1$.

To extend this model to cases where $K < 8$, Dell, Bray, and Xiao introduced the DBX model [22], [23]. It defines four structural regimes that describe how Na_2O interacts with boron species in the glass:

1. **Regime I ($R < 0.5$)**: In this regime, all Na_2O is used to convert BO_3 units into BO_4. The network becomes highly polymerized, and N_4 increases sharply, often approaching 1 [22], [23].

2. **Regime II ($0.5 \leq R \leq R_{max}$)**: Additional Na_2O supports the formation of reedmergnerite-type structures where BO_4 units link with SiO_4 tetrahedra, further strengthening the network.

3. **Regime III ($R_{max} < R \leq R_{D1}$)**: Beyond BO_4 saturation, excess Na_2O generates non-bridging oxygens (NBOs) on silicate tetrahedra, reducing network connectivity. The transition point is given by:

$$R_{D1} = \frac{1}{2} + \frac{K}{4} \tag{1.5}$$

4. **Regime IV ($R_{D1} < R \leq R_{D3}$)**: Sodium begins to interact with diborate units, further breaking down the network and increasing its vulnerability to corrosion. The fraction of tetrahedral boron is given by:

$$N_4 = N_{4,\max} - \frac{0.25}{1+K}(R - R_{\max}) \tag{1.6}$$

The upper limit of this regime is defined by:

$$R_{D3} = 2 + K \tag{1.7}$$

An alternative expression for N_4, applicable near $R_{\max}$, is:

$$N_4 = \frac{8+K}{12} - R \cdot \frac{8+K}{12(2+K)} \tag{1.8}$$

To improve the accuracy of the original model, Manara et al. [24] proposed a refined equation for $R_{\max}$, accounting for specific structural units:

$$R_{\max} = \frac{1}{2} + \frac{K}{2N} \tag{1.9}$$

Here, N depends on the dominant structural motif:

- $N = 5$ for danburite-type units ($Na_2O{\cdot}B_2O_3{\cdot}2SiO_2$),
- $N = 6$ for reedmergnerite-type units ($Na_2O{\cdot}B_2O_3{\cdot}6SiO_2$).

The DBX model overestimates N_4 in glasses containing Al_2O_3, as it does not account for aluminum's contribution to the tetrahedral network. To resolve this, Du and Stebbins introduced the D&S model [25], which modifies the DBX ratios:

- $R' = \frac{[Na_2O]}{[B_2O_3]+[Al_2O_3]}$,

- $K' = \frac{[SiO_2]}{[B_2O_3]+[Al_2O_3]}$.

The total fraction of tetrahedrally coordinated boron and aluminum (N_4') is first calculated using the DBX model with these modified ratios. The specific fraction of four-coordinated boron is then obtained via:

$$N_4 = \frac{N_4' \cdot (B_2O_3 + Al_2O_3) - Al_2O_3}{B_2O_3} \tag{1.10}$$

Other Elements

Other elements, such as zirconium, molybdenum, and actinides (e.g., uranium, plutonium), may be present in nuclear waste glasses, particularly in complex compositions like France's R7T7 glass. Zirconium typically adopts a six-fold coordination (ZrO_6), acting as an intermediate or modifier , and can enhance chemical durability by strengthening the network . Molybdenum often forms isolated MoO_4 tetrahedra or clusters , which can lead to phase separation if not properly incorporated . Actinides, due to their large ionic radii, tend to occupy high-coordination sites (6–8), behaving as modifiers and requiring careful integration to prevent crystallization or leaching [17].

Conclusion

Glasses derive their properties from their amorphous networks, where silicon, boron, and aluminum are central to the overall connectivity. The distribution of these species governs both mechanical strength and chemical reactivity. Modifiers such as sodium or calcium break up the network, while aluminum tends to reinforce it when properly charge-balanced. Boron, in contrast, is easily leached, creating sites of weakness in the gel that develops during alteration. The way these elements are incorporated into the initial structure is thus directly reflected in the resistance of the glass to corrosion.

1.3 Glass Alteration

When a glass comes into contact with water, it undergoes a series of transformation processes collectively known as glass alteration. This includes the conversion of the glass into solid alteration products and dissolved aqueous species [15].

Glass alteration progresses through several well-defined stages, as illustrated in Figure 1.4 [26]. The process begins with an initial stage characterized by a high dissolution rate, known as the initial dissolution rate. This is followed by a gradual decline in the rate of alteration, eventually reaching a much slower, steady-state rate

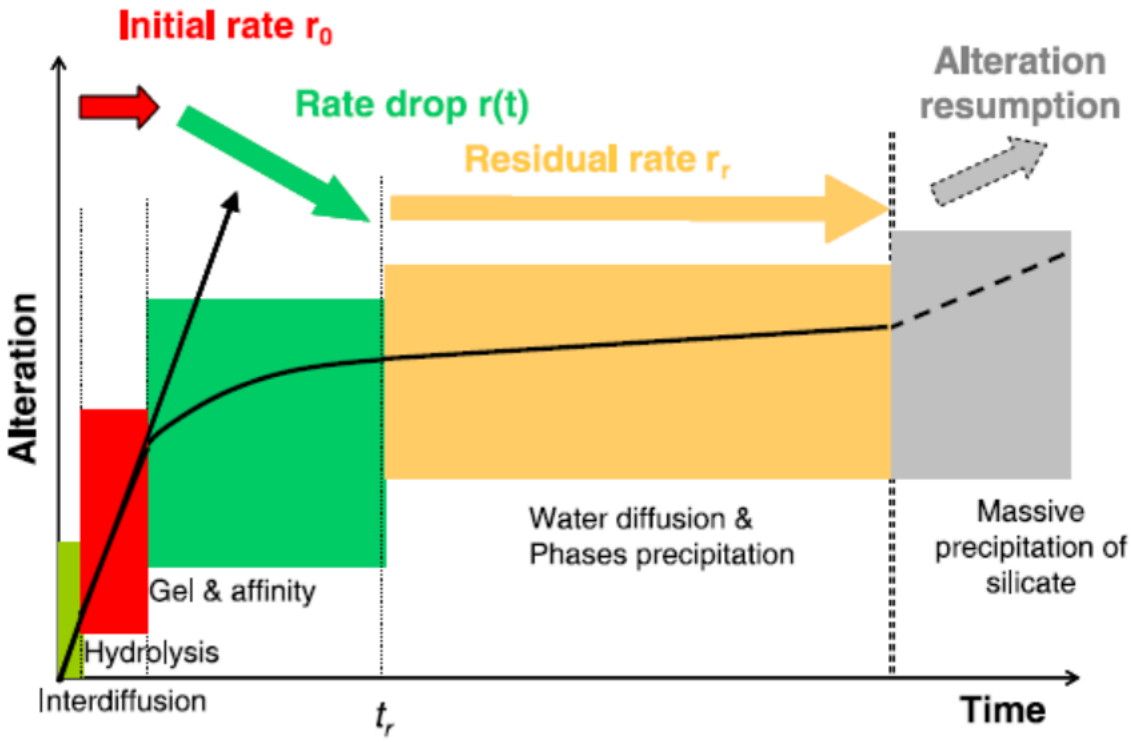

Figure 1.4: *The stages of nuclear glass alteration and their associated mechanisms vary based on the glass composition and leaching conditions, such as temperature, pH, solution composition, and renewal rate. The duration of each kinetic regime is influenced by these factors. [26]*

referred to as the residual rate. In some cases, a third stage may occur, during which the alteration rate can increase again, signaling a potential resumption of glass alteration [27], [28], [29] . Each of these stages exhibits distinct kinetic and mechanistic characteristics, influenced by factors such as the glass composition, the chemistry of the surrounding aqueous environment (e.g., solution pH, ionic strength), and external conditions like temperature.

A key feature in the alteration process is the formation of an alteration gel—a hydrated, amorphous layer that develops on the glass surface. This gel plays a crucial role in limiting further corrosion by serving as a diffusion barrier to reactive species. The gel's effectiveness is determined by its properties, including porosity, thickness, and chemical composition, all of which are closely tied to the glass's elemental constituents [14], [15]. Notably, boron and aluminum are critical in influencing the structure and protective capacity of this alteration layer [30].

1.3.1 Initial Dissolution rate

Overview and Mechanisms

The first stage of glass alteration, commonly referred to as the *initial dissolution regime*, is governed by processes occurring under far-from-equilibrium conditions, prior to solution saturation . Ion exchange represents the earliest and most rapid mechanism, whereby alkali ions such as sodium Na^+ and lithium Li^+ are replaced by protons or hydronium ions H^+/H_3O^+ from the contacting solution. This exchange is particularly enhanced under acidic conditions (pH < 7) and results in the formation of a dealkalized surface layer depleted in network modifiers . The removal of these mobile cations weakens the glass structure and facilitates further alteration [3], [31].

Concurrently, hydrolysis of the glass network is initiated, involving nucleophilic attack by water molecules on covalent bonds—particularly Si–O–Si, Si–O–B, and Si–O–Al. This reaction leads to the formation of silanol (Si–OH) and boranol (B–OH) groups, progressively destabilizing the glass network . Among these bonds, Si–O–B bonds are most susceptible to hydrolytic cleavage due to their lower bond energy, making boron-rich glasses especially prone to rapid dissolution [31], [32]. The combined action of ion exchange and hydrolysis results in congruent dissolution of the glass, characterized by the proportional release of key constituents such as silicon, boron, sodium, and aluminum into the aqueous phase .

Kinetics and Influencing Factors

The kinetics of initial dissolution are governed by a complex interplay of factors, including glass composition, temperature, solution chemistry, and surface area [33]. Dissolution rates during this stage typically range from 1 to 50 $g{\cdot}m^{-2}{\cdot}d^{-1}$ for borosilicate nuclear waste glasses, while broader glass families (e.g., alkali-rich silicates, phosphates) can exhibit significantly higher rates under comparable conditions [33]. Temperature is a primary driver: higher temperatures enhance the rate of bond cleavage, leading to faster release of glass components.

Solution chemistry, particularly pH, plays a critical role in modulating the balance between hydrolysis and ion exchange [10], [34]. In acidic environments, ion exchange dominates, as protons readily replace alkali ions, while in alkaline conditions (pH > 9), hydrolysis of Si–O–Si and Si–O–B bonds is favored, often leading to the formation of a silica-rich surface layer [34]. The initial dissolution rate far from equilibrium, r_0, can be described by the following equation 1.11.

$$r_0 = k_i \left[\exp\left(\frac{-E_{a,H^+}}{RT}\right) a_{H^+}^{\eta_{H^+}} + \exp\left(\frac{-E_{a,H_2O}}{RT}\right) + \exp\left(\frac{-E_{a,OH^-}}{RT}\right) a_{OH^-}^{\eta_{OH^-}} \right] \tag{1.11}$$

The initial dissolution rate r_0, expressed in units such as $mol{\cdot}m^{-2}{\cdot}s^{-1}$, depends on contributions from acid-, water-, and base-activated mechanisms. The terms E_{a,H^+},

E_{a,H_2O}, and E_{a,OH^-} represent the activation energies (in kJ·mol^{-1}) associated with each of these pathways. The activities of the hydrogen and hydroxide ions, denoted by a_{H^+} and a_{OH^-}, are dimensionless and reflect the effective concentrations of these species. Their respective reaction orders are given by η_{H^+} and η_{OH^-}. The gas constant R appears in the Arrhenius-type exponential terms and has units of kJ·mol^{-1}·K^{-1}, while T is the absolute temperature in Kelvin. Finally, k_i is the intrinsic rate constant, which scales the overall reaction rate and has the same units as r_0 [35].

Glass composition is a fundamental determinant of the initial dissolution rates. Boron-rich glasses exhibit higher rates due to the prevalence of hydrolysable Si–O–B bonds, which form a sub-network that is easily disrupted by water [36]. Conversely, glasses with elevated zirconium content demonstrate greater resistance, as Zr acts as a strong network former that stabilizes the silicate network [37]. The role of aluminum is more complex. Its influence depends strongly on its concentration in the glass and on the alteration regime under consideration. At relatively low concentrations (around 3.5 mol%), Al tends to reduce dissolution by reinforcing the silicate network, as AlO_4 tetrahedra increase the strength of Si–O bonds [38], [39], [40]. At intermediate levels (3.5–19 mol%), this beneficial effect persists, though less markedly. However, at higher concentrations (above 19 mol%), the overall alteration rate increases, likely due to the greater proportion of weaker Al–O bonds that are more susceptible to hydrolysis. The ratio of soluble (Na, Ca) to insoluble (Si, Al) elements also plays a key role: higher proportions of soluble species relative to network formers accelerate the initial dissolution rate [41].

1.3.2 Residual rate

Overview and Mechanisms

According to Grambow, borosilicate glasses corrosion never really stops but, unlike minerals, after achieving saturation concerning silica, there is a subsequent drop in the alteration rate, and corrosion is led by hydrolysis and release of soluble elements . A general rate law is given in equation 1.12.

$$r = r_0 \left(1 - \frac{[H_4SiO_4]}{K}\right) + r_r \tag{1.12}$$

In the equation 1.12, r is the corrosion rate of the glass, r_0 is the initial dissolution rate (mentioned in section 1.3.1) and $[H_4SiO_4]$ is the activity of orthosilicic acid at the glass interface and K denotes the equilibirium constant refering to the activity of orthosilicic acid at saturation. After the solution become silica saturated the dissolution rate stabilizes at a low, steady-state value known as the residual rate r_r.

During this stage, hydrolysis of residual Si–O–Si and Si–O–Al bonds continues,

albeit at a significantly reduced rate, driven by the diminished chemical affinity in silica-saturated solutions [16]. The alteration gel acts as an effective diffusion barrier, with water diffusion coefficients ranging from approximately 10^{-9} $m^2 \cdot s^{-1}$ in connected pores to as low as 10^{-23} $m^2 \cdot s^{-1}$ in closed pores [15], [42]. The gel thus formed is not a static entity and evolves over time [16], [43]. The morphology of the gel and its evolution are discussed in detail in the coming section 1.3.5.

The residual alteration stage is critical for assessing the long-term durability of alumino-borosilicate glasses, as it reflects their ability to resist corrosion over extended timescales. The residual rate serves as a key metric for predicting the material's performance in aqueous environments, informing the design of glasses for applications requiring sustained stability. Understanding the factors that govern r_r, particularly the role of the alteration gel, is essential for developing compositions that minimize corrosion and maintain structural integrity.

1.3.3 Resumption of alteration

After the residual rate regime, glass alteration may resume, a stage often referred to as Stage 3. This resumption occurs when solution conditions destabilize the alteration gel. At high pH (pH > 10.5) and/or elevated temperatures (T > 90 °C), zeolitic secondary phases can precipitate, incorporating silicon and aluminum from the gel [27], [28], [29]. Similar processes are promoted by the presence of cations such as Mg or Fe, which enhance secondary phase precipitation and remove silicon from solution [44]. As these phases grow at the expense of the gel, its protective capacity decreases, leaving more glass surface exposed to attack. Under these conditions, the alteration rate rises again after the residual regime, but it remains lower than the initial dissolution rate, as shown in Figure 1.4.

1.3.4 Experimental characterization of glass alteration

Techniques such as inductively coupled plasma (ICP) methods, time-of-flight secondary ion mass spectrometry (ToF-SIMS), small-angle X-ray scattering (SAXS), and transmission electron microscopy (TEM) are commonly employed to measure the alteration rate, with ICP providing direct quantification of elemental release that defines the residual rate. ICP techniques, including ICP-mass spectrometry (ICP-MS) and ICP-optical emission spectroscopy (ICP-OES), analyze leachate solutions to detect elements released during glass alteration. ICP-MS offers high sensitivity, detecting trace elements such as boron and sodium at parts-per-trillion levels, while ICP-OES is effective for major elements such as silicon and calcium. These measurements enable precise determination of residual rates, often as low as 10^{-4} $g/m^2/d$ in borosilicate glasses, by tracking elemental release over time. ToF-SIMS complements ICP by analyzing the surface chemistry of altered glass, mapping elemental

depletion (e.g., B loss) or enrichment (e.g., Si, Al) in the top few nanometers, thereby providing a mechanistic explanation for the protective layers inferred from ICP data.

SAXS and TEM provide structural and morphological information that complements the chemical quantification obtained by ICP. SAXS probes nanoscale features (1–100 nm), such as porosity in the alteration gel, revealing how changes in pore size and distribution influence the transport of water and solutes, and hence the dissolution rates measured by ICP. For example, denser gels with smaller pores correlate with lower residual rates in ICP-MS data. TEM, coupled with energy dispersive X-ray spectroscopy (EDS), provides atomic-resolution imaging and compositional analysis of altered layers, identifying features such as silica-rich gels or crystalline precipitates that act as barriers to further dissolution. These altered layers, typically 10–100 nm thick, are consistent with the low residual rates detected by ICP in nuclear waste glasses. By combining the quantitative elemental release data from ICP with surface information from ToF-SIMS, nanoscale structural insights from SAXS, and high-resolution imaging from TEM, researchers obtain a comprehensive understanding of the mechanisms controlling the residual rate.

1.3.5 Alteration dynamics of gel: Formation to Passivation

This section is structured to move from mechanisms to consequences. We begin with the fundamental *gel formation mechanisms*, outlining the two main conceptual models (classical interdiffusion and dissolution–precipitation) and illustrating how they apply to different glass compositions (CJ1 vs. CJ2). We then turn to the *morphology of the gel*, where microscopic observations highlight the development of porosity, density gradients, and the role of silica and alumina enrichment in passivation. Next, we consider *transport and maturation of the alteration gel*, emphasizing how pore reorganization and self-healing processes progressively reduce diffusivity and water accessibility. Finally, we examine the *role of boron and aluminum*, showing how these elements modulate both the kinetics and the structural pathways of gel formation and maturation.

Gel formation Mechanisms

During the transition from initial dissolution to the residual rate regime, both thermodynamic and kinetic transport-limiting effects work in conjunction . The thermodynamic effect arises from a reduction in the chemical affinity for the hydrolysis of the silicate network (Si -O -*M* bonds, where *M* represents glass formers). On the other hand, the transport-limiting effect is associated with the formation of a Si-rich gel layer.

The alteration gel that forms in these conditions is a hydrated, amorphous layer that forms on the glass surface during aqueous corrosion, serving as the primary

barrier against further degradation. It forms isovolumetrically, i.e., the gel occupies the same volume as the altered glass, and is mainly composed of silica, but can also incorporate poorly soluble elements such as Al, Zr, and Ca . The gel reduces further alteration by limiting both water diffusion and reactivity at the alteration front[45], [46].

Two main models have been proposed to explain gel formation. The *classical interdiffusion model* (CID) [47], [48] considers the formation of a hydrated glass zone by ion exchange, followed by hydrolysis of Si–O–Si bonds and subsequent *in situ* condensation of silanol groups, leading to a reorganized silica-rich framework. In contrast, the *interfacial dissolution–precipitation* (IDP) model proposes that gel formation occurs via congruent glass dissolution, followed by reprecipitation of dissolved species once the solution becomes supersaturated with silica [49], [50].

Neither model alone fully accounts for observed concentration profiles and isotopic tracers in the gel. Instead, it is now accepted that both mechanisms may coexist, depending on glass composition and alteration conditions [32]. In the dissolution/precipitation pathway, glass components dissolve congruently into the solution, reaching supersaturation and precipitating as a silica-rich layer [49], [50]. This mechanism is more prevalent in glasses with low aluminum content, where silica solubility drives gel formation [50]. In contrast, the CID/*in situ* reorganization pathway involves the selective leaching of mobile elements, such as B, Na, and Ca, leaving behind a restructured silica- or aluminosilicate-rich network that forms the gel. This pathway is favored in aluminum-rich glasses, where the aluminosilicate framework resists complete dissolution [32], [42], [51].

These two mechanisms are very important to understand gel formation and there is no reason to oppose one model for the other[18] [36]. In fact, both may operate simultaneously, depending on composition and solution chemistry. Gel formation is highly composition-dependent. For instance, comparative studies of two simplified borosilicate glasses, CJ1 (aluminum-free) and CJ2 (aluminum-bearing), revealed that even slight differences in chemistry can result in different alteration pathways and gel properties [52], [53]. The tests were performed at 90°C in a solution of pH 9 saturated with respect to amorphous silica to favour an early formation of the passivating gel. CJ1 released silica into the silica-saturated solution, indicating that CJ1 is more soluble than amorphous silica, and it can be deduced that Si saturation limit is composition dependent [52].

The glass containing Al exhibited slower dissolution kinetics, consistent with previous experimental and modeling studies [38], [53]. In CJ1, rapid dissolution leads to a significant release of both Si and B into solution, even under conditions initially saturated with amorphous silica. Isotopic tracing shows that the outer gel is enriched

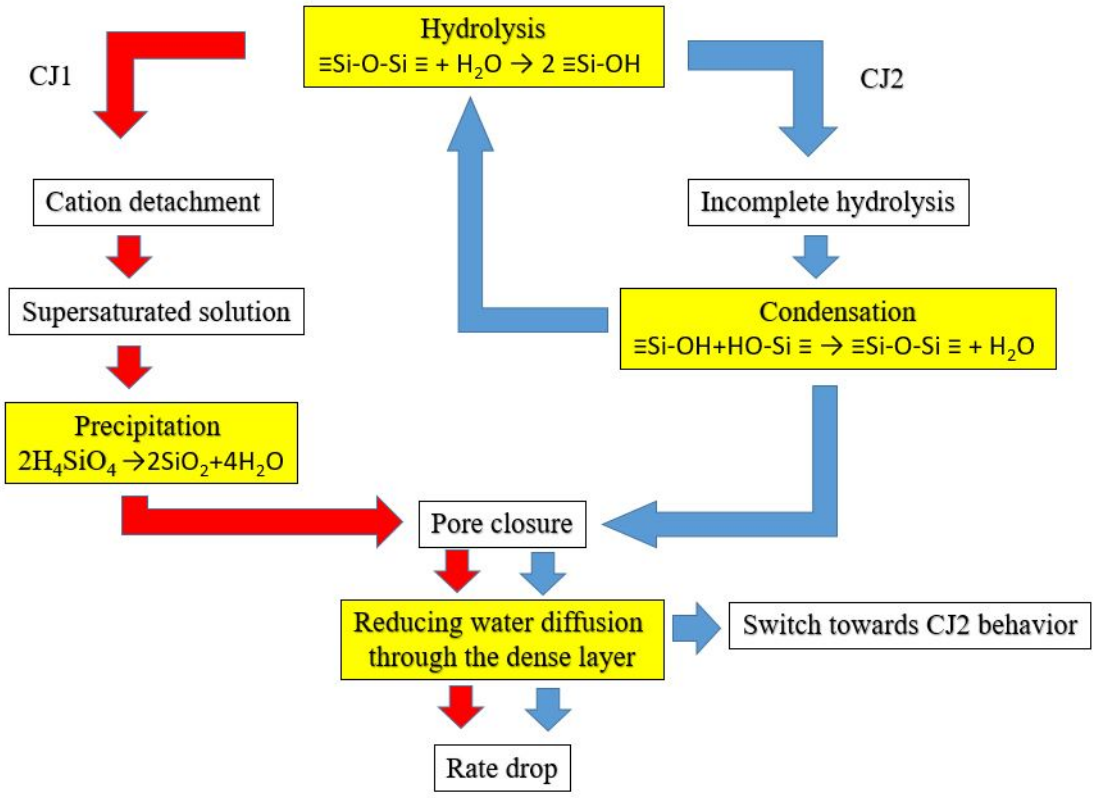

Figure 1.5: *Different dissolution behavior of CJ1 and CJ2*

in ^{29}Si, reflecting extensive dissolution of the network followed by reprecipitation once the solution reached supersaturation. This process results in the formation of silica sols and a dense water-facing layer that progressively limits transport, explaining why CJ1 achieves passivation despite its higher intrinsic solubility. In contrast, CJ2 undergoes only limited hydrolysis of the silicate framework due to the presence of Al. The measured B release is much lower, and most of the gel retains the isotopic signature of the pristine glass, indicating that network reorganization occurs mainly *in situ* rather than through dissolution and reprecipitation. The incorporation of Al strengthens the network, reduces Si mobility, and favors the development of a nanoporous but mechanically rigid gel that progressively densifies over time. This delayed restructuring slows the approach to steady-state conditions but ultimately produces a more effective passivating layer than in CJ1, as seen by the lower long-term residual rate. These contrasting behaviors highlight that CJ1 is governed by rapid dissolution and precipitation-driven gel formation, while CJ2 is dominated by incomplete hydrolysis and *in situ* condensation processes. This experimental evidence complements the conceptual mechanisms summarized in Figure 1.5.

Morphology of the gel

The alteration gel formed during glass corrosion is a generally amorphous and porous material whose porosity and density evolve with both time and glass composition. Figure 1.6 shows a sequence of SEM images at different magnifications highlighting the morphology of such gels.

In Figure 1.6a, the gel layer appears as a lighter zone on top of the unaltered glass, illustrating the development of an alteration film several hundred nanometers thick. A closer view (Figure 1.6b) reveals the heterogeneous structure of the gel, with a denser external region at the interface that acts as a diffusive barrier. At even higher magnification (Figure 1.6c), nanometer-scale porosities are observed, characteristic of the reorganized gel network.

The gel is enriched in silica and, in aluminum-bearing glasses, alumina, while mobile elements such as boron and sodium are preferentially leached. In boron-rich glasses, this extensive depletion increases porosity, as the removal of boron generates silanol groups that subsequently condense, modifying the connectivity of the gel network. Over time, reorganization processes produce a density gradient, with the densest zone forming near the glass–gel interface, thereby reducing species transport and slowing alteration kinetics [45], [46], [54].

Both the external and internal regions of the gel can contribute to reduced alteration. Depending on how the gel is formed (as discussed in the previous section), different portions of the gel act as the primary diffusion barrier. For instance, in CJ1 glass, the formation of a dense external layer leads to passivation, whereas in CJ2 glass, it is the inner part of the gel network that provides the dominant barrier to transport [52]. The transport properties of gel is discussed in Section 1.3.5

Thus, the protective character of the gel arises both from its chemical composition (retention of network formers such as Si and Al, partial incorporation of Ca or Zr) and from its evolving morphology, which transitions from open porosity to a compact structure capable of passivating the glass surface.

Transport and Maturation of the Alteration Gel

The gel layer's properties, particularly its pore network, can evolve over time, through a process known as gel maturation [52]. In general, small pores connect together over time to create bigger pores leading to diminishing pore connectivity . This happens through hydrolysis and condensation reactions which minimizes the free energy of the gel [55], [56], [57]. This process transforms open channels into isolated pores, significantly lowering water diffusivity and restricting water access to the pristine glass [42].

A systematic study was conducted on International Simple Glass (ISG), a six-oxide

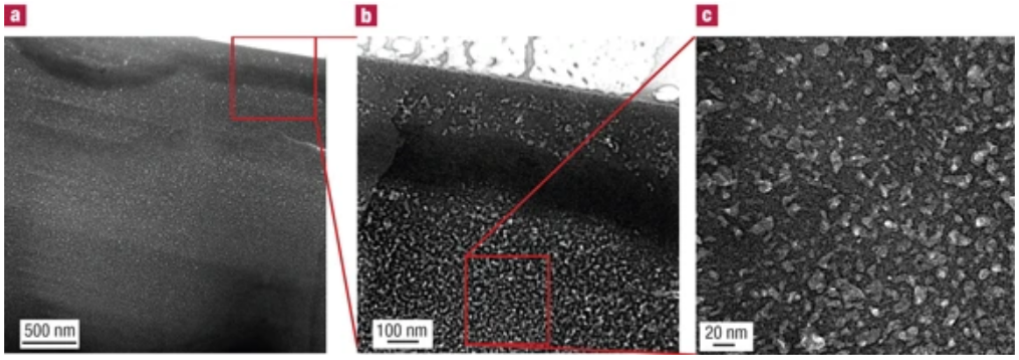

Figure 1.6: *SEM images of an alteration gel at different scales [46]: (a) cross-sectional view showing the gel (lighter contrast) on top of the unaltered glass, (b) zoom on the gel revealing a denser external zone, (c) high-magnification view of nanometer-scale porosities in the gel network.*

borosilicate reference composition widely used to model nuclear waste glass alteration [42]. The aim was to investigate how water penetrates and interacts with the passivating gel layer, and how the pore structure reorganizes over time to influence transport. To this end, isotopic tracing experiments were performed using $H_2{}^{18}O$, which provide direct insight into both water ingress through open pores and oxygen exchange within the reorganized gel network.

In this experimental design, ISG samples were first altered under reference conditions (90 °C, pH 7, solution saturated with respect to amorphous silica). After one year, the glass developed a 1.5 µm amorphous gel layer formed by reorganization of the Si–Zr–Al network, with a pore size of about 1 nm. These altered samples were then immersed in solutions containing $H_2{}^{18}O$ for durations ranging from a few minutes to three months. Depth profiles of oxygen isotopes were subsequently measured by time-of-flight secondary ion mass spectrometry (ToF-SIMS).

The measurements showed that water penetrates the gel rapidly, reaching the pristine glass interface within minutes . However, the exchange of ^{18}O with ^{16}O in the gel network remained limited, especially in mature gels where closed pores dominate, indicating restricted oxygen mobility and enhanced passivation. A measurable exchange of ^{18}O with ^{16}O was observed after only three minutes of immersion, and the $^{18}O/^{16}O$ profile showed that exchange increased over time but never approached full equilibration (Figure 1.7).

The result from the experiment above is consistent with the network of pores made up of substantially penetrative open channels as well as closed pores that hinders the exchange between the silanols and water molecules. The basic assumption being that the water molecules randomly explore their path in the open porosity

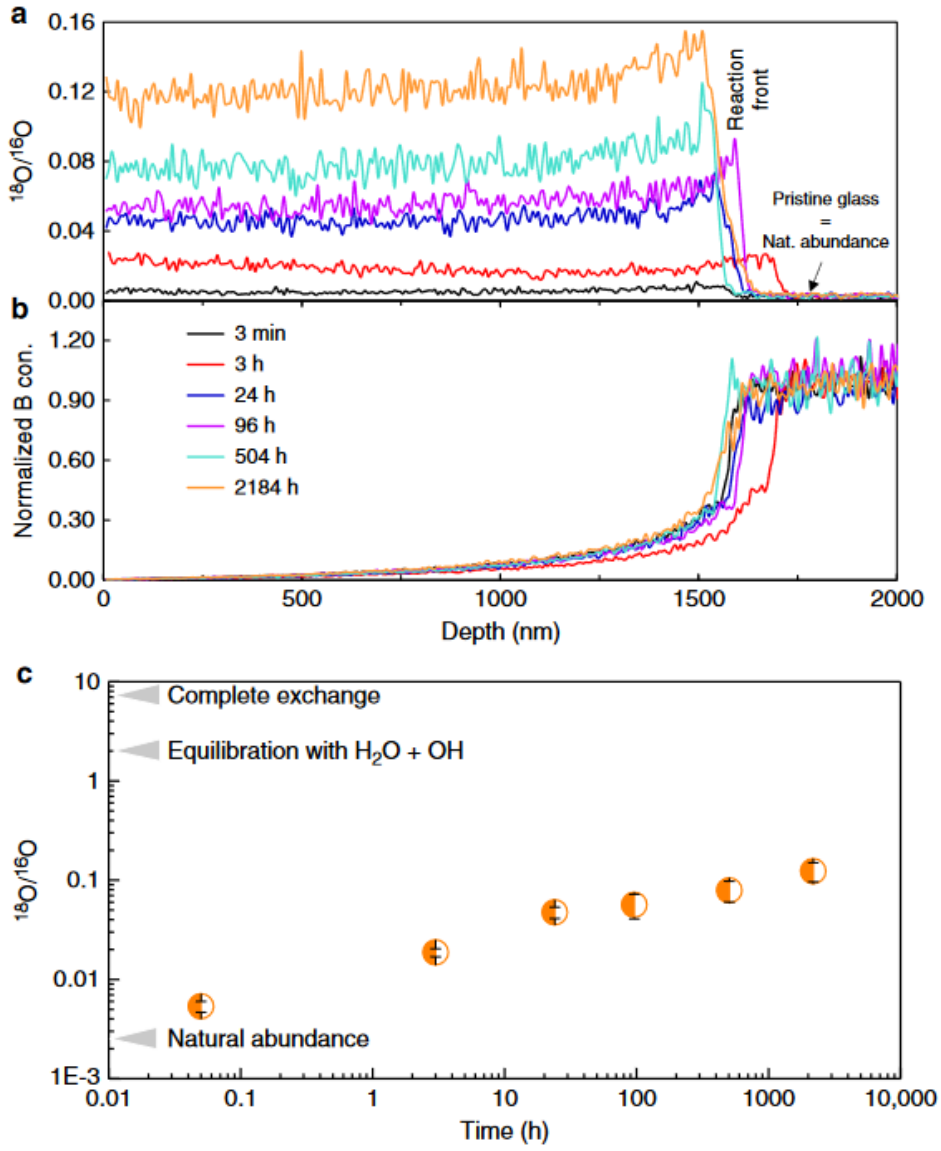

Figure 1.7: *Water mobility in the gel monitored by time-dependent ToF-SIMS. (a) Quantitative $^{18}O/^{16}O$ profiles for different contact durations; the pristine glass value (2.2×10^{-3}) agrees with natural abundance. (b) Normalized B profiles for the same durations; the alteration front ($C/C_0 = 0.5$) is at 1574 ± 20 nm. B profiles are anti-correlated with $^{18}O/^{16}O$, indicating tagged water reached the dissolution front, with some B retained in the gel (undissolved clusters). (c) Mean $^{18}O/^{16}O$ ratio in the gel vs. contact time, with error bars from pristine glass uncertainties [42].*

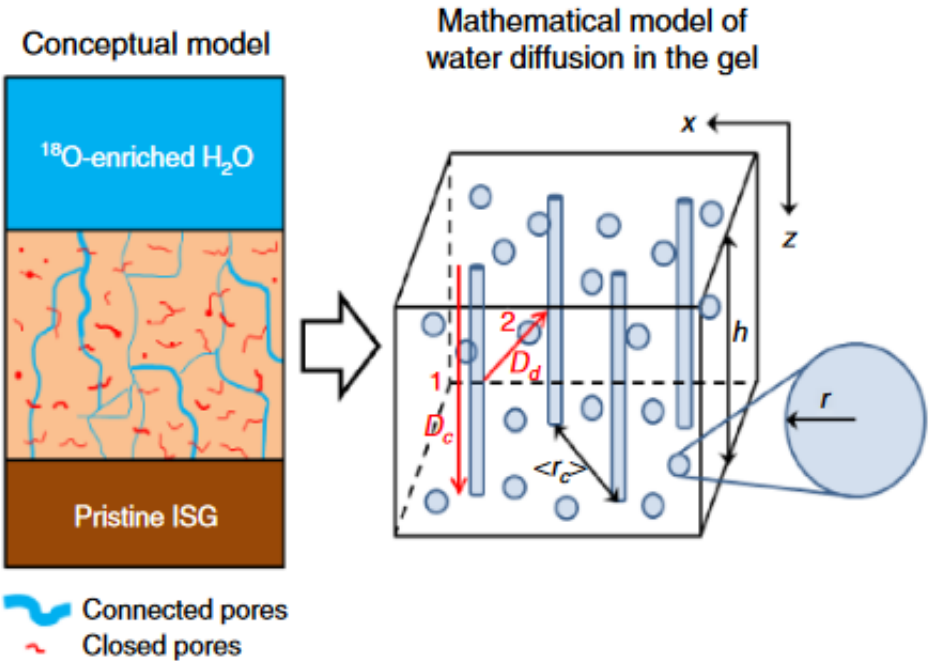

Figure 1.8: *Conceptual and mathematical model of water diffusion in passivating gels. Left: schematic representation where the gel contains spherical pores (mean radius r), with some connected in aggregates modeled as cylinders (mean separation $\langle r_c \rangle$) spanning the solution/gel to gel/glass interface. Right: mathematical model used to derive water diffusion coefficients. Two exchange modes are shown in red, with diffusion coefficients D_c and D_d [42].*

and interact with Si-O-M (Si, Al or Zr) and undergo hydrolysis and condensation along their path. A simplified model corresponding to diffusion of water molecules in the gel structure is shown in Figure 1.8.

The interpretation of the experimental isotopic exchange results was carried out using a continuum diffusion model that *assumes* water transport occurs through both connected and closed pores. In this framework, the diffusion coefficient in connected pores, D_{C}, is expected to be greater than $10^{-11}\,\mathrm{m^2 s^{-1}}$, consistent with open pathways that allow relatively fast water movement. In contrast, diffusion into closed or dead-end pores, D_{d}, decreases markedly over time, reflecting the progressive self-reorganization of the gel. Within one day, D_{d} dropped to approximately $10^{-21}\,\mathrm{m^2 s^{-1}}$, and after about 90 days it reached $6 \times 10^{-23}\,\mathrm{m^2 s^{-1}}$. This behavior suggests that the gel acts as a selective filter containing a limited number of connected channels and a large fraction of closed pores, which together strongly restrict water diffusion [58]. It is important to emphasize that this model represents an *assumption-based interpretation*, not a direct measurement of diffusivity.

Water transport was also investigated at the nanometer scale (0.5–4 nm pores) us-

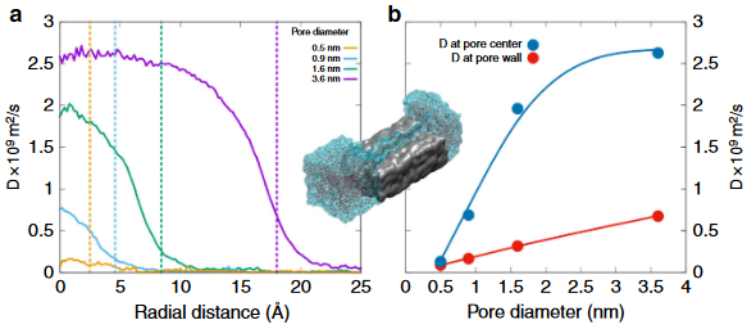

Figure 1.9: *Self-diffusion of water in amorphous silica pores. (a) Radial profiles of water diffusion coefficients in cylindrical pores of diameters 0.5, 0.9, 1.6, and 3.6 nm from reactive force field MD simulations. Diffusion is higher at the pore center, where water is less constrained, and reduced near oxygen-terminated, rough pore walls that undergo structural changes upon hydration. Dashed lines mark pore walls. (b) Mean diffusion coefficients at pore centers and walls across pore sizes. Inset: Snapshot of the 0.9-nm pore system, with part of the silica removed (gray) to reveal confined water (blue) [42].*

ing molecular dynamics (MD) simulations with reactive force field potentials [42]. A major result was that water molecules close to pore walls experienced reduced mobility due to hydrogen bonding with silanol groups and oxygen ions on the glass surface, whereas water molecules in the pore center diffused more freely. This spatial heterogeneity implies that overall water diffusivity is reduced compared to the bulk liquid because of drag exerted near the walls. For pores larger than about 0.5 nm, however, the confinement effect on diffusion was relatively minor, as illustrated in Figure 1.9.

Role of boron and aluminum in Alumino-Borosilicate Glass Alteration

Boron in alumino-borosilicate glasses can exist in trigonal BO_3 or tetrahedral BO_4 coordination, depending on the presence of alkali or alkaline earth cations [41]. Its incorporation into the silicate network forms Si–O–B bonds, which are more susceptible to hydrolysis than Si–O–Si or Si–O–Al bonds, leading to higher initial dissolution rates. This is because the weaker Si–O–B bonds break more readily under aqueous attack, releasing soluble boron species (primarily $B(OH)_3$ and $B(OH)_4^-$) into solution along with alkalis such as Na.

In the residual alteration stage, however, boron's role changes fundamentally. The release of B during the early stages produces silanol-rich surfaces, which can undergo condensation to form new Si–O–Si bonds. This process reduces pore connectivity in the alteration gel, enhancing its passivating properties and lowering the residual corrosion rate [16]. The retention of B in the gel has been shown to hinder the dissolution of other soluble elements such as Na and Ca, indicating a coupled

behavior.

According to Gin et al. [16], the release rate of B in silica-saturated conditions—and by extension the residual corrosion rate—can be limited by three main mechanisms: (i) the rate of hydrolysis of B–O–Si bonds, parameterized as a function of pH and time for the diffusive regime (i.e., the stage where B release follows a parabolic, square-root-of-time dependence due to diffusion through the maturing Si-rich gel); (ii) the inward diffusion of H^+ or H_3O^+ through the passivating gel; and (iii) the outward diffusion of aqueous B species through the passivating gel, potentially accompanied by precipitation in nanopores. These mechanisms are interdependent and influenced by the structural evolution of the alteration gel.

The removal of B, Na, and Ca from the glass alters the alteration layer by promoting repolymerization of the silicate network, which then controls the release and transport of mobile species [32]. In neutral and basic pH, dissolution is generally congruent, whereas in acidic pH it is often incongruent, continuing until silica saturation marks the onset of passivation.

Beyond saturation, B dissolves until a significant fraction of gel pores close. The dissolution of Ca and Na is largely coupled to that of B and can be approximated with a first-order rate law including an affinity term for the pseudo-equilibrium between the Si-rich gel and bulk solution [16]. As the gel matures, its pore network evolves which sharply limiting water diffusion (see Section 1.3.5) and reducing the diffusivity of B(aq) and Ca(aq). [16], [58]

Elevated local concentrations of B(aq) and Ca(aq) at the glass interface can further slow B dissolution, with possible precipitation of borate or Ca–borate phases in the pores [16]. These processes collectively restrict water transport and reinforce the long-term stability of the passivating layer [16].

Diffusion properties are closely governed by the size and hydration of the mobile species. In altered glass, the nanoconfined, silica-enriched gel acts as a molecular sieve with pore sizes typically below 1 nm [58] , strongly hindering transport. Similar to the restricted mobility of water in nanoconfined environments, the diffusion of ions within this gel is also significantly reduced.

Aluminum, as a network former, plays a role that contrasts with that of boron in enhancing the structural integrity of alumino-borosilicate glasses. The incorporation of aluminum as a second neighbor to silicon primarily increases the energy barrier required for Si–O bond rupture, thereby strengthening the silicon network [38]. Nevertheless, the presence of aluminum also influences the dynamics of structural relaxation in more subtle ways. While it can promote local, short-range reorganization of the network, this tendency may simultaneously restrict the medium- to long-range rearrangements needed to close free volumes. As a result, the overall

maturation process of the glass is decelerated, despite the enhanced stability of the local silicon network [38], [53].

A similar structural role of aluminum is observed in the alteration gels formed on CJ1 and CJ2 glasses. The ^{27}Al MAS and ^{27}Al{^{1}H} REDOR NMR results indicate that aluminum remains largely embedded within the solid gel network and is only weakly accessible to pore water. Even in the altered state, Al does not form a highly hydrated, mobile species but instead contributes to a rigid, polymerized framework. This Al-rich network limits pore connectivity and weakens the development of an extended hydrogen-bonded proton network, as evidenced by the ^{1}H MAS and Hahn-Echo measurements. Consequently, aluminum plays a key structural role in gel densification and stabilization, indirectly governing transport by constraining water mobility [59].

In the residual alteration stage, aluminum's influence is more complex. High aluminum content can increase the residual rate by stiffening the aluminosilicate network, which slows the reorganization of the alteration gel and maintains higher pore accessibility [30], [41], [53]. This delay in gel maturation can lead to prolonged corrosion, as water and dissolved species continue to penetrate the gel more readily. Aluminum's role in gel formation and reorganization is a critical factor in determining residual rates [30]. The role of Al is similar to the role of Zr in glass which controls the residual rate by creating a rigid alteration gel with low rate of reorganization [56]. Recent work by Kamalesh et al. [53] compared glasses with low (SBNA1) and high (SBNA4) aluminum contents under silica-saturated conditions. SBNA1 ($63.0\,\%$ SiO_2, $18.7\,\%$ B_2O_3, $17.3\,\%$ Na_2O, $1.0\,\%$ Al_2O_3) has lower Al content than SBNA4 ($64.9\,\%$ SiO_2, $17.3\,\%$ B_2O_3, $13.7\,\%$ Na_2O, $4\,\%$ Al_2O_3). Figure 1.10 shows the alteration profiles of SBNA1 and SBNA4. Although SBNA1 exhibited a higher initial dissolution rate than SBNA4, its residual rate was lower. This behavior correlates with the observed retention of boron in the alteration gel of SBNA1, suggesting that boron retention can slow the long-term alteration process despite faster early-stage dissolution.

The interplay between boron and aluminum in alumino-borosilicate glasses is a delicate balance, with their effects modulated by their relative concentrations [41]. Boron's tendency to accelerate initial dissolution can be mitigated by the presence of aluminum, which strengthens the network and reduces early corrosion rates [38]. Conversely, aluminum's potential to hinder gel reorganization in the residual stage can be counteracted by boron's ability to generate silanol groups, promoting rapid condensation and passivation.

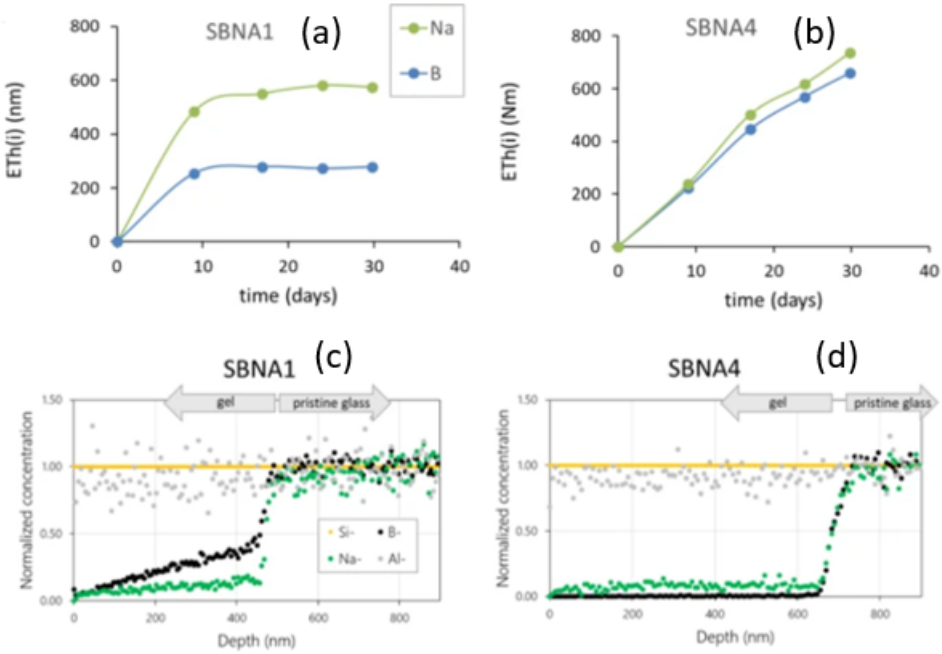

Figure 1.10: *Experiments conducted for 1 month in a Si-saturated solution at 90 °C. (a) Equivalent thickness of B and Na for SBNA1 glass. (b) Equivalent thickness of B and Na for SBNA4 glass. (c, d) ToF-SIMS depth profiles of B, Na, and Al (recorded in negative mode) normalized to Si for SBNA1 and SBNA4 [53]*

Conclusion

Glass alteration starts with a fast *initial dissolution stage*, where alkali ions are exchanged with protons and weak bonds such as Si–O–B break easily, releasing elements like B, Na, and Si into solution. The rate in this stage depends on composition, pH, temperature, and surface area, and can be described as the sum of acid-, water-, and base-activated pathways. As silica in solution approaches saturation, the process slows to a *residual rate*, controlled by both chemical affinity and the properties of the alteration gel. Under alkaline or high-temperature conditions, a third stage of *resumed alteration* may occur, driven by the precipitation of zeolitic phases that consume silica and weaken the gel. A passivating *alteration gel* forms during this evolution, either through direct reorganization of the glass network or through dissolution followed by reprecipitation; in practice, both mechanisms often operate together. The gel is silica-rich, may contain Al, Zr, or Ca, and its porosity and density change over time. With *gel maturation*, open pores reorganize into fewer connected pathways and many closed pores, reducing water and ion transport, as shown by isotope-tracing and molecular dynamics studies. *Boron* promotes fast initial dissolution because Si–O–B bonds break easily, but its early release also fosters silanol condensation that helps passivation and slows later release of B, Na, and Ca. *Aluminum* has the opposite effect: at low to moderate levels it strengthens the silicate network and lowers the initial rate, but at higher contents it stiffens the gel, slows its reorganization, and can raise the long-term residual rate. *Zirconium* plays a similar stabilizing role by reinforcing the network. Overall, the long-term durability of nuclear glasses depends on how composition, especially the balance between boron and aluminum, shapes the formation, structure, and slow maturation of the alteration gel.

1.4 Modelling glass corrosion

Computational simulations complement the experimental approaches outlined above by providing atomistic-to-mesoscale insight into glass–water interactions and corrosion. Methods span quantum mechanical models to mesoscale and macroscale frameworks (Fig. 1.11), each with distinct strengths and limitations. Together, these multiscale approaches offer complementary perspectives that clarify the underlying mechanisms driving glass corrosion [60].

Despite substantial progress, key challenges remain. The coupled processes of hydrolysis, ion exchange, and network dissolution are difficult to resolve at the

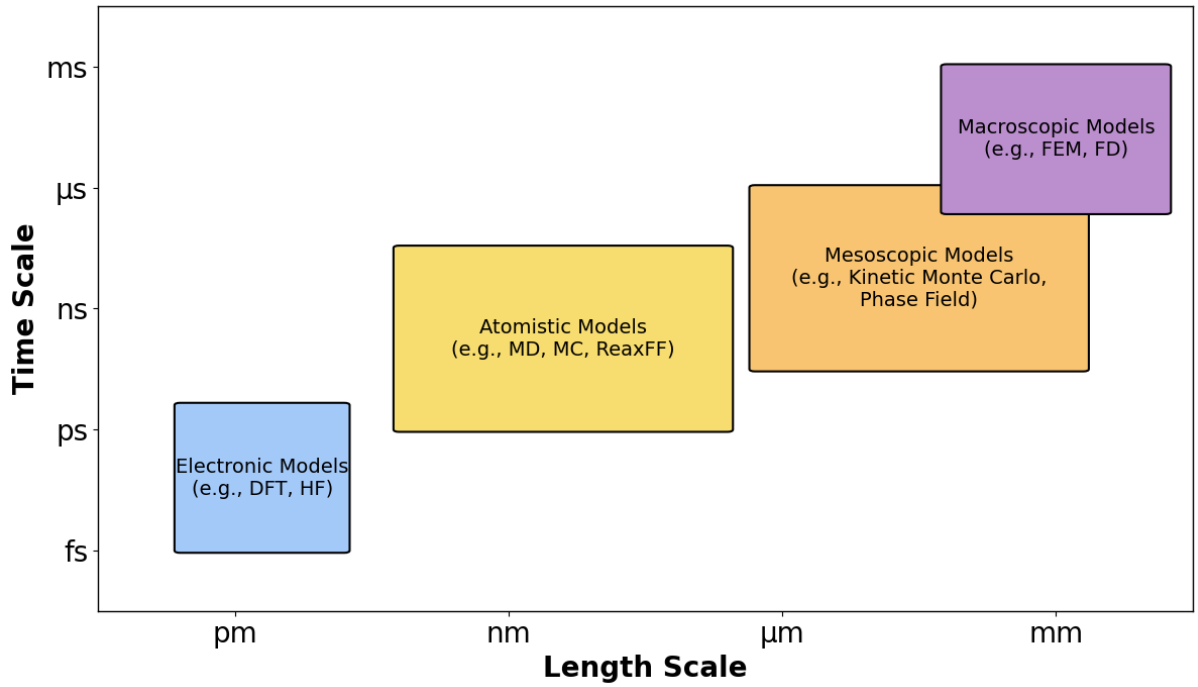

Figure 1.11: *Modelling approach at different stage*

atomic scale. The amorphous nature of hydrated glass and gel layers, combined with micro- and nano-porosity, complicates structural characterization. Moreover, capturing ion and water transport through evolving porous networks requires integrating experimental constraints with simulation to represent diffusion and permeability faithfully. The following sections summarize the characteristics and trade-offs of the main modeling scales used in this work.

We proceed from electronic to atomistic to meso–macro descriptions. Section 1.4.1 reviews *DFT* studies of bond hydrolysis, ion exchange, and pH effects at the atomic scale. Section 1.4.2 presents *classical molecular dynamics*: Subsec. 1.4.2 introduces force-field energy terms; Subsec. 1.4.2 covers rigid-ion models for structure and dynamics; Subsec. 1.4.2 treats polarizable models for interfacial response; Subsec. 1.4.2 discusses reactive and data-driven potentials for bond breaking, gel formation, and transport. Finally, Section 1.4.3 outlines *Monte-Carlo* approaches for the stochastic evolution of alteration layers and gel maturation, linking back to the multiscale view in Fig. 1.11.

1.4.1 DFT simulations

The interaction between glass and aqueous environments is a critical determinant of material durability. These interactions, occurring at the atomic scale, encompass hydrolysis, ion exchange, and the formation of alteration layers, which collectively govern the long-term chemical stability of glasses. In the literature, density func-

tional theory (DFT) has been widely employed to explore these mechanisms, and the results from previous studies have been summarized below, providing atomistic insights into the fundamental processes underlying glass–water interactions.

Hydrolysis Mechanisms and Energy Barriers

Hydrolysis, the process by which water cleaves glass network bonds, is fundamental to glass dissolution. DFT simulations provide detailed insights into the mechanisms and energy barriers associated with this process, particularly for Si–O–Si bonds prevalent in silicate glasses. Surface hydroxylation, when water molecules react with nonbridging oxygens (NBOs) or under-coordinated silicon atoms to form silanol (Si–OH) groups , is characterized as an activationless process, exhibiting no discernible energy barrier for proton transfer from the aqueous phase to the glass surface [61]. This rapid formation of silanol groups facilitates subsequent network degradation.

For Si–O–Si bond hydrolysis, DFT calculations indicate energy barriers ranging from 70 to 205 kJ·mol^{-1} on unconstrained silica and cristobalite surfaces [62], [63]. The presence of additional water molecules reduces this barrier by 20–40 kJ·mol^{-1}, as they stabilize transition states through proton transfer [64]. The connectivity of silicon atoms, denoted by Q_n speciation (where n represents the number of bridging oxygens per [SiO_4] tetrahedron), significantly influences reactivity. Silicon atoms with lower connectivity (Q_1, Q_2, Q_3) exhibit reduced barriers, although Q_2 configurations occasionally display higher activation energies, suggesting their potential as rate-limiting steps in dissolution [65].

Two primary mechanisms for Si–O–Si bond hydrolysis were identified. The first involves the coordination of a water molecule's oxygen to a silicon atom, forming a transient pentacoordinated silica defect (Si^5). This intermediate state precedes Si–O bond cleavage, with a proton transferring to the resulting NBO to form two Si–OH groups. The energy barrier for this proton transfer can reach 44 kJ·mol^{-1} [66]. The second mechanism, observed in small cluster models with a single water molecule, entails a water molecule's hydrogen atom bonding to the bridging oxygen, followed by Si–O–Si cleavage to yield two Si–OH groups. This pathway is less stable on hydroxylated surfaces, as bridging oxygens are weaker proton acceptors compared to water or terminal groups [67], [68].

Strained Si–O–Si bonds, such as those in two-membered rings (edge-sharing tetrahedra), demonstrate enhanced reactivity. DFT simulations report activation energies of 100–120 kJ·mol^{-1} with one water molecule and 60 kJ·mol^{-1} with two or three water molecules, reflecting the destabilizing effect of structural strain [69]. In molecular silica chains composed of linked two-membered rings, hydrolysis initiates centrally, with each ring exhibiting distinct energy barriers, underscoring the role of

local topology [70]. Larger ring structures, including three- and four-membered rings, also exhibit increased susceptibility to hydrolysis compared to six-membered rings, further highlighting the influence of strain [71].

Multicomponent Glass Systems

The incorporation of aluminum and boron in aluminosilicate and borosilicate glasses, commonly used in nuclear waste immobilization, introduces compositional complexity. DFT simulations of aluminosilicate glasses reveal that Si–O–Al bond hydrolysis in cluster models exhibits low energy barriers, ranging from 4 to 32 kJ·mol^{-1}, although these increase to 171 kJ·mol^{-1} in strained three-membered rings [72], [73]. The reaction proceeds via the Si^5 mechanism, with additional complexity arising from ion dynamics. Calcium ions (Ca^{2+}) transition from network modifiers to charge-compensating roles, while protons bind to bridging oxygens, altering the electronic environment and facilitating bond cleavage [74].

In borosilicate glasses, DFT studies indicate that B–O–B bonds have energy barriers of 98–129 kJ·mol^{-1}, while Si–O–B bonds range from 102–151 kJ·mol^{-1} [75]. Boron atoms coordinated with two bridging oxygens exhibit lower barriers, rendering them more reactive [76] . This compositional effect is critical, as boron leaching increases porosity in alteration layers, while aluminum retention enhances their stability, influencing long-term durability [51].

Ion exchange processes, particularly Na^+/H^+ exchange in borosilicate glasses, are energetically favorable and facilitate water diffusion into the glass matrix, initiating dissolution by cleaving Si–O–B bonds [77]. In bioactive glasses, DFT simulations reveal surfaces rich in NBOs, exposed network modifiers (Na^+, Ca^{2+}), and small rings, which are rapidly hydroxylated upon water exposure. Notably, two-membered rings in bioactive glasses are more stable than those in pure silica, suggesting competitive reactivity among surface sites [78], [79]. These findings elucidate how glass composition modulates dissolution kinetics and pathways, informing the design of materials for specific applications.

Environmental Effects: Influence of pH

The pH of the aqueous environment significantly affects glass-water interactions. DFT simulations have modeled pH effects by modifying structural configurations to simulate acidic or alkaline conditions. Protonated Si–O–Si bonds, indicative of low pH, exhibit an energy barrier of 65 kJ·mol^{-1}, while deprotonated bonds, representative of high pH, show 90 kJ·mol^{-1}, both substantially lower than the 147 kJ·mol^{-1} observed under neutral conditions [80]. This reduction accounts for the accelerated dissolution observed at extreme pH values, as protons or hydroxide ions destabilize network bonds.

In borosilicate glasses, an adsorbed proton on a bridging oxygen reduces energy

barriers by 50–100 kJ·mol^{-1} for B–O–B bonds and 45–70 kJ·mol^{-1} for B–O–Si bonds, enhancing reactivity in acidic environments [75]. Simulations incorporating hydronium ions (H_3O^+) with Si–O–Si bonds report a barrier reduction of 20–40 kJ·mol^{-1}, highlighting the destabilizing effect of excess protons [76]. Reactions involving hydroxide ions (OH^-) with neutral Si–OH surfaces yield barriers of approximately 80 kJ·mol^{-1} for Si^5 defect formation and 20 kJ·mol^{-1} for bond cleavage, reflecting the catalytic role of OH^- in alkaline conditions [76].

1.4.2 Classical molecular dynamics simulations

Molecular dynamics (MD) simulations have emerged as a pivotal computational technique in the study of glass corrosion, offering atomistic insights into processes that are otherwise challenging to capture experimentally due to the amorphous nature and long timescales involved in glass alteration [81]. While DFT allows for highly accurate modeling of specific reactions, classical MD simulations combine atomistic precision and time/length scales relevant to realistic corrosion processes. This section presents the role, methodology, and findings of classical molecular dynamics simulations in the context of glass corrosion, with a particular emphasis on insights into structure, dynamics, interfacial behavior, and gel formation.

Force field

To describe the potential energy of N interacting atoms, the total energy can be decomposed into several contributions. These include the individual (one-body) term U_i, the pairwise term U_{ij}, the three-body term U_{ijk}, and higher-order contributions that depend on the chemical and physical interactions present:

$$U = \sum_i U_i + \sum_i \sum_{j>i} U_{ij} + \sum_i \sum_{j>i} \sum_{k>j>i} U_{ijk} + \dots \tag{1.13}$$

For simulating the structural properties of oxide glasses and their interaction with water, atomic interaction potentials are often categorized into three major classes: (i) rigid ion models, (ii) polarizable ion models (PIM), and (iii) variable or diffusive charge models. In addition, many other empirical and machine-learned approaches have been developed in recent years, including models based on neural networks and Gaussian approximation potentials.

Rigid ion model

Rigid ion models, which describe interatomic interactions using fixed charges and empirical potential functions, have been central to these simulations . Over decades, these models have evolved from simplistic pair-wise potentials to sophisticated Machine learning potentials [82].

Rigid Ion Models for Glass Simulations. The development of rigid ion models for glass simulations began with pair-wise potentials, notably the Born-Mayer-Huggins (BMH) potential, which approximated atomic interactions as two-body forces combining long-range Coulombic attractions with short-range repulsive terms . The BMH potential captured the disordered network structure of silicate glasses but relied on full formal charges (e.g., Si^4 , O^2) , oversimplifying the partially covalent Si-O bond and leading to inaccurate bond lengths and structural defects, such as over-coordinated silicon ions . It also failed to reproduce boroxol rings in borate and borosilicate glasses [83], [84]. To address these limitations, three-body potentials were introduced in the late 1980s by Feuston and Garofalini, targeting O–Si–O and Si–O–Si triplets to account for angular dependencies. These potentials significantly improved agreement with experimental data for bond distances, tetrahedral angles, and network structures, enabling studies of the mixed alkali effect in silicate glasses, where ionic conductivity varies with cation substitution [85], [86], [87]. The transition to quantum-derived and empirical potentials marked further progress . Tsuneyuki's TTAM potential [88], using partial charges to reflect Si-O bond covalence, enhanced structural accuracy, while van Beest's BKS potential [89], parameterized with experimental and quantum data, accurately reproduced intratetrahedral angles without three-body terms, though it overestimated intertetrahedral angles and struggled with vibrational properties . The Pedone (PMMCS) potential [90] introduced a Morse potential for short-range interactions, parameterized against experimental crystal structures, and was extended to multi-component oxide glasses, improving mechanical property predictions. In 2018, Sundararaman's SHIK potential [91], [92], derived from ab initio MD simulations, used a Buckingham functional form and the Wolf truncation method, offering high accuracy for silicates, aluminosilicates, and borosilicates without empirical fitting.

Rigid Ion Models for Glass-Water Interactions. Efforts to model glass-water interactions through MD simulations have similarly advanced, focusing on surface chemistry and dynamics in aqueous environments . Early models employed pair-wise potentials with partial charge-based Coulombic terms and short-range repulsion-dispersion interactions. Garofalini's Rahman-Stillinger-Lemberg (RSL) potential was a pioneering development , enabling water molecule dissociation and supporting reactive simulations at silica-water interfaces. However, these early models often struggled to capture the full complexity of water dynamics at glass surfaces. There have been development of nonreactive, non-dissociable water models, such as TIP and SPC enabling detailed studies of water structure, dynamics, and surface phenomena like wettability [93], [94], [95], [96]. Other advanced force fields like ClayFF and CSH , which combine Coulombic and Lennard-Jones interactions with harmonic

bond and angle terms, effectively modeled ion transport and surface reactivity in silicates and clay-like minerals, despite their nonreactive framework [97], [98], [99], [100].

PIM Potentials

Traditional rigid ion models, based on fixed atomic charges, fail to capture the dynamic charge redistributions induced by water molecules or ionic species, leading to oversimplified representations of interactions. To address this limitation, two classes of polarizable models were developed: the **core–shell model** by Dick and Overhauser [86], and the Polarizable Ion Model (PIM) by Madden and Wilson [101].

Polarizable ion models (PIM), later refined by Madden and co-workers [101], [102], [103], [104], [105], have been widely used to simulate the interactions between ions in complex oxides and glasses. The polarizable force field is composed of pairwise terms—charge–charge, repulsion, and dispersion—augmented by a polarization contribution:

$$V_{\text{Total}} = V_{\text{Charge}} + V_{\text{Dispersion}} + V_{\text{Repulsion}} + V_{\text{Polarization}} \tag{1.14}$$

Each term is described below.

Electrostatic interactions

Electrostatic interactions follow Coulomb's law:

$$V_{\text{Charge}} = \sum_{i<j} \frac{q_i q_j}{r_{ij}} \tag{1.15}$$

where q_i and q_j are the charges of ions i and j, and r_{ij} is their separation.

Dispersion interactions

Dispersion is modeled using damped multipolar contributions:

$$V_{\text{Dispersion}} = -\sum_{i<j} \left[f_6^{ij}(r_{ij}) \frac{C_6^{ij}}{(r_{ij})^6} + f_8^{ij}(r_{ij}) \frac{C_8^{ij}}{(r_{ij})^8} \right] \tag{1.16}$$

where C_6^{ij} and C_8^{ij} are dipole–dipole and dipole–quadrupole dispersion coefficients. The damping functions are:

$$f_n^{ij}(r_{ij}) = 1 - e^{-b_n^{ij} r_{ij}} \sum_{k=0}^{n} \frac{(b_n^{ij} r_{ij})^k}{k!} \tag{1.17}$$

which are Tang–Toennies functions correcting short-range behavior.

Repulsive interactions

Short-range overlap of electronic densities is described by:

$$V_{\text{Repulsion}} = \sum_{i<j} A^{ij} e^{-B^{ij} r_{ij}} \tag{1.18}$$

Polarization interactions

Polarization includes charge–dipole and dipole–dipole contributions together with the dipole self-energy:

$$\begin{aligned} V_{\text{Polarization}} = \sum_{i<j} \Bigg[& \frac{q_i \, r_{ij} \cdot \mu_j}{r_{ij}^3} g_4^{ij}(r_{ij}) - \frac{q_j \, r_{ij} \cdot \mu_i}{r_{ij}^3} g_4^{ij}(r_{ij}) \\ & + \frac{\mu_i \cdot \mu_j}{r_{ij}^3} - \frac{3(r_{ij} \cdot \mu_i)(r_{ij} \cdot \mu_j)}{r_{ij}^5} \Bigg] + \sum_i \frac{|\mu_i|^2}{2\alpha^i} \end{aligned} \tag{1.19}$$

Here, α^i is the polarizability of ion i, and μ_i the induced dipole. The short-range damping is:

$$g_4^{ij}(r_{ij}) = 1 - e^{-b_D^{ij} r_{ij}} \sum_{k=0}^{4} \frac{(b_D^{ij} r_{ij})^k}{k!} \tag{1.20}$$

Application to silicate and borosilicate glasses

PIM potentials have been successfully applied to reproduce the structure of silicate and borosilicate glasses. For instance, Pacaud and co-workers [106] simulated $Na_2O{-}B_2O_3{-}SiO_2$ compositions. Comparison between experimental and simulated neutron structure factors (Fig. 1.12) shows that the PIM model reproduces structural features of the glass with good accuracy, especially boron coordination and Si–O–B linkages.

Importance of polarizability at the glass–water interface

Standard rigid-ion models ignore ion polarizability, which is problematic for simulating interfaces. At the glass–water interface, the local electric field can strongly polarize ions, altering structure and energetics. This effect has been well established in ion hydration studies [107], [108], [109].

Although few studies have explicitly modeled glass–water interactions with polarizable force fields, similar approaches have been applied to hydrated dioctahedral clays [110]. In these systems, PIM parameters for dry clays were combined with polarizable water models [107], [111]. Extending this methodology to glasses is challenging because ion polarizabilities in the glass matrix differ significantly from those

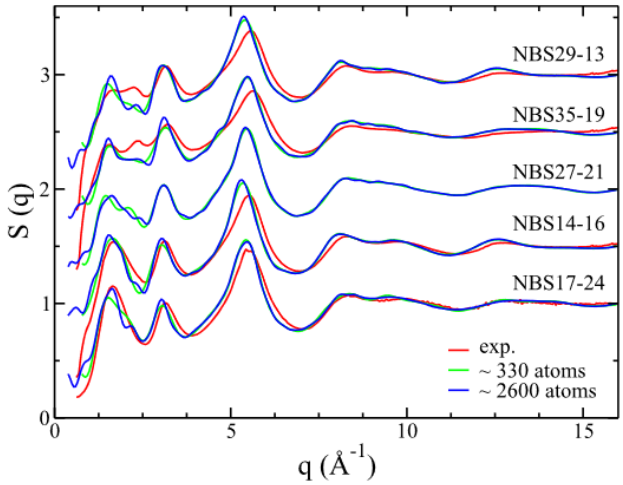

Figure 1.12: *Neutron structure factor of* $Na_2O - B_2O_3 - SiO_2$ *glasses at room temperature [106]. The close agreement illustrates the accuracy of the PIM model compared with experiments.*

of hydrated ions in solution.

For example, Pacaud [106] reported polarizabilities of $\alpha_O = 9.868\,Å^3$ and $\alpha_{Na} = 0.775\,Å^3$, much larger than the isolated ionic values ($\alpha_O = 0.907\,Å^3$, $\alpha_{Na} = 0.180\,Å^3$). This discrepancy highlights the difficulty in transferring parameters between different environments (e.g., from clays to glasses).

Machine-learning potentials

Neural network (NN)-based potentials, trained on large datasets from first-principles calculations, can capture complex interactions with high accuracy while maintaining computational efficiency. For example, Agrawal et al. developed NN potentials for SiO_2 dissociation, demonstrating their ability to model bond breakage with accuracy comparable to QM methods [60], [112]. Similarly, Morawietz et al. used NN potentials to study water's unique properties, highlighting their potential for glass-water systems. These potentials could enable simulations of multicomponent glasses with improved fidelity [60], [113].

Reactive force field

This section explores the development, applications, and challenges of reactive potentials in classical MD simulations of glass–water interactions.Traditional nonreactive potentials, such as Lennard-Jones (L-J) or Buckingham potentials, are limited in their ability to model chemical reactions because they cannot account for electron transfer between ions. As a result, they fail to capture processes such as bond formation, bond breakage, or charge redistribution, which are central to glass dissolution. Reactive potentials, such as ReaxFF [114], [115], [116], [117], [118] and the Charge-

Optimized Many-Body (COMB) potential [119], address these limitations by incorporating dynamic bond-order and charge equilibration mechanisms. These features enable the simulation of hydrolysis reactions, ion exchange, and other chemical processes at the glass–water interface [114], [115], [116], [117], [118], [120], [121], [122].

Among reactive force fields, ReaxFF is the most widely used for silica–water systems. Originally developed by van Duin et al. [115] for hydrocarbons, it was later extended to oxides and aqueous environments. ReaxFF employs a bond-order formalism to describe chemical bonds dynamically and incorporates charge equilibration to account for environment-dependent charge variations. Early adaptations for silica–water interactions were carried out by Larsson et al. and Yeon et al. [116], [117], whose parameterizations were benchmarked against *ab initio* MD (AIMD) simulations and shown to reproduce Si–O–Si bond breakage and hydroxylation rates with good accuracy. For example, Rimsza et al. used ReaxFF to study nanoporous silica hydration, capturing silanol (Si–OH) formation and bond-breaking kinetics in two-membered rings [123]. Subsequent developments expanded ReaxFF to multicomponent systems. Hahn et al. introduced a force field for Na–silicate/water systems to study sodium and proton diffusion [124]. These extensions now allow simulations of complex aluminosilicate and multicomponent glass–water interactions.

An alternative approach is the diffusive charge reactive potential (DCRP), originally developed by Mahadevan and Garofalini for silica–water systems [125]. Unlike ReaxFF, which is fully general but computationally expensive, the DCRP introduces a flexible, dissociable model for water molecules while still enabling bond formation and charge transfer. This makes it approximately an order of magnitude faster than ReaxFF, while retaining comparable accuracy in silica dissolution simulations [126].

Reactive potentials have been particularly valuable in quantifying the hydrolysis of Si–O–Si and Al–O–Si bonds, which are key steps in the dissolution of silicate and aluminosilicate glasses with applications ranging from nuclear waste storage to biomedical materials. Using the Mahadevan–Garofalini dissociative potential, potential of mean force (PMF) calculations showed that $Q_3 \rightarrow Q_2$ and $Q_2 \rightarrow Q_1$ transitions have the highest activation energies (~14.1 kcal/mol or ~0.61 eV), identifying them as rate-limiting steps in bulk silica dissolution [65], [127]. These values align with the lower range of experimental estimates (14–24 kcal/mol) but fall below cluster-based *ab initio* predictions (18–39 kcal/mol).

In aluminosilicate glasses, hydrolysis of Al–O–Si bonds proceeds more readily, with average activation energies of ~0.49 eV, compared to ~1.0 eV for Si–O–Si bonds in pure silica [38]. However, the presence of Al as a second neighbor to Si often increases Si–O–Si hydrolysis barriers beyond 1.0 eV, particularly in Q_4 (Si with four bridging oxygens) and Q_3 (Si with three bridging oxygens and one non-bridging

oxygen) environments [38].

Ion exchange, such as the Na^+/H^+ exchange in sodium silicate glasses, initiates glass dissolution by creating pathways for water diffusion into the bulk [78]. Reactive potentials were used to model this process, providing insights into the kinetics and structural changes at the glass surface. Hahn et al. used ReaxFF to simulate sodium and proton self-diffusion in $NaSiO_x$/water systems, demonstrating how the removal of Na^+ ions creates free space for water penetration [124], [128]. Similarly, Mahadevan and Du employed ReaxFF to study hydration mechanisms on sodium silicate glass surfaces, revealing the influence of local atomic environments on ion exchange rates [120], [126].

Reactive potentials were used to simulate the structure and evolution of these gel layers, capturing their porosity, diffusion properties, and protective effects. Rimsza and Du used ReaxFF to model nanoporous silica gel structures, showing how the gel layer forms through the reorganization of the glass network following hydrolysis and ion exchange [129] . These simulations also provided insights into the role of pore structure and chemical composition in controlling dissolution rates [121] .

Nanoconfinement and Diffusion: Nanoconfinement of water within porous silica structures, such as those formed during glass dissolution, significantly affects water diffusion and reaction kinetics due to the constrained geometry and interactions with the pore surfaces . The confined environment in nanoporous silica, characterized by pore sizes often ranging from a few angstroms to tens of nanometers, restricts water molecule mobility, leading to deviations from bulk diffusion behavior . These effects are driven by factors such as pore size, surface chemistry, and the presence of silanol groups (Si-OH) on the silica surface, which can form hydrogen bonds with water molecules, further influencing transport properties . To study these phenomena at the molecular level, reactive potentials, particularly the DCRP model described in the previous section, were employed in molecular dynamics simulations. The DCRP is a sophisticated force field designed to model the complex interactions in silica-water systems by accounting for dynamic charge transfer and chemical reactivity. For water diffusion in nanoporous silica, it captures the interaction between water molecules and the silica surfaces, including the effects of surface hydrophilicity or hydrophobicity, which can either enhance or impede diffusion depending on the degree of surface hydroxylation . For instance, highly hydroxylated surfaces with dense silanol groups tend to slow water diffusion due to strong hydrogen bonding, while less hydroxylated surfaces may facilitate faster transport. Studies using the DCRP showed that in smaller pores (e.g., < 2 nm), water diffusion coefficients can be orders of magnitude smaller than in bulk water [42], [130], with anomalous diffusion behavior arising from confinement-induced struc-

turing of water molecules. Additionally, the DCRP potential provides insights into reaction kinetics, such as proton transfer or silica dissolution, by modeling the dynamic formation and breaking of Si-O and O-H bonds. These capabilities make the DCRP potential a powerful tool for elucidating how pore size, surface chemistry, and confinement collectively govern the transport and reactivity of water in nanoporous silica, with implications for applications in catalysis, geochemistry, and materials science.

The development and application of reactive potentials for glass–water systems, while advanced, faces significant challenges that complicate their use in modeling complex multicomponent glasses. One major hurdle is the parameterization complexity, where incorporating additional elements into reactive potentials, such as those used in my thesis for developing the DCRP model to include boron, drastically increases the number of parameters to be optimized. For a system with N elements and M parameters, the optimization scales as $M \times N^2$, posing a substantial computational burden, particularly for multicomponent glasses critical to applications like nuclear waste storage and bioactive glasses. Extending parameterization to multivalent elements like boron, iron, or phosphorus is especially challenging due to their complex electronic interactions, which are difficult to fully capture in analytical potentials, thus hindering simulations of borosilicate or phosphate glasses used in nuclear waste and biomedical applications. Additionally, reactive potentials such as COMB or ReaxFF employ dynamic charge equilibration to account for changes in atomic charges based on local environments, requiring the solution of additional equations during MD simulations, which increases computational cost and limits simulation size and duration. For instance, ReaxFF's charge equilibration involves solving a separate Lagrangian for charge transfer, further slowing simulations. Another challenge is the temporal and spatial scale mismatch, as glass dissolution occurs over months or years, far exceeding the nanosecond timescales of MD simulations. Integrating reactive MD with mesoscale methods like kinetic Monte Carlo (KMC) could bridge this gap by modeling diffusion and reaction processes over larger scales, but coupling these frameworks remains difficult due to differences in computational approaches and the need for accurate transition rates. Finally, validating reactive potentials against experimental data is problematic, as atomic-scale processes like bond breakage or ion exchange are hard to measure directly. While reactive potentials can be benchmarked against DFT-based MD, experimental validation often relies on indirect metrics like pair distribution functions or dissolution rates, which may not fully capture the complexity of glass–water interactions.

In this thesis, two possible approaches were considered for modeling: polarizable ion models (PIM) and dynamic charge reactive potentials (DCRP). PIM approaches

are efficient for simulating long-range electrostatics and polarization in relatively simple systems, but they lack the flexibility to describe bond breaking and chemical reactions reliably in hydrated silica networks. The DCRP, in contrast, explicitly accounts for dynamic charge transfer and bond rearrangements, making it more suitable for capturing the coupled transport and reactivity governing water confined in nanoporous silica. For this reason, the DCRP approach was selected and will be presented in detail in Chapter 4. In particular, I am extending its parameterization to include boron, aiming to enhance the understanding of boron transport in aqueous environments within silica nanopores, a critical step for advancing simulations of complex glass systems.

1.4.3 Monte-Carlo Model

Monte-Carlo (MC) simulations offer a probabilistic framework for modeling the complex, stochastic processes of glass corrosion, providing critical insights into surface interactions and alteration layer dynamics. By leveraging random sampling to explore a range of possible reaction pathways, MC models capture the inherent variability of amorphous glass systems, where deterministic approaches may falter. In the context of nuclear waste immobilization, these simulations are particularly valuable for studying the formation and evolution of the alteration gel—a hydrated, amorphous layer that governs the long-term durability of alumino-borosilicate glasses. In this thesis, MC simulations have been applied to investigate gel maturation during glass alteration, focusing on the mechanisms that control passivation and residual corrosion rates. A detailed description of the MC methodology, previous modeling approaches, is provided in Chapter 3.

Conclusion

Computational models provide a complementary path to experiments, offering access to scales and mechanisms that are otherwise difficult to observe. Atomistic simulations clarify bond breaking and water incorporation, stochastic lattice models capture the random nature of hydrolysis and diffusion, and mesoscale or continuum approaches extend predictions to repository conditions. By connecting these levels, one can build a coherent picture of how short-term mechanisms translate into long-term behavior. This multiscale perspective forms the rationale for combining experimental investigations, Monte Carlo simulations, and molecular dynamics in order to address the durability of borosilicate glass in its role as a nuclear waste form.

2 Experiments

Contents

2.1 Introduction

The alteration layer, primarily rich in silica (commonly referred to as a gel [15]) along with potential secondary phases, could serve as a diffusion barrier. This barrier impedes the movement of soluble elements released from the glass surface during hydrolysis (such as boron, alkaline metals, alkaline earths, or molybdenum), thereby limiting the continued dissolution of the glass. It is crucial to understand the characteristics of the gel layer and how it evolves over time, as the transport properties

of the gel profoundly affect the rate of glass alteration [16], [32], [42], [51], [58], [131], [132].

To gain insights into gel maturation, this study characterizes gel layers after different durations of alteration. A simplified borosilicate glass series with varying Al content (SBNA1, SBNA4, and SBNA6, containing 1, 4, and 6 mol% Al_2O_3, respectively, see Table 2.1) was used. The glasses were altered for 7 days, 2 months, and 1 year under conditions of pH 9, a temperature of 90 °C, and a large glass-to-solution volume ratio, which favors rapid solution saturation with respect to the gel. The choice of composition is based on the previous studies done by Damodaran *et al.* Their work points out the hardening role of Al in the restructuring of the gel because the presence of Al in the vicinity of Si-O bond increases the energy barrier to break the bond, hence strengthening the gel network [38], [53].

The porous nature of the gel layers was examined through the use of transmission electron microscopy (TEM), thermogravimetric analysis (TGA), and small-angle X-ray scattering (SAXS) techniques. The gel composition of the samples aged for 7 days, 2 months, and 1 year was analyzed using time-of-flight secondary ion mass spectrometry (ToF-SIMS). Isotope tracing experiments using ^{18}O and ^{10}B isotopes were conducted to study the transport of water and boron in the gel layer at various degrees of maturation. The kinetics of alteration were monitored through measurements of boron and sodium concentrations in the solution using inductively coupled plasma optical emission spectrometry (ICP-OES).

The main objective of this experimental study is to address the following questions:

- How does the composition of the glass influence the formation and restructuring of the gel layer?
- How do the properties of the gel layer, such as porosity, pore size, and diffusivity for boron (B) and water (H_2O), evolve over time?
- Can the maturation of the gel layer be linked to changes in glass dissolution kinetics?

2.2 Materials and Methods

Three SBNA glasses were synthesized using raw materials: SiO_2, H_3BO_3, Na_2CO_3, and Al_2O_3. The powders were melted in a Pt–Rh crucible at 1450 °C for 3 hours and 20 minutes. The melt was then cast onto a metal plate, allowed to cool, subsequently crushed, and remelted at 1450 °C to enhance homogeneity. After grinding, the glass was reheated to 1450 °C and transferred to a graphite crucible for refining at 550 °C for 1 hour. Finally, the glass was cooled to room temperature. The glass preparation

procedure closely follows that reported in previous works [53], where a similar set of SBNA glasses was studied.

The glasses were analyzed using scanning electron microscopy coupled with energy-dispersive X-ray spectroscopy (SEM-EDX) to determine the concentrations of Si, Al, and Na, and ICP-OES for all elements after acid dissolution. The results [53] demonstrate that the glasses are homogeneous at a scale of a few tens of nanometers. Chemical analyses confirmed that the compositions were within a $\pm 5\,\%$ margin of error. The nominal compositions are presented in Table 2.1. Boron speciation was determined using nuclear magnetic resonance (NMR) spectroscopy mentioned in Section 2.2.2.

Table 2.1: *Nominal compositions (mol%) of the three glasses. The density was calculated using Fluegel's model [133]*

Glass name	SiO_2	B_2O_3	Na_2O	Al_2O_3	B(IV)%	B(III)%	NBO %	NBO/Si	Density (g/cm^3)
SBNA1	63.0	18.7	17.3	1.0	71	29	3.7	0.20	2.46
SBNA4	64.9	17.3	13.7	4.1	54	46	0.25	0.00013	2.41
SBNA6	66.8	15.9	11.3	6.0	31	69	0.45	0.00023	2.36

The amount of non-bridging oxygen (NBO) can be calculated by the formula given in previous studies [18] and mentioned in equation 1.1.

The N_{NBO}/N_{Si} ratio was calculated using the ratio of NBO in the glass and the molar fraction of Si in the glass.

2.2.1 Sample preparation

Rectangular cuboid samples measuring 20 mm × 20 mm × 1 mm were prepared by polishing all six faces to a surface roughness below 5 nm, using successive grades of polishing up to a final treatment with 1 µm diamond paste. Each monolith was then cut into four pieces of approximate dimensions 10 mm × 10 mm × 1 mm, resulting in two polished faces and edges and two as-cut edges. Glass powders were obtained by crushing glass pieces and separating them into size fractions of 20–40 µm, 40–100 µm, and 60–125 µm. The powders were rinsed multiple times with absolute ethanol and acetone to eliminate fines. Their surface area was measured using the Brunauer–Emmett–Teller (BET) technique, and the geometrical surface area values were calculated for comparison. The corresponding values of both geometric and BET surface areas for the different particle size ranges are summarized in Table 2.2.

Three experiments were conducted over the course of one year to monitor the glass dissolution rate and gel formation features at 90 °C and pH 9, with a controlled glass surface-to-solution volume (S/V) ratio. The pH was initially adjusted to 9 using diluted LiOH, and no further pH adjustments were made throughout the duration of the experiments. All chemicals used were of *Suprapur* grade, and ultrapure

Table 2.2: *Surface area (geometric and BET) for aluminoborosilicate glasses in 40–100 µm and 20–40 µm particle size ranges.*

Glass	S_{Geo} (40–100 µm) (cm^2g^{-1})	S_{BET} (40–100 µm) (cm^2g^{-1})	S_{Geo} (20–40 µm) (cm^2g^{-1})	S_{BET} (20–40 µm) (cm^2g^{-1})
SBNA1	354	690	407	1605
SBNA4	353	720	414	1870
SBNA6	363	780	423	1530

water with a resistivity of 18.2 MΩ·cm was employed to ensure high experimental purity.

Experiment 1a

Glass powder from the 40–100 µm fraction was exposed to 50 mL of ultrapure water (18.2 MΩ·cm) with a surface-to-volume ratio of 50 cm^{-1}, while maintaining a pH of 9.0 ± 0.1 using a 10^{-2} M LiOH solution at a temperature of 90°C. The specific surface area (S) was estimated from BET Kr adsorption analysis. The values are listed in Table 2.2 along with the geometrical surface area.

In each reactor, six glass coupons were placed slightly above the powders in a perforated Teflon basket. The coupons were added 4 days after the experiment was started with powders, to ensure that the solution was close to saturation with respect to silica. This procedure was done to prevent faster dissolution of the monolith compared to the powder. The choice of 4 days is based on previous work on the same glasses [53].

Sampling was done at regular intervals by taking 0.5 mL solution samples, which were filtered (0.2 µm) and diluted in 2.0 mL of 0.5 N ultrapure HNO_3. The samplings were not replaced, resulting in a decrease of the volume of solution with time, in order to avoid potential effects of dilution. The samples were analyzed by ICP-OES.

After 7 days of alteration, two of the six monoliths were removed. After 2 months of alteration, two more monoliths were removed and after 1 year of alteration, the last two monoliths were removed. After removal, the monoliths were rinsed in DIW (Deionised water), dried in a piece of tissue and stored at ambient conditions until characterization. These monoliths were used for characterization using ToF-SIMS and TEM.

After a first characterization by ToF-SIMS where positive ions were analysed, the monoliths were immersed in a tracing solution at pH 9 (fixed with 0.038 mol/L LiOH) containing 1000 ppm of B (introduced as $B(OH)_3$ with 99% ^{10}B from Aldrich) and 67 % ^{18}O (added from pure H_2O with 99 atom % enrichment in ^{18}O from Cortecnet) for 24 hours under ambient conditions (to prevent further alteration). At the end of the tracing experiment, the monoliths were removed from the tracing solu-

tion and immediately plunged into liquid nitrogen, and a second ToF-SIMS analysis was carried out under cryogenic mode to study the diffusion of the tracer isotopes in the gel layer.

Experiment 1b

This experiment was dedicated to SAXS analysis was conducted only with glass powder. Experiments were conducted with the fraction 20-40 µm glass powders. The temperature, pH, and S/V ratio were fixed at 90°C, 9, and 50 cm^{-1}, respectively. For each glass, altered powders were retrieved after 7 days, 2 months and 1 year. After removing the powders from the reactor, they were washed and stored in same manner as in Experiment 1a. The glass powders were then characterized using TGA and SAXS.

Experiment 1c

A third experiment was conducted to decipher the role of Si_{aq} in the formation of the gel. The procedure for this experiment is similar to that of Experiment 1a, except that the starting solutions for glass alteration were adjusted to include 10% of ^{29}Si relative to the saturation levels, corresponding to 46 ppm for SBNA1 and 9.5 ppm for SBNA6. Additionally, in this experiment, the glass powders and glass coupons were kept in the leaching solution at the same time, as opposed to Experiment 1a, where the glass coupons were introduced only after the solution was silica-saturated with respect to the glass powders. The chemical depth profiling for SBNA1 and SBNA6 glass compositions was performed by ToF-SIMS analysis over multiple time intervals (2 months and 6 months). Sampling was done at regular intervals by taking 0.5 mL solution samples, which were filtered (0.2 µm) and diluted in 2.0 mL of 0.5 N ultrapure HNO_3. The samples were then analyzed by ICP-OES.

The characteristic time of the transition between the initial and residual alteration regimes, denoted as τ, was determined from long-duration experiments. It was obtained by fitting the normalized boron mass loss data, $NL(\mathrm{B})$, to the following exponential function

$$NL(\mathrm{B}) = a + b \cdot e^{-t/\tau} \tag{2.1}$$

where a and b are fitting parameters, and τ represents the characteristic time.

Assuming a specific geometry for the particles—such as treating glass grains as spheres or cubes—allows for the calculation of their geometric surface area based on particle size. For smooth, non-porous glass grains with a normal size distribution, the geometric surface area of a spherical particle can be calculated using the expression

$$S_{\text{Geo}} = \frac{3}{\rho \cdot R} \tag{2.2}$$

where S_{Geo} represents the geometric surface area of the glass ($cm^2\ g^{-1}$), ρ is the density of the glass ($g\ cm^{-3}$), and R is the average radius of the particles in µm.

As shown in Table 2.2, the measured BET surface areas are consistently higher than the calculated geometric surface areas, in some cases by more than a factor of four. This discrepancy arises because the BET method probes the real surface accessible to adsorbates, which includes contributions from surface roughness and sub-micron porosity not captured by simple geometric estimates. Using BET surface areas for rate calculations also facilitates comparison with long-term data reported in the literature, where BET is commonly used as the normalization basis [53]. In this study, the ratio between BET and geometric surface areas is approximately 2 for the 40–100 µm fraction and 4 for the 20–40 µm fraction, which justifies our choice of BET normalization. It is also important to note that estimating the average radius R typically involves implicit assumptions about the distribution of particle sizes, surface area, or volume.

2.2.2 NMR

NMR was used to quantify the various B coordination states in the glasses. A Bruker 500WB Avance II spectrometer operating at an 11.72 T magnetic field was utilized for NMR data collection. A 4-mm Bruker CP-MAS probe was employed with a spinning frequency of 12.5 kHz. Quantitative ^{11}B spectra were obtained using a short single pulse excitation lasting 1 µs, achieving a tip angle of approximately 15°-20°. The recycle delay for ^{11}B was set to 2 seconds. Two types of ^{11}B multiple-quantum MAS experiments were conducted to optimize the signal from BO_3 and BO_4 units, as described in previous literature [134]. All data processing and fitting were carried out using in-house software developed by T. Charpentier, and procedures followed the literature [58], [134], [135].

2.2.3 ICP-OES

The solutions were analyzed using ICP-OES (using a Thermo Scientific iCAP^{TM} 6000 series spectrometer) by Filab, France and analyzed using for Si, B, Na, and Al concentrations with an uncertainty of ±5%.

Normalized mass losses $NL(i)$ and equivalent alteration thicknesses $ETh(i)$ were calculated based on element concentrations in solution $C(i)$, solution volume V, glass surface area, element fractions x_i, and the glass density ρ using the equations

$$NL(i)_t = NL(i)_{t-1} + \frac{[C(i)_t - C(i)_{t-1}]\,.V_t}{S.x_i} \tag{2.3}$$

$$ETh(i) = \frac{NL(t)}{\rho} \tag{2.4}$$

The density of SBNA1, SBNA4 and SBNA6 is 2.46, 2.39 and 2.36 g/cm^3 as given in Table 2.1.

The residual rate r_r ($g.m^{-2}.d^{-1}$) is given by the formula below

$$r_r = \frac{d\,(NL(t))}{dt} \tag{2.5}$$

The rate is determined based on the release of boron, utilized as a tracer. The uncertainties in equivalent thicknesses were approximately 10%, accounting for measurement uncertainties in solution concentrations and the surface-to-volume ratio.

2.2.4 TEM

The transmission electron microscopy (TEM) analyses were conducted on ultra-thin microsections approximately 80 nm thick. These microsections were prepared using a double beam focused ion beam coupled with a scanning electron microscope (FIB/SEM) FEI, Helios 600 Nanolab. The analysis was performed at Aix Marseille university. Before sample preparation, the surface was coated with a layer of Au-Pd and carbon. Prior to machining with Ga^+ ions, the area of interest was locally coated with a 1.5 µm -thick layer of platinum through ion-assisted deposition. Two wide trenches were then machined on either side of this protective layer using an ion beam accelerated to 30 kV with a beam current of 9.3 nA. The current was progressively reduced to 0.92 nA until a thickness of approximately 800 nm was achieved. The lamella was then cut and transferred to a copper grid. The current was further reduced to 0.28 nA and 93 pA until a thickness of around 250 nm was reached. To minimize Ga^+ ion damage to the sides of the lamella, the voltage was lowered to 5 kV and the current to 47 pA. These parameters were used to thin the top of the lamella to a depth of about 2 µm below the surface, resulting in a thickness of 70 to 100 nm as measured in SEM on the lamella. Final cleaning was performed on each side of the lamella at 2 kV, -10 pA, and 1 kV, -14 pA. Once the lamella was bonded to the copper grid, care was taken to avoid exposing both sides of the lamella to the electron beam to prevent altering the porosity of the gel.

The TEM images of the porous gel were acquired using a field emission gun (FEG) microscope (JEOL 2200FS) operating at 200 kV. This analysis was performed at the *Centre de Biologie Structurale* (CBS) at the university of Montpellier. This microscope is equipped with a GATAN K3 direct detector for image recording and features an in-column energy filter (Omega filter) and a cryogenic pole piece, allowing for the observation of samples frozen in liquid nitrogen at -180°C. The implemented iMDS

software facilitated low-dose acquisition, which is suitable for the porous gel layer sensitive to electron damage. Images were acquired in bright-field TEM under sub-focusing conditions ($-3\,\mu m$). It was confirmed that the pore structure did not change during the image acquisition process.

2.2.5 TGA

Thermogravimetric analysis (TGA) was conducted on glass powders that had been altered over periods of 7 days, 2 months, and 1 year, in order to evaluate the porosity of the gel layer through the quantification of water released upon heating. Prior to the analysis, the altered glass powders were placed in a sealed chamber with a tray of saturated K_2SO_4 solution at room temperature for 24 hours. This setup created a relative humidity of 97%, ensuring that the pores in the gel layer of the powders were fully saturated with water.

After this conditioning, the powders were transferred to a platinum crucible and heated at a rate of 10°C per minute. The mass loss observed up to 400°C was attributed to the water content within the gels, which could be present as either free water or hydroxyl (–OH) groups. Specifically, the water loss up to approximately 150°C was primarily due to free water in the gel layer. Beyond 150°C, the mass loss was caused by the recondensation of silanol groups, which released additional water molecules from the gel layer.

The TGA measurements were performed using a SETARAM SETSYS TMA S60/58507 apparatus. The analysis was carried out at Prime verre, Montpellier.

2.2.6 ToF-SIMS

The depth profiles of elements in the monolith samples were obtained using ToF-SIMS analysis on TOF (IONTOF 5). For the secondary positive ion analysis before the isotopic tracing, 25 keV Bi_1^+ primary ions at 1 pA was used for the analysis cycle. The analyzed area was 50 µm × 50 µm^2. The extended dynamic range (EDR) was applied to avoid saturation of the signals in case of a higher concentration. A pulsed flux of low-energy electrons (< 20 eV) was used for surface charge compensation. The abrasion cycle was carried out using 1 keV O^{2+} primary ions at 200 nA. The abraded area was about 200 × 200 µm^2.

For the secondary negative ion analysis following isotopic tracing experiments, the analysis cycle was conducted similarly to the previous one. However, during the abrasion cycle, 1 keV Cs^+ ions were utilized at a current of 80 nA. Additionally, the analyses were performed in cryogenic mode to prevent the loss of pore water in the gel layer while in the vacuum chamber. However, 1 keV Cs^+ ions at 80 nA were used for the abrasion cycle. At the end of the analysis, the depth calibration was performed by measuring the depth of the crater left by the sample analyzed

using a mechanical profilometer. Thus, the intensities of the elements present in the sample as a function of the depth of analysis was obtained. The intensities were normalized as a function of the intensity of each element in the zone corresponding to the pristine glass and the intensity of Si at each depth. More information on the application of depth profiling is given in the reference [136]. Both the positive and negative mode analysis are carried out at Tescan analytics, Fuveau.

The profile of elements were treated through double normalization with respect to silica, the equation of double normalization is given in the equation

$$N(q) = (\frac{q}{Si})/(\frac{q(pristine\ glass)}{Si_{mean}(pristine\ glass)} \tag{2.6}$$

where $N(q)$ is the normalized profile of the element q.

Assuming that glass alteration occurs as an isovolumic process, this is supported by the consistency between the gel layer thickness estimated from solution analysis and ToF-SIMS characterization. Under this assumption, the pore volume of the gel can be theoretically calculated from the fractions of boron and sodium that leached out, combined with the ionic radii of these elements [58].

The amount of free volume generated is obtained from the number of mobile elements (Na, B(III), and B(IV)) released from the gel. Each atom is approximated as a sphere, with its volume $V_i = \frac{4}{3}\pi r_i^3$ determined from the ionic radius r_i reported in the literature [58]. The porosity is then expressed as

$$\text{Porosity} = \sum_{i=1}^{N} N_i V_i, \tag{2.7}$$

where N_i is the number of depleted ions of type i per unit volume, V_i is the effective volume of ion i, and N is the total number of mobile ion types considered.

The solution saturation limit for the tracing experiment (i.e., the isotopic ratio of ^{18}O and ^{16}O when the porosity is completely filled) is calculated as

$$\text{Saturationlimit} = \frac{N_{^{18}O}^{\text{dep+gel}}}{N_{^{16}O}^{\text{dep+gel}}}, \tag{2.8}$$

where $N_{^{18}O}^{\text{dep+gel}}$ and $N_{^{16}O}^{\text{dep+gel}}$ denote the total numbers of ^{18}O and ^{16}O molecules, respectively, in the depleted volume plus the gel prior to tracing.

2.2.7 SAXS

The SAXS analyses (performed at CEA in Saclay) were carried out on the glass powders from the aforementioned experiments, using unaltered glass powders in the 40–100 µm size fraction. This technique was used to quantify the nanostructure of

the gel layer, in particular the pore size, porosity, and specific surface area. The measurements were conducted using a Xeuss 3.0 apparatus under vacuum conditions, with a Cu source ($\lambda = 1.54\,\text{Å}$). The apparatus was calibrated on silver behenate. The powder samples were filled in a 1 mm thick plastic sample holder with several equally spaced 5 mm holes. The powders were placed in the holes between two 7.5 µm thick polyimide (Kapton) films that were 1 mm apart. A reference spectrum was acquired with nothing between the two polyimide films. The spectra were collected between q values of 0.009–8.5 Å^{-1}, with an acquisition time of 1800 s for each sample. The inter-grain porosity of each sample was filled with air, while the inner porosity of the gel layer could be partially filled with water and partially with air.

The raw intensity ($I^{'}$) obtained was scaled to an absolute intensity (I_{abs}) using

$$I_{abs} = \frac{1}{K\, e_B} \left(\frac{I^{'}_{\text{sample}}}{T_{\text{sample}}\, t_c} - \frac{I^{'}_{\text{ref}}}{T_{\text{ref}}\, t_c} \right), \tag{2.9}$$

where K is an instrument-specific correction coefficient, T is the transmission, t_c is the acquisition time, and e_B is the sample thickness, calculated as

$$e_B = \frac{-\ln\left(\frac{T_{\text{sample}}}{T_{\text{ref}}}\right)}{\mu_{\text{sample}}}. \tag{2.10}$$

The X-ray linear attenuation coefficient μ_{sample} of the unaltered glass is calculated from the glass composition in mass fractions x_i, density ρ, and the X-ray mass attenuation coefficient μ/ρ of each element in the glass (at $\lambda = 1.54$ Å) [137], using

$$\mu_{\text{glass}} = \rho_{\text{glass}} \sum_i x_i \frac{\mu_i}{\rho_i}. \tag{2.11}$$

The composition of the altered glass was adjusted to account for the loss of boron and sodium from the gel. In addition, 50% of the pore volume in the altered sample was assumed to be filled with water. This adjusted composition was then used to calculate the X-ray linear attenuation coefficient of the altered glass.

In the graph of I_{abs} as a function of q, if one or more regions follow Porod's law, *i.e.* $I_{\text{abs}}(q) \propto q^{-4}$, then the specific surface area Σ and the porosity Φ can be calculated using

$$\Sigma = \frac{\lim_{q\to 0} I_{\text{abs}} q^4}{2\pi\Delta\rho^2 \rho_{\text{sample}}}, \tag{2.12}$$

and

$$\Phi = \frac{\int_{q_{\min}}^{q_{\max}} I_{\text{abs}}\, q^2\, dq}{2\pi^2 \Delta\rho^2}, \tag{2.13}$$

where $\Delta\rho$ is the difference in scattering length density (SLD) between the scattering surface (glass or gel) and the medium (air or water). The SLD of a sample is calculated from its composition in mole fraction m_i, atomic number Z_i, molecular weight M_{sample}, the Avogadro number , and the classical electron radius r_e as

$$\text{SLD} = \frac{\rho \sum_i m_i Z_i r_e}{M_{\text{sample}}}. \tag{2.14}$$

Knowing the specific surface area, density, and porosity (calculated from equations 2.12 and 2.13 or from other characterization techniques), the pore radius r can be estimated from

$$r = \frac{3\Phi}{\Sigma \cdot \rho}. \tag{2.15}$$

The SAXS calculations performed here is similar to the calculation performed in previous work [59].

2.3 Results

2.3.1 Results from the literature

Initial dissolution rate r_0

Before presenting the results of this thesis, key literature findings on the three studied glasses are briefly recalled. K. Damodaran reported the normalized Si mass loss over time under diluted conditions (90 °C, pH 9, low surface area–to–volume ratio) for 6 h [53], from which the initial dissolution rate r_0 was obtained by linear regression of mass loss as a function of time.

The values assigned to r_0 in Figure 2.1 distinctly indicate congruent dissolution across all glass compositions. Notably, a substantial disparity emerged concerning the Al content present in the glasses. The r_0 values for glasses with low Al content (e.g., SBNA1, with 5.7 g $m^{-2}d^{-1}$) were markedly higher than those for glasses containing higher Al levels (e.g., SBNA4, with 1 g $m^{-2}d^{-1}$, and SBNA6, with 0.6 g $m^{-2}d^{-1}$), calculated with a margin of 30% uncertainty.

The ratio r_0(SBNA1)/r_0(SBNA6), standing at 9.5, is consistent with findings from experiments on two distinct glass sets—CJ1 (low Al content) and CJ2 (high Al content)—where the influence of Al on glass properties yielded comparable trends [52].

The durability of glass in dilute media is reduced by aluminum through two main mechanisms: the coordination environment of sodium with oxygen is modified, and

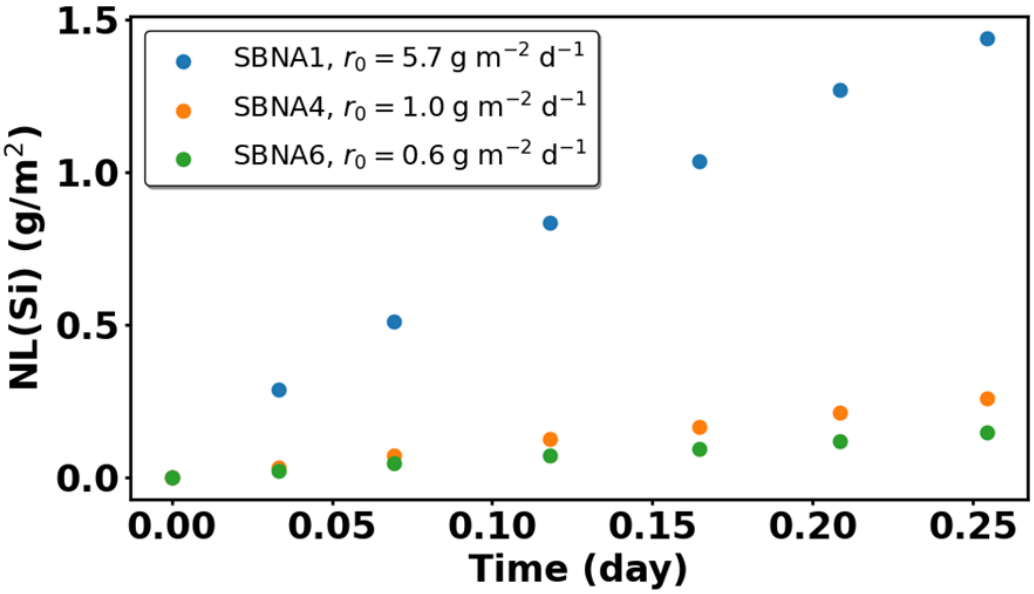

Figure 2.1: *Normalized mass loss of Si as a function of time for different SBNA glasses: The slope derived from linear regression represents the initial dissolution rate, r_0, measured at 90 °C in a solution with a pH of 9. The uncertainty associated with r_0 is ±30 % [53]*

the network connectivity is increased, both of which lower water mobility. Molecular dynamics simulations further support these results, showing that the activation energy for bond dissociation around silicon increases in the presence of aluminum, which slows water diffusion in aluminosilicate glass compared to pure silicate glass and thus modifies its durability [38], [39], [138].

Residual rate r_r

Long-term static experiments performed in the previous studies on the set of SBNA glasses aimed to investigate the effect of aluminum on the saturation concentration of silica and the reduction in glass dissolution rates. Conducted at a high surface area-to-volume ratio (S/V), at 90 °C and a pH of 9 over six months, the reactors were housed in an additional water-filled container to minimize evaporation. Throughout the duration of the experiments, the pH remained stable and close to the target value of 9.0 ± 0.2. The results, illustrated in Figure 2.2, show that the concentration of silica C(Si) initially rises and eventually reaches a plateau, indicating saturation with respect to the gel. This plateau varies depending on glass composition; glasses with the lowest aluminum content (SBNA1) achieved the highest saturation concentrations of silica, between 400 and 500 mg.L^{-1}, while those with higher aluminum concentrations exhibited lower levels.

This result suggests that presence of aluminum in the glass effectively regulates the release of silica into the solution, as indicated by the balance between dissolution

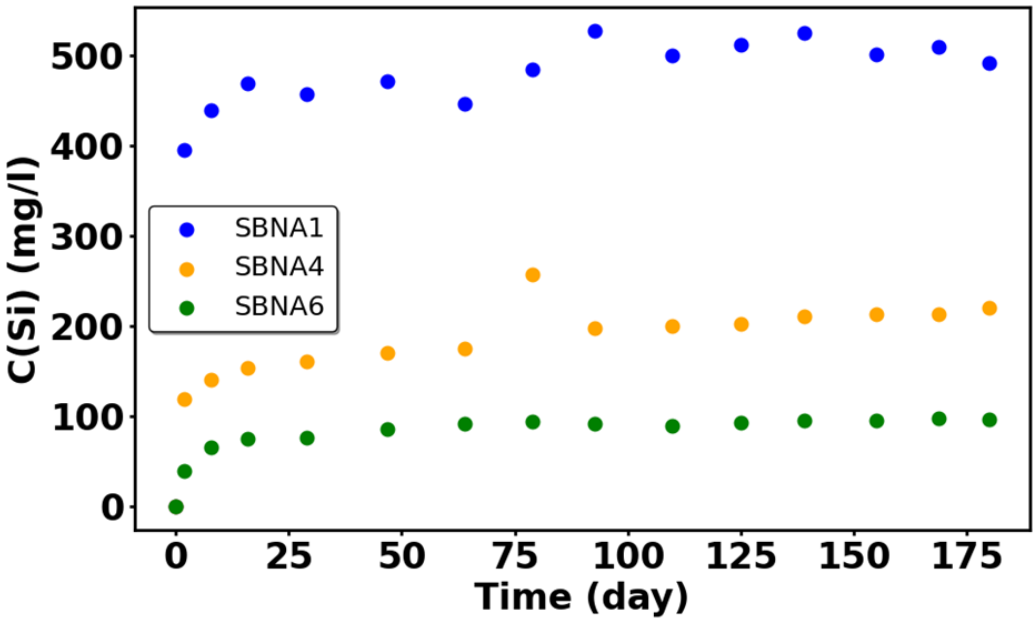

Figure 2.2: *Experiments performed at 90 °C, pH 9 for 6 months, and S/V = 50 cm^{-1}. The silicon concentration in the leaching solution is shown as a function of time [53].*

and condensation reactions at equilibrium. The recent atomistic simulations show Al as a second neighbor to Si in aluminosilicate glass enhances the activation energy for breaking Si–O bonds while lowering the energy barrier for reformation [38]. Additional MD calculations further confirmed that the activation energies for these processes are higher and lower, respectively, in aluminosilicate glass compared to pure silicate glass. Consequently, aluminosilicate gels require less energy to form than pure silica gels, which is correlated with their lower solubility [38], [53].

Figure 2.3 shows the equivalent thickness, calculated using boron as a tracer, in the alteration experiment [53]. SBNA1, the glass with the lowest Al content, displays a rapid initial release of boron followed by a clear stabilization, indicating that alteration has essentially stopped. In contrast, SBNA4 and SBNA6 (with higher Al contents) show a slower but continuous boron release, meaning that the glass continues to alter. The residual rate of SBNA1 is on the order of 2.5×10^{-5} $\mathrm{g{\cdot}m^{-2}{\cdot}d^{-1}}$, while those of SBNA4 and SBNA6 are 8×10^{-3} $\mathrm{g{\cdot}m^{-2}{\cdot}d^{-1}}$ and 7.6×10^{-3} $\mathrm{g{\cdot}m^{-2}{\cdot}d^{-1}}$, respectively. As a result, the rate drop r_0/r_r is much more pronounced for SBNA1 than for SBNA4 and SBNA6.

2.3.2 Results

The long-term experiments aimed to understand the temporal evolution of gel during glass alteration. The experiments were conducted at high S/V ratios at 90 °C and a pH of 9 over a period of 1 year, following the protocol described in Section 2.2.1. The reactors were placed inside a secondary container filled with water, minimiz-

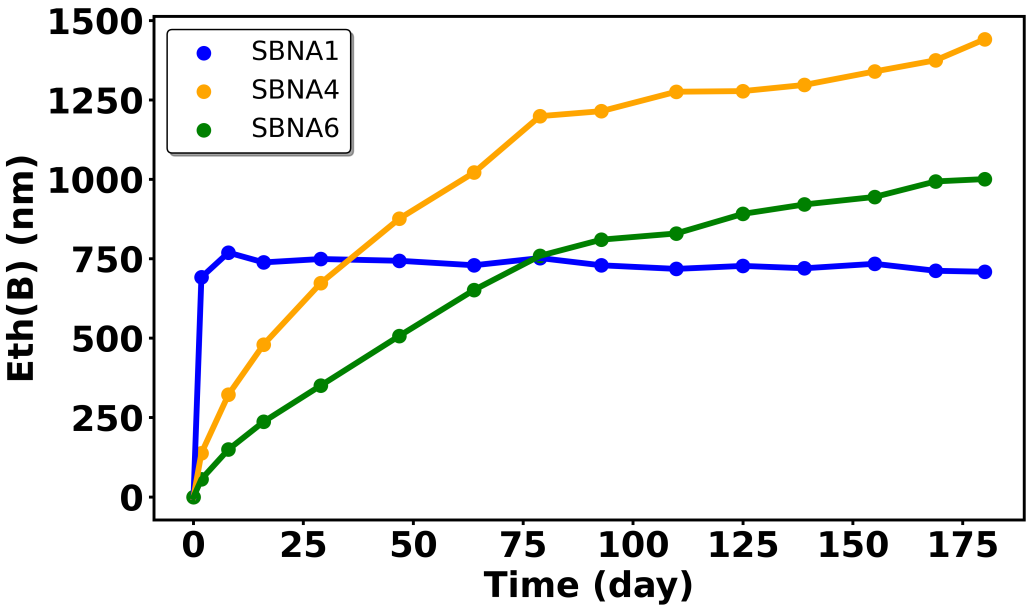

Figure 2.3: *Experiments performed at 90 °C, pH 9 for 6 months, and S/V = 50 cm^{-1}. The results represent the long-term dissolution behavior of the SBNA glass series, expressed as the equivalent thickness based on boron as a tracer, with time [53]*

ing solution evaporation. Throughout the experiments, the pH remained stable and close to the target value of 9.0 ± 0.2. For most of the tested glasses, alteration follows an isovolumic process, meaning that the gel occupies the same volume as the altered glass; however, this is not the case if the gel of SBNA1 forms by precipitation. In addition, no secondary crystalline phases formed during alteration.

Figure 2.4 illustrates the change in silicon concentrationin solution C(Si) over time. In all cases, C(Si) initially increases and eventually reaches a plateau, indicating saturation of the solution with respect to the gel. The plateau is achieved at different concentrations depending on glass composition. The glass with the lowest Al content (SBNA1) exhibit the highest concentration at saturation, ranging between 400 and 500 mg/L. In contrast, glasses with higher Al concentrations show lower C(Si) at saturation.

Boron was used as a tracer, and the Equivalent thickness of the altered glass was calculated using B concentrations and plotted against time (Figure 2.5). The release of sodium (Na) was also investigated. The behavior of Na closely resembles that of B, although the values for Na are lower in glasses with high aluminum (Al) content. This observation suggests that Na may be retained in the gel to charge compensate for four-fold coordinated Al atoms. The raw ICP data has been given in Appendix A.

Further examination of B behavior reveals that the glass with low Al content exhibit rapid dissolution during the initial days, eventually reaching a very slow dis-

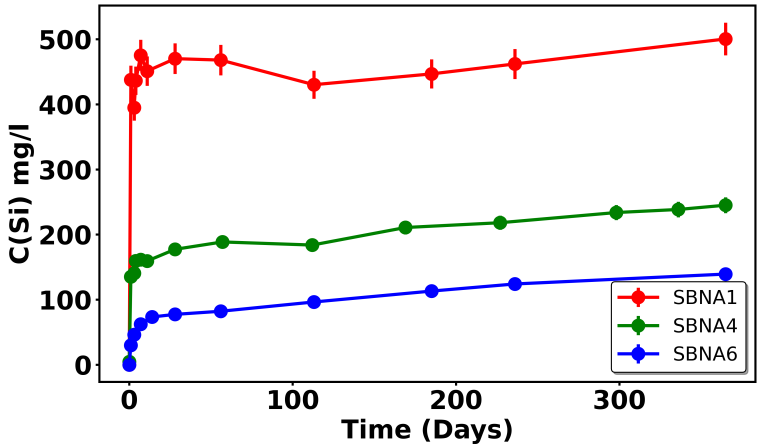

Figure 2.4: *Concentration of Si released into the solution as a function of time. The error bars show a 5 % uncertainty in measurements.*

solution rate. In contrast, the glasses with higher Al content dissolve slowly at first, but their dissolution rate decreases gradually over time.

Figure 2.6 (a), (b) and (c) display the normalized depth profiles (wrt silicon) of B obtained through ToF-SIMS analysis (see section 2.2.6) for the three glasses for duration of 7 days, 2 months and 1 year. The gel corresponds to the zone where the normalized intensity is less than 1.0 (1.0 represents the normalized concentration in pristine glass). The region where the normalized intensity sharply rises to 1.0 represents the gel-glass interface, beyond which lies the unaltered pristine glass. The gel layer is distinctly characterized by the depletion of boron, allowing for the estimation of its thickness.

It is important to note that the monoliths were introduced into the alteration solution four days after the experiment began with the powders. The alteration kinetics observed through solution analysis reflect the changes in the powders, as powder represents the vast majority of the surface in contact with water. To ensure that the alteration kinetics were comparable between the monoliths and the glass powders, the gel layer thickness measured by ToF-SIMS was compared with the equivalent thickness of the altered glass determined through solution analysis, starting from four days of alteration. Overall, the alteration kinetics of the monolith samples align closely with those of the glass powders except for SBNA1 where the altered thickness of the glass powder was four times as compared to the alteration thickness of the monolith but the quantitative comparison for SBNA1 glass powders and monoliths had similar trend, the alteration thickness calculated from ICP and ToF-SIMS has been mentioned in Table 2.3. The difference in gel thickness calculated from solution data (for altered glass powders) and ToF-SIMS (for glass monoliths) for SBNA1 can likely be attributed to the rapid release of silica from the powders may

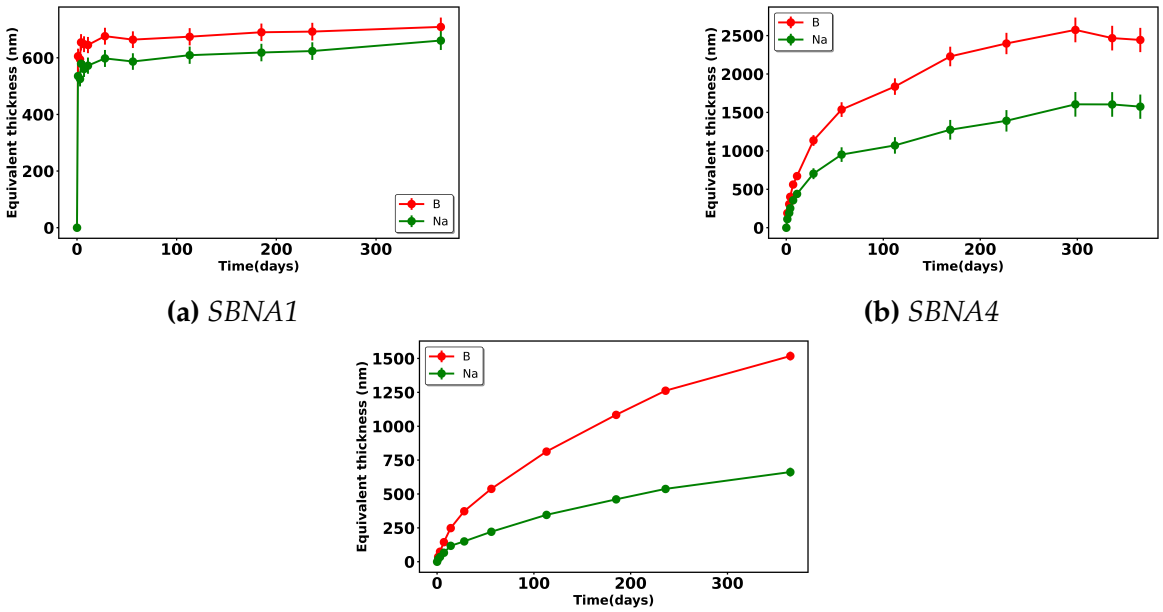

(a) *SBNA1*

(b) *SBNA4*

(c) *SBNA6*

Figure 2.5: *Equivalent thickness of B and Na resulting from the 1 yr long experiment conducted at 90°C, pH 9 with powder and monoliths obtained from ICP for (a) SBNA1, (b) SBNA4, and (c) SBNA6.*

have led to the early formation of a silica-enriched layer. Since the glass monoliths were introduced into the reactor after the solution had already reached silica saturation, this pre-existing condition may have influenced the alteration behavior of the SBNA1 glass and contributed to the observed discrepancy.

Table 2.3: *Alteration thickness measurements for different glass samples.*

	SBNA 1	SBNA 4	SBNA 6
Alt. Thickness, ICP: 7 days (nm)	648	516	144
Alt. Thickness, ToF SIMS: 7 days (nm)	150	175	195
Alt. Thickness, ICP: 56 days (nm)	664	1485	538
Alt. Thickness, ToF SIMS: 56 days (nm)	181	1000	424
Alt. Thickness, ICP: 1 year (nm)	709	2443	1518
Alt. Thickness, ToF SIMS: 1 year (nm)	200	2592	1082

It is important to note that the alteration thickness in SBNA1 does not evolve over time, as seen by both ICP and ToF-SIMS, and we observe a boron retention in the depth profiling of SBNA1 (presented using ToF-SIMS). The boron retention in the SBNA1 glass increases from $\sim 15\%$ at 7 days to $\sim 24\%$ at one year, while the boron retention in the SBNA4 and SBNA6 glasses remains between 1% and 2% over a period of 7 days. Boron retention does not change significantly between 2 months and 1 year. Compilation of boron retention data calculated using the ToF-SIMS profile shown in Figure 2.6 is provided in Table 2.4. The boron retention observed for gel matured for one year is maximum for the lowest Al content glass (SBNA1), interme-

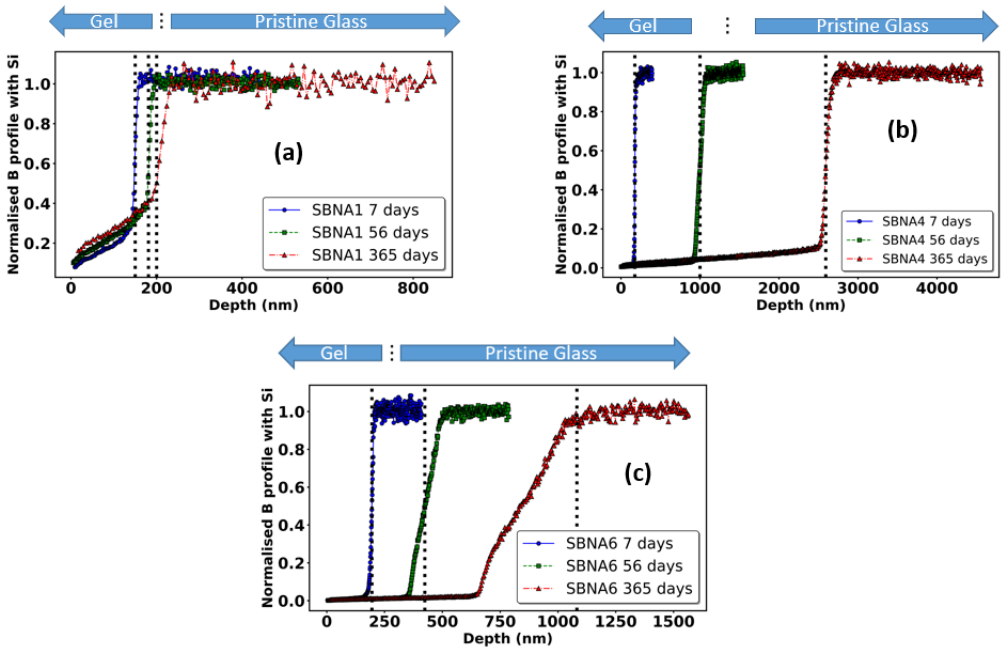

Figure 2.6: *Normalized ToF-SIMS secondary positive profiles of boron in the 7-days, 2-months and 1-year samples for (a) SBNA1, (b) SBNA4 and (c) SBNA6 (The broadness of the SBNA6 sample represents the roughness of the gel surface)*

diate for SBNA4, and close to none for SBNA6.

The percentages reported in Table 2.4 correspond to average values obtained from normalized boron depth profiles, and thus represent the mean fraction of boron retained across the altered layer. In the case of SBNA1, this average reflects the fact that boron retention is higher near the glass–gel interface than near the gel–solution interface.

Table 2.4: *Boron retention (expressed as the fraction of boron remaining in the altered glass) at different durations of alteration, calculated from normalized boron depth profiles obtained by ToF-SIMS*

Duration (days)	SBNA1	SBNA4	SBNA6
7	15%	1%	2%
56	24%	2%	1%
365	24%	5%	1%

Following the ToF-SIMS analysis of secondary positive ions, the monolith samples were immersed in an isotopically labeled solution containing approximately 67% ^{18}O and 1000 ppm boron (with 99% enrichment in ^{10}B) at ambient conditions for 24 hours. After immersion, the samples were removed from the solution, plunged into liquid nitrogen , and subjected to ToF-SIMS analysis of secondary negative ions

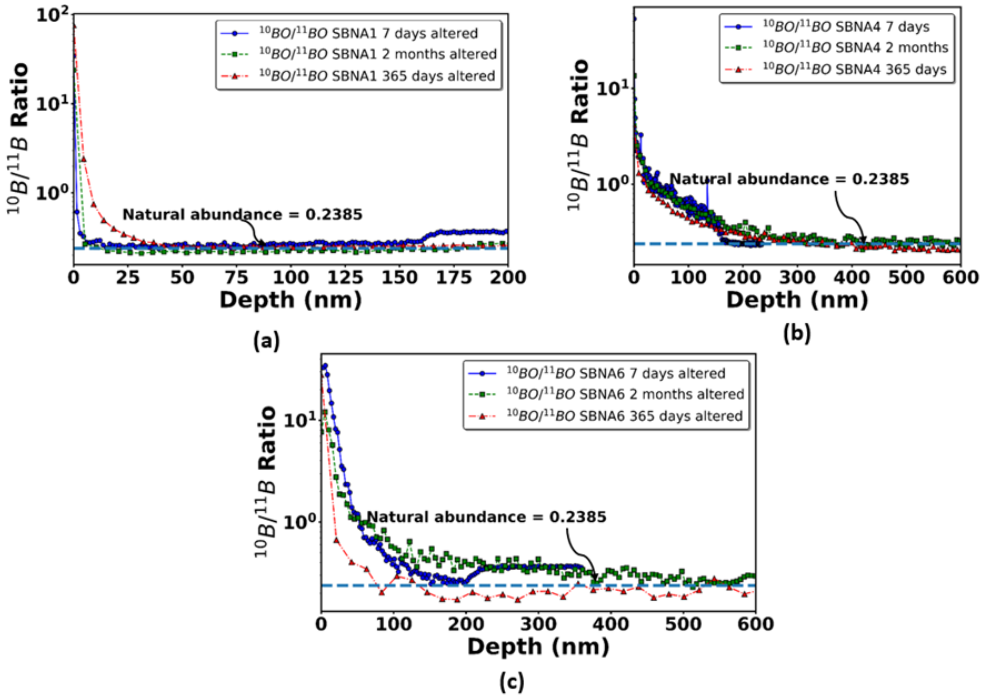

Figure 2.7: *^{10}B diffusivity in gels formed in silica-saturated solutions at 90°C and pH 9. (a) SBNA1,(b) SBNA4 & (c) SBNA6 represent the depth profile of $^{10}B/^{11}B$ ratio in the gel for the glasses altered for 7, 56, and 365 days kept in an isotopically spiked ^{10}B tracing solution for 24 hrs.*

in cryogenic mode. Notably, the gel layer thickness did not increase during the 24-hours tracing experiment at ambient temperature. Figure 2.7 shows the $^{10}B/^{11}B$ ratio in the gels after the three selected alteration durations for the three glass compositions. The diffusion of the ^{10}B isotope is not significant for 7 days and 56 days in the gel of the SBNA1 glass. However, in the 1-year altered sample there diffusion is noticeable up to 40nm. The possible reason has been explored in section 2.3.2 . In contrast, the penetration of ^{10}B in the gel was up to 200 nm for SBNA4 and 100 nm for SBNA6. The diffusion coefficient calculated by fitting Fick's law to the ^{10}B profile for glass altered for 56 days is 1.5×10^{-19} m^2/s for SBNA4 and 4×10^{-20} m^2/s for SBNA6. The possible explanation for the varying diffusive profile of the gel based on glass composition and time can be attributed to the restructuring of the gel layer. The restructuring can be majorly influenced by the presence of Al which makes the gel difficult to reorganize because of the strengthened silicate network in the vicinity of Al. Restructuring could lead to the diminishing of connections between pores [55], [56]. The mobility of solvated boron ions through the gel layer is constrained by the size of their first hydration shell, which limits their movement within narrow channels. This argument about the mobility of boron in nanoconfined silica nanopores has been explored in Chapter 4.

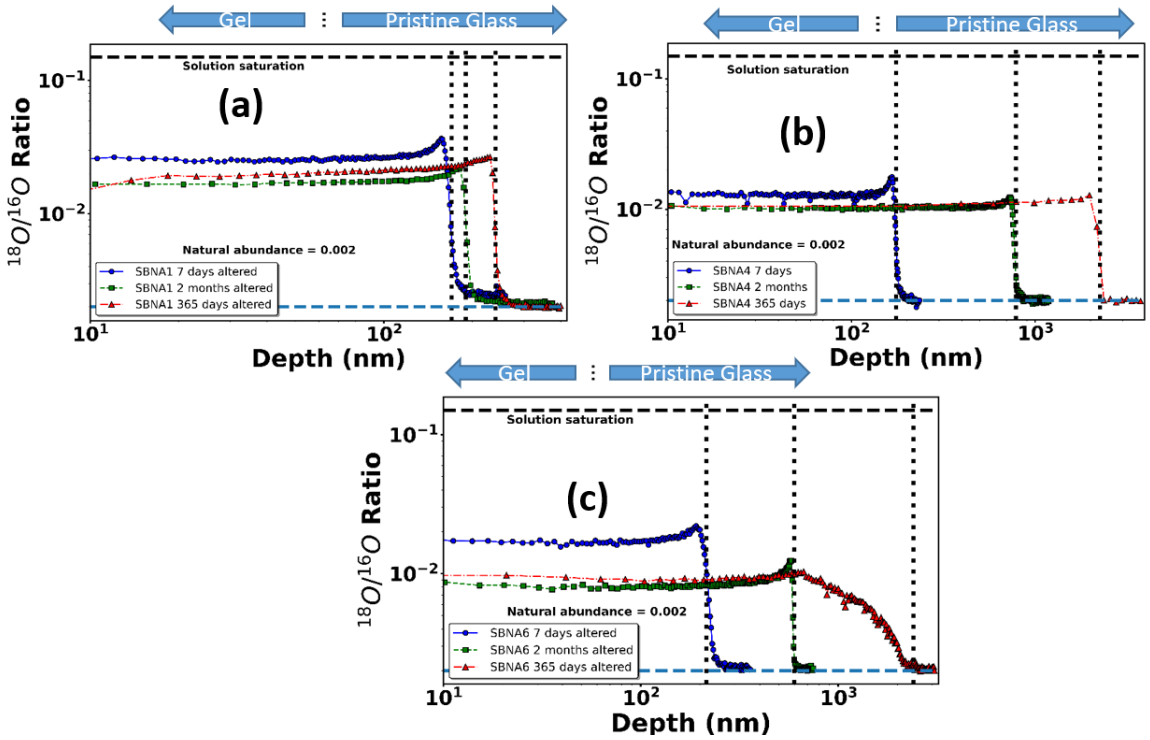

Figure 2.8: *Oxygen isotopic ratio profiles after tracer uptake for (a) SBNA1, (b) SBNA4, and (c) SBNA6. The broader profile for SBNA6 reflects gel-surface roughness. Solution saturation refers to the tracer volume required to fill pore space; the saturation limit is computed using the formula given in the ToF-SIMS section.*

One significant finding is the distinct profiles of ^{18}O and ^{10}B within the gel, indicating that these two isotopes diffused into the gel layer differently. ^{18}O appears to be evenly distributed throughout the gel layer, with a slight enrichment near the gel-glass interface (see Figure 2.8 (a), (b) and (c)). However, the $^{18}O/^{16}O$ isotopic ratio in the gel layer is lower than expected if the entire porosity of the gel was filled with the tracing solution as shown in Figure 2.8. This suggests that only a portion of the pore volume in the gel layer is occupied by the tracing solution. Approximately 5–10% of the porosity was filled, based on the sample's pore volume. Additionally, the $^{18}O/^{16}O$ ratio in the 7-days sample was slightly higher than in the 2-months and 1-year samples, this trend is observed for all glasses. However, no significant decrease in the $^{18}O/^{16}O$ ratio was observed between the 2-months and 1-year samples for all glasses, possibly due to slightly higher B retention in the 1-year sample. This indicates that at least some of the porosity in the gel layer is not readily accessible to water, potentially resembling closed porosity. Water molecules may need to navigate through the gel network between pore walls via interdiffusion or network hydrolysis to access all the porosity. Additionally, it suggests that a small fraction of the pores are sufficiently connected to form channels, facilitating rapid diffusion between the gel-solution interface and the gel-glass interface.

According to the ToF-SIMS profiles, the porosity ranges from 30% to 34% for all glasses (SBNA1, 4, and 6). The porosity can be theoretically estimated by using the fraction of boron and sodium leached out and the radius of these ions [58]. The porosity values are calculated using ToF-SIMS data and are reported in Table 2.5. The porosity values obtained from ToF-SIMS are consistent with those derived from TGA analyses, which carry an experimental uncertainty of ±10%. The measured porosity varies between 26% and 33%, but there is no clear trend related to the age of the gel, indicating that no significant changes correlate with the duration of alteration.

Table 2.5: *Porosity in altered glass samples (%)*

Glass	7 Days		56 Days		365 Days	
	ToF SIMS	TGA	ToF SIMS	TGA	ToF SIMS	TGA
SBNA1	34	27	32	31	29	41
SBNA4	33	27	33	33	31	30
SBNA6	30	27	29	34	29	25

Figure 2.9 (a) and (b) are TEM images of two altered glass monolithic samples. The altered thickness of both monoliths was consistent with the observation from ToF-SIMS analysis. We can observe qualitatively on these images that after 7 days of alteration, the SBNA1 glass monolith has larger pores than SBNA4. It is difficult

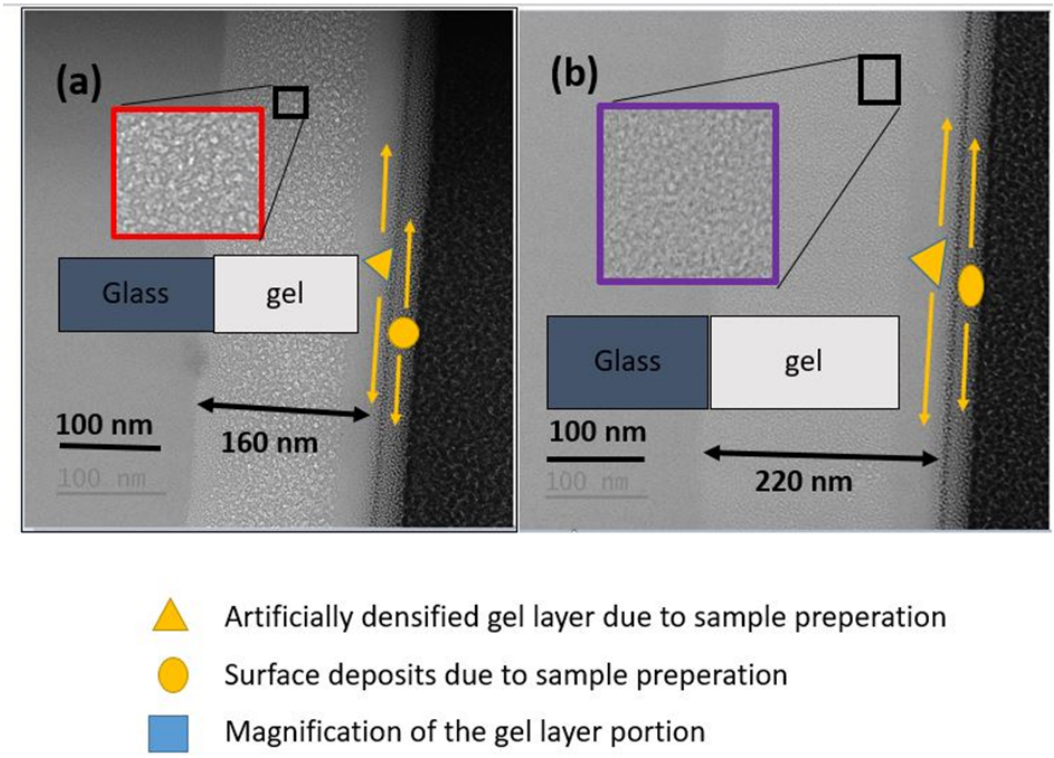

Figure 2.9: *TEM image of 7 days altered glasses: (a) SBNA 1 and (b) SBNA4*

to determine quantitatively the exact size of the pores using TEM, which provides a two-dimensional image of a three-dimensional pore structure. This can lead to pore shapes, sizes, and distributions misinterpretations as overlapping features may not accurately represent the actual 3D arrangement. The visibility of pores is also dependent on the contrast between the pores and the surrounding matrix. Low contrast can hinder accurate identification and measurement of pores and therefore quantification of the pore sizes. Despite these limitations, TEM observations do not provide a quantitative pore size value, but they show that the SBNA1 sample altered for 7 days exhibits more well-defined pores than SBNA4. This qualitative difference is also reflected in the SAXS profiles (see Figure 2.10), where SBNA1 follows Porod's law in the high-q region, consistent with sharper and smoother pore–gel interfaces, while SBNA4 does not. This profile clearly shows the evolution of pore sizes. The absolute intensity for all samples was calculated using equation 2.9 mentioned in the methods (see 2.2.7). The SAXS curve for the unaltered glass exhibited a portion that follows Porod's law (linear correlation with q^{-4} behavior) [139], [140], attributed to the scattering contrast between the glass grains and air. In contrast, the intensity curves for the altered samples displayed one Porod regime for small q, due to the scattering contrast between the glass grains and air, and a second regime for larger values of q, resulting from the scattering contrast between the pores in the gel and air or water. At higher q values (~ 0.01 to 0.1 Å^{-1}), another Porod law can be attributed

to the creation of a large surface area and to the presence of the well-defined pores observed in the 7-days altered sample of SBNA1. In contrast, the profile for SBNA4 does not follow Porod's law [139], [140], which is consistent with the TEM observation concerning larger pores for altered monolith of SBNA1 (altered for 7 days) as compared to SBNA4. The pores for SBNA1 at higher q values ($\sim$ 0.01 to 0.1 Å^{-1}) depict the smooth and sharp interface between the pores and the gel frame. The average pore size calculated from SAXS was not very different for 7 days (2.8 nm), 56 days (3 nm), and 365 days (2.6 nm) while it was difficult to calculate the average pore size from the SAXS curve that does not follow Porod's law because it is harder to define a smooth and sharp interface between the gel skeleton and water. The SAXS spectra for SBNA4 were used to calculate the average pore size of the 365-days altered sample, which is around 3 nm, close to that of SBNA1. TEM images for SBNA6 are not shown; however, its SAXS profile (Figure 2.11 (c)) suggests that the pores formed in this glass are not well defined, making quantitative determination of pore size from SAXS challenging.

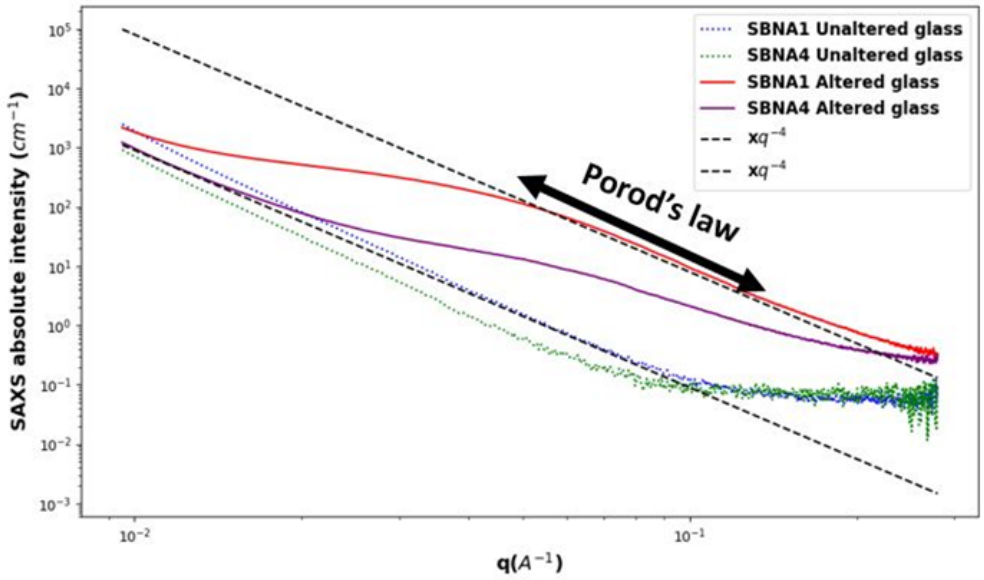

Figure 2.10: *Small-angle X-ray scattering patterns of SBNA1 and SBNA4 for unaltered and 7 days altered glass samples.*

Figure 2.11 (a), (b), and (c) present the SAXS profiles for SBNA1, SBNA4, and SBNA6, respectively. For SBNA1 and SBNA4, data are shown for samples altered for 7, 56, and 365 days, while for SBNA6 the profiles correspond to 56 and 365 days of alteration. The pore structure of SBNA1 shows little variation with alteration time and consistently follows the Porod law regime, indicating the presence of well-

defined pores. In contrast, SBNA4 exhibits a clear evolution of its pore structure over time: the 7-day and 56-day samples do not follow the Porod law regime, whereas the 365-day sample shows the development of well-defined pores. SBNA6 does not display any indication of well-defined pores for either alteration duration.

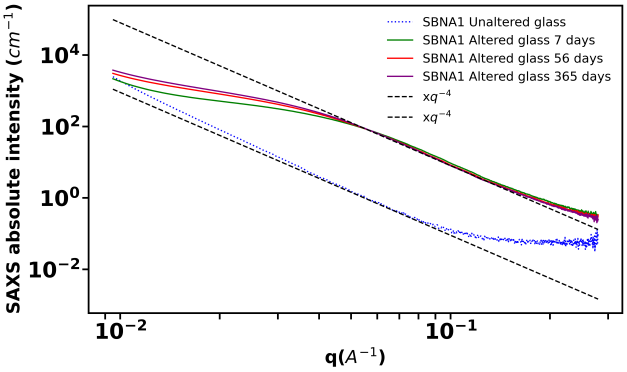

(a)

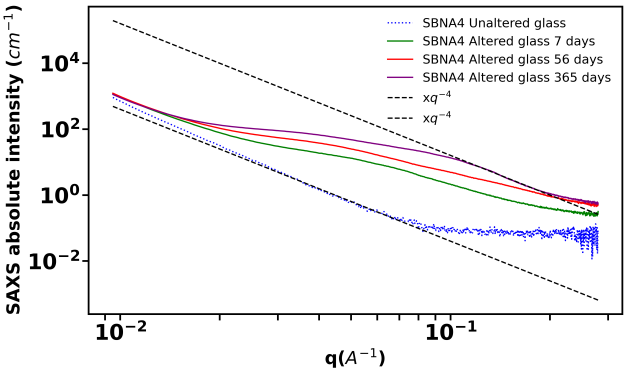

(b)

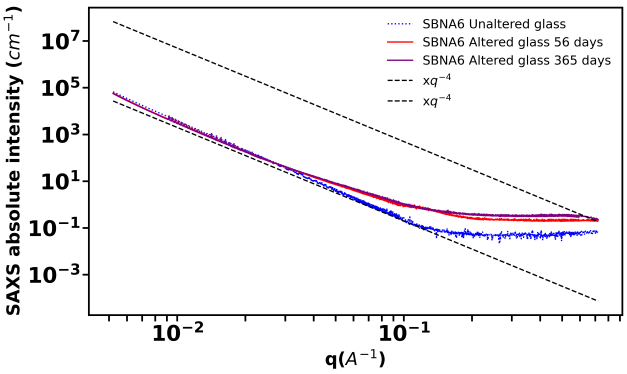

(c)

Figure 2.11: *Small-angle X-ray scattering patterns of the glasses for (a) SBNA1 (b) SBNA4 (c) SBNA6*

Impact of dense layer

One argument on the passivation of SBNA1 may be attributed to the formation of a dense layer near the interface. The literature indicates that gel formation in glasses during aqueous alteration can occur through two primary mechanisms [52]: dissolution/precipitation, where silica dissolves in an interfacial film of water and re-precipitates to form a gel layer, or in-situ reorganization, where the glass network restructures locally without significant silica precipitation. To investigate which mechanism governs gel formation in glasses with varying aluminum content (1 and 6 mol% Al_2O_3, corresponding to SBNA1 and SBNA6), we analyzed the enrichment in ^{29}Si of the gel layer using ToF-SIMS. Dissolution/precipitation typically results in ^{29}Si enrichment due to preferential silica precipitation, whereas in-situ reorganization involves minimal isotopic enrichment.

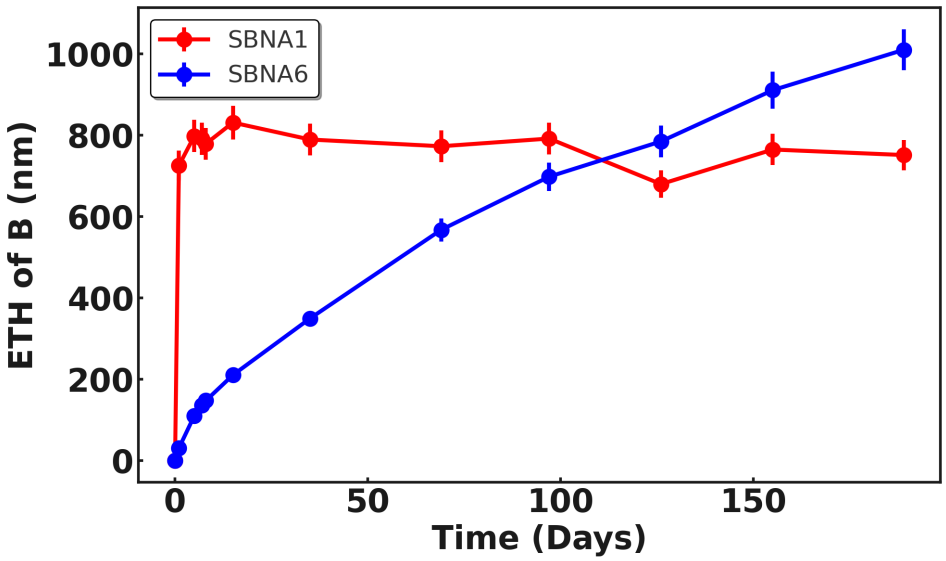

Figure 2.12: *Normalized boron mass loss, $NL(\mathrm{B})$, as a function of the square root of time for SBNA1 and SBNA6 during Experiment 1c. The experiments were conducted at $90\,^{\circ}\mathrm{C}$ and pH 9, with a surface-area-to-volume ratio of $50\,\mathrm{cm}^{-1}$. Data were obtained from ICP–OES measurements.*

In Experiment 1c (See section 2.2.1), the equivalent thickness for the altered glass (with boron as a tracer) is shown in Figure 2.12 which is consistent with the results obtained in Experiment 1a(Figure 2.5) confirming similar dissolution behaviors for glass powders despite different initial conditions (10% ^{29}Si-saturated solution and simultaneous powder-coupon alteration). The gel layer thicknesses measured by ToF-SIMS and equivalent thicknesses (ETH) calculated from ICP-OES for SBNA1 and SBNA6 are presented in Table 2.6.

For SBNA1 (glass monolith), ToF-SIMS indicated a gel layer thickness of 136 nm after 2 months, increasing to 580 nm after 6 months, while ICP-OES showed ETH val-

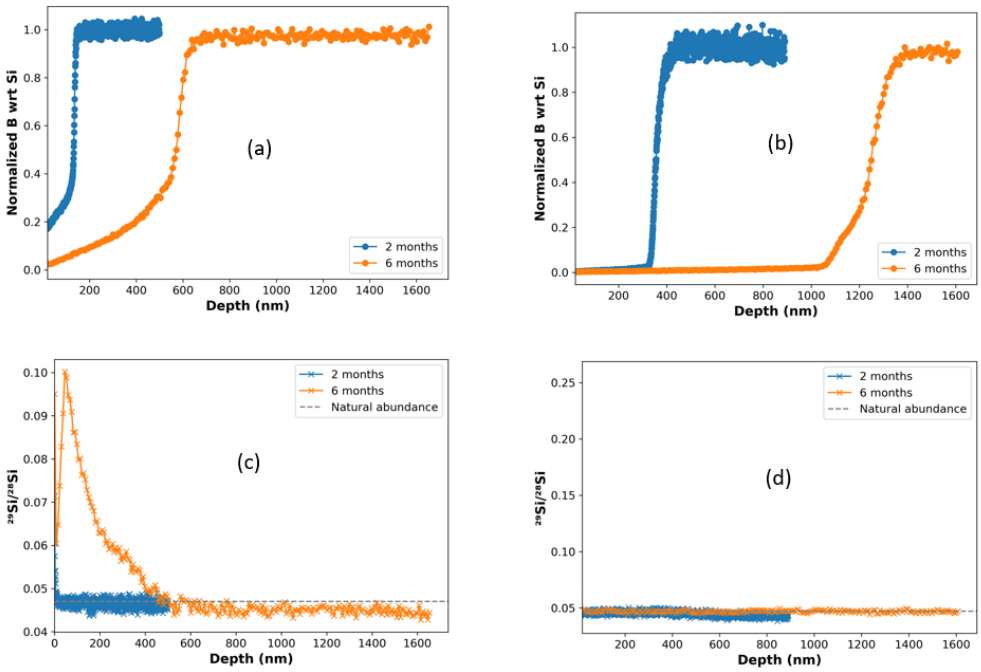

Figure 2.13: *a,b B profiles recorded using ToF-SIMS normalized to Si for SBNA1 and SBNA6. c, d $^{29}Si/^{28}Si$ profiles compared to the natural abundance indicated as dotted line for SBNA1 and SBNA6.*

Table 2.6: *Equivalent thickness calculated from ToF-SIMS and ICP-OES for experiment1c*

Name of Glass	2 Months		6 Months	
	ToF-SIMS (nm)	ETH from ICP (nm)	ToF-SIMS (nm)	ETH from ICP (nm)
SBNA1	136	772	580	750
SBNA6	360	567	1130	1009

ues of 772 nm at 2 months and 750 nm at 6 months. For SBNA6, ToF-SIMS measured gel layer thicknesses of 360 nm at 2 months and 1130 nm at 6 months, with ETH values of 567 nm at 2 months and 1009 nm at 6 months. The discrepancy between ToF-SIMS and ICP-OES for SBNA1 suggests differences in alteration dynamics between glass powders and monoliths. In contrast, SBNA6 shows closer alignment between ToF-SIMS and ICP-OES, indicating more consistent alteration behavior.

ToF–SIMS analysis of ^{29}Si enrichment (Figure 2.13) reveals distinct behaviors in the two glasses. In SBNA1, no enrichment is observed after two months, in line with earlier reports of in-situ reorganization [53]. After six months, however, an enrichment of about 10% appears, suggesting that dissolution and reprecipitation may also occur. In contrast, SBNA6 shows no measurable enrichment at either two or six months, which supports in-situ reorganization as the prevailing mechanism.

The isotopic results are consistent with the elemental profiles. SBNA1 retains boron within the gel, a sign that the gel layer develops passivating properties, whereas

SBNA6 retains very little boron, consistent with a gel that is less protective. These observations are in qualitative agreement with Experiment 1a (Figure 2.5), where SBNA1 again shows more resistance to alteration than SBNA6.

The mechanistic interpretation follows naturally. In SBNA1, Si–O bonds break quickly enough that silicon species can dissolve completely, exchange with the solution, and re-incorporate into the gel. This exchange produces progressive ^{29}Si enrichment and an external gel structure that becomes less compact over time. The penetration of ^{10}B into the SBNA1 gel (see Figure 2.7) after one year supports this view, pointing to a progressively more open gel network. SBNA6 behaves differently. Its higher aluminum content increases the activation energy for Si–O bond rupture, preventing the simultaneous breaking of all bonds around a given Si atom. This restricts exchange with the solution and suppresses both ^{29}Si enrichment and tracer penetration.

The apparent duality in SBNA1—sometimes consistent with in-situ reorganization, sometimes with dissolution/precipitation—likely reflects its position at a compositional threshold. With intermediate aluminum content, small variations in solution chemistry, pH, temperature, or hydrodynamics can shift the balance between mechanisms. Previous studies show that gel solubility rises as aluminum content decreases, and that in compositions such as SBNA0 or SBNA1 it can even exceed that of amorphous silica [52], [53]. Because supersaturated silica solutions are highly reactive and sensitive to minor perturbations [141], differences in surface area between powders and monoliths—and therefore in silicon release rates—can readily alter the outcome. Taken together, the evidence indicates that Al-rich glasses such as SBNA6 consistently favor in-situ reorganization, Al-free glasses such as SBNA0 undergo dissolution and reprecipitation, and SBNA1 lies between these endmembers, where both mechanisms compete and the dominant pathway depends on subtle shifts in experimental conditions.

2.3.3 Summary of results

The present research outcomes are consistent with previous studies on the same glass composition [53], particularly in the observed qualitative trends of alteration thickness measurements. However, a significant discrepancy arises for SBNA1 between thickness values obtained via ICP and ToF-SIMS analyses: the alteration thickness measured by ICP is nearly four times greater than that determined by ToF-SIMS. This divergence is likely linked to the activity of silica—given its higher solubility compared to amorphous silica—which governs the alteration dynamics between glass powders and monoliths, even though both monolith types display qualitatively similar behavior.

It is worth emphasizing that SBNA1, due to its relatively low Al content, exhibits distinct alteration behavior compared to SBNA4 and SBNA6. While SBNA1 undergoes a rapid initial dissolution stage, it subsequently shows a low residual alteration rate; in contrast, SBNA4 and SBNA6 display the opposite trend, with slower initial dissolution followed by more sustained alteration.

2.4 Discussion

The purpose of this discussion is to synthesize and interpret the experimental findings in relation to glass composition, gel layer evolution, and alteration kinetics. These insights not only enhance our understanding of the mechanisms governing glass durability but also lay the groundwork for supporting the Monte Carlo (Chapter 3) and molecular dynamics simulation (Chapter 4) approaches presented in the coming chapters.

2.4.1 How does the composition of the glass influence the formation and restructuring of the gel layer?

The role of aluminum in glass alteration is complex. Its effect varies depending on the specific alteration regime under consideration. Within the initial alteration rate regime, extensive research has explored the influence of aluminum, particularly in relation to the Al_2O_3 content in the glass [38], [39], [40]. At low concentrations (around 3.5 mol%), an increase in aluminum content is found to notably diminish glass alteration. At intermediate levels (3.5 mol% $\leq x \leq$ 19 mol%), aluminum continues to exert a beneficial effect on alteration, albeit to a lesser degree. In contrast, at higher concentrations (above 19 mol%), the alteration rate demonstrates a significant increase.

Recent investigations shed light on the fact that aluminum readily dissolves during the early stages of alteration while also reinforcing the vitreous network. Notably, the dissociation activation energy of silicon atoms in proximity to aluminum atoms as second neighbors surpasses that of silicon atoms within a pure silica network [38]. For the glass series of the present study, an increase in both silicon and aluminum content is associated with a reduction in the initial alteration rate. This observed effect can be attributed to the enhanced polymerization and stability of the glass network, as the presence of network formers resistant to hydrolysis increases [40].

The current study points out increase in aluminum content correlates with an increase in residual alteration rate. This trend can be linked to the effect of zirconium in glasses, where higher zirconium concentrations tend to reduce the initial dissolution rate. At lower zirconium concentrations, the residual rate significantly reduces,

whereas at higher concentrations, it tends to increase [142], [143]. This behavior is attributed to the effect of zirconium on the dissolution of surrounding atoms, impeding the restructuring and recondensation of silicon atoms and thereby impeding the formation of a protective gel. Our experiments underscore the pivotal role

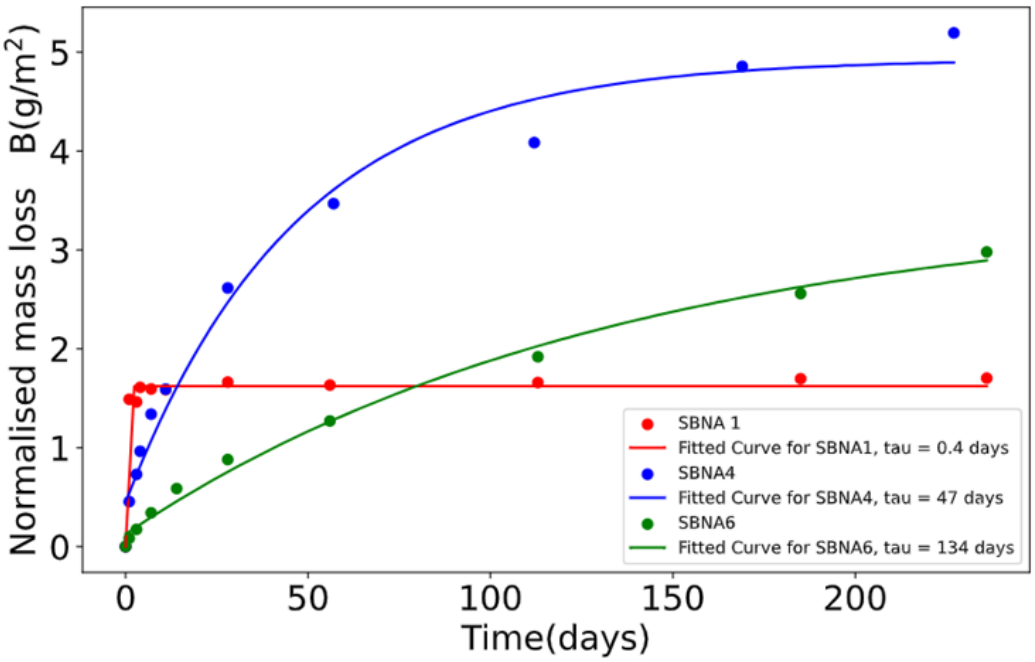

Figure 2.14: *Fitted Normalised mass loss of Boron for SBNA1, SBNA4 and SBNA6 for transition time τ*

of aluminum in regulating the restructuring of the gel, subsequently impacting the residual alteration rate of the glass, in line with previous studies. As indicated in Table 2.7, the transition time (τ) for SBNA1 is significantly lower than that of both SBNA4 and SBNA6 (Figure 2.14). Following the transition from the initial dissolution rate of the glasses to the residual rate, the alteration gel skeleton becomes more rigid. This observation aligns with the experimental result that the glass with the lowest aluminum content (SBNA1) matured faster than those with higher aluminum content (SBNA4 and SBNA6).The rapid reorganization effect is influenced not only by low Al content but also by elevated concentrations of B [30], [41]. In contrast to Al, B disrupts the silicate network by introducing Si–O–B linkages, which are more susceptible to hydrolysis than Si–O–Si bonds [144]. This increased susceptibility facilitates faster gel reorganization.

2.4.2 How do the properties of the gel layer, such as porosity, pore size, and diffusivity for boron and water, evolve over time?

The SAXS profile of the SBNA1 glass sample (altered at 7 days, 56 days, and 1 year) reveals that the pore morphology remains constant throughout the alteration dura-

Table 2.7: *The initial dissolution rates, residual rates, rate drops, and parameters τ for the three glasses of this study have been determined at $90°C$ and $pH = 9$.*

Glass	r_0 (g.m^{-2}.d^{-1})	r_r (g.m^{-2}.d^{-1})	$\frac{r_0}{r_r}$	τ (days)
SBNA1	5.79	4.0×10^{-4}	1.43×10^{4}	0.4
SBNA4	1.9	2.4×10^{-3}	4.25×10^{2}	47
SBNA6	0.69	9.5×10^{-3}	6.34×10^{1}	134

tion. The profile obtained from SAXS also highlights the presence of well-defined pores (in agreement with Porod's law) and an average pore size of approximately $3\,\mathrm{nm}$, irrespective of the alteration duration. In contrast, the pore morphology of SBNA4 evolves with time, and the SAXS profile for the alteration durations of 7 days and 56 days suggests that the pores are not well defined and do not follow Porod's law. However, for the alteration duration of 1 year, the pores follow Porod's law with an average pore size of approximately $3\,\mathrm{nm}$. The observation from SAXS is supported by the TEM images, which indicate that the pores formed during 7 days of alteration for SBNA1 are larger than those of SBNA4 altered during 7 days. The porosities of all the glasses do not change drastically throughout the duration of the experiment and remain around 30–34% for all glasses. Hence, the evolution of the pore structure can be attributed to the reorganization (hydrolysis and condensation of siloxane bond driven by a global decrease of the free energy of the gel). If one consider that total pore volume remains constant over time while mean pore size increases through ripening, it results an increasing distance between pores, with potential implication on the transport of hydrogenated species and mobile elements form the glass (particularly B). The transport of elements such as boron in the gel plays an important role in understanding some of the mechanisms that control the residual rate [16]. The gel structure formed by SBNA1 was highly passivating, with low boron diffusivity in the gel and boron being retained in the gel, as revealed by ToF-SIMS. In contrast, boron diffusivity in the gel was relatively high for SBNA4 and SBNA6, according to the ToF-SIMS experiments.

2.4.3 Is it possible to establish a connection between the maturation of the gel layer and its impact on the glass dissolution kinetics?

Studies of SBNA1 glass dissolution kinetics reveal a marked decrease in alteration rate over time. While an affinity-driven dissolution rate law successfully explains the release of silicon into solution, it fails to capture the behavior of boron, a well-established tracer of glass alteration (Figure 2.4 and 2.5). This discrepancy is particularly evident for SBNA1, which rapidly reaches silica saturation. In this case, boron

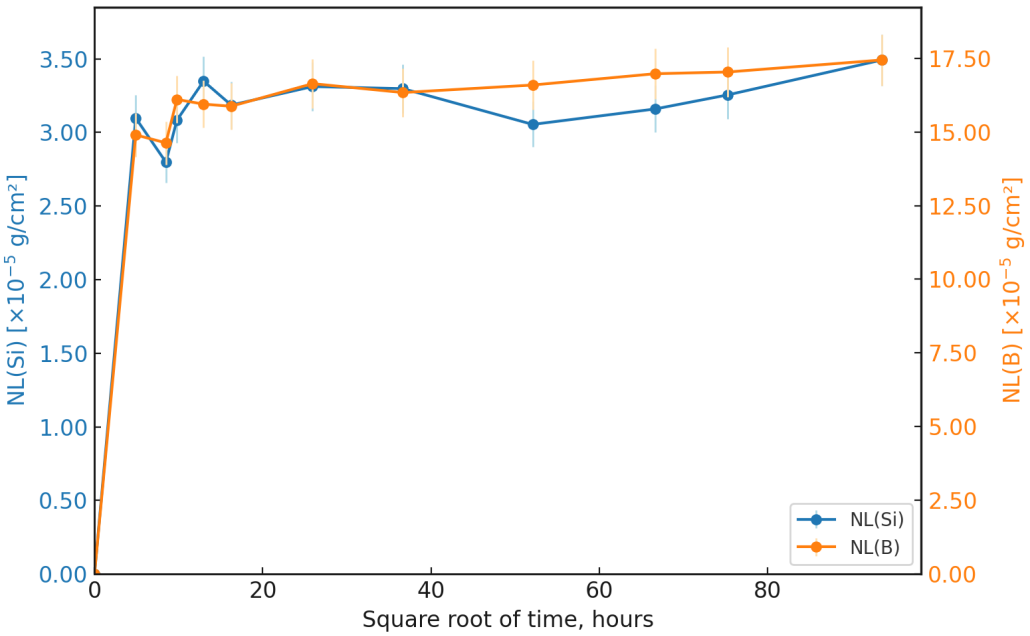

Figure 2.15: *Normalised Mass for B and Si plotted in primary and secondary axes for SBNA1 glass*

release is not expected to be affected by feedback from the solution; if the affinity model were valid, boron release should continue steadily. Instead, as shown in Figure 2.15, boron release in SBNA1 ceases after only a few days, indicating a passivation mechanism not captured by the affinity framework.

The passivation of SBNA1 cannot be explained by the early formation of an outer, silica-rich surface layer as observed in CJ1 glass (Al-free) [52], since no enrichment in ^{29}Si is detected in the gel up to two months of alteration in a 10% ^{29}Si-enriched solution. This finding is consistent with literature on one-month altered samples in silica-saturated conditions (relative to amorphous silica) [53]. Although an outer layer that is silica-enriched in some cases appears after six months to one year, it is not protective, as it remains permeable to species such as ^{10}B. In fact, progressive gel dissolution and enrichment in ^{29}Si seem to produce a less protective outer layer over time. Therefore, the passivation already evident at 7 days and 2 months is better explained by the intrinsic passivating properties of the alteration gel, rather than by the later-formed outer layer.

As discussed in Section 2.4.1, Al (and B) controls the restructuring of gel during glass alteration and controls the residual rate regime which is consistent with the literature [30], [41]. Low Al content in the glass leads to quick maturation and the gel morphology reaches a quick pore saturation (see Section 2.4.2) . The pores evolve in such a way that smaller pores coalesce to form larger ones, which typically increases the inter-pore distance and reduces pore connectivity. This happens through hydrol-

ysis and condensation reactions which minimizes the free energy of the gel [55], [56], [57]. The mechanism by which the gel maturates has been modeled using Monte-Carlo in Chapter 4. We observed significant boron retention in the gel for SBNA1 which is consistent with the results in previous literature [53]. In the case of SBNA4, we saw that the boron retention was more visible as the pore structure evolved while we didn't see any significant retention in SBNA6 which correlated with it's slow re-organisation.

For SBNA1, the initial high dissolution rate is followed by a rapid drop, coinciding with the formation of a gel that strongly retains boron: retention increases from ~15% at 7 days to ~24% after one year. The negligible outward diffusion of boron from the altered glass volume indicates highly passivating properties, likely arising from a combination of solid-state diffusion and molecularly constrained aqueous diffusion. This behavior corresponds to a low residual rate of 4.0×10^{-4} g·m^{-2}·d^{-1}. Given the low Al content of SBNA1, this strong passivation probably results not only from the precipitation of secondary phases at the gel surface, but also from rapid inward network reorganization that reduces pore connectivity.

In contrast, SBNA4 and SBNA6 exhibit slower gel maturation ($\tau \approx 47$ days and 134 days, respectively) due to their higher Al content. This leads to greater boron mobility, lower boron retention (~5% for SBNA4 and negligible for SBNA6), and higher residual rates of 2.4×10^{-3} and 9.5×10^{-3} g·m^{-2}·d^{-1}, respectively. The estimated boron diffusion coefficients in the gels formed by these glasses ($\sim 10^{-20}$ m^2/s) are orders of magnitude lower than in bulk solution ($\sim 10^{-9}$ m^2/s), yet still high enough to reflect more open structures than in SBNA1. Combined isotope tracing with ^{10}B and ^{18}O confirms this: ^{18}O penetrates the gel–glass interface over the tracing period, whereas ^{10}B does not. This implies that the $B(OH)_3$ species is too large to traverse the available nanochannels, supporting the notion of size-selective transport through an evolving pore network.

Overall, the alteration rate decreases with time for all SBNA glasses as their gels mature, but the extent and timing of passivation depend strongly on gel structure and composition. Both the chemical reactivity and the structural characteristics of the gel evolve continuously, governing species transport and ultimately controlling long-term dissolution kinetics.

Conclusion

This experimental study aims to examine how glass composition affects gel layer formation and restructuring, investigate the evolution of gel layer properties—such as porosity, pore size, and diffusivity of boron and water—over time, and establish the relationship between gel layer maturation and glass dissolution kinetics. From the results obtained after the aqueous alteration experiment conducted on a simplified sodium-alumino-borosilicate glass over a period of one year, it can be concluded that the glass alteration rate is significantly influenced by the Al concentration in the glass. Although Al has a positive role in limiting the initial dissolution, Al controls the restructuring of the glass, which in turn leads to the evolution of gel properties and affects the dissolution kinetics in the residual rate regime. Using the solution data (ICP) and the ToF SIMS data we observe that the amount of Al in the glass affects the gel morphology. With a low Al content, glass forms a very passivating gel quickly as compared to higher Al content glass, this maybe because for one glass the rate of reorganization is much higher than that of the other [38], [53]. The concentrations of B, Na, and Si in the solution suggest that the drop in the glass alteration rate is attributed to the transport properties of the gel layer rather than a decrease in affinity from the solution. The SAXS data suggest growth of pores with the alteration time. The low Al content glass reached a pore saturation quickly as compared to other glasses with high Al content as the pores become bigger and disconnected. This results suggest that a matured gel is less connected and the diffusion of water and boron is restricted. The gel does not just evolve in terms of its physical structure, but also its chemical reactivity. The experiments also suggest the drop in reactivity as the gel matures, which is evident from the tracing experiments where less ^{18}O is exchanged from the tracing solution to the gel with time.

Overall, these findings have provided valuable insights into the mechanisms controlling the glass alteration rate of simplified sodo-alumino-borosilicate glass. The results highlight the importance of understanding the transport properties of the gel layer and the mechanisms by which they affect the glass alteration rate to have a global alteration model. The mechanism can be linked with other methods such as Monte-Carlo and Molecular dynamics to develop accurate models of global alteration behavior.

3 Monte-Carlo Modeling

Contents

3.1 Introduction

Over the past few decades, stochastic lattice models based on the Monte-Carlo (MC) method have been widely used to simulate glass corrosion. These models have offered valuable insights into the microscopic processes that govern glass-water interactions, including the effects of network modifiers such as sodium (Na), the roles of glass components like zirconium (Zr) and aluminum (Al), and, more recently, the coupling between hydrolysis and diffusion. Through these studies, Monte-Carlo simulations have significantly enhanced our understanding of the atomic-scale mechanisms driving glass alteration [56], [138], [145], [146], [147].

This chapter introduces a novel Monte-Carlo approach to explore key mechanisms occurring at the glass-solution interface and during gel maturation. Specifically, it aims to address the following questions:

1. What interactions and transformations occur at the glass-solution interface, and how can these be linked to the kinetics of alteration as observed in experimental studies?
2. What mechanisms influence the restructuring of gel, particularly in relation to the role of aluminum (Al) in glass?

3. Is it possible to establish an interplay between the parameters controlling the gel characteristics?

4. How can we link the evolution of MC gel structure over time to diffusive processes, and can it be linked to experimental observations from small-angle X-ray scattering (SAXS) and transmission electron microscopy (TEM) in order to link it to the alteration kinetics?

Addressing these questions is crucial for elucidating the fundamental mechanisms that govern glass alteration, particularly those related to the formation of protective layers and the long-term diffusion characteristics of alteration gels. The Monte-Carlo model utilized in this study employs a dual-network representation to simulate water diffusion within the solid matrix, with a specific focus on the structural evolution of the gel. Critical structural features, including pore size and channel diameters, are systematically analyzed, and simulation parameters are meticulously calibrated to facilitate a qualitative as well as quantitative comparison with experimental data derived from SAXS and TEM.

This chapter is organized into several key sections to guide the reader through the development and application of the Monte-Carlo modeling approach. Following the introduction, the first section provides an overview of previous Monte-Carlo methods used in the study of glass alteration, highlighting the evolution of modeling strategies and their respective limitations. The next section introduces a newly developed Monte-Carlo algorithm, detailing its dual-network architecture and the mechanisms governing water diffusion, hydrolysis, and redeposition. The subsequent sections present simulation results for different glass compositions, comparing model outputs to experimental data to validate parameter choices. Finally, the chapter explores gel maturation dynamics and analyzes the morphological evolution of the altered layer, including pore size distribution and channel connectivity, culminating in a discussion that links simulation insights to experimental observations and broader implications for long-term glass stability.

3.2 Description of the methods

3.2.1 Previous Monte-Carlo methods

Monte-Carlo (MC) methods are a widely used class of computational algorithms that rely on repeated random sampling of a stochastic process to obtain an average result. These methods, which are based on probabilities of occurrence of selected events, were first developed by mathematician Stanislaw Ulam in the late 1940s during his work on nuclear weapons at the Los Alamos National Laboratory. Since their inception, MC methods have been extensively applied across various fields,

including the simulation of complex physical, biological, and chemical systems.

Aerstens and Van Iseghem introduced MC modeling to study the dissolution of glasses [145], [148]. Aertsens's method utilizes a diamond network structure consisting of two types of elements: a sparingly soluble element (Si) and a soluble element (Na). The Si and Na atoms are randomly distributed throughout the network. The solid network is in contact with a solution. In this method, there are two important probabilities.

The first probability, denoted as P^+, determines the likelihood of breaking Si–Si bonds within the diamond network. This process allows Si atoms to detach from the network and enter the solution. The second probability, denoted as P^-, determines the likelihood of reforming a Si–Si bond, causing Si atoms to be redeposited back onto the diamond network. Together, these opposing processes of dissolution and redeposition create the possibility for a protective layer to form at the interface.

The released Si atoms are capable of freely diffusing within the solution. This diffusion process is governed by another probability, P_{diff}, which is much higher than both P+ and P-. This indicates that Si atoms have a strong tendency to move and spread throughout the solution.

Additionally, the Na ions within the network can undergo an exchange process with water molecules present in the solution. The likelihood of this exchange occurring is determined by the probability P_{ion}.

$$\mathrm{Si-O-Si + H_2O \rightarrow Si-OH + Si-OH} \tag{3.1}$$

$$\mathrm{Si-O-Na + H^+ \rightarrow Si-O-H + Na^+} \tag{3.2}$$

Aertsens simulations show how sodium in glass affects how it dissolves when there's no silica in the solution and the glass surface-to-volume ratio is zero [148] (i.e. infinite volume). With low sodium, the glass dissolves slowly and evenly because sodium can't escape without silica breaking down first. But with more sodium, paths form inside the glass, letting sodium leak out quickly and unevenly, even when silica levels are maxed out, creating thick surface layers. There's a tipping point—called the percolation threshold—where below it, sodium stops leaching once silica saturates, but above it, sodium keeps going. The more sodium in the glass, the thicker the surface layer gets, though a higher P_+/P_{ion} ratio can thin it out. These results match up with surface layer types described by Hench and Clark and sodium patterns seen in SIMS analyses, making the simulations a good fit for real-world observations.

Aertsens's method involves the dynamic processes of Si-Si bond breaking and re-

forming, Si diffusion within the solution, and Na ion exchange with water molecules. These characteristics define how the system behaves and interacts with the surrounding solution. The main drawback of the model came from the restriction in the size of the system due to simulation of the diffusion of Si in solution that is very time consuming.

Building on Aerstens work, Devreux and colleagues developed a similar MC model, but without explicitly modeling species diffusion [143]. This simplification allowed them to simulate larger systems. Their work examined the effects of glass morphology, composition, and dissolution probabilities. Their simulations suggested that the altered layer could act as a passivating barrier. Once this gel layer forms, it significantly restricts the further release of soluble species by acting as a compact, less permeable barrier. Additionally, their model explained the delayed formation of the passivation layer in glasses containing insoluble oxides.

Devreux and Ledieu's method models the atomic structure and reactivity of glass, particularly for studying water-induced alteration in nuclear glasses [138], [146]. The glass structure is represented as a network of tetrahedral sites mapped onto a cubic lattice, topologically equivalent to a diamond lattice as shown in Figure 3.1(a). To achieve fourfold coordination, two bonds per site are removed—upward and forward for even sites, downward and backward for odd sites—enabling efficient site labeling and management of systems with over 10^8 sites. Network-forming cations (e.g., silicon, aluminum, boron) are randomly distributed on lattice vertices based on glass composition, with oxygen atoms at bond midpoints and modifier cations (alkalis or alkaline earths) in interstitial positions to balance charge defects. Silicon and aluminum are typically fourfold coordinated, while boron can be threefold (B(III)) or fourfold (B(IV)), with ratios determined via ^{11}B NMR or literature data (representations of these three fold and fourfold coordinates is mentioned in Figure 3.1(b)). Elements with higher connectivity (e.g., Zr, Fe^{III}) are approximated as fourfold coordinated sites, adjusting reactivity parameters to reflect their bonding tendencies.

Reactivity at the glass–water interface is modeled using kinetic Monte–Carlo simulations, focusing on the hydrolysis and condensation of dissolved species. Dissolution probabilities are determined by cation type and local environment, such as the number and type of bonds. Weaker bonds, such as B–O, are assigned a probability of 1, indicating immediate dissolution. For silicon, dissolution probabilities (denoted w_n) depend on the number of siloxane bonds (ranging from 1 to 3) and are adjusted by a factor (r) when bonded to other cations (e.g., Si–O–X), as illustrated in Figure 3.2. Redeposition probabilities (w_c) are proportional to solution concentrations, though boron and sodium are assumed to be infinitely soluble and thus do not redeposit. This approach results in a first-order kinetic law for dissolu-

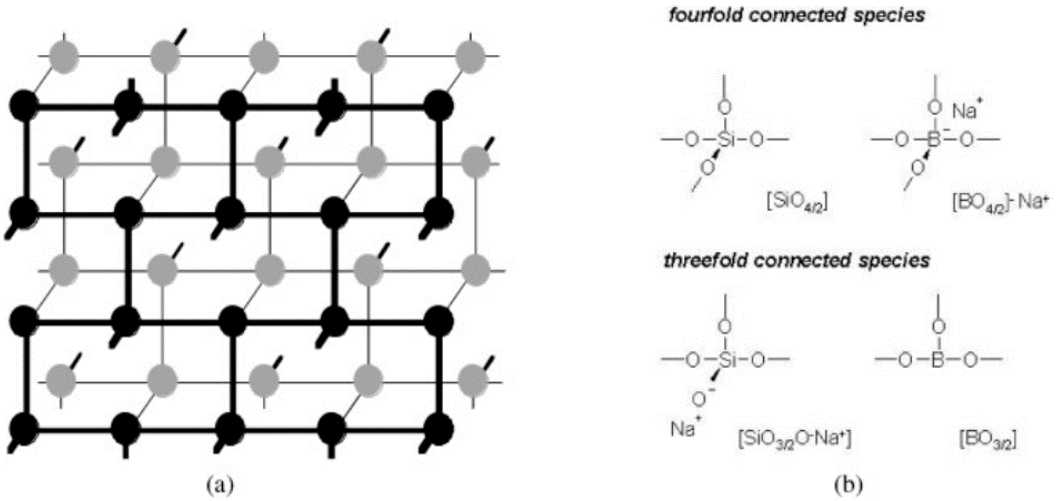

Figure 3.1: *(a) The diamond structure is projected onto a cubic lattice, where two bonds are alternately removed, one oriented upward and forward, and the other downward and backward. (b) Vertices of the lattice are occupied by a random distribution of fourfold and threefold coordinated species. Glass modifier cations are inserted into interstitial sites to balance the charge imbalances [142].*

tion rates, with stationary concentrations emerging from a balance between dissolution and condensation, influenced by interface composition and leaching conditions. The model prioritizes simplicity, intentionally omitting complex refinements such as clustering or aluminum avoidance, to efficiently capture the primary physics of glass alteration. However, this method cannot assess the residual alteration rate, as alteration ceases once a protective layer forms because no water diffusion is allowed.

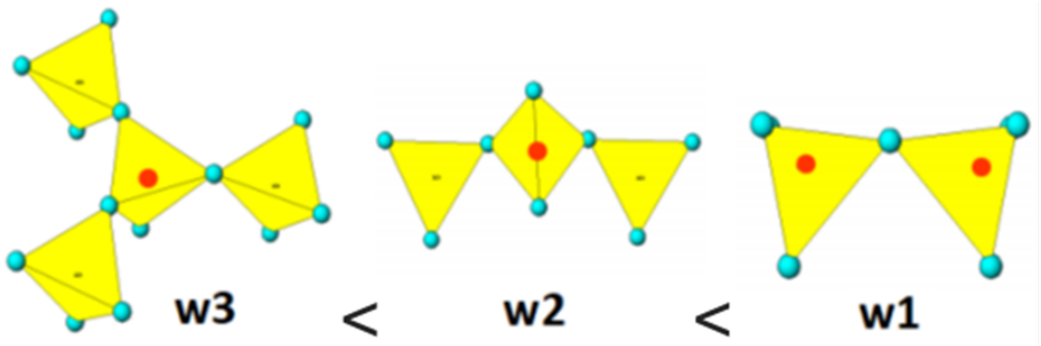

Figure 3.2: *The glass dissolves atom by atom, rather than bond by bond, with probabilities that depend on the local reticulation level.*

In this study [138], the dissolution kinetics of borosilicate glasses, as observed experimentally, were compared with predictions from numerical simulations to evaluate a simplified model centered on silica reactivity. A reference glass (66% SiO_2–17.4% B_2O_3–16.6% Na_2O) mimicking the SON68 composition, altered at 90°C, pH

8.5, and SA/V = 100 m^{-1}, showed saturation of silicon, boron, and sodium concentrations. Silicon saturated at ~125 mg/L (close to amorphous silica solubility), while boron and sodium concentrations plateaued at ~55 mg/L and ~110 mg/L, respectively, indicating corrosion blocking by a passivating layer. The simulations with parameters w_1=10^{-2}, w_2=10^{-3}, w_3=10^{-4}, w_c=10 qualitatively matched these trends, though initial parameter sets overestimated saturation values. A slight adjustment in the dissolution and condensation probabilities achieved exact agreement with experimental saturation values, validating the model's predictive capability when fine-tuned. The comparison with experiments and simulations are shown in Figure 3.3(a) and (b).

This approach was validated for a ternary sodium borosilicate glass, where corrosion behavior in a free-pH solution mirrored that in a pH-buffered solution. The simulations, optimized against experimental data with a Na/B ratio of 1 (representative of nuclear waste confinement glasses), highlighted the competing roles of soluble element loss and reversible silica hydrolysis-condensation in determining corrosion extent. Boron oxide, a key component, influenced durability by consuming glass modifiers and resisting depolymerization, yet its rapid dissolution and network percolation significantly accelerated corrosion and shaped the porosity of the altered layer. Figure 3.3 (c) and (d) illustrate a two-dimensional slice of the sample at the simulation's conclusion. It reveals a porous surface layer, approximately 310 nm thick (calculated using a 0.3 nm/pixel scale), which is nearly devoid of sodium and boron, consistent with experimental findings. Due to the dynamics of silicon dissolution and recondensation, this surface layer has undergone reconstruction throughout the process: the pores have enlarged, the pore walls have thickened, and the porosity has eventually sealed, leading to a corrosion-blocking effect that prevents further removal of soluble components. This model offered a clear explanation for the formation of a protective passivating layer on the glass surface. It also accounted for the paradoxical behavior of weakly soluble oxides like zirconium, which slow corrosion kinetics (low initial dissolution rate) yet increase the final residual rate in glass alteration. According to the model this occurs because the addition of Zr hinders the reorganization of the gel network.

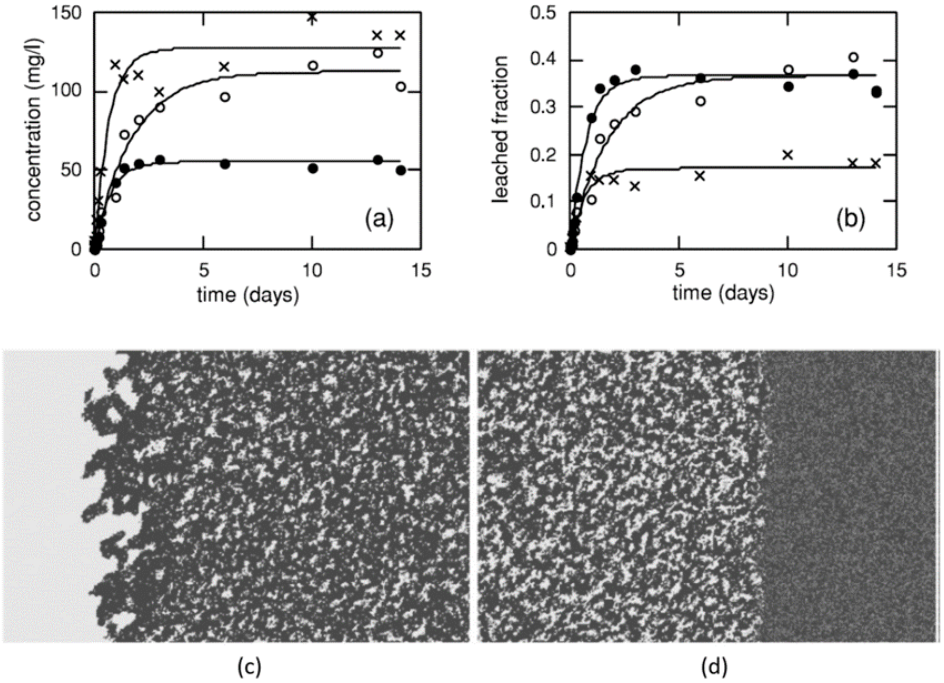

Figure 3.3: *The changes in (a) the concentrations and (b) the leached proportions of silicon (marked with crosses), boron (indicated by filled black circles), and sodium (represented by open circles) are shown for the reference glass subjected to leaching at a temperature of 90°C, a pH of 8.5, and a surface area-to-volume ratio of* $100\,\mathrm{m}^{-1}$*. The second part (down) of the figure depicts a two-dimensional slice of the surface layer, known as the gel, at the conclusion of the simulation. In this representation, water appears white, silicon is shown in dark gray, boron is in light gray, and sodium is omitted. The entire simulated sample measures* $256 \times 256 \times 2048$ *units. The figure highlights two specific regions: (c) the area close to the gel-water boundary and (d) the area near the gel-glass boundary. Notably, the porosity varies between these two sections. The gel layer has a total thickness of* $310\,\mathrm{nm}$*, calculated based on a scale of* $0.3\,\mathrm{nm/pixel}$ *[142]*

Later, Devreux et al. modified the code to explore gel aging by allowing silicon atoms dissolved in closed pores to diffuse on the pore surfaces [149]. This method simulates gel maturation even after the alteration process has ceased, although it does not account for the residual alteration phase. Both studies found that a thick, silicon-enriched layer develops on the gel's surface when in contact with water. This layer is thought to restrict water movement through the gel, thereby limiting the release of boron (B) and sodium (Na) into the solution.

Incorporating zirconium (Zr), which is an extremely low solubility element, into the glass delays the formation of this silicon-enriched barrier. Zr hinders the reorganization of silicon bonds, preventing the formation of the blocking layer and allowing the alteration process to continue until the glass is fully transformed into gel. Cailleteau explored the effect of Zr in controlling the morphology of the gel [56], [150]. The code used by Cailleteau is a slight modification of the Devreux code done by M. Arab [150], in which the Zr coordination is considered to be 6 instead of 4. The corrosion behavior of glasses labeled xZr (where $x = 0, 2, 4, 6, 8$) was modeled using a surface-area-to-volume ratio [56] (SA/V) of $15\,\mathrm{cm}^{-1}$. Figure 3.4 illustrates the 2D longitudinal cross-sections of the corrosion layers after 3×10^5 simulation steps, revealing how layer morphology explains the differing behaviors between glasses with low and high Zr content. In glasses with low Zr (e.g., 0Zr, 2Zr, 4Zr), the outer layers fully dissolve, and the external gel layers densify, leading to shrinkage. This reduces porosity, making the pore network non-percolating, which blocks the movement of soluble species and halts corrosion. Conversely, in glasses with high Zr (e.g., 6Zr, 8Zr), nearly insoluble clusters around zirconium atoms stabilize the gel structure, preventing shrinkage and densification. As a result, the porous network remains percolating, allowing corrosion to persist.

The advancement in recent past for MC modeling was made by Kerisit and collaborators [147], [151], [152]. Their work, inspired by Devreux's model, introduced new features to better understand the effects of glass structure, such as non-bridging oxygens and boroxol rings, as well as corrosion conditions like flow-through environments. Most recently, they incorporated the diffusion of silicon species into their simulations, further enhancing the model's capability to study glass dissolution processes.

The algorithm proposed by Kerisit et at. extends its capabilities to investigate the alteration of glass compositions and the role of aluminum (Al) in glass corrosion [147], [151], [152]. This advanced MC code represents the glass structure as a three-dimensional (3D) cubic lattice, where network formers such as Si, B, and Al are distributed according to their proportions in the glass composition. The algorithm simulates dissolution and condensation reactions using predefined probabili-

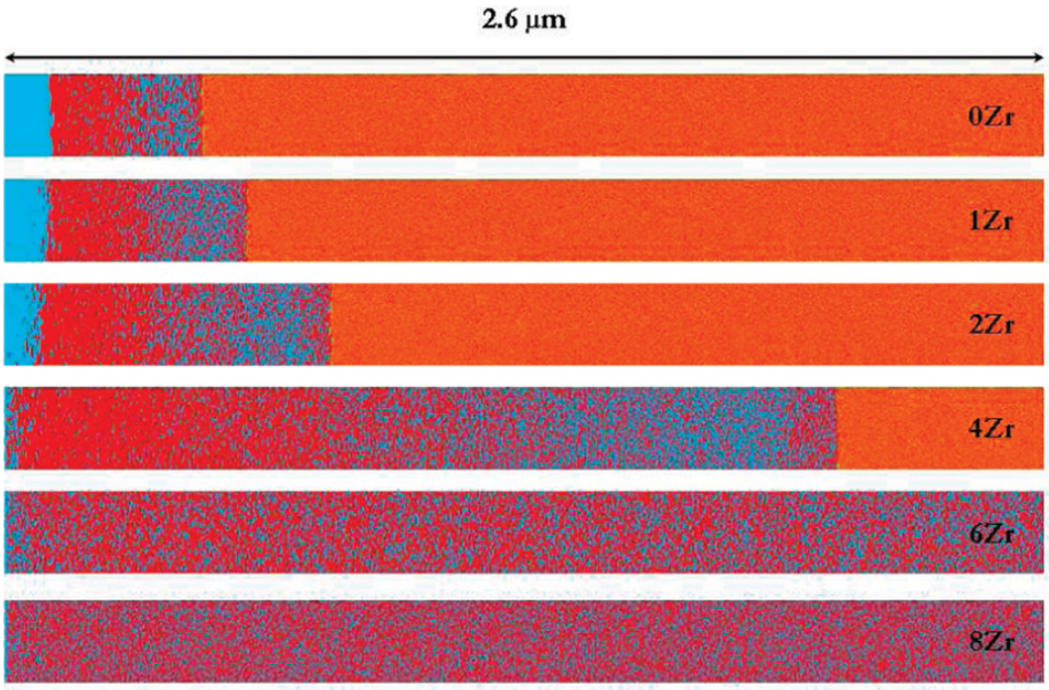

Figure 3.4: *Longitudinal 2D cross sections of the simulated corrosion layer after 300,000 computer steps for the glasses XZr (where X = 0, 2, 4, 6, and 8). The lattice nodes for silicon are represented in red, Boron in yellow, and water in blue [56].*

ties, with a particular focus on the influence of Al on the corrosion process. The dissolution probabilities for Si sites are defined based on the number of nearest neighbors and Al neighbors, following the formulation introduced by Ledieu et al. These probabilities, denoted as w_1, w_2, and w_3, correspond to Si sites with one, two, or three Si nearest-neighbor sites, respectively as mentioned previously in Figure 3.2. Additionally, a strengthening factor f accounts for the relative strength between Si–O–Al and Si–O–Si linkages. The redeposition probabilities (w_r) for Si and Al are proportional to their concentration in the solution, with condensation probabilities (w_{c-Si} and w_{c-Al}) set to values that yield saturation concentrations in agreement with experimental measurements [138], [146]. The dissolution and redeposition probabilities are mentioned in Equations 3.3–3.5. Here, n and m denote the total number of nearest neighbors, n, and the number of Al nearest neighbors, m and C_x is the concentration of Si or Al in the solution.

$$w_d(\mathrm{Si}, n, m) = \frac{w_n}{f^m} \tag{3.3}$$

$$w_d(\mathrm{Al}, n, m) = \frac{w_n}{f^{m+1}} \tag{3.4}$$

$$w_r = w_{c-x}\, X c_x \quad (x = \mathrm{SiorAl}) \tag{3.5}$$

The simulation process is structured into five key stages, which are iteratively executed until the glass is completely dissolved or a predetermined number of steps is reached.

- **Dissolution Evaluation and Execution**: Each site in contact with water is evaluated for dissolution based on defined probabilities, and dissolved species are replaced by water.
- **Glass Connectivity Evaluation**: The glass configuration is assessed to determine connectivity, with isolated clusters of sites being dissolved.
- **Condensation**: Si and Al redeposit at the glass surface according to redeposition probabilities, which are proportional to their concentration in the solution.
- **Liquid Connectivity Evaluation**: The connectivity of water sites is evaluated to distinguish between the main solution and closed pores, ensuring that dissolution and condensation processes occur only for sites connected to the main solution.
- **Coordination Evaluation**: The coordination of each site is re-evaluated for the new glass configuration, reflecting changes due to dissolution and condensation events.

Their findings showed that the glass dissolution rate increased with the number of non-bridging oxygens (NBOs) across all Si/B ratios [153], as depicted in Figure 3.5. This increase was tied to the presence of Si sites with higher NBO counts. Since boron (B) dissolution from glass was assumed to be instantaneous, the presence of boroxol rings or boron clusters was found to further elevate the dissolution rate at all Si/B ratios [153]. Additionally, applying the aluminum avoidance rule, as opposed to a random distribution, led to an increased dissolution rate [153]. In these simulations, aluminum (Al) dissolution probabilities were set higher than those for Si, reflecting the general observation that adding Al enhances glass durability against water [147], [153]. However, some recent studies points out that Al dissociates more readily from glass than Si, and the improved durability with higher Al_2O_3 content stems from strengthened bonds around Si [38]. This raises questions about the appropriateness of the Si and Al dissolution probabilities chosen in Kerisit's study. Correction of this bias has been taken into account in the new Monte-Carlo study (mentioned in the next section).

The study done on two model glasses, a ternary borosilicate (CJ1) and the same glass doped with 4.1 mol % of Al_2O_3 (CJ2) uses Monte-Carlo (MC) simulations to investigate why a passivating layer forms earlier on glass CJ1 compared to CJ2 [52].

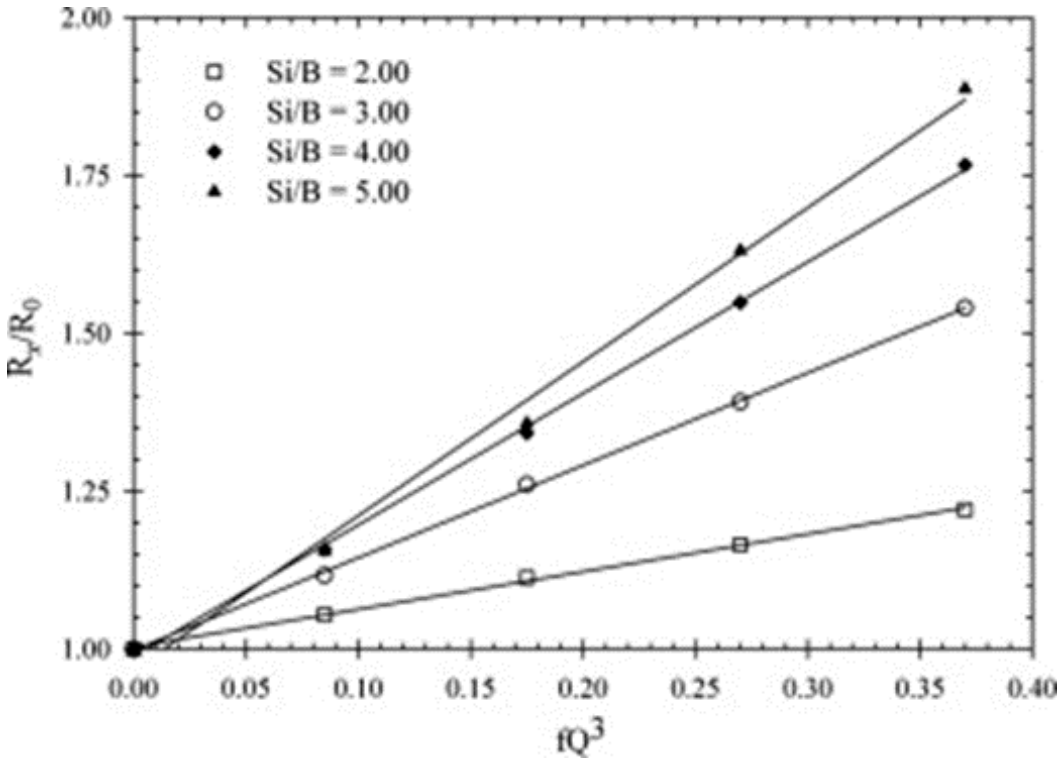

Figure 3.5: *The rate at which glass dissolves (Rx) compared to the rate when there are no non-bridging oxygens (NBOs) (R0), depending on the proportion of silicon sites that have an NBO , across various Si/B ratios. [153].*

The simulations model the corrosion of both glasses under static conditions, starting with no dissolved silica in the solution. Initially, Si from the glasses dissolves. As the Si concentration in solution increases, redeposition begins, eventually leading to an equilibrium state after around 5000 steps. Over time, a dense Si blocking layer forms at the top of the alteration layer, which prevents water from percolating through to the pristine glass. This blocking layer develops faster in CJ1 (around 10,000 steps) compared to CJ2 (around 20,000 steps), resulting in a reduced reactive surface area as shown in Figure 3.6a.

Additionally, the concentration of Si (or Si + Al for CJ2) drops sharply to zero at the gel-solution interface. This decline is more pronounced for CJ1 compared to CJ2, indicating that the gel/solution interface is rougher in CJ2 than in CJ1 as shown in Figure 3.6(b). The presence of aluminum (Al) slows down the dissolution process by creating "hard spots" that are resistant to dissolution. This leads to heterogeneities and increased roughness and tortuosity in the alteration layers of CJ2 compared to CJ1 as shown in Figure 3.7.

In summary, the MC simulations demonstrate that the earlier formation of a passivating layer on CJ1, compared to CJ2, is due to differences in dissolution and redeposition dynamics, influenced by the presence of Al in CJ2. This results in a rougher

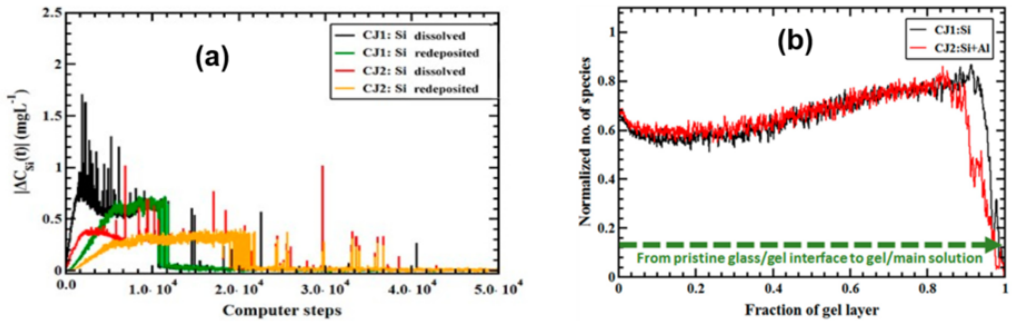

Figure 3.6: *(a) An instantaneous change in the concentration of Si dissolved and redeposited during alteration of CJ1 and CJ2 versus the number of MC steps. (b) Fraction of Si (for CJ1) and Si + Al (for CJ2) sites as a function of depth inside the gel layer (normalized by the gel layer thickness; 0 and 1 on the x-axis are thus the locations of the pristine glass/gel and gel/solution interfaces, respectively) [52].*

and more heterogeneous alteration layer for CJ2, delaying the formation of its blocking layer.

To capture irradiation effects using the algorithm [147], [151], [152] developed by Keresit et al.—where recoil nuclei disrupt the glass structure, altering boron coordination and generating non-bridging oxygens (NBOs)—the study introduced modifications to Si dissolution probabilities. The study was done on the CJ2 (64.9% SiO_2, 17.3% B_2O_3, 4.1% Al_2O_3, 13.7% Na_2O) glass using this MC algorithm [154]. A normal distribution was applied, using fixed values as means and varying standard deviations up to 100% of the mean, thereby incorporating randomness to reflect structural disorder (see Figure 3.8).

The primary effects of heavy ion irradiation include swelling, a decrease in boron coordination number, and an increase in disorder. However, the MC model explicitly accounts only for changes in boron coordination, while the induced disorder is approximated probabilistically. Notably, studies [154] have shown that irradiation also affects the medium-range order of the glass, such as through changes in ring size distributions. This suggests that modifications in medium-range order likely contribute significantly to the observed corrosion behavior. Nevertheless, such structural effects are not explicitly resolved in the MC approach.

The MC simulation results are benchmarked against experimental data, particularly from Mougnaud et al. [155], who studied the corrosion of ISG monoliths pre-irradiated with low-energy gold ions (0.5 to 3.5 MeV) to mimic irradiation effects, delivering a total energy of 10^{21} keV cm ^{3}. After 13 days of aqueous corrosion, their experiments showed a six-fold increase in alteration layer thickness in irradiated zones compared to non-irradiated ones, with changes in Vickers hardness indicat-

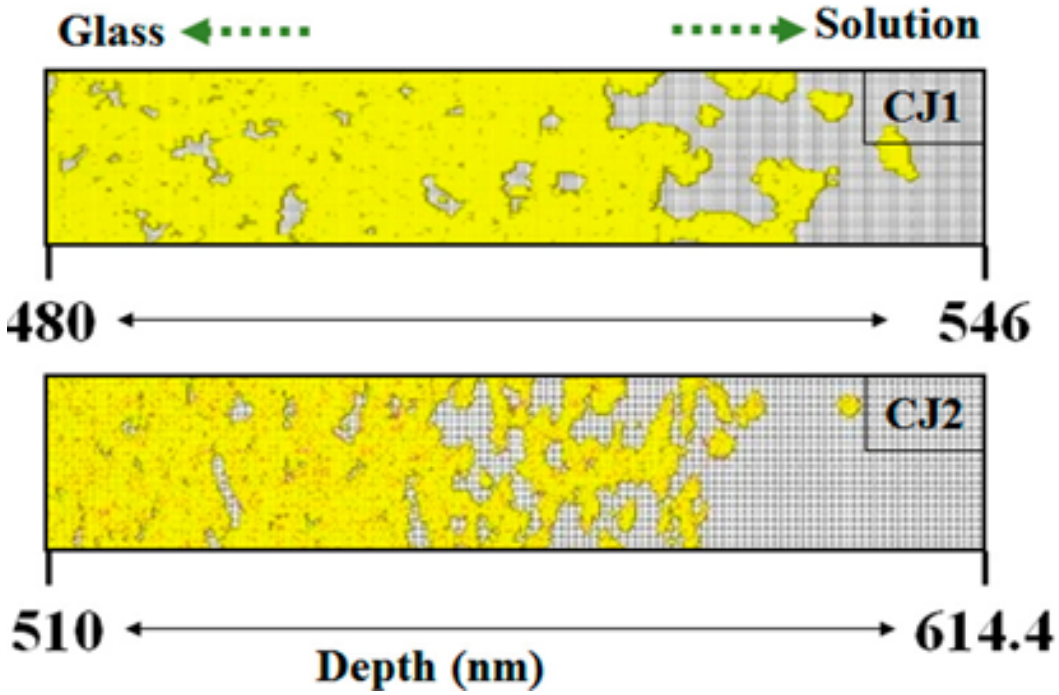

Figure 3.7: *Snapshot of the CJ1 and CJ2 gel layers (Si sites are shown in yellow, Al sites in red, and water sites in gray) [52].*

ing structural modifications from irradiation's ballistic damage. In contrast, the MC simulations of CJ2, incorporating pseudo irradiation effects through depolymerization and distribution of hydrolysis probabilities predict only a 15% increase in boron leached thickness as shown in Figure 3.9. This discrepancy suggests that while the simulations effectively model short-range structural changes caused by irradiation, they fall short of capturing the full experimental increase in alteration.

The dissolution probabilities—established under baseline conditions and adjusted to investigate linkage disorder—effectively quantify how these changes accelerate corrosion. However, the discrepancy between the simulated 15% increase and the experimental six-fold increase underscores significant limitations in our ability to capture medium-range order dynamics.

Since water molecules cannot diffuse within the glass network, it's not feasible to depict the residual alteration rate or the significant increase in the width of the alteration layer following irradiation. The acceleration of water diffusion can help us to justify the experimental findings. Consequently, a new Monte-Carlo method has been developed, and this algorithm will be discussed in the next section.

3.2.2 Description of the New Monte-Carlo method

The simulations were performed using a new Monte Carlo code developed by our team [156]. The innovative aspect of this algorithm is the use of two interconnected

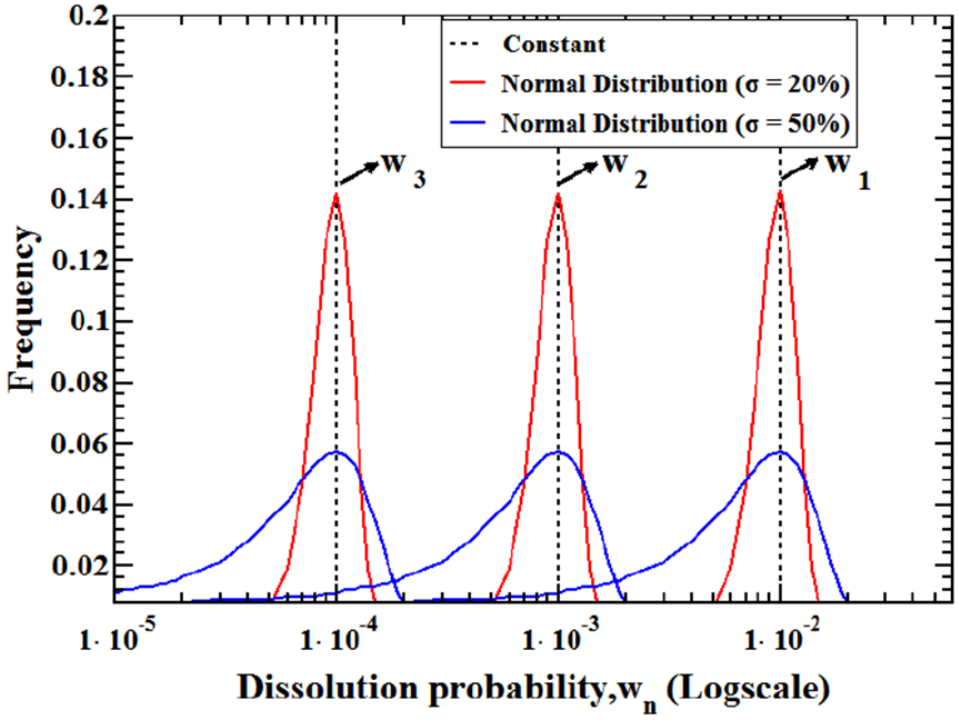

Figure 3.8: *The likelihood of silicon dissolution is depicted by probabilities (w_1, w_2, w_3). Black dotted lines indicate constant probabilities, while the solid red and blue lines show dissolution probabilities derived from normal distributions, with standard deviations set at 20 % and 50 % of the mean, respectively [154].*

networks: one representing the solid glass structure and the other the aqueous solution—offering a significant advancement over previous methodologies [56], [138], [145], [146], [147]. Here, we describe the algorithm's design, its key mechanisms, and its application to glass compositions of the SiO_2–Al_2O_3–B_2O_3–Na_2O type, highlighting its capacity to simulate water diffusion, hydrolysis, element release, and alteration layer formation with high fidelity.

The Dual-Network Framework: Solid and Liquid Networks

At the heart of this Monte Carlo algorithm lies its dual-network architecture, a departure from the single-network models of earlier studies [56], [138], [145], [146], [147]. The solid network is constructed as a cubic lattice, a structure familiar to traditional Monte Carlo simulations. Each node in this lattice corresponds to a vertex of a cube, connected to six neighboring nodes via bonds, representing the atomic framework of the glass. To accurately model the coordination environments of glass-forming elements—silicon (Si), aluminum (Al), and boron (B)—specific bonds between neighboring nodes are selectively removed. This adjustment ensures that Si and Al atoms maintain their characteristic tetrahedral (4-fold) coordination, while B atoms can adopt either tetrahedral (B(IV)) or trigonal (B(III)) coordination, depend-

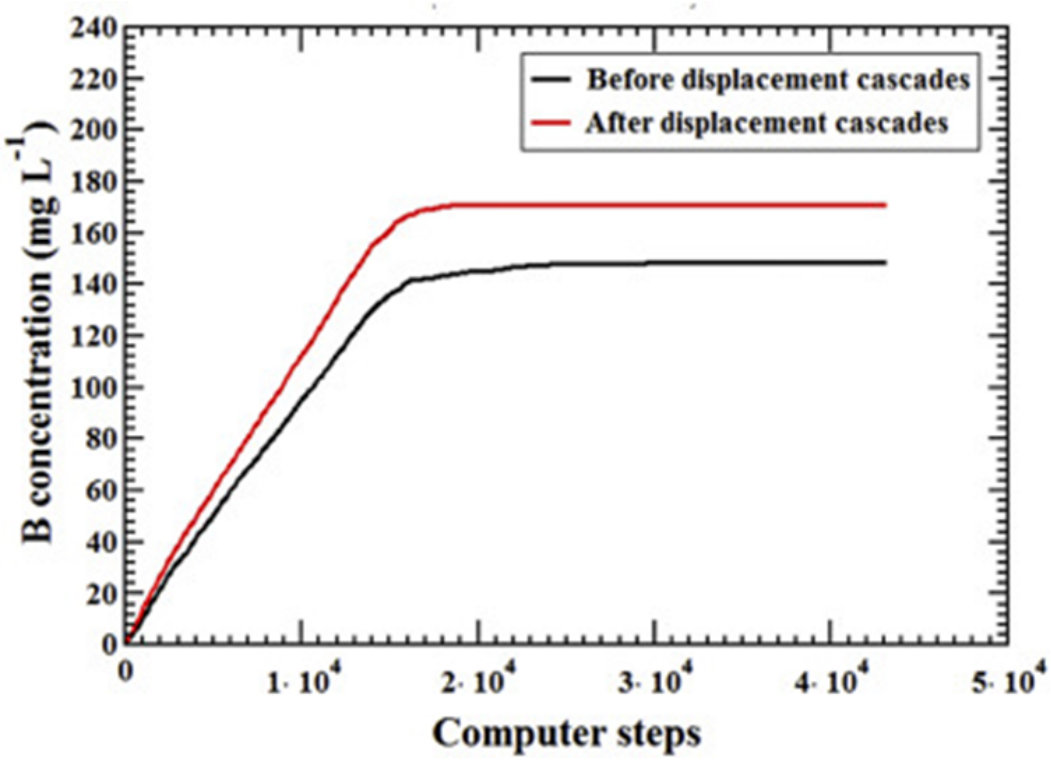

Figure 3.9: *Release of B from Monte-Carlo simulations examining the corrosion of both pristine (prior to displacement cascades) and irradiated (following displacement cascades) CJ2 compositions [154].*

ing on the glass composition and sodium (Na) concentration.For instance, in glasses of the SiO_2–Al_2O_3–B_2O_3–Na_2O system, Si, Al, and B atoms are randomly distributed across the lattice nodes, with their coordination states dictated by the presence of Na_2O—though Na atoms themselves are not explicitly placed on the network. The representation of the Monte Carlo network is shown in Figure 3.10.

The role of Na_2O is modeled indirectly through its influence on coordination. Experimental evidence suggests that Na atoms preferentially charge-compensate Al atoms, ensuring that all Al adopts tetrahedral coordination in the compositions studied here (where $\%Na_2O$ exceeds $\%Al_2O_3$) [157]. Any remaining Na atoms stabilize B(IV) by facilitating its tetrahedral bonding. If insufficient Na is available, uncompensated B atoms revert to trigonal coordination (B(III)). To incorporate B(III) into the solid network, a specific procedure is employed: two B(III) atoms are placed on adjacent nodes, and the bond between them is severed. This mimics structural features observed in borosilicate glasses and aligns with techniques used in prior Monte Carlo models [56], [138], [145], [146], [147]. Notably, in the glass compositions simulated here, all Na is consumed by Al and B compensation, leaving no excess to form non-bridging oxygens (NBOs), which simplifies the network structure.

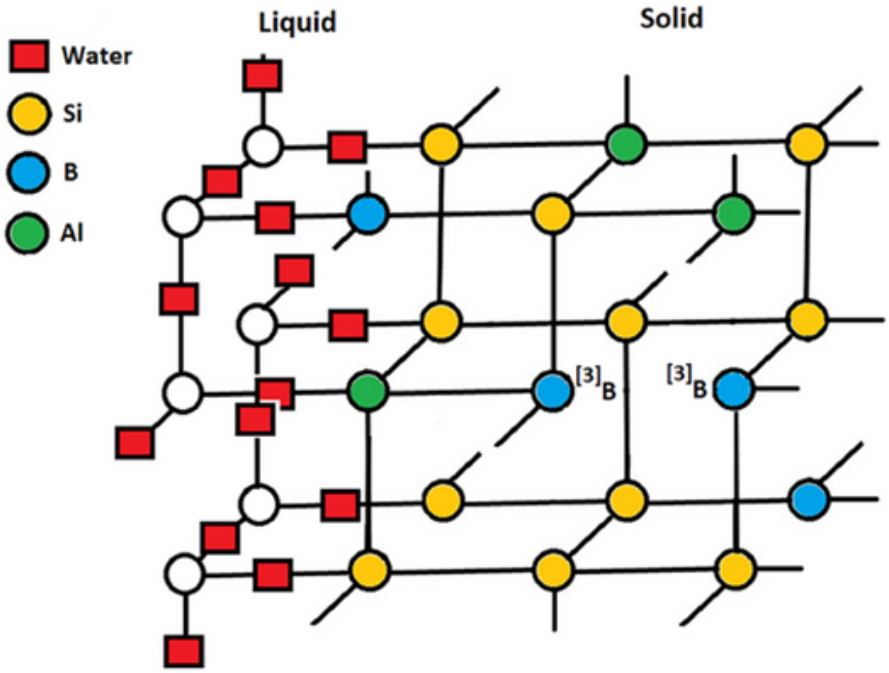

Figure 3.10: *Representation of the initial network used to begin a Monte-Carlo calculation. On the right-hand side, the solid network is shown, comprising Si (yellow), Al (green), and B (blue) atoms. An example of inserting two B(III) atoms as a pair is also illustrated. On the left-hand side, water molecules (red) are displayed within the liquid network, positioned at the midpoint between two nodes of the "solid network."*

In the current context of the study, three glass compositions are used, given in Table 3.1.

Table 3.1: *Composition of Glass Types (mol%)*

Glass Type	SiO_2	B_2O_3	Na_2O	Al_2O_3
SBNA3.5	60.5	20.1	15.9	3.5
SBNA4	64.9	17.3	13.7	4.1
SBNA6	66.8	15.9	11.3	6.0

The second innovation is the liquid network, a subnetwork designed to represent the aqueous solution and its dynamic interactions with the glass. Unlike the solid network's nodal representation of atoms, the liquid network positions its nodes at the midpoints of bonds (edges) connecting two nodes in the solid network. This geometric intertwining ensures that the two networks are structurally interdependent, allowing for realistic simulation of processes at the glass–solution interface. Initially, water molecules are placed on the liquid network nodes within the "empty" volume

adjacent to the solid network, establishing a flat interface between the dry glass and the solution. This setup marks a significant evolution from previous Monte-Carlo methods, where water diffusion into the glass was exclusively tied to bond hydrolysis. In our model, the liquid network enables water to penetrate the solid network independently, providing a more comprehensive depiction of dissolution dynamics.

Monte-Carlo Simulation Workflow

The rationale of this Monte-Carlo modeling is to replicate the physical processes occurring during glass dissolution by progressing through discrete steps, each representing elementary mechanisms with assigned probabilities or parameters. The simulation begins with the preparation of an initial structure: a pristine glass (solid network) interfaced with a solution (liquid network). As the simulation advances, water molecules diffuse from the liquid network into the solid network, triggering the hydrolysis of chemical bonds, releasing glass constituents into the solution, and facilitating the formation of an alteration layer. This process is governed by the probabilities that control the various mechanisms within the Monte-Carlo algorithm. Below, we outline the simulation workflow and the key mechanisms driving these transformations.

Key Mechanisms of the Monte-Carlo Model

The algorithm incorporates several mechanisms, each tailored to simulate a specific aspect of glass–solution interactions.

1. **Water Molecule Diffusion in the Liquid Network**

    a. Process: Water molecules migrate through the liquid network by jumping to adjacent, unoccupied sites, eventually infiltrating interstitial spaces within the solid glass network.

    b. Parameter: *nc_vois* represents the number of times the diffusion subroutine is executed per Monte-Carlo step to regulate frequency.

    c. Rules: Jumps are permitted only to unoccupied neighboring sites; water molecules are categorized as part of the "main solution" (interconnected and linked to the initial solution) or "isolated" (no continuous path to the main solution).

    d. Details: During each Monte-Carlo step, the subroutine identifies all possible jumps and the loop is applied *nc_vois* times. This adjustment enhances diffusion rates compared to hydrolysis rate to match both experimental boron and silicon releases.

2. **Hydrolysis of Glass Network Bonds**

a. Process: A water molecule positioned at the midpoint of an X–Y bond (where X, Y = Si, Al, or B) in the solid network triggers hydrolysis, breaking the bond into hydroxyl groups.

b. Parameter: *wbreak* sets the probability of bond breaking, uniform for Si–O–Si, Si–O–Al, and Al–O–Al within a glass composition but adjusted between compositions; bonds with B hydrolyze instantly (probability = 1.0) due to higher reactivity.

c. Rules: Hydrolysis can occur only when a water molecule occupies the bond midpoint, reflecting the chemical necessity of water as a reactant.

d. Details: The reaction X–O–Y + H_2O → X–OH + HO–Y results in non-bridging oxygens, such as silanol (Si–OH) or aluminol (Al–OH) groups, driving glass depolymerization.

3. **Bond Reformation in the Glass Network**

a. Process: Broken bonds between Si or Al atoms in the solid network recombine, expelling a water molecule back into the liquid network.

b. Parameter: *wrefor* = 1/1000, a fixed probability indicating a 0.1% chance of reformation per step.

c. Rules: Reformation is prohibited for bonds involving B atoms or those intentionally broken initially to create tri-coordinated B sites in the network.

d. Details: The reaction X–OH + HO–Y → X–O–Y + H_2O reverses hydrolysis. The released water molecule can diffuse again, but the low *wrefor* value reflects its minor impact on overall dynamics.

4. **Release of Glass Elements into the Solution**

a. Process: Atoms (Si, Al, or B) fully surrounded by broken bonds detach from the glass network and enter the solution, simulating dissolution.

b. Parameter: No explicit probability; release is governed by spatial and connectivity rules.

c. Rules: Si and Al atoms require direct contact with the main solution for release; B atoms detach immediately, regardless of location, due to their assumed rapid diffusion post-hydrolysis.

d. Details: This mechanism reflects the progressive breakdown of the glass structure. B's instant release simplifies its faster kinetics compared to Si and Al, which remain stationary without main solution access.

5. **Redeposition at the Glass–Water Interface**

   a. Process: Dissolved Si and Al atoms in the main solution redeposit onto sites at the glass–water interface, forming an alteration layer.

   b. Parameter: *wred* determines the redeposition rate, calculated as *wred* × *C_Si/Al*, where *C_Si/Al* is the concentration of Si (*C_Si*) or Al (*C_Al*) in the solution.

   c. Rules: Redeposition is restricted to unoccupied sites at the interface (solid network sites adjacent to the main solution).

   d. Details: Atoms are randomly placed on available interface sites within a virtual solution volume of 33,333 layers (30×30 sites, surface-to-volume ratio = 1000 cm^{1}). This process builds a Si- and Al-enriched layer, distinct from internal bond reformation.

6. **Vacancy Migration in the Solid Network**

   a. Process: Vacancies, or empty sites left by released atoms, migrate within the solid network by exchanging positions with neighboring atoms.

   b. Parameter: *wvacan1=wvacan2=4* (indicting there are 4 sites available for vacancy migration in 1000), a fixed probability giving a 0.4% chance of migration per step. For gel maturation study, the *wvacan1* and *wvacan2* is varied from 0 to 1000. If the value is equal to 0, it means that no vacancy migration is applied and if the value is equal to 1000, it means that all the possible vacancy migrations are applied.

   c. Rules: Migration does not involve hydrolysis, reformation, or redeposition; broken bonds reorganize to maintain their total count during jumps.

   d. Details. The ability for vacancies (mainly the voids formed after the release into the solution of B atoms and few Si, and Al atoms) to diffuse within the solid network was introduced using probability parameters denoted as *wvacan1* and *wvacan2*.

   e. *wvacan1*: probability applied for the vacancy jump when the number of vacancy – vacancy pairs decreases or remains unchanged, this parameter does not favor forming of large pores in the Monte-Carlo gel structure.

f. *wvacan2*: probability applied for the vacancy jump when the number of vacancy – vacancy pairs increases. This probability favors the growing of pores.

g. In practice, vacancy jumps are simulated as follows. First, all potential vacancy jumps in every direction are listed. These are then randomly mixed to avoid favoring any specific jump direction. Each potential vacancy jump is then applied with probability *wvacan1* if the jump results in a decrease or stabilization of the number of vacancy-vacancy pairs, and with probability *wvacan2* if the jump leads to an increase in the number of vacancy-vacancy pairs.:

h. This mechanism facilitates vacancy clustering and pore formation. Its value is fixed in first part of the study regarding the gel surface. During the study of gel maturation this mechanism is further exploited by varying the values of *wvacan1* and *wvacan2*.

7. **Water Molecule Jumps into the Solid Network**

a. Process: A water molecule in the liquid network moves into an adjacent vacancy within the solid network, integrating into the glass structure.

b. Parameter: No specific probability is associated with this process. A water molecule jumps to a neighboring vacant site on the solid network as soon as the event is possible.

c. Rules: The jump requires an adjacent vacancy in the solid network, ensuring spatial feasibility.

d. Details: The vacated liquid network site becomes available for further diffusion.

8. **Dissolution of Solid Clusters in the Main Solution**

a. Process: Isolated clusters of solid network atoms (Si, Al, B) detached into the main solution dissolve, releasing their constituent atoms.

b. Parameter: No explicit probability; dissolution occurs instantly upon cluster identification.

c. Rules: Clusters must be fully disconnected from the glass network for dissolution to proceed.

d. Details: This process increases Si, Al, and B concentrations in the solution, simulating the breakdown of small glass fragments isolated during depolymerization.

Table 3.2 describes the summary of parameters and mentions their characteristics describing whether they were fitted or fixed during the Monte-Carlo simulation.

Table 3.2: *Parameters and Their Roles in the Model*

Parameter	Role	Parameter (Fitted or Fixed)
nc_vois	Number of times the loop controlling the jumps of water molecules on the liquid network is called	Fitted
wbreak	Opening of chemical bonds	Fitted
wrefor	Reformation of chemical bonds	Fixed ($wrefor = \frac{1}{1000}$)
wred	Redeposition of Si and Al atoms at the glass–water interface	Fitted
wvacan	Jump of vacancies within the solid network	Fixed ($wvacan = 4$) / Varied (varied for gel maturation study, fixed for surface effect calculations)
srempt	Parameter introduced to limit the quantity of water molecules within the solid	Fixed (10%)

During a Monte-Carlo simulation, water molecules are categorized into two distinct groups: the main solution and isolated water molecules. The main solution consists of water molecules that are interconnected, meaning they occupy neighboring sites and are in contact with the initial solution. In contrast, isolated water molecules are those that, while located within the liquid network, are disconnected from the main solution. This disconnection indicates that there is no continuous path linking these isolated molecules to the main solution.

The identification of the main solution and isolated water molecules is crucial for understanding hydrolysis and redeposition mechanisms at the interface between the glass and the solution. It is essential to note that only water molecules within the liquid network are considered for this classification; those located inside pores of the solid network are excluded from the analysis.

The determination of the main solution sites is carried out through a systematic algorithm. Initially, a sequential index is assigned to each site in the liquid network, starting with the first layer of the initial solution, where index 1 always represents a site within the main solution. A loop is then executed over all occupied sites in the liquid network. If two neighboring water molecules are found, their indices are updated to reflect the lower of the two indices. This process is repeated until a steady

state is achieved, meaning that no further changes occur in the indices. At the conclusion of this procedure, all sites marked with index "1" are identified as being part of the main solution, while those with different indices are categorized as isolated water molecules. Isolated clusters of water molecules, therefore, correspond to groups that share identical indices.

Similarly, an equivalent algorithm is employed to identify isolated solid clusters within the main solution. Initially, the set of isolated solid clusters is determined, and then those clusters that are in contact with any water molecule from the main solution are dissolved. This dual approach allows for a comprehensive understanding of both the water network and the interactions at play within the system.

Implementation and Calibration

The Monte-Carlo code is implemented by initializing a 3D lattice with a flat glass–solution interface, then iterating through the mechanisms outlined above.

The execution of the Monte-Carlo algorithm involves a series of structured steps applied to a system consisting of a solid portion, a solution portion, and their interface. Below is an organized breakdown of the process:

1. Initial Setup

- Prepare the system structure, defining the solid portion, the solution portion, and the interface between them.

2. Monte-Carlo Steps

Each Monte-Carlo iteration consists of the following sub-steps:

1. **Water Molecule Classification (First Pass)**

- Identify water molecules within the main solution and distinguish isolated water molecules.

2. **Water Molecule Movement**

- Facilitate jumps of water molecules within the liquid network, repeating the process *nc_vois* times.

3. **Bond Breakage Assessment**

- Evaluate potential chemical bond breakages in the solid network, executing them based on the probability *wbreak*.

4. **Bond Reformation Events**

- Determine opportunities for bond reformation within the solid network, applying them according to the probability *wrefor*.

5. **Water Molecule Re-evaluation (Second Pass)**

- Re-assess the classification of water molecules in the main solution versus isolated ones.

6. **Atom Release into Solution**
   - Release fully hydrolyzed Si and Al atoms into the solution if they are in contact with the main solution.
   - Release fully hydrolyzed B atoms into the solution unconditionally.
7. **Water Molecule Re-evaluation (Third Pass)**
   - Reclassify water molecules as belonging to the main solution or isolated clusters.
8. **Cluster Removal**
   - Eliminate isolated solid clusters present within the main solution.
9. **Redeposition Events**
   - Detect opportunities for Si and Al redeposition at the glass–water interface, implementing them based on the probability *wred*.
10. **Water Molecule Re-evaluation (Fourth Pass)**
    - Reassess water molecule classification between the main solution and isolated entities.
11. **Vacancy Filling**
    - When a vacancy in the solid network is adjacent to a water molecule in the liquid network:
    - Fill the vacancy with a water molecule.
    - If multiple adjacent water molecules are available, randomly select one.
    - Remove the selected water molecule from the liquid network.
12. **Vacancy Dynamics**
    - Identify events where vacancies (filled or empty) may shift within the solid network, executing them based on the probability *wvacan1* and *wvacan2*.
    - Enhance vacancy clustering by adjusting probability values as needed.

Each step involves multiple passes to update water populations and apply events, ensuring dynamic consistency. The Monte-Carlo steps are calibrated to align with the experimental timeline, taking into account composition-specific diffusion coefficients—such as the 30-fold variation observed between SBNA3.5 and SBNA6. The calibration of time and MC steps is mentioned in the results section. Parameters like *nc_vois*, *wbreak, wred* and *wvacan* are fine-tuned based on measured release rates of Si, Al, and B. Additionally, the surface-to-volume ratio is utilized as an adjustable factor in redeposition calculations. In the current calculations S/V is kept constant and

the redeposition probability is adjusted accordingly. It means that throughout the simulation S/V is constant and the redeposition probability is adjusted to take into account this value of S/V.

We introduce a parameter, *srempt*, to control the amount of water within the solid matrix. Without this regulation, the diffusion processes governed by *nc_vois* would lead rapidly to the saturation of all sites in the liquid network within the glass. The parameter *srempt* sets the maximum percentage of sites in the liquid network that can be occupied by water molecules, specifically those not part of the main solution.

The probability of a water molecule jumping within the liquid network is linked to the value of (*srempt*−*srempli*)/*srempt*, where *srempli* denotes the current percentage of sites occupied by water molecules. When the maximum capacity for water occupancy is reached, the jump probability becomes zero, preventing any additional water molecules from the main solution from diffusing into the liquid network. However, water molecules will continue to diffuse deeper into the network, which reduces *srempli* (as *srempli* reflects the concentration of water molecules in the liquid network, and the volume they occupy increases in this process). This reduction allows the diffusion of water molecules from the main solution to resume.

In practice, a steady state is achieved after several thousand steps. Without a limit on the number of water molecules in the liquid network, saturation would occur rapidly, which is not physically realistic. Thus, the parameter *srempt* is consistently maintained at 10% throughout all calculations.

The study concerning the gel maturation was studied by splitting the Monte-Carlo simulations into two parts. A first calculation concerns creating the alteration gel, taking into account all the mechanisms mentioned in this section. The second calculations comprised in this study concerns specifically the ripening of the alteration gel by simulating the migration of vacancies on the solid network. The other mechanisms (water diffusion *[nc_vois]*, hydrolysis *[wbreak]* and redeposition *[wred]*) are not considered during the simulation of the gel ripening.

3.3 Results

3.3.1 Glass – solution interface

Tuning of parameter using experiments. A systematic series of calculations was conducted to optimize the parameters *wbreak*, *wred*, and *nc_vois*, aiming to best replicate the experimental data from previous studies on the glasses [53].

The simulation used a box size of 1,755,000 sites, arranged in a grid of dimensions **30 × 30 × 1950** for the solid network. This network consisted of **1,059,980 Si atoms**, **190,418 Al atoms**, and **504,602 B atoms**. The total simulation box size, including

the liquid phase, was **30 × 30 × 2000**, with the last 50 layers reserved for the initial solution. The glass–water interface was initially positioned at **Z = 1950**, and periodic boundary conditions were applied along the X and Y axes.

Each Monte-Carlo simulation was performed for **10^6steps** (sometimes less due to unexpected shutdowns of the computing cluster), with the Z-axis defined as perpendicular to the solid–solution interface.

The best fit to experimental data for SBNA6 was achieved using the following parameter set:

- *wbreak* = 0.003,
- *wred* = 0.42,
- *nc_vois* = 16.

The parameter *wred* = 0.42 represents the redeposition probability of Si or Al atoms, calculated as a function of the Si or Al solution concentration $\mathbf{C_X}$ ($p_{redep} = w_{red} * C_x$). The parameter *nc_vois* = 16 indicates that water diffusion loops were executed 16 times more frequently than other mechanisms, which was critical to accurately reproduce the experimental release of B into the solution.

Comparison with Experimental Data. Figure 3.11 compares the amounts of Si and B released into solution as a function of the square root of time for both the simulation and the experiment. While the simulation accurately replicates the experimental Si release over time, saturation occurs more rapidly in the Monte-Carlo calculations. The initial slope of B release is well reproduced, but the simulation does not reflect the nonlinearities observed in the experimental data, which could potentially be attributed to measurement uncertainties . Due to computational constraints, the simulation was limited to **10^6 steps**, which prevented the simulation of the entirety of the experimental curve.

At steady state, the final concentrations of Si and Al in the solution, expressed as percentages of sites, were found to be **0.11%** and **0.02%**, respectively. To establish a time equivalence between Monte-Carlo steps and real time, the number of Monte-Carlo steps required to reach Si saturation was determined to be **120,000 steps**, corresponding to **191.8 hours experimentally**. This results in a time conversion factor of **5.75 seconds per Monte-Carlo step**.

Depth Profiles of Si+Al and Cross-Linking. Figure 3.12 presents the profiles of the Si+Al concentration and the degree of cross-linking (percentage of closed bonds between Si, Al, and B atoms) as functions of depth within the alteration gel. These profiles were calculated layer by layer on the solid network, where each layer corresponds to a plane of **30 × 30 sites containing a maximum of 1800 closed bonds**. The depth was converted to Angstroms, assuming a layer spacing of **3.5 Å**.

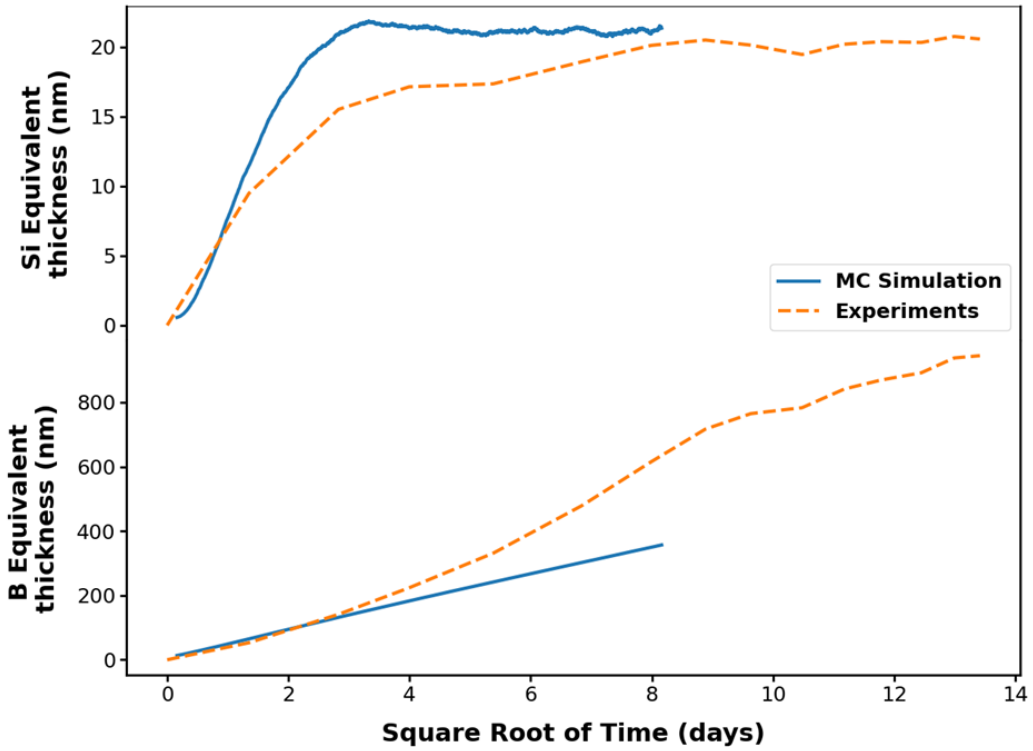

Figure 3.11: *Equivalent thicknesses determined from the quantities of (a) Si and (b) B dissolved into solution for glass SBNA6, using the parameters* $w\mathrm{break} = 0.003$, $w\mathrm{red} = 0.42$, *and nc_vois = 16. The results from the Monte Carlo simulation are shown in blue, while the experimental data are represented in orange.*

When we look at the reference parameter set (the orange curves), the simulation showed that a steady state was reached for water diffusion within the gel, as the degree of cross-linking remained constant throughout the glass. However, at the gel–solution interface, an outer layer enriched in Si+Al was observed, corresponding to a peak in the degree of cross-linking. This compact zone, formed through a combination of hydrolysis and redeposition mechanisms, is shown in Figure 3.13.

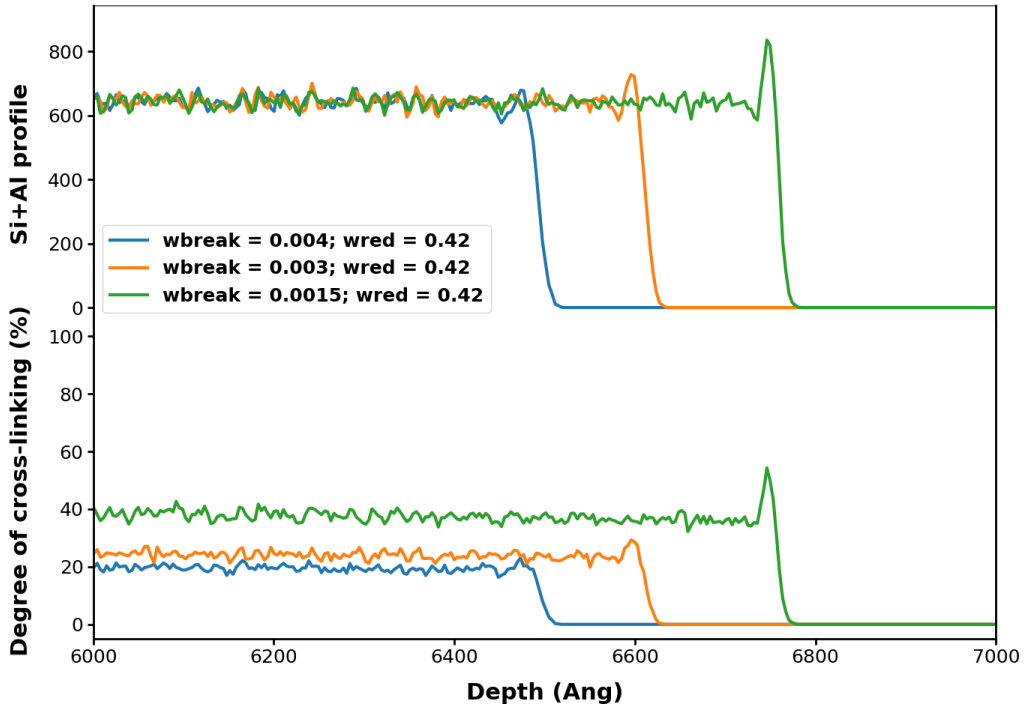

Figure 3.12: *Monte Carlo simulations for glass SBNA6, examining the Si+Al concentration and cross-linking degree at the gel–solution interface. Parameters were set with* `nc_vois` *= 16. Monte Carlo timesteps:* 778 500 *(wbreak = 0.0015),* 1 000 000 *(wbreak = 0.003), and* 635 100 *(wbreak = 0.004).*

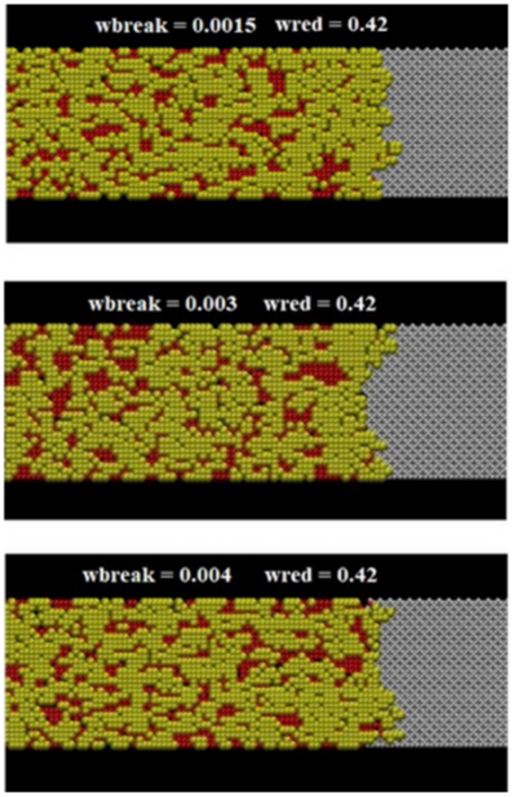

Figure 3.13: *Monte-Carlo simulations were conducted for the glass SBNA6, focusing on the morphologies of alteration gels formed outside the gel under varying parameter conditions. In these simulations, silicon (Si) is represented in yellow, water molecules occupying vacancies within the solid network are shown in red, and water molecules from the primary solution are depicted in gray. The simulations correspond to different Monte-Carlo timesteps and parameter settings: 778,500 timesteps with wbreak = 0.0015, 1,000,000 timesteps with wbreak = 0.003, and 635,100 timesteps with wbreak = 0.004.*

In this Figure 3.13, water molecules in the main solution are depicted in gray, while water molecules trapped in vacancies within the solid network are shown in red. Morphological differences in the gel structure under different parameter settings are also displayed and will be discussed in subsequent sections. It is important to note that the width of dense layer decreases with increase in *wbreak.*

SBNA4 Glass: Optimal Parameters. For glass SBNA4, the optimal parameter set was found to be:

- *wbreak* = 0.0035,
- *wred* = 0.3,
- *nc_vois* = 16.

Figure 3.14 compares the equivalent thicknesses of Si and B released into solution between the experimental and Monte-Carlo data for this parameter set. The Monte-Carlo time step for SBNA4 glass corresponds to **0.775 seconds**. Similar to SBNA6, the simulation for SBNA4 showed a slightly faster attainment of steady-state Si release compared to the experiment. However, the slope of B release was closely matched to the experimental curve.

At steady state, the final concentrations of Si and Al in the solution, expressed as percentages of sites, were **0.20%** and **0.025%**, respectively.

Figure 3.15 illustrates the profiles of the Si+Al concentration and the degree of cross-linking at the gel–solution interface. Similar to SBNA6, a Si+Al-enriched outer layer with a peak in cross-linking was observed. A series of calculations were then conducted to test the role of the parameters wbreak and wred on both the SBNA6, SBNA4 and SBNA3.5 glasses, using the same parameter sets to highlight the influence of glass composition, which will be explored in coming sections.

This denser layer forms due to the interplay between hydrolysis and redeposition mechanisms and is visualized in Figure 3.16, along with alternative gel morphologies obtained under different parameter settings.

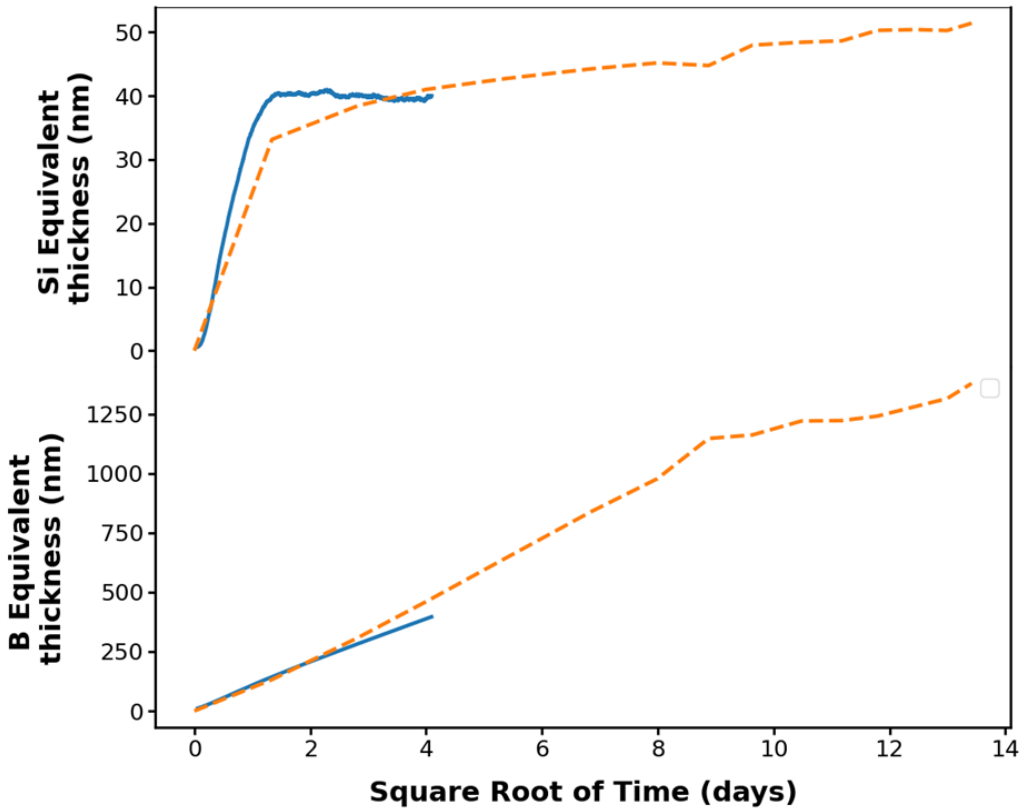

Figure 3.14: *Equivalent thicknesses derived from the quantities of Si and B dissolved into solution for glass SBNA4, using the parameters wbreak = 0.0035 , wred = 0.3 , and nc_vois = 16. The Monte Carlo simulation results are shown in blue, while the experimental data are represented in orange.*

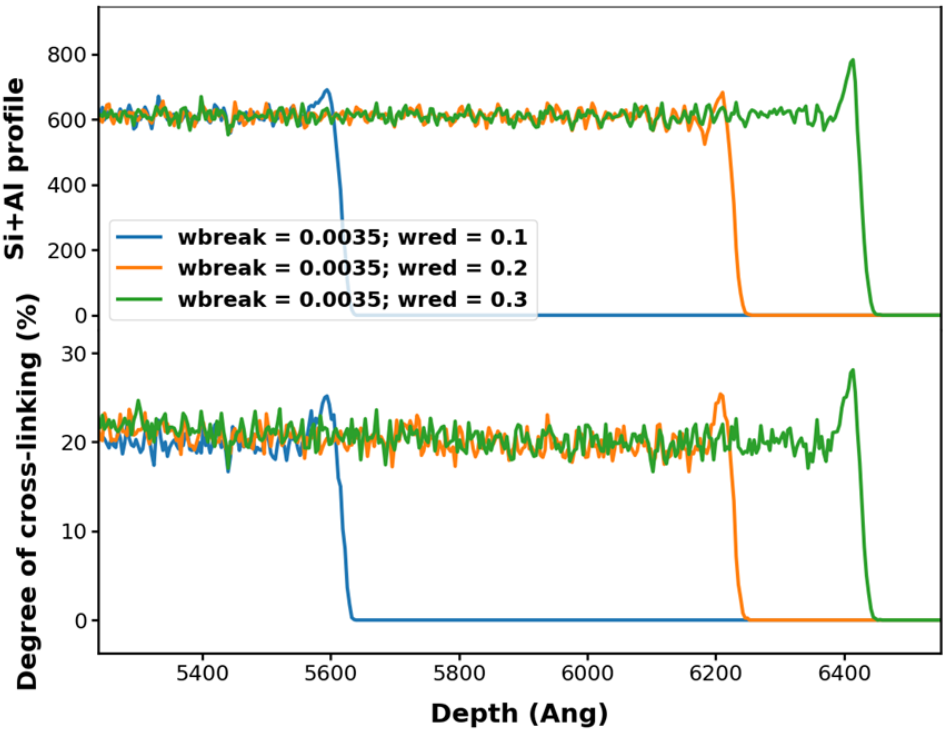

Figure 3.15: *The Monte-Carlo simulations for the glass SBNA4 are illustrated with two profiles: the top profile shows the concentration of Si+Al at the interface between the gel and the solution, while the bottom profile depicts the degree of cross-linking, indicating the percentage of closed bonds in each layer parallel to the glass-solution interface. Various scenarios with different parameter settings are presented, as detailed in the accompanying text, with each calculation performed over 1,000,000 Monte-Carlo timesteps.*

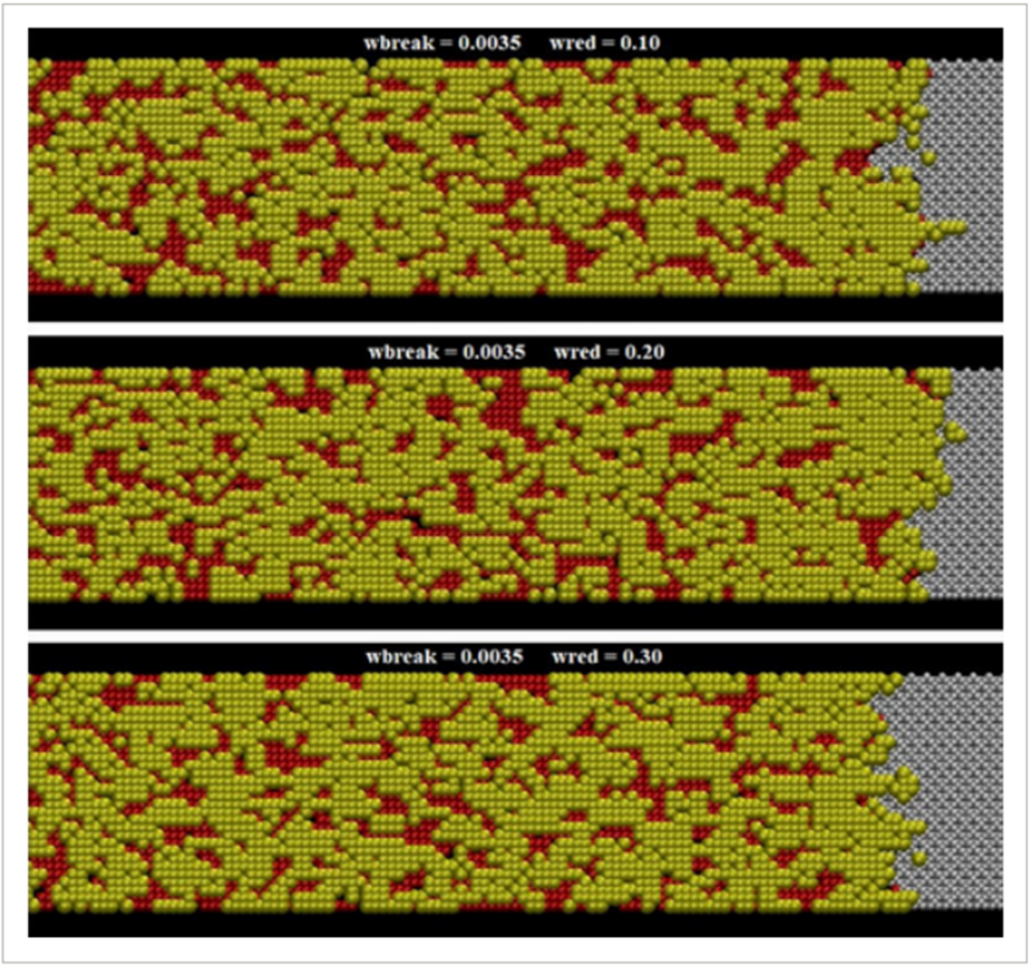

Figure 3.16: *The Monte-Carlo simulations for the glass SBNA4 reveal the morphologies of alteration gels formed outside the gel under various parameter settings. In these simulations, Si is represented in yellow, water molecules occupying the vacancies within the solid network are shown in red, and water molecules from the main solution are depicted in gray. Each calculation is conducted over 1,000,000 Monte-Carlo timesteps.*

Differences in Parameter Tuning: SBNA6 vs SBNA4. To reproduce the experimental results for SBNA4, it was necessary to increase *wbreak* (enhancing hydrolysis) and decrease *wred* (reducing redeposition). This adjustment increased the amount of Si released into solution relatively to the redeposition mechanism, bringing the simulation closer to experimental observations. Furthermore, the shorter Monte-Carlo time step for SBNA4 compared to SBNA6 resulted in a closer match between the simulated and experimental B release curves.

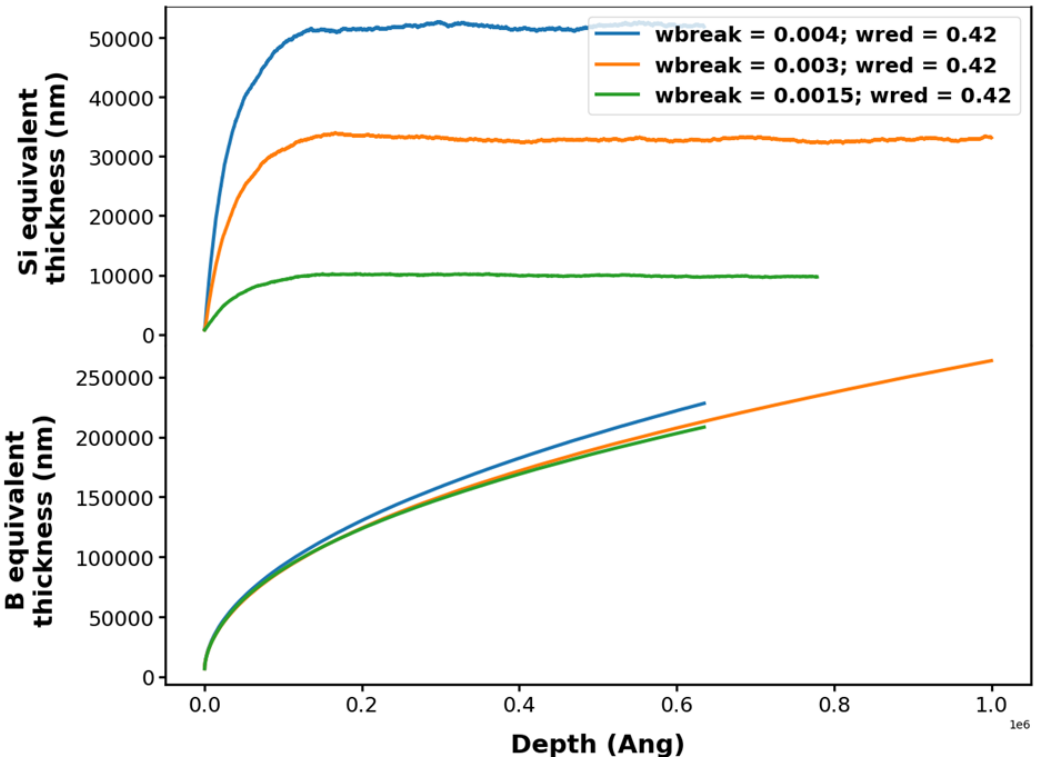

Figure 3.17: *The equivalent thicknesses for SBNA6 glass, derived from the amounts of Si and B released into the solution, are presented as a function of the time step number for various wbreak values. In all calculations, wred = 0.42, and* `nc_vois` *is maintained at 16.*

Parametric Study . To better understand the effects of the parameters *wbreak* and *wred*, systematic variations were performed around the reference values obtained for SBNA6 glass.

Effect of wbreak on SBNA6 Glass. For SBNA6, *wbreak* was varied between **0.0015** and **0.004**, while *wred* and *nc_vois* were held constant at **0.42** and **16**, respectively. As shown in Figure 3.17, increasing *wbreak* resulted in accelerated hydrolysis, leading to greater amounts of Si being released into the solution. At steady state, the final concentrations of Si (Al), expressed as percentages of sites, were:

- 0.032% (0.005%) for *wbreak = 0.0015*,

- 0.11% (0.02%) for *wbreak* = *0.003*,
- 0.17% (0.031%) for *wbreak* = *0.004*.

The profiles of Si+Al concentration and cross-linking (Figure 3.12) demonstrated that the height of the Si+Al peak at the gel–solution interface decreased with increasing *wbreak*, indicating reduced outer layer enrichment. Increase in wbreak disfavours the formation of a layer enriched in Si+Al.

Effect of wbreak on SBNA4 Glass. For SBNA4, *wbreak* was varied between **0.0015** and **0.004**, with *wred* = 0.42 and *nc_vois* = 16. At higher *wbreak* values, peaks of Si release were observed (Figure 3.18), corresponding to intermittent cluster hydrolysis. These peaks were caused by the formation of a poorly adherent outer layer, characterized by high interface roughness. This layer, weakly connected to the underlying solid, readily transformed into isolated clusters upon dissolution. Figure 19 points out the fact that there is a very small modification of the B equivalent thickness because it mainly depends on water diffusion and not and the hydrolysis or redeposition rates.

Effect of wred on SBNA4 glass. Figure 3.19 shows the equivalent thicknesses for SBNA4 glass measured from the quantities of Si and B released as a function of time steps across various Monte-Carlo simulations. Here, the parameter wred was varied between 0.1 and 0.3, while the parameters wbreak and nc_vois were held constant at 0.0035 and 16, respectively.

The data presented in Figure 3.19 indicate how variations in wred affect the release dynamics of Si and B from SBNA4 glass. By maintaining a fixed wbreak, the analysis highlights the sensitivity of the alteration process to changes in wred.

As wred decreases, indicating a lower rate of redeposition onto the gel surface, there is a notable rise in the amounts of Si and B released into the solution (see Figure 3.19). This outcome was anticipated since reduced redeposition increasingly offsets hydrolysis. Additionally, with a decrease in wred, the Si+Al-enriched outer layer becomes less pronounced (Figure 3.15). Figure 3.16 displays a morphology of the gels.

At steady state, the final concentrations of Si (Al) in solution for various *wbreak* values were:

- 0.036% (0.004%) for *wbreak* = 0.0015,
- 0.208% (0.026%) for *wbreak* = 0.004.

Figure 3.19 and Figure 3.18 points out that the equivalent thickness of B undergoes only a slight change, as it is primarily influenced by water diffusion rather than the rates of hydrolysis or redeposition for both SBNA4 and SBNA6.

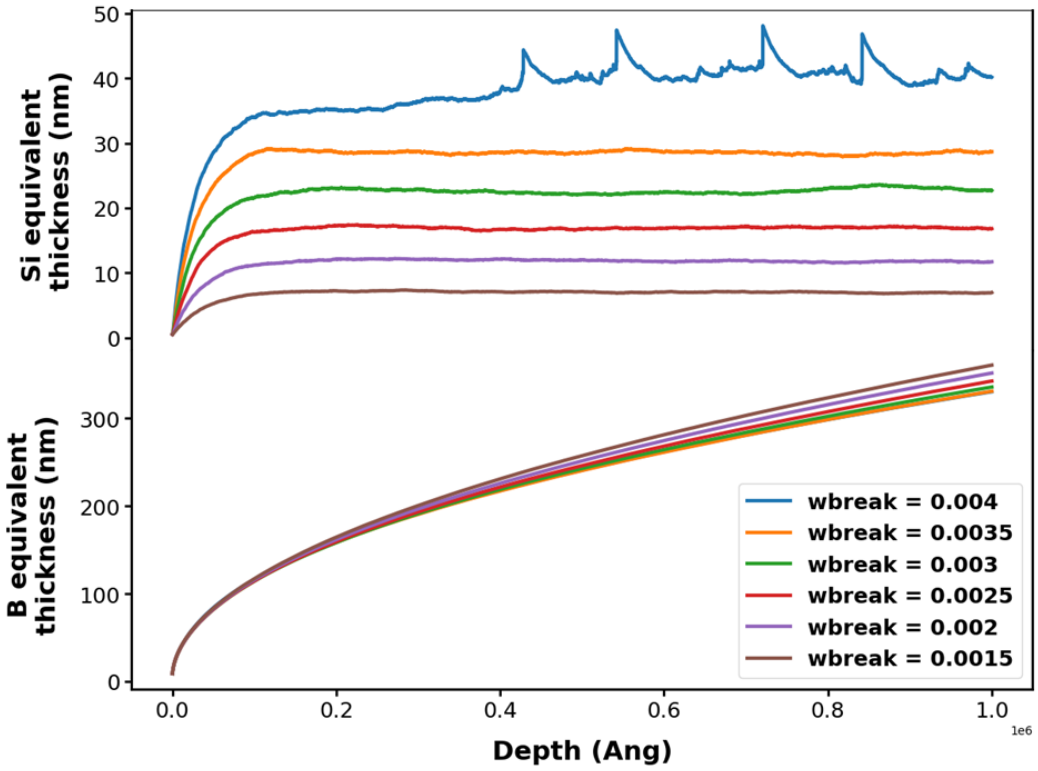

Figure 3.18: *For SBNA4 glass, the equivalent thicknesses, determined from the amounts of Si and B released into the solution, are analyzed as a function of the time step number for different wbreak values. All calculations assume wred = 0.42 and nc_vois = 16.*

Through a parametric study involving the variation of wbreak, we observed that the Si+Al-enriched outer layer completely vanished at *wbreak* = 0.004, giving rise to a highly porous zone. This finding is corroborated by Figure 3.20. Additionally, the gel morphology presented for various wbreak values reveals the emergence of a highly porous zone(for wbreak=0.004 and wred=0.42), as depicted in Figure 3.21.

We finally underline that a dense layer enriched in Si and Al can form when hydrolysis proceeds at a moderate rate. Additionally, an increased hydrolysis rate alters the switch the nature of dissolution to cluster-based alteration. Notably, the rates of hydrolysis and redeposition have a minimal impact on the release of B.

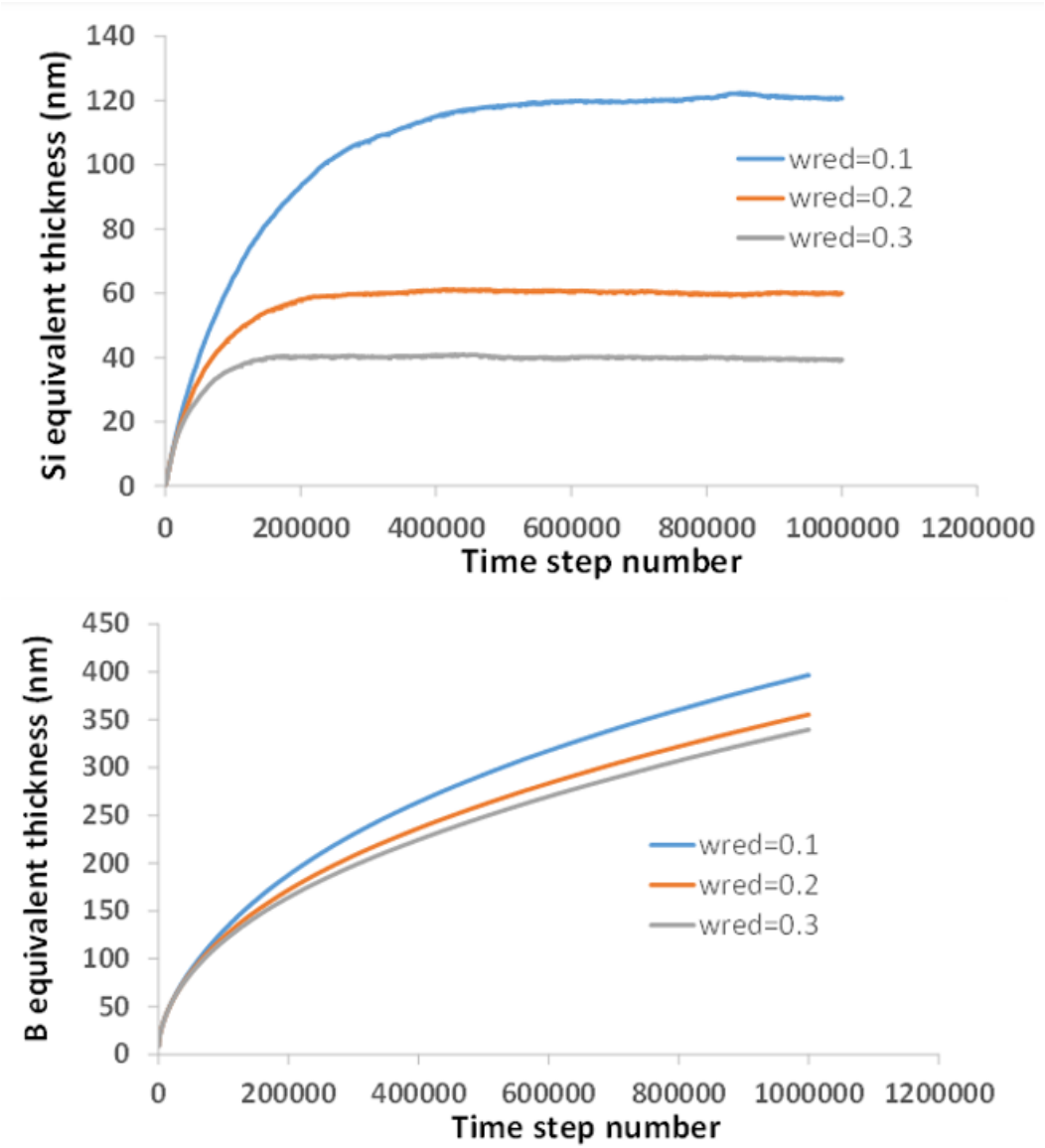

Figure 3.19: *Equivalent thicknesses calculated from the quantities of Si and B released into solution for SBNA4 glass as a function of the number of time steps for different wred values. In all calculations, wbreak=0.0035 and ncvois=16.*

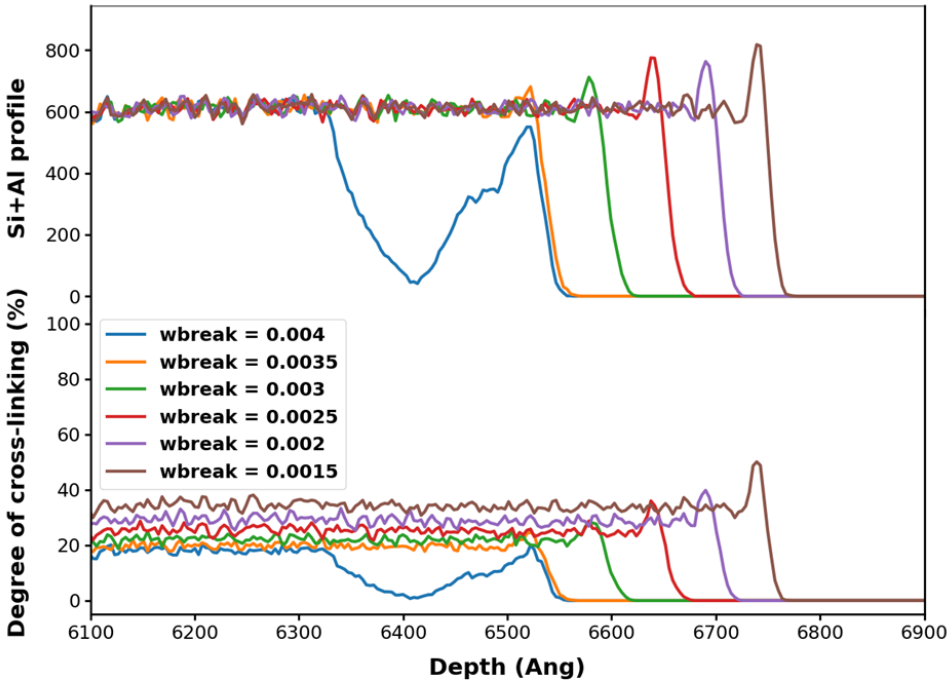

Figure 3.20: *Monte-Carlo simulations for SBNA4 glass are presented. The top graph illustrates the Si+Al concentration profile at the gel-solution interface, while the bottom graph depicts the cross-linking degree, expressed as the percentage of closed bonds in each layer parallel to the interface. Multiple cases with different parameter settings are included (refer to the text for details). The simulations are conducted with wred = 0.42 and nc_vois = 16, using 1,000,000 Monte-Carlo timesteps per calculation.*

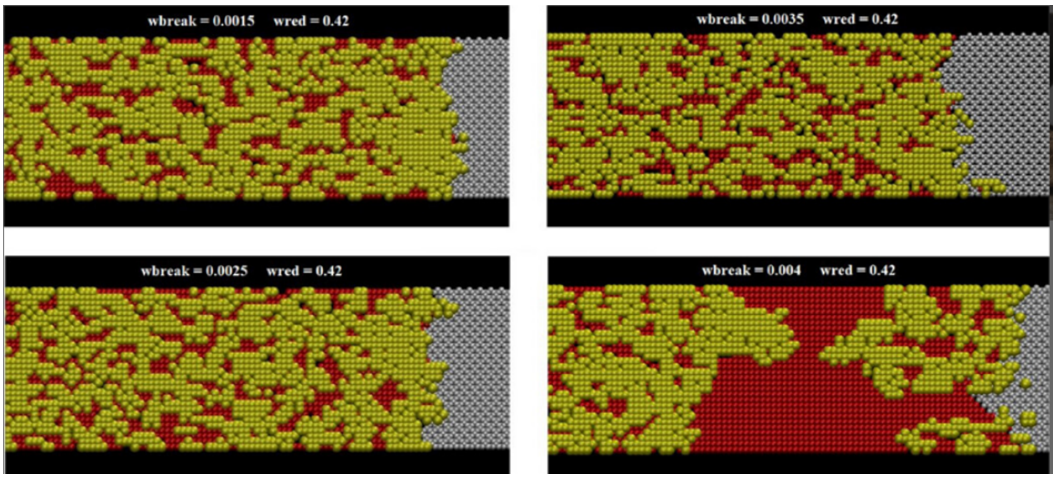

Figure 3.21: *Monte-Carlo simulations for glass SBNA4. Morphologies of alteration gels formed outside the gel for different parameter settings. The calculations are performed with wred = 0.42 and nc_vois = 16. Si: yellow, water molecules in the vacancies of the solid network: red, water molecules from the main solution: grey. The number of Monte-Carlo timesteps is set to 1000 000 for each calculation.*

Parametric study of SBNA3.5. Figure 3.22 provides a comprehensive view of the equivalent thicknesses calculated from the quantities of silicon (Si) and boron (B) released into solution over various time steps in Monte-Carlo simulations performed on SBNA3.5 glass. In these simulations, the parameter wbreak was varied between 0.0005 and 0.004, allowing for an exploration of the impact of this variable on the alteration behavior of the glass. The constants wred and nc_vois were maintained at 0.42 and 16, respectively, ensuring that the focus remained on the influence of wbreak.

The results reveal a notable trend: as wbreak exceeds 0.0035, there is a significant increase in the number of released clusters. This finding suggests a lower threshold for cluster release in SBNA3.5 glass compared to SBNA4 glass, indicating that the composition of the glass plays a crucial role in its alteration behavior. Such insights could help for understanding the long-term stability and durability of glass materials in various environmental conditions.

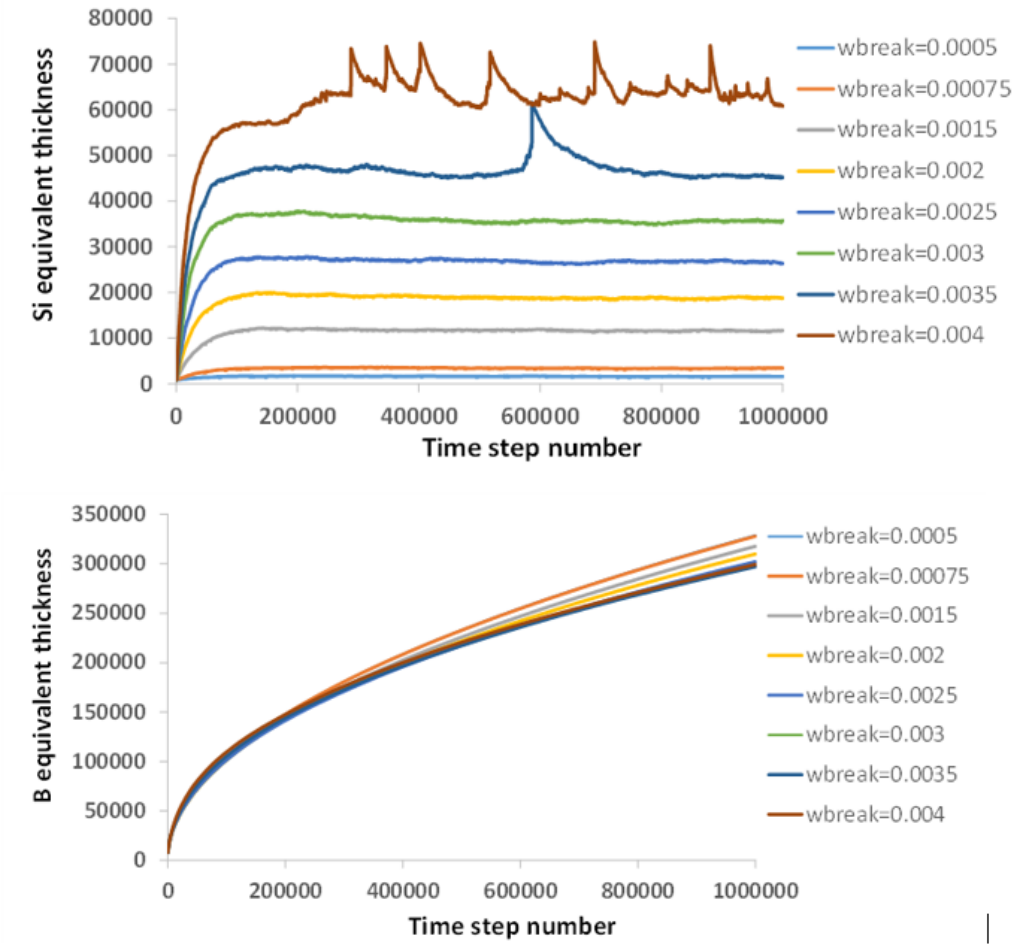

Figure 3.22: *Equivalent thicknesses calculated based on the quantities of Si and B released into solution for SBNA3.5 glass as a function of the number of time steps for varying wbreak values. In all simulations, wred=0.42 and ncvois=16.*

There is an intricate interplay between the glass composition and the parameters governing its alteration behavior. To conclude, the processes occurring at the glass-solution interface reveal several key insights. When hydrolysis proceeds at a moderate pace, it allows for the formation of a dense outer layer enriched in silicon (Si) and aluminum (Al), which can influence the glass's stability and reactivity. However, as the hydrolysis rate increases, the alteration behavior shifts significantly, with degradation occurring in clusters rather than uniformly, reflecting a more aggressive breakdown of the material. Notably, the rates of hydrolysis and redeposition appear to have minimal impact on the release of boron (B), suggesting that other factors may predominantly govern its behavior in this context.

3.3.2 Gel ripening

Preparation of the initial gel structure. The gel maturation simulations involve two successive steps. The first simulation consists in using the Monte-Carlo algorithm with all the mechanisms (see method section)[156] to reproduce the asymptotic release of Si and B in solution in order to obtain initial configurations of altered glasses to simulate gel ripening. As mentioned in the previous section with the current Monte-Carlo code [156], various combinations of the parameters wbreak, wred, and *nc_vois* were systematically tested across a wide range of values to determine the optimal set that accurately replicates the experimental release of Si and B in the solution for the glasses considered in this study[156]. The simulation was a box containing **1755000** sites arranged in a **1950×30×30** grid representing the solid network. This box was composed of **1059980** Si, **190 418** Al, and **504 602** B atoms, representing the SBNA4 composition. A total of $\mathbf{2{\times}10^6}$ simulation steps were executed. The overall box size, encompassing both solid and liquid components, was **2000×30×30** sites, with the solution initially occupying the last **50** layers on one end. The glass–water interface was initially a flat plane perpendicular to the z axis. Periodic boundary conditions were enforced along the x and y axes.

In previous works[156], we found that one set of parameters that reproduced the asymptotic release of both boron and silicon was $wbreak = 0.0035$, $wred = 0.3$, and $nc\_vois = 16$ for the glass SBNA4. We reused this set of parameter for the simulations discussed here. A total of $2\text{x}10^6$ simulation steps were executed in order to obtain one alteration gel used hereafter to simulate the ripening (discussed in next section) by applying the vacancy migration mechanisms.

Parametric study of gel ripening. The second part of the Monte-Carlo calculation consists in applying only the vacancy migration mechanisms on the alteration gel prepared by the first calculation in order to reproduce the ripening of gel morphology. The gel obtained at the end of the first calculation is maturated using the two

probabilities *wvacan1* (which disfavours pore growth) and *wvacan2*(which favours pore growth). The *wvacan1* values have been tested between 10 and 100 and *wvacan2* has been tested for values between 400 and 900. The simulations were carried out for $2{\times}10^5$ simulation steps.

The effect of the values used for *wvacan1* and *wvacan2* are shown in Figure 3.23, which shows snapshots of gel simulated by Monte-Carlo for 100k Monte-Carlo steps using different values for these parameters. A small increase in the values of wvacan1 leads to a decrease of the formation of vacancy clusters. This is apparent when wvacan1 is varied while keeping wvacan2 constant. According to Figure 3.23 (b) and (c), a smaller value for wvacan1 results in increased clustering of vacancies and the formation of larger pores.

In Figure 3.23, a noticeable concentration of vacancies appears in the region of the gel adjacent to the solution (on the interface of gel and solution). This distribution is partly attributed to the asymmetry of the Monte Carlo network employed in the simulations. Specifically, to accurately reflect the differing coordination numbers of Si, Al, and B atoms in the initial configuration, edges were selectively removed along the x- and y-axes, but not along the z-axis (see the Monte Carlo grid described in previous studies [156]). As a result, vacancy jumps occur more frequently along the z-axis than in the perpendicular directions. Moreover, the initial alteration gel used in the ripening calculation already contained a vacancy-enriched region near the gel-solution interface. This pre-existing zone may serve as an attractor for additional vacancies, leading to a gel morphology that progressively evolves toward greater asymmetry over time.

In the remaining of the text, in order to avoid this bias, we analyze only the inner portions of the alteration gels.

Figure 3.24 shows cumulated distributions of pore sizes at different steps during ripening. Each morphology of the alteration gels was analyzed using the Zeo++ software [158], [159], [160], [161] with a probe radius of 1 Å. We observe a stabilization of the cumulated distributions for both cases. Figure 3.24 (a) shows the cumulative distribution for *wvacan1* = 50 and *wvacan2* = 600, and Figure 3.24 (b) for *wvacan1* = 100 and *wvacan2* = 600. In order to enhance pore growth, we need to increase *wvacan2* relative to *wvacan1*. The presence of some large pores already at the first step is partly an artifact, originating from the effect of surface pores in the analysis.

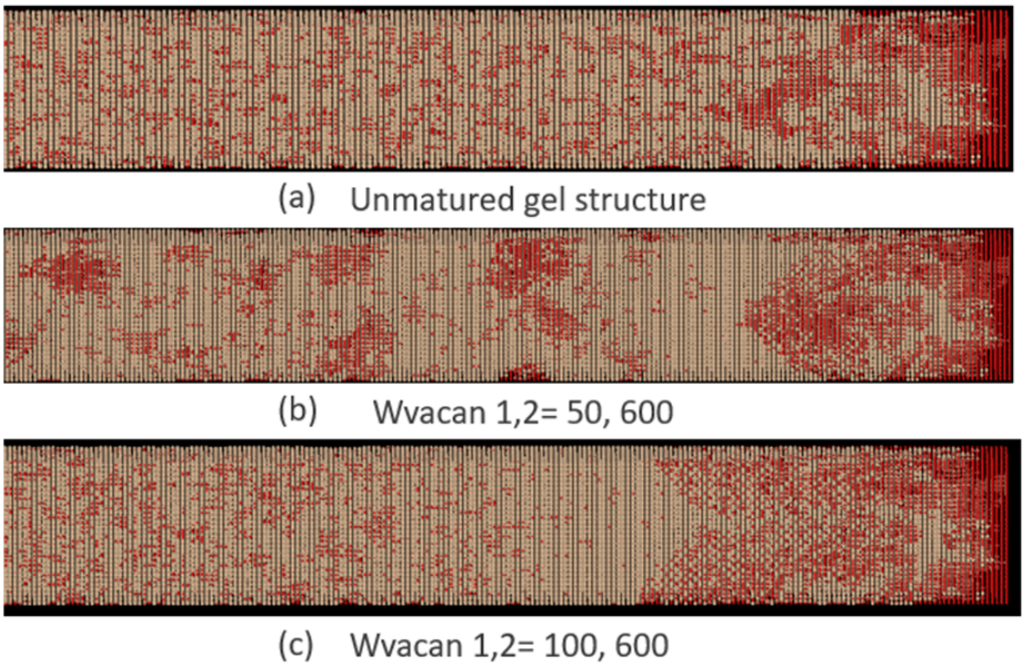

Figure 3.23: *Morphologies of gels for different parameter settings. Glass: brown, water molecules in the vacancies of the solid network: red. The number of Monte-Carlo steps is set to 100000 for each calculation. (a) initial unmatured gel structure (b) MC structure for wvacan1= 50 and wvacan2 = 600 (c) MC structure for wvacan1 = 100 and wvacan2 =600*

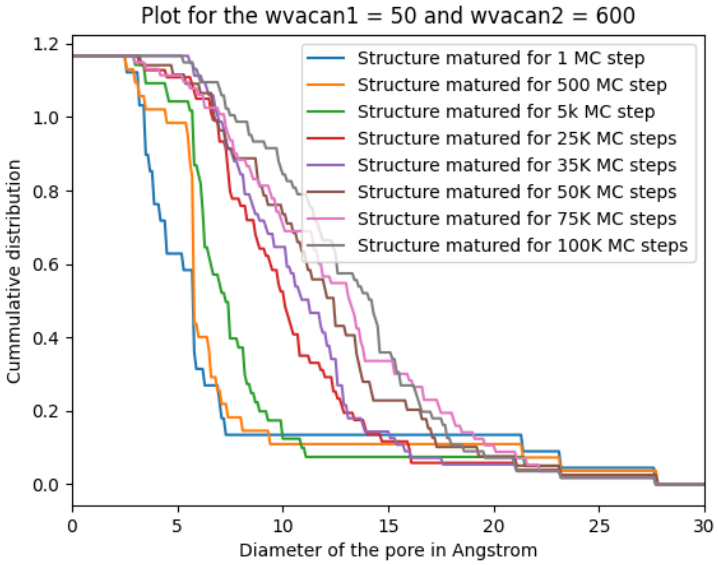

(a) *Distribution for* $w\mathrm{vacan}1,2 = 50, 600$

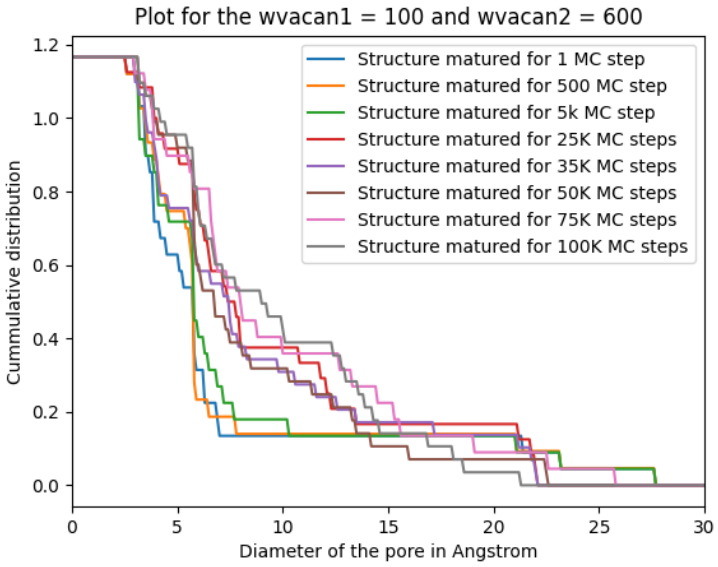

(b) *Distribution for* $w\mathrm{vacan}1,2 = 100, 600$

Figure 3.24: *Cumulated distributions of pore sizes at different steps during the ripening. (a) Distribution for* $w\mathrm{vacan}1,2 = 50, 600$. *(b) Distribution for* $w\mathrm{vacan}1,2 = 100, 600$.

Figure 3.25 shows the SAXS profiles calculated from the MC structures after different maturation times. The structure factors of the simulated 3D corrosion layers were calculated with a view comparing to the SAXS experiments. It can be computed for solid (S) sites. where n_S is the number of samples and N_S the total number of solid sites in the sample. The SAXS absolute intensity was calculated using the equation 3.6 and equation 3.7:

$$I(q) = b^2(\rho_s - \rho_w)a^3F(q_s) \tag{3.6}$$

$$F(q_s) = \frac{1}{n_s}\sum_{n=1}^{n_s}\frac{1}{N_s}\left\{\left[\sum_{i\in S}\cos(q_s\cdot r)\right]^2 + \left[\sum_{i\in S}\sin(q_s\cdot r)\right]^2\right\} \tag{3.7}$$

Where q_s=qa and a=0.35 corresponds to the Si-O distance and $F\left(q_s\right)$ is the structure factor calculated for the solid sites [56]. Structure factor is averaged over about 1000 samples by choosing randomly the orientation of one module of vector q_s. More details on the method is mentioned in previous works [56]. To have a reference corresponding to the initial structure before any alteration, the SAXS profile has been also calculated on the grid totally filled with atoms. We see the evolution of bigger pores and we observe that the scattering intensity of these structures at different duration.

Figure 3.25 gives the numerical scattering curves for five simulation times. The results are in agreement with the experimental trend (mentioned in the experimental section regarding the SBNA glasses) regarding the evolution of the SAXS profile ($I(q)xq^2$ vs q) . Figure 3.25 shows the initial gel structure in blue, as well as the structure after 15k, 50k, 100k and 200k maturation steps. The SAXS profile of gel matured at 100k and 200k is similar. The gel reaches the plateau at 0.2 Ang^{-1} for the initial gel structure, as the gel maturates the plateau shifts to 0.4 Ang^{-1}. The position of the plateau is around the similar value as observed in the works of Cailleteau [56]. The SAXS profile fails to follow the Porod's law regime (linear correlation with q^{-4} behavior) [139], [140] although it is observed that as the gel structure maturates, it tends to closer to follow the Porod's law regime. This is due to the fact that the pores are not perfectly spherical since there is a bias of vacancy migration along the z axis. The SAXS profile points out the pore saturation as the difference between the SAXS profile for 100k and 200k Monte-Carlo steps.

We conducted a parametric study to differentiate the roles of the parameters *wvacan1* and *wvacan2* in controlling gel maturation. Figure 3.26 shows the median pore size as a function of time, which provides a representative measure of the distribution of pore sizes. The median pore size was chosen as the parameter because it is

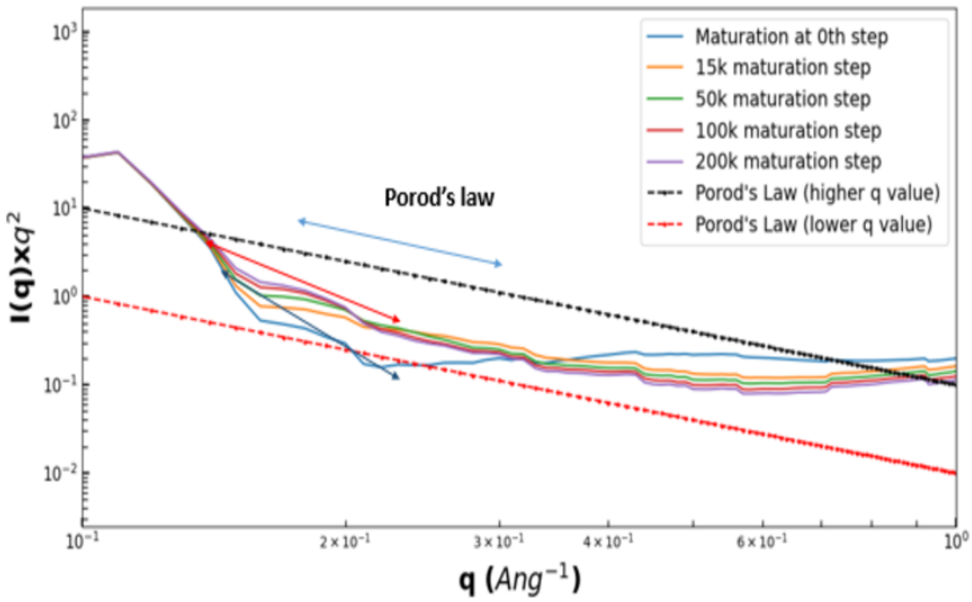

Figure 3.25: *SAXS profiles comparing the initial gel matured during Monte-Carlo gel simulations of 15k, 50k, 100k and 200k maturation steps.*

less influenced by extreme values compared to the mean, making it a robust metric for characterizing pore structures. The characteristic time, fitted from the median pore size distribution using the profile $a + be^{-t/\tau}$, reveals the characteristic time (in terms of Monte Carlo steps) required to reach maturation. Figure 3.26(a) highlights the effect of a change of *wvacan2* while keeping *wvacan1* constant, The characteristic time τ increases when *wvacan2* decreases from around 17000 to 55000 MC steps when *wvacan2* is varied from 900 to 600 while *wvacan1* is kept at a constant value of 50. Figure 3.26(b) represents the variation of *wvacan1* when *wvacan2* is kept constant. Even the slightest increase of *wvacan1* leads to the increase of characteristic time which varies from 19000 to 42000 MC steps when *wvacan1* is varied from 50 to 90 keeping *wvacan2* constant at 900. Increasing *wvacan1* also leads to a decrease of the final equilibrated pore size after maturation. Although the gel morphology depicted in the Figure 3.23 makes it challenging to definitively assess channel connectivity, this loss of connection can be interpreted by analogy with the observed reduction in interconnectedness. The initial configuration of the Monte-Carlo structure contains low median pore size (analogous to possibly higher connected channels). When the averaged pore size increases, it leads to the analogy of losing channels (since the total porosity is constant). In terms of gel maturation, we can assign the role of Al as high value of *wvacan1* or low value of *wvacan2*. In order to favor the growth of pores the role of *wvacan2* is crucial. There has been attempt to quantify the channel

size with Zeo++ but it hasn't led to a conclusive result. One reason for this can possibly be that due to the irregular shape of pores, it is harder to distinguish between a pore and a channel. There has been an attenmt in the coming section to explore the channel size of the final maturated structure by finiding an appropriate cutoff to separate the big clusters to get a rough estimation of the channel size.

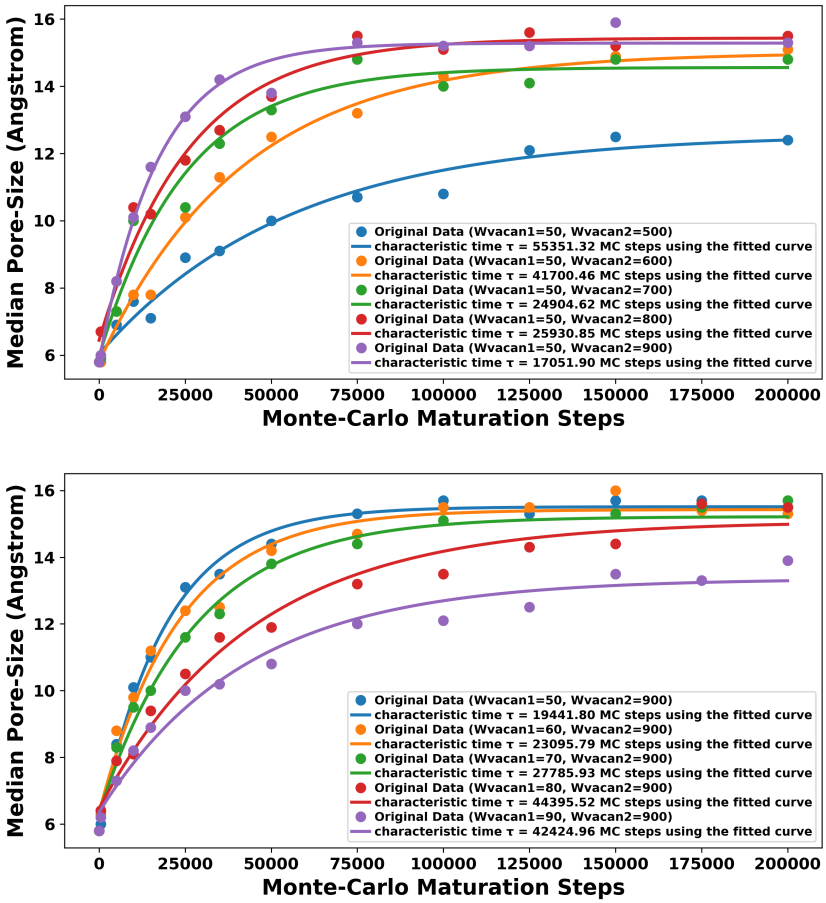

Figure 3.26: *Median pore size from Monte Carlo simulations as a function of maturation steps: (a) constant* wvacan1*, varying* wvacan2*; (b) constant* wvacan2*, varying* wvacan1*.*

Analysis of the channels of gel structures. To distinguish between compact pores and narrow connecting channels, we performed a cluster connectivity analysis based on a nearest-neighbor criterion. Vacancies were placed on a 3.5 Å grid, and connectivity between them was defined by first and second nearest neighbors. A cluster was considered valid only if each vacancy had a minimum number of neighboring vacancies, allowing us to tune a cutoff to differentiate high-density pores from sparsely connected channels. To illustrate the conceptual role of the cutoff, Figure 3.28a schematically shows how connections are progressively removed as the

cutoff increases: at low cutoffs, tenuous links are preserved, while at high cutoffs only compact clusters remain.

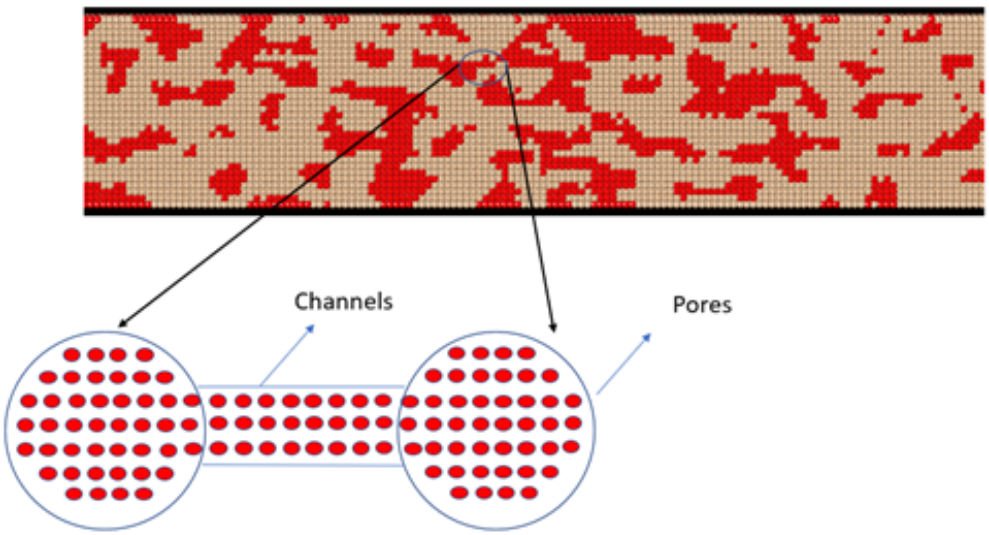

Figure 3.27: *Monte-Carlo structure of SBNA4 maturated at 200K MC steps.*

We applied this method to a matured Monte Carlo–generated gel structure obtained after complete boron leaching and subsequent evolution over 200,000 steps. This configuration corresponds to a fully altered gel stabilized by vacancy migration, where pore saturation has been reached. In this matured structure, we observed a highly connected porous network, with the largest vacancy cluster extending up to 5844 lattice units in the z-direction, indicating long-range percolation. Figure 3.28 summarizes the analysis: as the cutoff increases, the length of the largest connected cluster decreases sharply. Beyond **12** neighbors, the percolation network collapses and only small, disconnected clusters remain.

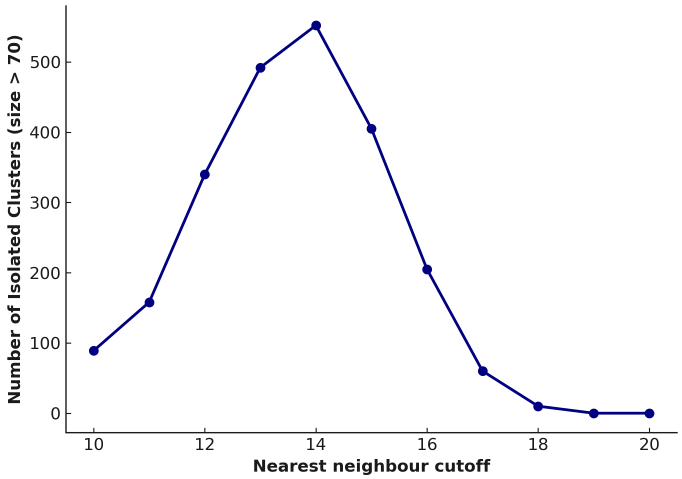

(a) *(a)*

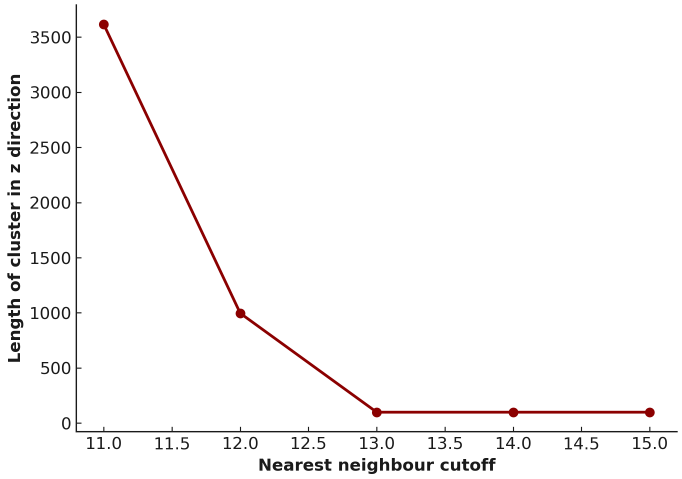

(b) *(b)*

Figure 3.28: *Cluster properties as a function of nearest-neighbor cutoff: (a) number of clusters vs. cutoff, (b) cluster length in the z direction vs. cutoff.*

The length of the largest connected cluster in the z-direction as a function of the nearest-neighbor cutoff shows a rapid drop beyond a cutoff of **12** neighbors, marking the disintegration of continuous channel networks.

To estimate the physical size of the narrowest connections that still percolate, we take the critical threshold to be $n = 12$ neighboring vacancies on a cubic grid of spacing $a = 3.5$ Å. The bottleneck volume is then

$$V_{\text{bottle}} = n\, a^3 = 12 \times (3.5\ \text{Å})^3 = 514.5\ \text{Å}^3.$$

Assuming a spherical equivalent, the effective diameter is

$$d = \left(\frac{6V_{\text{bottle}}}{\pi}\right)^{1/3} \approx 9.94\ \text{Å}\ \ (\approx 10\ \text{Å}).$$

Thus, the narrowest channel bottlenecks that still maintain connectivity have an effective diameter of about **10** Å, providing a useful characteristic dimension for linking structure to diffusivity or transport in the gel.

3.4 Discussion

What chemical interactions and morphological transformations occur at the glass–solution interface, and how are these processes connected to the kinetics of alteration observed in experimental studies?

Monte-Carlo simulations on aluminoborosilicate glasses, SBNA3.5, SBNA4, and SBNA6 reveal two distinct alteration behaviors, governed by glass composition and the hydrolysis rate at the gel-solution interface. At low hydrolysis rates, sufficient time is available for the formation of a dense, external layer enriched in Si and Al. However, as the hydrolysis rate increases, dissolution occurs primarily through the release of clusters, preventing the formation of such an enriched layer.

For a constant redeposition parameter (*wred*), increasing the hydrolysis rate (*wbreak*) leads to a shift in alteration behavior for all three glasses studied—SBNA3.5, SBNA4, and SBNA6—though at different thresholds. This threshold is influenced by the combined quantity of B_2O_3 and Na_2O: the higher this quantity, the lower the threshold.

A possible explanation is that as B_2O_3 and Na_2O content increases, the glass-solution interface becomes rougher due to the higher concentration of soluble elements. This increasing irregularity hinders the formation of a Si- and Al-enriched external layer through redeposition mechanisms.

Experimentally, two distinct alteration behaviors are observed. In glasses with low Al content, rapid glass dissolution occurs, followed by silica precipitation at

the surface, leading to a sharp decrease in the alteration rate. Conversely, in glasses with higher Al content, the dissolution rate is lower, and the alteration layer forms through in-situ dissolution and recondensation mechanisms.

Previous studies [52] highlights the differing alteration behaviors of a ternary borosilicate glass (CJ1) and its Al_2O_3-doped counterpart (CJ2, with 4.1 mol% Al_2O_3). In CJ1 (Al-free), the alteration mechanism is primarily governed by dissolution and precipitation at the glass-solution interface. In contrast, in CJ2 (Al-enriched), alteration is dominated by local structural reorganization.

Although the current Monte-Carlo model is too simplified to fully capture precipitation mechanisms or in-situ dissolution and recondensation, it is tempting to draw parallels between the Monte-Carlo results and experimental observations. Modifying the hydrolysis rate in Monte-Carlo simulations can be seen as an analog for varying the Al_2O_3 content: a low hydrolysis rate corresponds to glasses with high Al_2O_3 content, while a high hydrolysis rate represents glasses with low Al_2O_3 content.

This interplay can be associated with alteration mechanisms observed experimentally.

Glasses with low Al_2O_3 content: Dissolution and Precipitation

Glasses with low Al_2O_3 content exhibit a fast dissolution rate, followed by a rapid decrease in alteration rate due to silica precipitation at the glass surface.

While the Monte Carlo calculations do not directly simulate this process, they offer the following interpretation: a low Al_2O_3 content corresponds to a high hydrolysis rate, i.e., large *wbreak* values. In this case, the release rate and surface roughness are so significant that the formation of an external Si- and Al-enriched layer becomes impossible. The resulting surface irregularity leads to alteration via cluster release, which could represent the initial stage of silica precipitation at the glass–solution interface, as observed experimentally due to a rapid increase in dissolved Si concentration.

Currently, Monte Carlo simulations do not account for silica precipitation, as this mechanism is not implemented. However, the cluster-based alteration behavior observed in simulations may also explain the experimental behavior of glasses with low Al_2O_3 content: the rapid release of elements creates a rough glass–solution interface, preventing the formation of a passivating layer through local reorganization. As a result, silica precipitation at the interface becomes the dominant mechanism.

Glasses with higher Al_2O_3 content: in-situ reorganization

In contrast, glasses with higher Al_2O_3 content do not exhibit silica precipitation at the glass-solution interface. Instead, a passivating alteration gel forms through in-situ dissolution and recondensation mechanisms. The initial alteration rate for these glasses is lower than that of glasses with low Al_2O_3 content.

This behavior can be paralleled with Monte-Carlo calculations using a lower hydrolysis rate (*wbreak*). In these simulations, alteration occurs atom by atom, allowing the formation of a dense, external layer enriched in Si and Al. Since the surface remains relatively smooth, redeposition mechanisms can progressively "plug the holes."

Although the Monte Carlo model does not explicitly simulate in-situ dissolution and recondensation, it indirectly represents this process through the stepwise dissolution and redeposition of individual atoms at the glass-solution interface.

Based on these simulations, it is suspected that the in-situ reorganization mechanisms observed experimentally are favored by a low hydrolysis rate and a more uniform glass-solution interface.

Is it possible to establish an interplay between the parameters controlling the gel characteristics?

Two parameters are related to the physical processes associated with Ostwald ripening. The parameter *wvacan1*, which promotes the separation of vacancies, can be seen as a representation of the diffusion of individual vacancies. The parameter *wvacan2*, which promotes the clustering of vacancies, can be linked to the surface tension of pores, whose minimization leads to the growth of spherical pores. The values of these two parameters are currently chosen empirically due to a lack of sufficient knowledge to adjust them based on physical values.

Whatever the values of *wvacan1* and *wvacan2*, the median pore size evolved with Monte-Carlo steps until a stationary state where the pore morphology no longer changes as we can see from both the cumulative distributions (Figure 3.25) and SAXS profiles (Figure 3.25). The balance between the values of *wvacan1* and *wvacan2* controls the pore growth. The increase in the value of *wvacan1* introduces a delay in the growth of pores and the increase in the value of *wvacan2* leads to decrease the characteristic time necessary to reach a stationary state.

How does the MC gel structure evolve over time, and how can this be related to diffusion processes and experimental observations (SAXS, TEM) to explain alteration kinetics?

The reorganization of porosity within the gel network happens in such a way that the connectivity between the pores is rapidly lost. This conclusion comes from the fact that the total porosity is constant and the growing of the average pore size will eventually induce a reduction of the pathways connecting the pores. We even observe that at no point do well-defined channels connecting the pores to each other exist. This observation, although currently visual, stems from the fact that the available free volume is not sufficient to allow the coexistence of both channels and pores. Larger quantities of soluble elements, particularly boron, would be necessary to fur-

ther open up the gel morphology.

A quantitative channel analysis reveals confined channels approximately 10 Å in diameter, which is similar to the ~1 nm size reported in experimental studies [58] for ISG glasses. Since there are no continuous channels connecting the pores, the only viable pathway for boron diffusion is through the gel skeleton. This observation explains the low boron diffusion coefficients (on the order of 10^{-19} to 10^{-20} m^2/s) seen in SBNA glasses.

Such low diffusivity suggests a solid-state diffusion mechanism occurring within the cross-linked gel network. Over time, boron atoms do not diffuse through interconnecting channels between pores, but rather migrate through a gel structure that is slowly relaxing. The precise cause of the gradual slowing down of boron diffusion through the alteration gel is not yet fully understood, but is likely related to the reorganization mechanisms of the reticulated gel network.

What mechanisms influence the restructuring of gel, particularly in relation to the role of aluminum (Al) in glass?

As mentioned in the Experimental section, the experimental trend highlights the key role of Al in controlling the restructuring of the gel, which in turn impacts the residual alteration rate of the glass, consistent with previous studies [53], [56]. The characteristic time τ for SBNA1 is notably shorter than that of both SBNA4 and SBNA6. It is essential to clarify that the characteristic time referenced here differs from the saturation time of pores discussed in the results section. In this context, τ pertains to the transition between the initial and residual alteration regimes. This value was derived from long-duration experiments, utilizing a fitting function of the form $NLB(t) = a + b \cdot e^{-t/\tau}$ to analyze the normalized boron mass loss, as mentioned in the experimental section. The presence of aluminum as a second neighbor to silicon has a dual effect on the Si-O bonds. On one hand, it increases the energy barrier required to break these bonds, thereby enhancing the strength of the silicon network. On the other hand, it reduces the energy barrier for reforming Si-O bonds, facilitating the reformation of the silica network [38], [53]. During the transition from the initial dissolution rate to the residual rate, the alteration gel skeleton becomes more passivating, and the transition rate depends on the Al content. The glass with the least Al content (SBNA1) matures faster than those with higher Al contents (SBNA4 and SBNA6).

In the current simulation, we do not implement the composition effect directly, in particular the impact of Al content. In order to simulate the role of Al using the current Monte-Carlo code, we rely on the interplay between the parameters *wvacan1* and *wvacan2*. We can vary the relative values of *wvacan1* and *wvacan2* while keeping a constant ratio. In Figure 3.29, the blue and orange curves correspond to constant

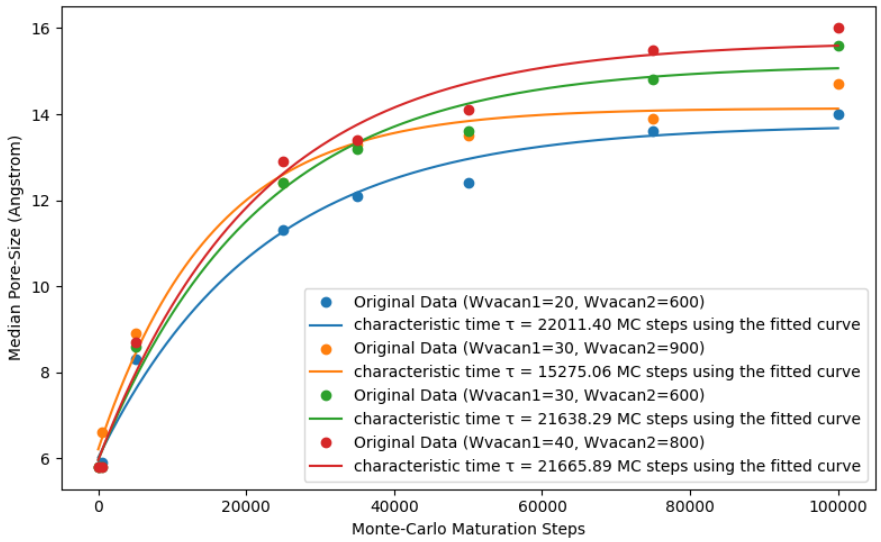

Figure 3.29: *Median pore size versus the number of Monte-Carlo steps for wvacan2/wvacan1 ratios equal to 30 and 20.*

ratio of *wvacan2/wvacan1* = 30 and red and green curves correspond to a constant ratio *wvacan2/wvacan1* = 20. For a given ratio, we reach the same plateau of median pore size but with different characteristic times. The characteristic time is extracted by fitting the function

$$a + b \cdot e^{-\frac{t}{\tau}}$$

on the median pore size change versus time. On the contrary, when the $\frac{\text{wvacan2}}{\text{wvacan1}}$ ratio decreases, the height of the final plateau increases.

This behavior can be explained by the competition between two mechanisms. When *wvacan2* is high, the probability of vacancy migration is high, leading to a faster transition time because vacancies gather more quickly. However, if *wvacan1* is very low while *wvacan2* remains high, the vacancies tend to gather locally rather than redistribute broadly throughout the network. This results in a lower final median pore size, despite the shorter transition time. This effect is demonstrated in Figure 3.30, where different combinations of *wvacan1* and *wvacan2* lead to different balances between fast local clustering and long-range redistribution of vacancies.

It is interesting to link this observation to experimental results. Experimentally, for SBNA1 and SBNA4, the average pore sizes converge to a similar value although the maturation rates are different. This suggests some conclusions about the Ostwald ripening process in these glasses. The Ostwald ripening is driven by the hydrolysis and reformation reactions that lead to a progressive gathering of free volume to create growing pores [162]. This process is driven mostly at basic pH. The

presence of Al can control the hydrolysis and reformation reactions and in consequence the vacancy migration [38], [53]. On the other hand, the dynamics of pore growth is also regulated by the surface energy of the pores, which tends to minimize as the pores enlarge and decrease in number.

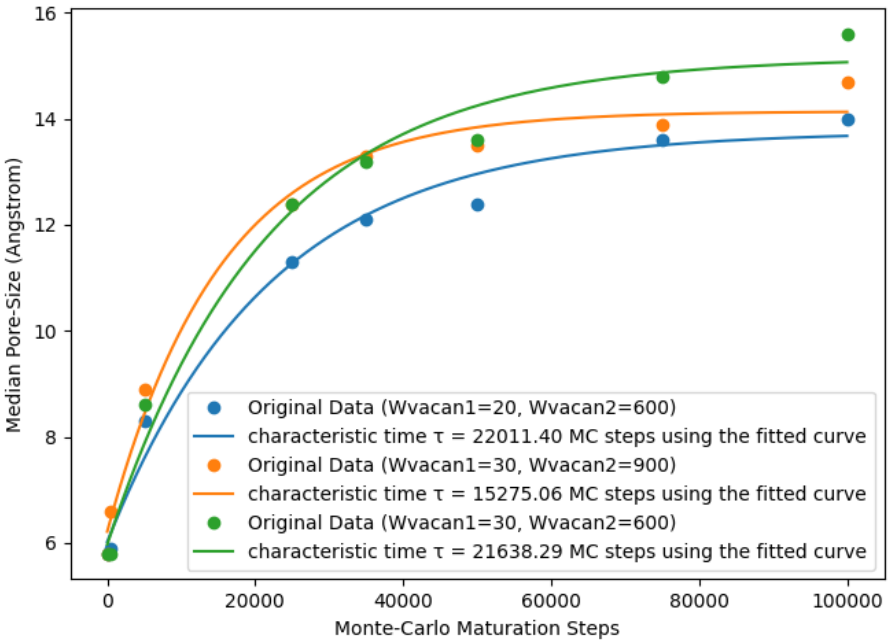

Figure 3.30: *Median pore size versus the number of Monte-Carlo steps for wvacan2/wvacan1 ratios equal to 30 and 20.*

Although the mechanisms implemented in the Monte-Carlo method are a simplification of reality, it is interesting to note that in the SBNA1 and SBNA4 glasses, the final average pore sizes are similar, which, from the Monte-Carlo approach, means that the ratios between the *wvacan1* and *wvacan2* parameters are also close. The increase in Al content in the SBNA4 glass compared to the SBNA1 glass induces a greater rigidity in the gel reticulated network, which therefore takes a longer time to become passivating. The vacancy migration dynamics are likely reduced, which would correspond to a lower value of the *wvacan1* parameter for a constant *wvacan2* parameter. If the final pore size is similar between the SBNA1 and SBNA4 glasses, it means that the ratio between the *wvacan1* and *wvacan2* parameters remains similar between these two glasses. This would only be possible if the *wvacan2* parameter also decreases in the SBNA4 glass, meaning that the driving force for pore growth through surface energy minimization is less effective. In other words, a weaker dependence of the surface energy of the pores on their size in the SBNA4 glass compared to the SBNA1 glass. It will be interesting to verify if this statement is true

through complementary molecular modeling calculations in the future.

Conclusion

The newly developed Monte–Carlo algorithm for modeling the alteration of alumino–borosilicate glasses addresses the limitations of previous approaches by explicitly enabling the simulation of water diffusion within the glass network, in addition to the classical mechanisms of hydrolysis and redeposition. This is achieved through the use of two shifted subnetworks: one hosting the solid phase and the other the liquid phase. By incorporating a new diffusion mechanism, the model reveals novel alteration behaviors that depend strongly on the hydrolysis rate at the gel–solution interface.

At low hydrolysis rates, an external layer enriched in Si and Al gradually forms at the interface during alteration. By contrast, at high hydrolysis rates, alteration occurs predominantly through the release of clusters, preventing the development of this enriched layer. Instead, a more porous and jagged outer zone emerges. The glass composition also governs this transition: glasses with higher B_2O_3 and Na_2O contents undergo the switch from enriched-layer formation to cluster release at lower hydrolysis rate thresholds. These results emphasize the role of interface morphology, controlled by both hydrolysis/redeposition kinetics and glass composition, in dictating the formation of protective outer layers.

The new Monte–Carlo algorithm also reproduces the maturation of the alteration gel, enabling a closer comparison between simulation and experiment. This improved capability provides insight into the connection between pore evolution, transport properties, and alteration kinetics.

The difference in alteration behavior between SBNA1 (low-Al glass) and SBNA6 (high-Al glass) can be clarified by combining experimental observations and Monte–Carlo simulations. **Experimentally**, boron diffusivity within the gel is found to be extremely low, with a diffusion coefficient characteristic of solid-state diffusion rather than transport through open aqueous channels. **Simulations** provide a structural explanation for this observation: during gel maturation, no large or percolating channels form, even at the earliest stages of ripening. This limited connectivity between pores hinders long-range diffusion and is consistent with the experimentally observed transport properties. **Finally**, analysis of pore morphology suggests that the surface energy of the pores, which may vary with glass composition, could further influence the kinetics of alteration.

Taken together, these insights highlight the interplay between solid-state diffusion, pore evolution, and composition-dependent interfacial properties in controlling the long-term alteration of alumino–borosilicate glasses.

4 Molecular Dynamics

Contents

4.1 Introduction

Boron plays a critical role in glass alteration, particularly its behavior in nanopores of the gel, which could influence the residual rate of the glass [52]. However, the chemical reactivity and the transport property of boron in confined environments remains poorly understood, making it critical for understanding transport processes in gel.

Molecular dynamics (MD) simulations, when coupled with appropriate interatomic potentials, provide a powerful approach to explore these interactions (for example: diffusion mechanisms) at the atomic level [82], [163]. Among various force fields, the Diffusive Charge Reactive Potential (DCRP)—a modified version of the rigid-ion water potential developed by Guillot and Guissani (GG)—stands out [164]. This potential was later enhanced by Mahadevan and Garofalini [125] to accurately reproduce

the bulk properties of water, including its dissociation. The DCRP is particularly effective in modeling interactions between water and silicate-based materials, such as glass-water interfaces and hydrated structures [126], [165]. Compared to other models, DCRP offers a significant advantage in computational efficiency, being approximately ten times faster than the ReaxFF potential—a bond-order-based reactive potential that accounts for charge transfer and chemical reactions—while maintaining comparable accuracy [126]. In contrast, more computationally demanding methods like ReaxFF and density functional theory (DFT), which are ten and one hundred times slower than DCRP, respectively, are limited by higher costs and smaller system sizes. Consequently, DCRP enables the calculation of diffusion coefficients at the necessary spatial and temporal scales [126].

In this chapter, I propose extending the DCRP force field to simulate boron's behavior in solution within silica nanopores. Nanoporous silica is used here as a model of the alumino silicate alteration gel formed during glass alteration. The study will emphasize examining the transport characteristics of boron, comparing its behavior in an unconfined aqueous solution to its dynamics when restricted within the confined environments of a simplified gel. This detailed analysis aims to uncover how spatial confinement influences boron's mobility, diffusion rates, and interaction with surrounding silica structures, providing insights into the physical and chemical processes that govern its behavior in these distinct settings. This investigation tries to answer several key questions:

- What are the transport properties of boron in an unconfined aqueous solution?
- How do these properties change when boron is confined within a nanoporous structure?
- Is there a relationship between boron's transport in these confined spaces and the observed deceleration in glass alteration rates?

To address these questions, the chapter begins with the refinement of boron interactions in the DCRP framework using a force-matching approach. The refined potential is then employed to simulate boron transport in both bulk water and nanoporous silica. Comparative analysis of these environments reveals how confinement affects boron's mobility and interactions, providing insight into its role in the deceleration of glass alteration.

4.2 Methods

4.2.1 Analytical form of the potentials

In this model, the total potential energy is expressed as the sum of two-body and three-body contributions. The two-body interactions account for the Coulombic, repulsive, and dispersive terms,

$$U_{ij}^{\text{2body}} = U_{\text{Coulombic}} + U_{\text{Repulsive}} + U_{\text{Dispersive}}, \tag{4.1}$$

while the three-body term introduces the angular dependence, $U_{ijk}^{\text{3body}}(r_{ij}, r_{ik}, \theta_{ijk})$.

Coulombic interactions are governed by both fixed and diffuse charges, as outlined in Equations 4.2–4.6. For each species i, a fixed charge q_i and a diffuse charge $q_{d,i}$ are defined, with the constraint that $q_{di} = -0.25\, q_i$. When considering two atoms i and j separated by a distance r_{ij}, the Coulombic interaction is described by four distinct terms, each involving combinations of their fixed and diffuse charges.

The contribution of the diffuse charge to the total charge of an ion i varies with distance and depends on the diffuse charge $q_{d,i}$, which has the opposite sign to q_i. This opposition reduces the effective charge on ion i as a function of the $i-j$ separation, with the rate of approach to the asymptotic value governed by the parameter ξ_{ij}. In the present parameterization, ξ_{ij} is chosen large, so the diffuse charges make only a small correction to the effective charge at typical intermolecular distances [125]. Independently of this, the Coulomb interaction is damped at long range by the Wolf screening, implemented via the complementary error function $\text{erfc}(\beta r_{ij})$. This erfc factor multiplies *all* Coulombic terms (fixed–fixed, fixed–diffuse, diffuse–fixed, and diffuse–diffuse) and represents a general large-distance screening.

The pair potential operates between all pairs of atoms as a non-bonded interaction, without distinguishing between atoms within the same molecule or across different molecules. This uniform treatment simplifies the interaction description, making it dependent solely on interatomic distance. As a result, the model captures a fully atomistic representation of water that inherently allows for bond dissociation and formation. By incorporating fixed and diffuse charges, the potential dynamically adjusts interatomic forces in response to local environments, enabling the realistic simulation of water dissociation processes. This provides a robust framework for exploring molecular interactions and chemical reactivity at the atomic level.

$$U_{q_i - q_j}(r_{ij}) = \left(\frac{q_i q_j}{r_{ij}}\right) \text{erfc}\left(\frac{r_{ij}}{\beta}\right) \tag{4.2}$$

$$U_{q_{di} - q_j}(r_{ij}) = \left(\frac{q_{di} q_j}{r_{ij}}\right) \text{erf}\left(\frac{r_{ij}}{\sqrt{2}\xi_{ij}}\right) \text{erfc}\left(\frac{r_{ij}}{\beta}\right) \tag{4.3}$$

$$U_{q_i-q_{dj}}(r_{ij}) = \left(\frac{q_i q_{dj}}{r_{ij}}\right) \mathrm{erf}\left(\frac{r_{ij}}{\sqrt{2}\xi_{ij}}\right) \mathrm{erfc}\left(\frac{r_{ij}}{\beta}\right) \tag{4.4}$$

$$U_{q_{di}-q_{dj}}(r_{ij}) = \left(\frac{q_{di} q_{dj}}{r_{ij}}\right) \mathrm{erf}\left(\frac{r_{ij}}{2\varepsilon_{ij}}\right) \mathrm{erfc}\left(\frac{r_{ij}}{\beta}\right) \tag{4.5}$$

The contribution corresponding to the repulsive interaction is described by Equations 4.6–4.8. The terms A_{ij}^{rep}, ε_{ij}^{r} , C_{ij}^{6} and D_{ij}^{8} (related to two body terms) are adjustable parameters with regards to the repulsive and dispersive terms given in Equations 4.6–4.8.

$$U_{ij}^{\mathrm{rep}}(r_{ij}) = A_{ij}^{\mathrm{rep}} \left(\frac{2\varepsilon_{ij}^{r}}{r_{ij}}\right) \mathrm{erfc}\left(\frac{r_{ij}}{2\varepsilon_{ij}^{r}}\right) \tag{4.6}$$

$$U_{ij}^{\mathrm{disp}}(r_{ij}) = -\frac{C_{ij}^{6}}{r_{ij}^{6}} \tag{4.7}$$

$$U_{ij}^{\mathrm{disp}}(r_{ij}) = \frac{D_{ij}^{8}}{r_{ij}^{8}} \tag{4.8}$$

The three-body term is described by the expression

$$U_{ijk}^{\mathrm{3body}}(r_{ij}, r_{ik}, \theta_{ijk}) = \lambda_{ijk} \exp\left(\frac{\Upsilon_{ij}}{r_{ij} - r_{ij}^{\circ}} + \frac{\Upsilon_{ik}}{r_{ik} - r_{ik}^{\circ}}\right) \left(\cos\theta_{ijk} - \cos\theta_{ijk}^{\circ}\right)^2 \tag{4.9}$$

for $r_{ij} < r_{ij}^{\circ}$ and $r_{ik} < r_{ik}^{\circ}$, and it is equal to 0 otherwise. The three-body function's purpose is to adjust the interactions among three atoms based on their deviation from an ideal angle, represented as $\cos(\theta_{ijk}^{0})$. By employing this function, the model can produce the desired angular configuration. The parameters in the three-body potential are configured to specifically regulate the angle between certain triplets of atoms to a predetermined value. To attain this target angle, θ_{ijk}^{0} is set to a specific value, which, in conjunction with repulsive interactions between certain pairs of atoms, results in an energy minimum at the intended angle [125]. This potential is designed to be active only for specific combinations of atoms i, j, and k, and it remains zero for all other combinations if the three body parameters are not specified. The three-body term has the adjustable parameters λ_{ijk}, $\Upsilon_{ij,}$, r_{ij}° and r_{ik}°. The full set of parameters in the Mahadevan-Garofalini potentials is given in Table 4.1.

The original version of the potential included parameters describing pure water and the interaction between water and silica. The parameterization was further ex-

Table 4.1: *Parameters used for Mahadevan and Garofalini model [125], [126], [165]*

Coulombic Terms	Repulsive and Dispersive Terms	Three-Body Term
β	A_{ij}^{rep}	λ_{ijk}
ξ_{ij}	ε_{ij}^{r}	γ_{ij}
ε_{ij}	C_{ij}^{6}	r_{ij}°
	D_{ij}^{8}	θ_{ijk}°

tended to include sodium, calcium, and aluminum [121], [165].

Boron is not included in the versions of this potential published in the literature. This chapter therefore describes an effort to parameterize the force-field terms involving boron. In aqueous environments, boron exists in a pH-dependent equilibrium between trigonal boric acid, $B(OH)_3$, and tetrahedral borate, $B(OH)_4^-$. In the present work, we focus on conditions representative of neutral pH, under which boron in solution is predominantly three-coordinated as $B(OH)_3$. The force field is therefore parameterized for $B(OH)_3$ in an aqueous environment, with possible interactions with silica surfaces. It is noted, however, that within the alteration gel the local chemical environment of boron may be more complex than in bulk solution and may involve coordination states not explicitly captured by the present parameterization.

4.2.2 DFT calculations

The DFT forces were calculated for these structures using the CP2K software package [166], a widely adopted tool for atomistic simulations and electronic structure calculations, particularly for condensed-phase and materials science applications.

We employed the double-zeta valence with one polarization term (DZVP) basis set for these calculations. This choice strikes an optimal balance between computational efficiency and accuracy for electronic structure calculations.

The Goedecker-Teter-Hutter (GTH) pseudopotentials [167] are widely used in computational simulations, particularly within density functional theory (DFT) , because they offer an excellent balance between computational efficiency and physical accuracy. These pseudopotentials replace the complex interactions of core electrons with a smoother, effective potential that accurately mimics their influence on valence electrons. With this potential we simplify the interaction by eliminating the need to explicitly compute tightly bound core states, which would otherwise require high plane-wave cutoffs and a large number of basis functions, at a significantly increased computational cost.

The exchange-correlation functional was the Perdew-Burke-Ernzerhof (PBE) func-

tional [168], formulated within the generalized gradient approximation (GGA) scheme. The PBE functional improves upon the local density approximation (LDA) by incorporating the electron density gradient, thereby enhancing the accuracy of electronic structure predictions [167].

To ensure the reliability of the calculations, we systematically tested the plane-wave energy cutoff to achieve convergence of the total energy and forces. After evaluating cutoffs ranging from 50 to 600 Ry ($1\ \mathrm{Ry} \approx 13.6057\ \mathrm{eV}$), we selected an energy cutoff of 500 Ry. This value was chosen as it provided a convergence of the total energy without significantly increasing computational cost. Single-point calculations were performed for each of the 32 structures to compute the DFT forces, which were subsequently used for the optimization of the classical potential parameters.

The binding energy of the $B(OH)_3$–H_2O complex was calculated by computing the total electronic energy of the optimized complex and subtracting the sum of the electronic energies of the isolated, optimized monomers—boric acid ($B(OH)_3$) and water (H_2O). The binding energy ΔE_{bind} was computed using the formula

$$\Delta E_{\mathrm{bind}} = E_{\mathrm{complex}} - \left(E_{\mathrm{B(OH)_3}} + E_{\mathrm{H_2O}}\right) \tag{4.10}$$

where E_{complex} is the energy of the $B(OH)_3$–H_2O adduct, and $E_{\mathrm{B(OH)_3}}$ and $E_{\mathrm{H_2O}}$ are the energies of the individual components. The basis set and pseudopotentials used are similar to the one's described in the previous paragraph of this section.

4.2.3 Force matching

To optimize the parameters of the interatomic potentials, we employed the force-matching method [105], [125]. This method was described in several papers [106], [169], [170]. The primary idea is to tune the parameters of the force field so that they are able to reproduce the atomic forces determined by DFT calculations. Figure 4.1 shows the flowchart for the force matching procedure. The DL_POLY code was used for the classical molecular dynamics simulations and CP2K was used for the DFT calculations.

Detailed force matching work flow

The aim is to minimize the difference between forces calculated from the classical potentials and forces calculated in DFT for identical atomic configurations, ensuring the classical potential replicated the forces and the correct local environment of the systems in the study.

We followed a step-by-step procedure for force matching. Here's how I carried it out:

1. **Defining the classical potential**

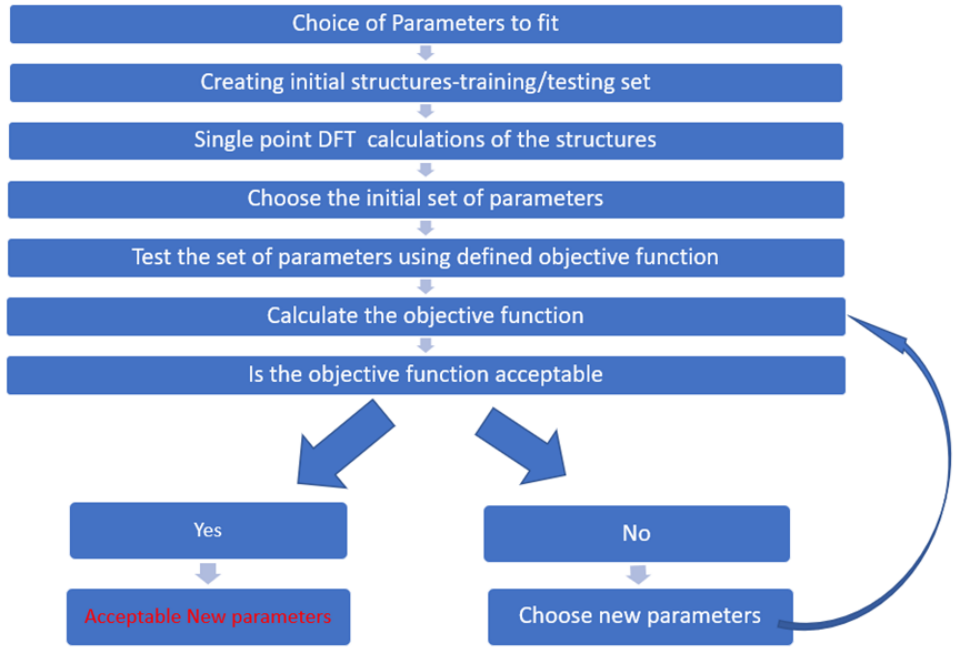

Figure 4.1: *A general force matching procedure used for the development of force fields.*

The first step is to choose a functional form for the classical potential. Here we selected the DCRP. The functions include adjustable parameters for the two-body and three-body terms considered for fitting (see section 4.2.1).

2. **Generating the initial structures**

The 32 structures were prepared using the DCRP potential, with parameters obtained from a refined initial parameterization. Each structure contained approximately 600 atoms and was generated independently with random atomic positions and varying concentrations of boron distributed across four distinct levels. These concentrations were chosen to span a wide range of chemical environments, enabling a comprehensive exploration of the structural and dynamic properties of aqueous boron systems. The preparation of the initial structures was carefully designed to ensure a diverse set of configurations, which is critical for mapping the majority of the forces in the phase space. This diversity was achieved by randomly positioning the atoms, including boron and other constituent atoms (O and H), within the simulation box (~18 Å), with a minimal approach distance of 1.9 Å enforced to prevent unrealistic steric clashes and ensure physical realism. The DCRP potential, described in Equations 4.1–4.9, was used to describe bond stretching, angle bending, and non-bonded van der Waals and electrostatic forces, thereby providing a consistent basis for the generation of these structures.

Each of the 32 structures underwent a multi-stage relaxation process to achieve equilibrium and stability. The process began with an initial relaxation of 10^6 timesteps at 500 K in the NVT ensemble (constant number of particles, volume, and temperature), which allowed the system to adjust thermally while maintaining a fixed volume. This was followed by a relaxation of 50,000 timesteps in the NPT ensemble (constant number of particles, pressure, and temperature) at the same temperature, enabling the system to find a new equilibrium density by allowing volume fluctuations under constant pressure. The initial density was set at 1.2 g/cm^3, and after these relaxations, the final density stabilized at approximately 1.1 g/cm^3, reflecting the system's response to the intermolecular forces and packing efficiency. A subsequent relaxation of 100,000 timesteps at 300 K in the NVE ensemble (constant number of particles, volume, and energy) ensured that the system reached a microcanonical equilibrium, where total energy was conserved, and dynamic properties could be accurately assessed. Visual inspection confirmed that the atoms, whatever the boron concentration, were randomly and uniformly distributed throughout the simulation box at the end of this stage, indicating a homogeneous and representative sampling of the configuration space. For all simulation stages, a timestep of 0.1 fs was used to ensure numerical stability and capture fast atomic motions accurately.

To facilitate force matching process, the dataset was split into two portions: 16 structures were reserved for training, allowing the development and optimization of models or potentials based on the observed data, while the remaining 16 structures were reserved for testing, providing an independent set to evaluate the predictive accuracy and generalizability of the trained models. This split ensures that the models are not overfitted to a specific subset of configurations and can perform reliably across the full range of boron concentrations and structural diversity.

The varying boron concentrations were strategically selected to map different local environments, from dilute systems where boron acts as a minor perturbation to concentrated systems where boron-boron interactions become significant.

3. **Generating DFT forces for parameter optimization**

We conducted high-accuracy DFT simulations on a set of 32 representative atomic configurations. These configurations were generated from the empirical potentials in step 2 to cover the range of states relevant to the classical potential. The computational details are mentioned in section above.

4. **Formulating the Objective Function**:

We defined an error function that quantifies the discrepancy between the DFT forces and the classical forces for all atoms in all configurations. We used a common form, the mean square error (MSE), which is the sum of the squared differences

between the two sets of forces:

$$\Phi = \frac{1}{N_a N_b} \cdot \frac{\sum_{j=1}^{N_b} \sum_{k=1}^{N_a} \left| \mathbf{F}_{k,j}^{cl} - \mathbf{F}_{k,j}^{DFT} \right|^2}{\sum_{j=1}^{N_b} \sum_{k=1}^{N_a} \left| \mathbf{F}_{k,j}^{DFT} \right|^2} \tag{4.11}$$

Here, N_a is the number of atoms in each configuration and N_b is the number of configurations in the training set. The force on atom k in configuration j is denoted as $\mathbf{F}_{k,j}^{cl}$ for the classical force field and $\mathbf{F}_{k,j}^{DFT}$ for the DFT calculation.

The numerator in Eq. 4.11 sums the squared differences between the classical and DFT forces over all atoms and configurations, so that larger discrepancies contribute more heavily. The denominator normalizes this error by the total squared magnitude of the DFT forces, making Φ dimensionless and allowing comparisons across systems with different absolute force scales. The prefactor $\frac{1}{N_a N_b}$ averages the error over all atoms and configurations, ensuring that Φ does not depend on system size or the number of sampled states.

This formulation is widely used in computational chemistry and materials science, particularly for parameterizing or validating classical force fields against high-fidelity DFT data. A similar strategy has been adopted in the literature [104].

5. **Optimizing the Parameters**

The objective function is minimized using the MINUIT library [171]. This library, developed at CERN from the 1970s, is a robust software package for function minimization and error analysis, widely used in scientific computing.

In the optimization process, the simplex minimization technique implemented in MINUIT's SIMPLEX subroutine is initially employed due to its derivative-free nature and stability [171]. The Nelder-Mead algorithm, based on the simplex method, adjusts a simplex of test points to explore the parameter space, making it ideal for objective functions that are noisy, discontinuous, or whose gradient is difficult to calculate reliably [171]. Its simplicity and broad exploratory capability ensure it can handle poor initial estimates efficiently, providing a rough minimum without requiring intensive computation, thus serving as an effective preliminary step before more precise methods [171].

Subsequently, the MIGRAD minimizer is applied to refine the solution, justified by its efficiency and accuracy as a variable-metric method. Leveraging gradient and Hessian information, MIGRAD converges rapidly to the minimum from a good starting point, such as that provided by SIMPLEX, and offers reliable error estimates via the Hessian matrix, crucial for scientific validity. Its robustness, including convergence checks and noise handling, ensures precise results, reducing the risk of local minima and enhancing the statistical reliability of the fit.

The iterative refinement process, testing the solution on new configurations or conditions, leverages both techniques to ensure robustness. After a rough minimum is identified using a simplex minimization, MIGRAD refines it, and further iterations adjust parameters or constraints, re-running the minimization to verify stability across datasets or scenarios. This approach, supported by MINUIT's tools, confirms the solution's insensitivity to initial conditions or noise, ensuring a precise, generalizable minimum with well-characterized uncertainties, maintaining scientific rigor.

4.3 Results: new empirical potential for boron

4.3.1 Performance of potential for Pure silica glass and water (reference)

The implementation and testing of the DCRP potential developed by Mahadevan and Garofalini, as reported in the current literature, provide a detailed assessment of its performance when applied to water and silica systems [125], [165]. In this section we evaluate the potential's effectiveness in reproducing forces for systems for which the parameters have already been tuned. It gives us an idea on the limit and precision of the potential in reproducing the forces. The analysis is based on structures initially generated using empirical potentials, with subsequent force calculations performed using DFT for comparison.

For creating initial structures, a 23x23x23 $Å^3$ simulation box containing ~1200 water atoms were used. The system underwent initial relaxation for 10^6 timesteps at 500 K in NVT conditions, allowing thermal adjustment at fixed volume. This was followed by 50,000 timesteps of relaxation in the NPT condition at the same temperature, enabling equilibrium density adjustment through volume fluctuations under constant pressure. The density was initially 1.1 g/cm^3, but it stabilized around 1.0 g/cm^3 during relaxation. Starting with a higher initial density of 1.1 g/cm^3 ensures the system begins in a compressed state, which can be crucial for accurately simulating the relaxation process. This approach helps the system stabilize at the desired density of 1.0 g/cm^3 while avoiding potential numerical instabilities or configuration issues during relaxation. Further relaxation for 100,000 timesteps at 300 K in NVE conditions ensured microcanonical equilibrium with conserved total energy for accurate dynamic property assessment. Atoms, whatever the boron concentration, were randomly and uniformly distributed, confirmed by visual inspection, indicating homogeneous configuration space sampling. All stages used a 0.1 fs timestep. This method aligns with force-matching initial structure creation (see section 4.2.3). The parameters used for simulation are kept in Table 4.2.

Table 4.2: *Parameters of the Two-Body Potential [125], [165]*

Parameter	Si-O	Si-Si	O-H	O-O	H-H
A_{ij}^{rep} (eV)	1666.67	436.95	1425.09	265.29	0
ε_{ij}^{r}	0.373	0.64	0.1998	0.61	1
C_{ij}^{6} (eV/Å^6)	43.6954	0	0	26.38	0
D_{ij}^{8} (eV/Å^8)	0	0	0	0	0

A simulation box of $18 \times 18 \times 18$ Å^3 was employed for silica. The silica glass melt was equilibrated at 4000 K under constant volume to stabilize the system in a liquid state. This temperature was chosen for consistency with studies from the literature [154]. The initial volume was chosen to achieve near-zero pressure at the end of the thermal quench. A thermal quench was then applied with a quench rate of 5×10^9 K/s, during which the volume remained fixed, allowing only the pressure to vary as the temperature decreased. Following the quench, a relaxation was performed at 300 K in the NPT ensemble (constant number of atoms N, constant pressure P, constant temperature T) for 20 ns to adjust the system to ambient conditions. Subsequently, a final relaxation was conducted at 300 K in the NVE condition for 5 ns, using the equilibrium volume obtained from the NPT relaxation. The NVT relaxations employed the Nosé–Hoover thermostat [172], [173], [174], [175] with a damping parameter of 0.1 ps, while the NPT relaxations used an additional barostat, also with a damping parameter of 0.1 ps.

These box sizes were selected to ensure computational feasibility while adequately representing the interactions. The empirical potentials provided the initial configurations, against which the DCRP potential's force predictions were compared to DFT-derived reference forces. The parameters for these calculations, including the DZVP basis set , GTH pseudopotentials , and PBE exchange-correlation functional [167], similar to what is mentioned in section 4.2.2.

The results indicate that the DCRP potential effectively reproduced the forces calculated by DFT for both water and silica, as demonstrated in Figure 4.2. This figure illustrates the comparison between the potential-derived forces and DFT reference forces, showing a reasonable level of agreement. This agreement between the DFT forces and those from the empirical potential suggests that the potential captures key interaction characteristics of the systems, making it a viable tool for simulating water and silica at a reduced computational cost compared to full DFT calculations.

However, a notable difference in precision was observed between the two systems. The potential performed with greater accuracy for water than for silica, a trend also evident in Figure 4.2. This variation is not unexpected, as the DCRP potential was

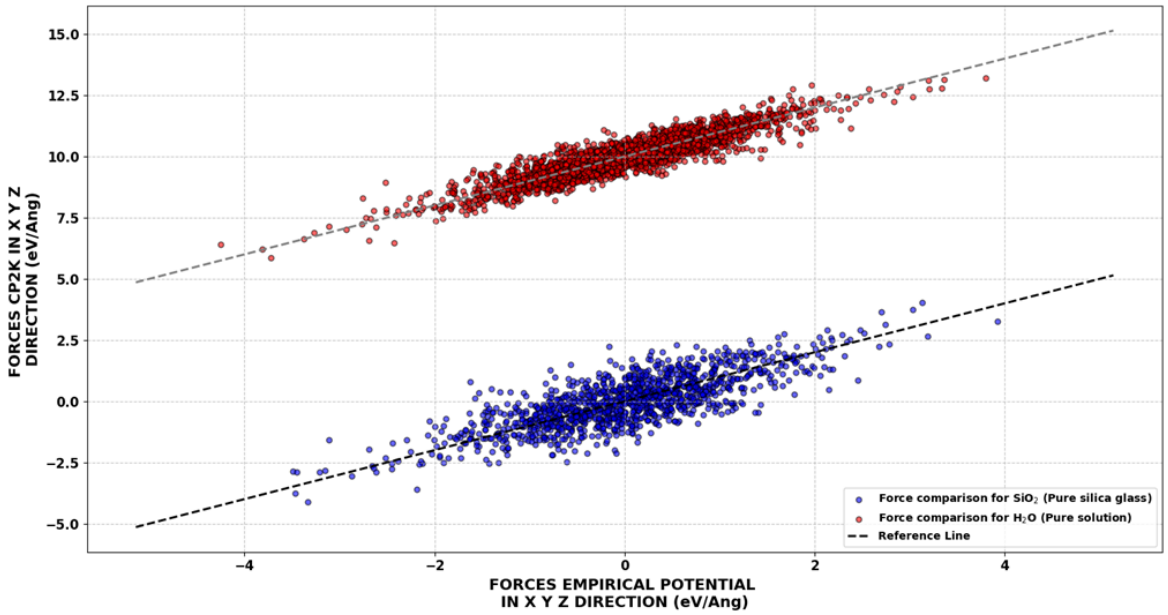

Figure 4.2: *The graph shows the x, y, and z components of the force, as calculated from empirical force fields, plotted against the corresponding components of the forces obtained from CP2K. The black dashed lines on the graph represent perfect correlation between the two sets of force components. The forces for silicon (Si) and oxygen (O) are shown in blue, while the forces for hydrogen (H) and oxygen (O) in water molecules are displayed separately. To make the water forces more distinguishable, they have been shifted upward by 10 eV/Å for clarity.*

originally parameterized and fitted for water, with its application to silica representing an extension of the model.

The analysis (Figure 4.2 and Figure 4.3) serves as a critical visual aid, highlighting both the strengths of the potential in replicating DFT forces and the differences in performance between water and silica, thereby providing a clear basis for interpreting the findings.

4.3.2 Empirical potential for Boron: pair interactions

This section describes the process of building, fitting, and validating this two-body potential (Equations 4.1–4.8), laying the groundwork for later improvements. The work focused on the B–O, B–H, and B–B interaction pairs while maintaining pre-existing water parameters to preserve consistency with validated models of H_2O behavior.

The potential form included the Coulombic, repulsive, and dispersive contributions described in Equations 4.1–4.8. A fixed charge q_i and a diffuse charge $q_{d,i}$ mentioned in Equations 4.1–4.5 were applied following the DCRP approach, with boron's charge estimated based on the known oxygen charge. During the force matching procedure, the fixed and diffuse charges remained constant. The oxygen

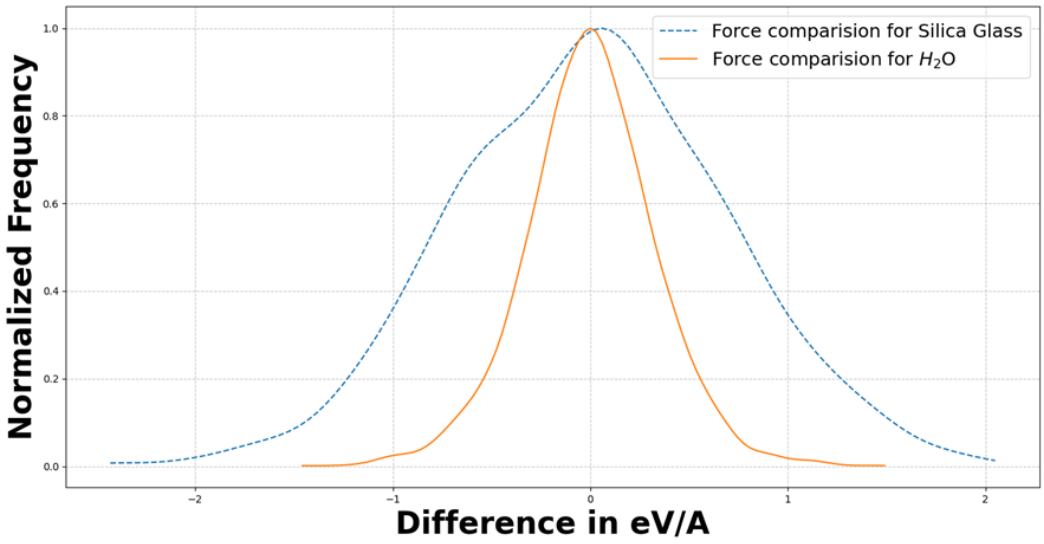

Figure 4.3: *The accuracy of the DCRP potential in reproducing forces is evaluated by comparing it to the forces calculated using Density Functional Theory (DFT). This precision is determined by calculating the difference between the forces obtained from the empirical DCRP potential and those from DFT, where the DFT forces are subtracted from the empirical potential*

charge is $q_O = -0.904$, while the other fixed charges are determined based on their ionic valence.

This approach involved generating atomic configurations representative of boron's behavior in aqueous systems and calculating the corresponding single-point DFT-based forces. These were then used to fit the parameters of the two-body potential as mentioned in section 4.2.1.

Parameters optimized included the repulsive term (A^{ij}_{rep}), the exponential decay distance (ε^r_{ij}), and the dispersion coefficients (C^6_{ij} and D^8_{ij}). These parameters were adjusted for B–O, B–H, and B–B interactions, enabling more flexible fitting.

Figure 4.4 shows a comparison of forces between empirical potentials and DFT. The forces for boron are more dispersed from the ideal forces compared to the reference (liquid water). Figure 4.5 shows that the forces of oxygen and hydrogen atoms are better reproduced than those of boron, indicating good transferability for the terms relating to hydrogen and oxygen. The comparison revealed that the model achieved an accuracy range of approximately -4 to +4 eV/Å, indicating that the predicted forces closely match DFT results within this margin, which is sufficient for many simulation purposes, as shown in Figure 4.6.

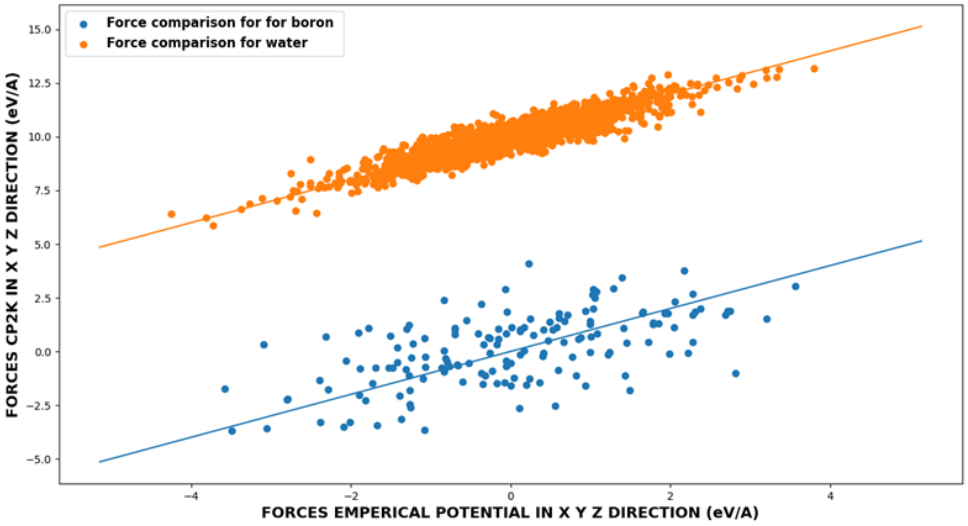

Figure 4.4: *The graph shows the x, y, and z components of the force, as calculated from empirical force fields, plotted against the corresponding x, y, and z components of the forces obtained from CP2K. The diagonal lines on the graph represent correlation between the two sets of force components. The forces comparison for Boron in the system is represented in blue while the reference forces for water (in orange) has been shifted upward by 10 eV/Å for clarity.*

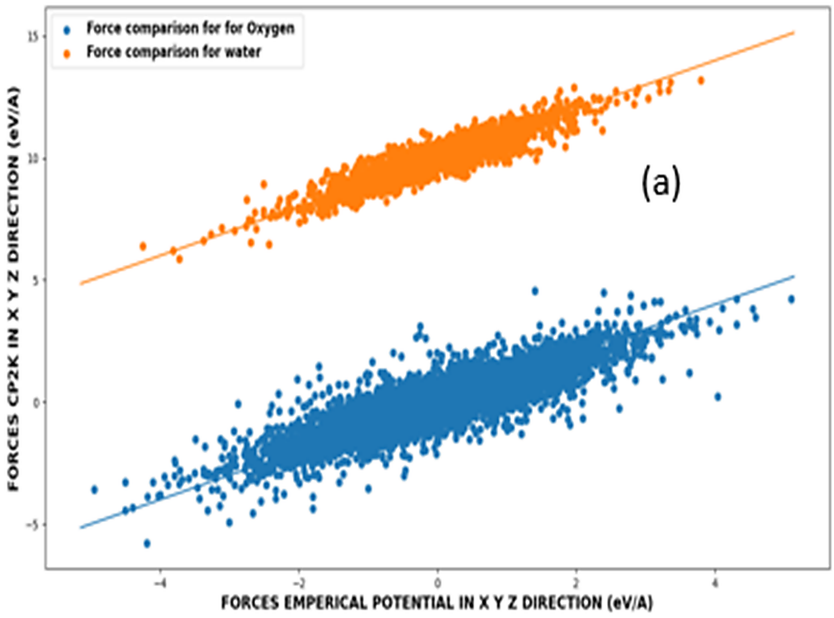

(a) *Force comparison for oxygen.*

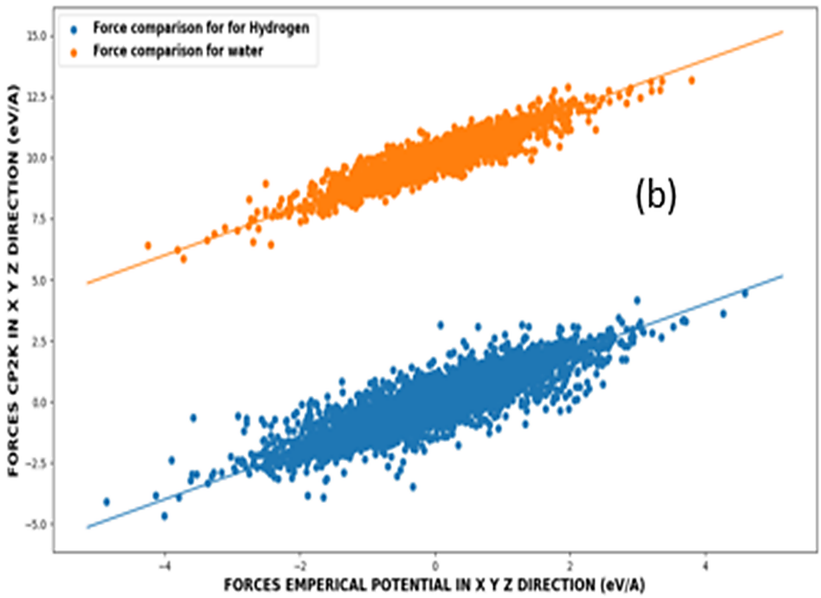

(b) *Force comparison for hydrogen.*

Figure 4.5: *The graph shows the x, y, and z components of the force, as calculated from empirical force fields, plotted against the corresponding x, y, and z components of the forces obtained from CP2K. The reference forces for water (in orange) have been shifted upward by 10 eV/Å for clarity.*

On Figure 4.6, the precision shows divergence from the forces reproduced for silica (-2 to +2 eV/Å) and water (-1 to +1 eV/Å). This can occur from the choice of keeping the parameters of oxygen and hydrogen constant in the boron-infused solution. Also, in the current simulation, we don't modify the charge of boron.

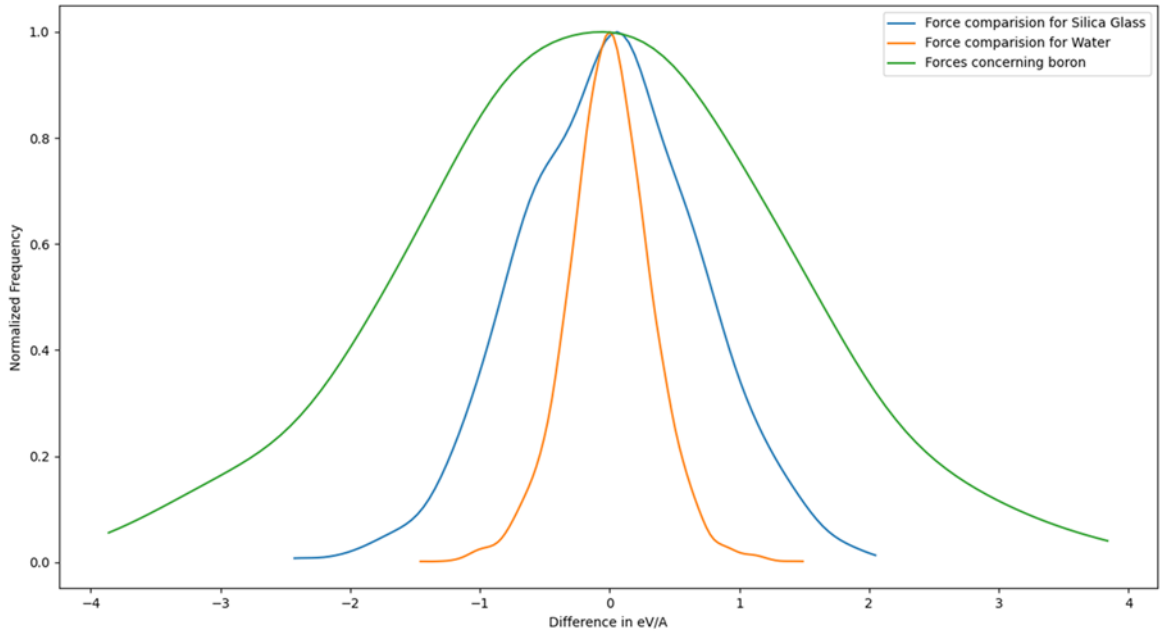

Figure 4.6: *Precision in which the DCRP potential can reproduce the forces for the new parameters concerning Boron in comparison to DFT forces.*

The potential energy for the pair interactions is a central element of this study, visually represented in Figure 4.7. It illustrates how energy varies with interatomic distance for the B-O, B-H, and B-B pairs. The energy profile shows a sharp increase at short distances due to the repulsive component, transitioning to a region of attraction at intermediate distances, and eventually decaying to zero at long ranges.

After minimization, the B–O first neighbor distances were about 1.38 Å, consistent with experimental values. B–H and B-B interactions do not have a minimum because both are cations. The final values of the parameters are mentioned in Table 4.3. The potential energy curves for the potentials are shown in Figure 4.7.

However, due to the lack of angular terms, the model was unable to enforce realistic bond angles. The average B–O–H angle in boric acid complexes deviated substantially from DFT predictions, reaching ~165°, in contrast to the expected ~110° planar geometry.

Fixed-charge models inherently restrict the adaptability of electrostatic interactions. In the DCRP approach, while diffuse charges help dampen the extremes of ionic charge interactions, they cannot capture real-time charge polarization or local

Table 4.3: *New parameterized term for pair term relating to Boron*

Parameter	B–O	B–H	B–B
A_{ij}^{rep} (eV)	0.73501	357.54	18.387
ε_{ij}^{r}	0.00015385	0.61923	0.99657
C_{ij}^{6} (eV/Å^6)	31.742	326.09	0.065946
D_{ij}^{8} (eV/Å^8)	42.782	93.790	1933.5

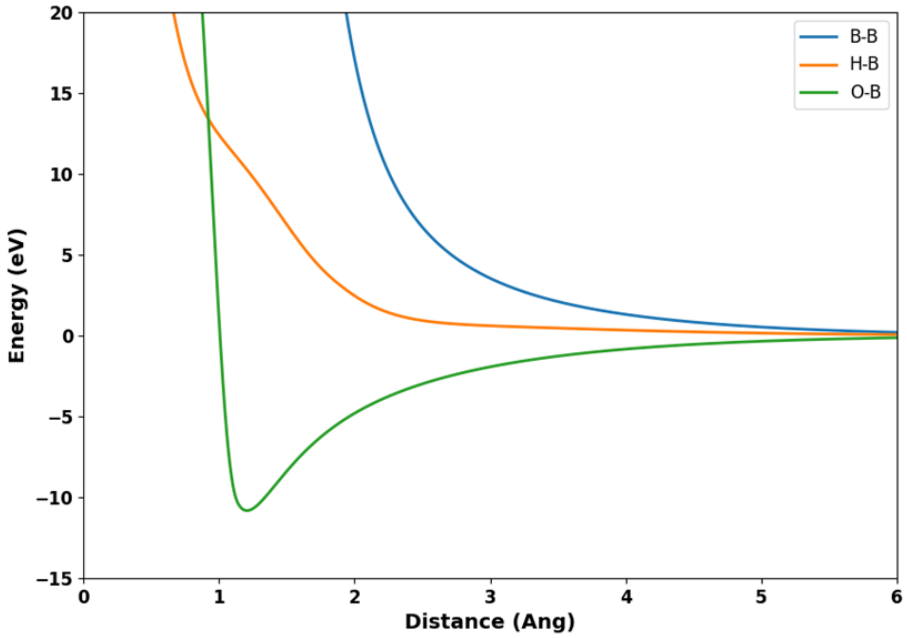

Figure 4.7: *Potential energy for B-O, B-H and B-B terms*

changes in electronic density. As such, while this model offers efficiency, it cannot capture the subtle polarization effects that may impact solvation energy, hydrogen bonding, or charge transfer behavior.

Notably, cohesive energy calculations were not reliable with this potential. The literature indicates a delicate interplay of donor and acceptor interactions in $B(OH)_3$ hydration, and fixed-charge models struggle to distinguish these subtle configurations. Consequently, cohesive energies derived from the two-body potential deviate significantly from reference values and are not discussed in depth. For future references this potential will be termed as Potential 1.

4.3.3 Empirical potential for Boron: three body interactions

To accurately capture boron's complex coordination chemistry (As described in Chapter 1) and angular interactions in aqueous environments, the empirical potential was

extended to include a three-body term described in equation 4.9, supplementing the previously fitted two-body potential. This modification was motivated by observations that the two-body- model only, although competent at reproducing pairwise interactions, failed to reproduce angular geometries with sufficient fidelity—particularly for the B–O–H angle which is crucial for modeling boron local environment in solution. The first choice was to begin with a two-body potential (the process is described in section)—excluding angular or three-body interactions in order to define the molecular interaction with minimum structural constraint. Then we add three-body term while keeping the parameters for two-body terms as a starting point and fitting the two body and three body parameters together.

The optimized parameters (after force matching) for the B–O–H three-body term were: $\lambda = 27.956$, $\theta^0 = 114°$, and a cutoff radius spanning approximately 1.05 Å to 2.98 Å between the relevant atomic pairs. These values correspond closely to the ideal geometry of boron in aqueous solution.

The inclusion of this angular term led to noticeable improvements in both local geometry and the accuracy of reproduced atomic forces. As shown in Figure 4.8 and Figure 4.9, the predicted force components from the modified potential correlated more strongly with DFT-derived forces for boron atoms, with deviations reduced from ±4 eV/Å in the two-body-only case to ±2 eV/Å.

Figure 4.10 shows the potential energy curves, the nature of forces is similar to that of the potential energy terms without the three body terms.

Furthermore, inclusion of the three-body term resulted in more physically realistic bond angle distributions (mentioned in section 4.3.4, Figure 4.11). The B–O–H angle distributions shifted from an unphysical average of ~165° in the two-body model to ~120°, closely matching experimental and DFT values (~114–118°). Table 4.4 and Table 4.5 shows the refined parameters with addition of three body terms.

Table 4.4: *New parameterized terms for pair term relating to Boron (when the three-body term is added)*

Parameter	B–O	B–H	B–B
A_{ij}^{rep} (eV)	571.63	152.95	20.351
ε_{ij}^{r}	0.00087691	0.61516	0.81820
C_{ij}^{6} (eV/Å^6)	38.486	130.80	1.4678
D_{ij}^{8} (eV/Å^8)	55.088	10.867	1934.4

While the three-body-enhanced potential shows substantial improvements, it introduces minor over-stabilization of certain transient species such as H_3O^+ and $[BO_3H]^{2-}$. This may be an artifact of the potential and also the rigidity of the O–H term around

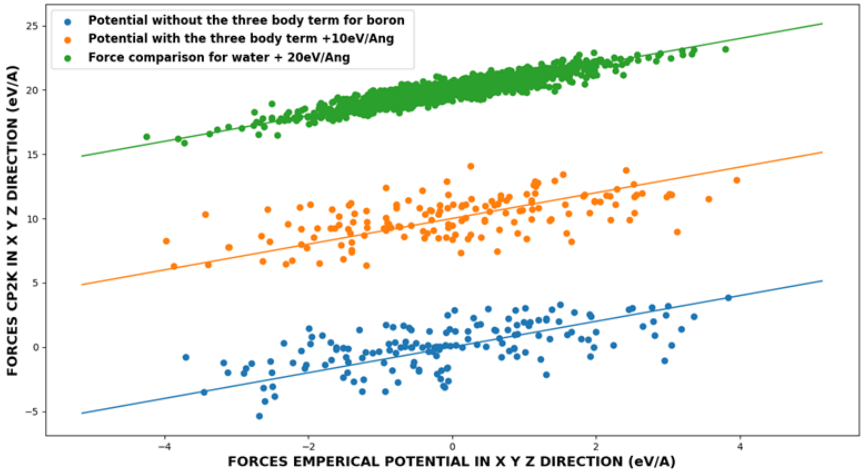

Figure 4.8: *The graph shows the x, y, and z components of the force, as calculated from empirical force fields, plotted against the corresponding x, y, and z components of the forces obtained from CP2K. The diagonal lines on the graph represent perfect correlation between the two sets of force components. The forces comparison for Boron in the system without the three-body term is represented in blue while the forces for boron with the three-body term are shown in orange, also the reference forces H_2O are displayed in green. To make the forces more distinguishable the forces have been shifted upward by 10 eV/Å and 20 eV/Å for clarity.*

Table 4.5: *Parameters concerning the three-body term for boron.*

Parameter	Value
λ (eV)	27.956
θ_{ijk} (deg)	104.0
γ (Å) (ij, ik when $j \neq k$)	1.0542, 2.9846
r_c (Å) (ij, ik when $j \neq k$)	2.9624, 2.4717

it. For future reference, this version of the potential will be referred to as Potential 2.

4.3.4 Local environment of Boron

To assess the effectiveness of the newly developed potential in reproducing the local coordination and bonding environment of boron, we carried out detailed analyses comparing simulations to DFT-derived reference data and literature benchmarks. This comparison focused on several structural descriptors: bond lengths, angles, radius of first and second hydration shells, species distributions, and energetic stability.

The simulation box was constructed to represent a system containing 50 $B(OH)_3$ molecules and 7,000 water (H_2O) molecules, resulting in a total of 21,350 atoms. The

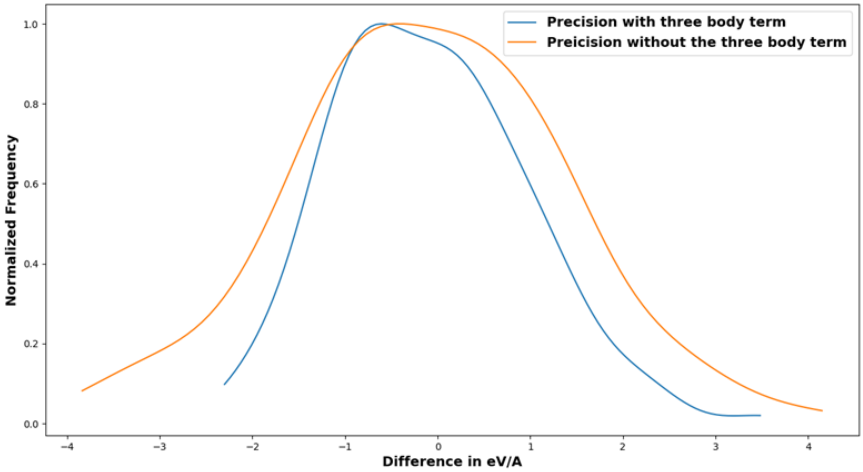

Figure 4.9: *Precision in which the DCRP potential can reproduce the forces for the new parameters concerning Boron in comparison to DFT forces.*

dimensions of the cubic simulation box were approximately 60 Å per side. This size was chosen to ensure that the system was large enough to capture intermolecular interactions accurately, while avoiding excessive computational cost.

To achieve a stable and physically realistic structure, the prepared simulation boxes underwent a series of relaxation steps under different conditions. For the boron-containing solution, the initial relaxation was performed at constant volume and temperature for 10^6 timesteps at 500 K. This high-temperature relaxation allowed for thermal adjustment at a fixed volume, enabling the system to overcome potential energy barriers and reach a more stable configuration. The timestep for all simulations was set to 0.1 fs to ensure numerical stability and accuracy in capturing fast molecular motions.

Following the NVT relaxation, the system was further relaxed under NPT conditions (constant number of particles, pressure, and temperature) for 50,000 timesteps at the same temperature of 500 K. The barostat allowed for volume fluctuations under constant pressure, facilitating equilibrium density adjustment. The initial density of the system was set at 1.1 g/cm^3, which stabilized at approximately 1.0 g/cm^3 post-relaxation. This density adjustment reflects the interplay of intermolecular forces, such as hydrogen bonding and van der Waals interactions, as well as the packing efficiency of the molecules within the box.

To ensure that the system reached a microcanonical equilibrium suitable for dynamic property assessment, an additional relaxation step was conducted in NVE conditions (constant number of particles, volume, and energy) for 100,000 timesteps at a reduced temperature of 300 K. NVE simulations conserve the total energy, pro-

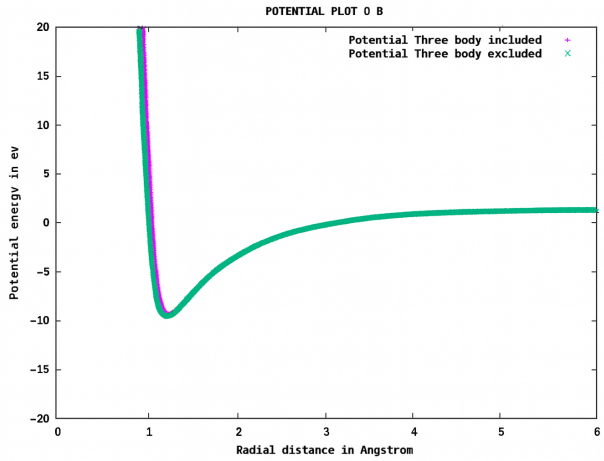

(a) *O–B potential*

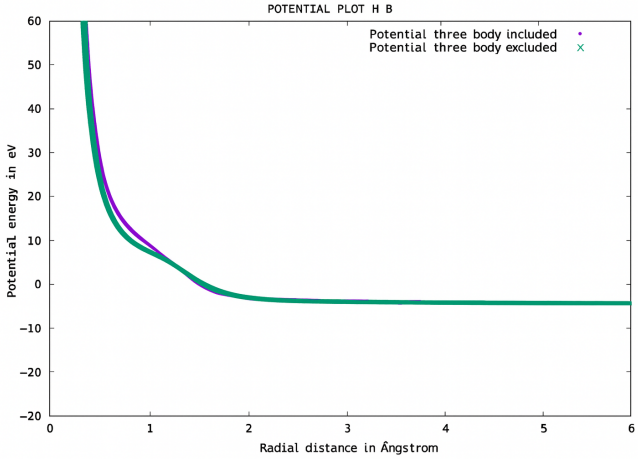

(b) *H–B potential*

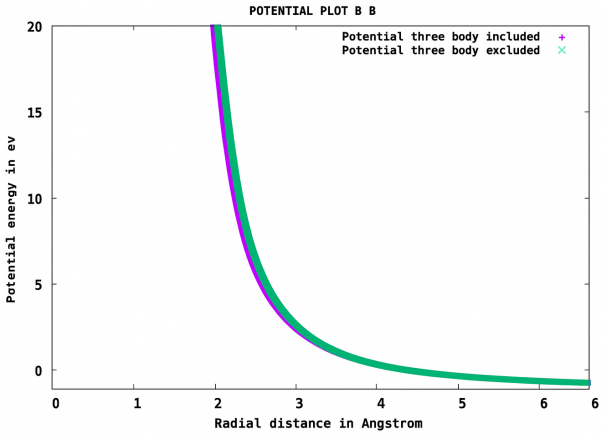

(c) *B–B potential*

Figure 4.10: *Comparison of the potential energy curves for the B–O, B–H, and B–B terms, with (purple) and without (green) three-body interactions.*

viding reliable trajectories to study time-dependent properties without external temperature or pressure controls.

A key benchmark was the reproduction of structural parameters (bond lengths and bond angles) for the solvated boric acid molecule ($B(OH)_3$). The reference DFT data lists B–O bond lengths of ~1.38 Å and O–H bond lengths of ~0.98 Å. Both the two-body and three-body fitted potentials accurately reproduced the B–O bond length, with the three-body potential yielding a slightly improved O–H bond length (~1.00 Å vs. 0.96 Å from the two-body-only case).

The B–O–H angle proved to be a critical differentiator. While the two-body potential resulted in an inflated average angle of ~165°, indicative of an overstretched geometry, the three-body term corrected this deviation, lowering the angle to ~120°, as shown in Table 4.7. This adjustment aligns closely with experimental and DFT values (~115°), validating the angular constraints introduced in Section 4.3.3.

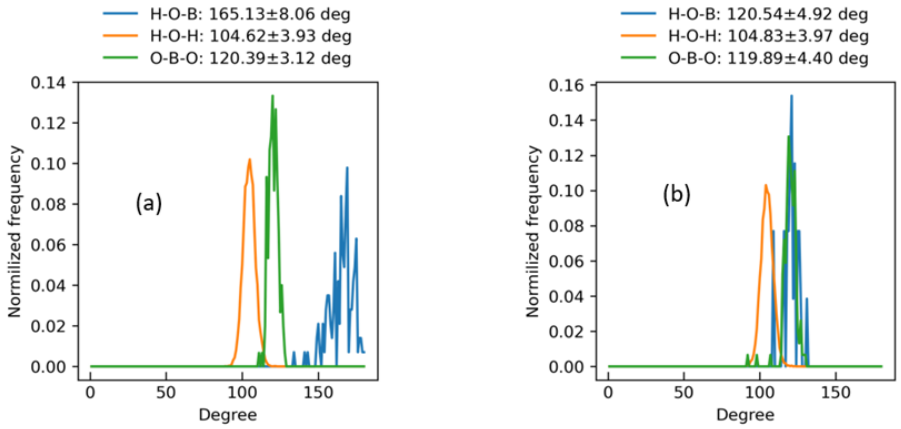

Figure 4.11: *Angle distribution of species as mentioned in (a) Potential without three body term and (b) Potential with the three-body term.*

Beyond isolated species, we examined the hydration shell and local speciation of boron in the aqueous simulation box. Figure 4.12 shows the radial distribution functions (RDFs) for the Potential 1, which revealed a clear first hydration shell around boron, with peak B–O distances near 1.4 Å, consistent with both experiment and DFT. The radial distribution of Potential 1 and Potential 2 were similar. The coordination number was computed to be approximately 3, confirming boron's tendency to form trigonal planar configurations which was true for both version of the potentials. Figure 4.13 represents the normalized intermolecular radial distribution function (between $B(OH)_3$ and H_2O molecules) to distinguish more clearly the peaks of the first and second hydration shells (calculated using potential 1). The Water molecule represents the first hydration shell peak at around 3.38 Å radius and the second hydration shell around 5.5 Å radial distance.

Species identification based on local bonding motifs (i.e., the number of hydro-

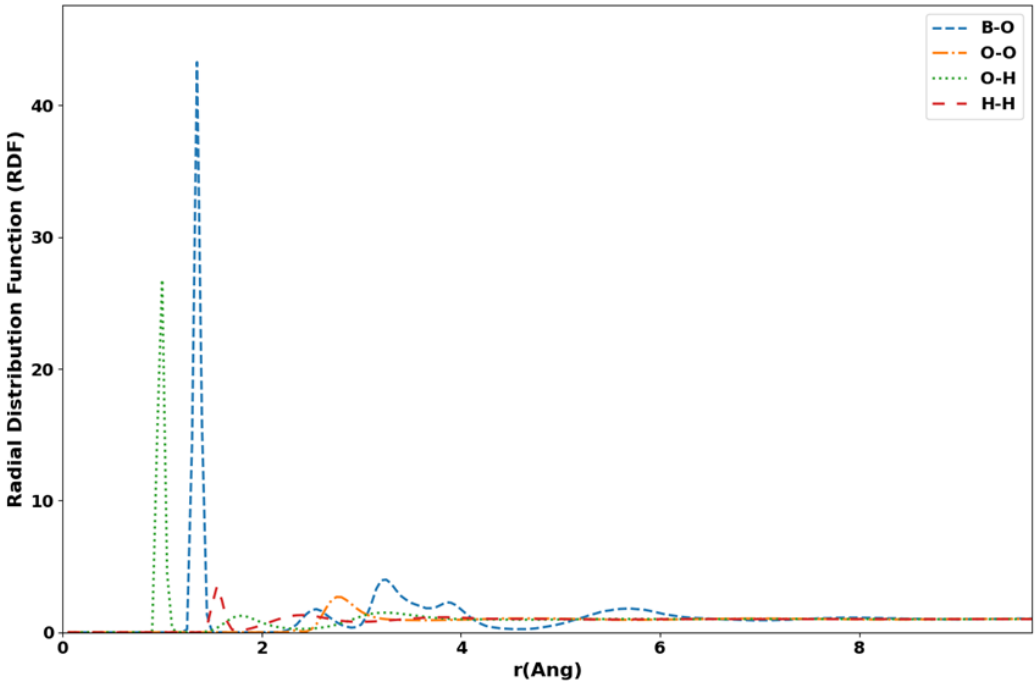

Figure 4.12: *Radial distribution functions (RDFs) for the B–O, O–H, O–O, and H–H atomic pairs obtained from molecular dynamics simulations*

gens and oxygens around the boron ions) provided deeper insights into solution chemistry. Using the three-body potential (*Potential 2*), under-coordinated anionic species such as $[BO_3H_2]^-$ and $[BO_3]^{3-}$ appeared frequently. In contrast, the potential without the three-body contribution produced more $B(OH)_3$ species as the dominant configuration, with only trace occurrences of anionic species and H_3O^+, aligning with experimental speciation in mildly acidic solutions. The speciation is shown in Table 4.6.

Table 4.6: *Boron speciation in structures prepared using two empirical potentials.*

Species	Potential 2	Potential 1
H_2O	6874	6979
H_3O^+	125	14
OH^-	0	7
$[BO_3H_3]$	0	43
$[BO_3H_2]^-$	2	7
$[BO_3H]^{2-}$	20	0
$[BO_3]^{3-}$	28	0

Energetic stability was assessed through cohesive energy and binding energy calculations. The binding energy of a $B(OH)_3$–H_2O complex was compared across methods.

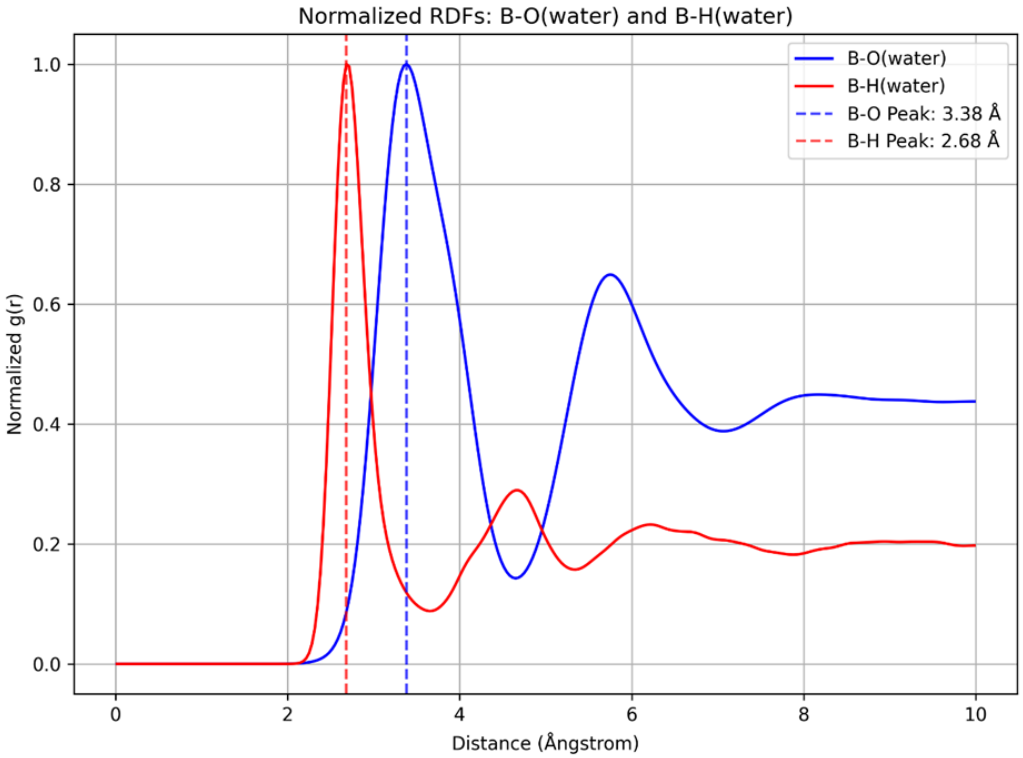

Figure 4.13: *Radial distribution function of Boron with respect to oxygen and hydrogen atoms of water. The first two peaks of the B-O radial distribution function represent the first and second hydration shells.*

DFT reports a cohesive energy of –2.5 kcal/mol, while the two-body potential showed significant disparities in calculating this value. Specifically, Potential 2 overestimated the cohesive energy at –15 kcal/mol. In a similar study, the calculated binding energies were in the –4.5 to –7.5 kcal/mol range, depending on conformation [176] (Table 4.6). These discrepancies in reproducing the cohesive energy can be attributed to the use of fixed charges in the empirical potential.

To assess the accuracy of the models, an additional comparison between the experimental structure factor and the results from Potential 1 and Potential 2 is provided in Appendix B.

4.4 Results: Diffusion coefficient calculation

4.4.1 Free solution diffusion coefficient of Boron

This section investigates the diffusive behavior of boron in bulk aqueous solutions, focusing on its transport properties as boric acid ($B(OH)_3$) at two distinct concentrations: 0.39 mol/L and 1.18 mol/L. Using molecular dynamics (MD) simulations with the DCRP potential (Potential 1), we quantify the diffusion coefficient of boron and compare it with that of water in both boron-infused and pure water systems,

Table 4.7: *Comparison of properties for boron compounds across different methods.*

Property	DFT data	Empirical (No 3-body)	Empirical (3-body)	Literature
Binding energy of $B(OH)_3$-H_2O	-2.5 kcal/mol	–	-15 kcal/mol	-4.5 kcal/mol, -7.5 kcal/mol
B-O (Å)	1.38	1.38	1.38	1.38
O-H (Å)	0.98	0.96	1.00	0.98
BOH angle (°)	110	160	120	115
OBO angle (°)	120	120	120	122

while also analyzing structural properties to elucidate the mechanisms governing boron's mobility. By examining concentration effects, residence times, and hydrogen-bond dynamics, we establish a comprehensive baseline for boron's behavior in bulk solution, which is critical for understanding its transport under confinement, as explored in subsequent sections. These findings address the first key research question:

What are the transport properties of boron in an unconfined aqueous solution? and provide insights into its role in glass alteration processes.

Simulation Setup and Methodology

To study boron's diffusion, two simulation systems were constructed to represent boric acid solutions at 0.39 mol/L and 1.18 mol/L. The 0.39 mol/L system consisted of 50 $B(OH)_3$ molecules and 7000 water (H_2O) molecules, totaling 21,350 atoms, within a cubic simulation box of 60 Å $\times$ 60 Å $\times$ 60 Å (see Figure 4.14). The 1.18 mol/L system contained 150 $B(OH)_3$ molecules and 6900 water molecules, yielding 21,450 atoms in a similarly sized box, ensuring comparable atom counts and a density of approximately 1.0 g/cm^3. A pure water system, comprising 8000 water molecules (24,000 atoms) in a 62 Å$\times$$62$ Å$\times$$62$ Å box, served as a reference to maintain consistent density and provide a baseline for water's diffusive behavior. Initial configurations were generated by randomly placing molecules, enforcing a minimum interatomic distance of 1.9 Å to prevent unphysical overlaps. The DCRP potential, meticulously parameterized for boron, oxygen, and hydrogen interactions, was employed to model interatomic forces, accurately capturing Coulombic, repulsive, and dispersive contributions.

System equilibration followed a rigorous three-stage protocol to ensure thermodynamic stability. First, each system underwent a 1,000,000-timestep (100 ps, with a 0.1 fs timestep) simulation in NVT condition (constant number of particles, volume, and temperature) at 500 K, facilitating thermal equilibration and allowing molecules to overcome local energy barriers. Next, a 50,000-timestep (5 ps) NPT (constant

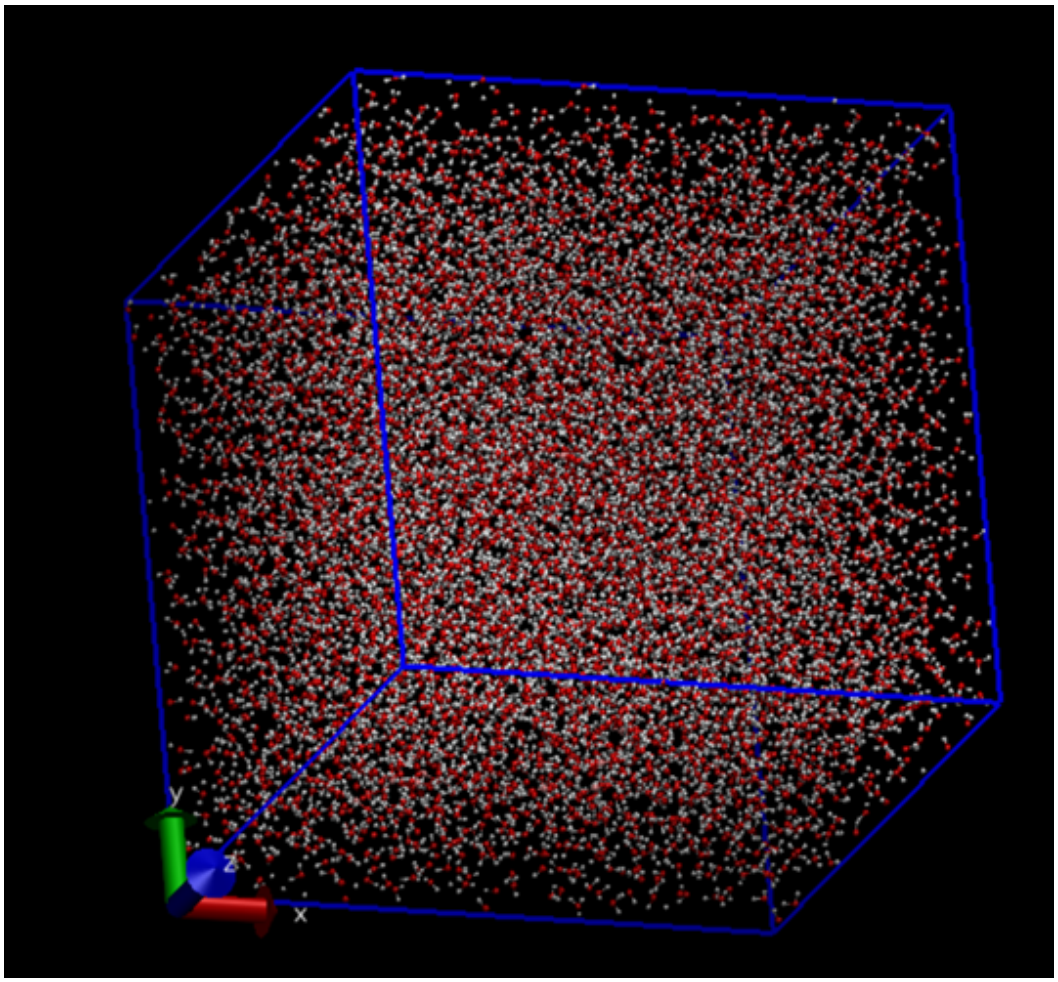

Figure 4.14: *Simulation box of size 60 Å × 60 Å × 60 Å representing boron in solution.*

number of particles, pressure, and temperature) simulation at 500 K and 1 bar enabled volume adjustments, stabilizing the density at ~1.0 g/cm^3. Finally, a 100,000-timestep (10 ps) NVE ensemble (constant number of particles, volume, and energy) simulation at 300 K achieved microcanonical equilibrium, ensuring conserved total energy for reliable dynamic analysis. The Nosé-Hoover thermostat and barostat, with a damping time of 0.1 ps, maintained precise temperature and pressure control during NVT and NPT stages.

To calculate the diffusion coefficient of the boron-containing solution, an additional simulation was performed in the NVT ensemble for 1,000,000 timesteps (equivalent to 100 ps, given the 0.1 fs timestep). This extended simulation provided sufficient statistical sampling to determine the self-diffusion coefficients of both water and boron molecules accurately. The diffusion coefficient is a critical parameter that quantifies the mobility of particles in the solution and is calculated from the mean-squared displacement (MSD) of the molecules over time, using the Einstein relation:

$$D = \lim_{t\to\infty} \frac{1}{6t} \left\langle |\mathbf{r}(t) - \mathbf{r}(0)|^2 \right\rangle \tag{4.12}$$

where D is the diffusion coefficient, r(t) and r(0) are the positions of a molecule at time t and time zero, respectively, and the angle brackets denote an ensemble average.

Residence times, which quantify how long water molecules persist in the solvation shells of boron or other water molecules, were calculated using the time correlation function $C_R(t)$.

$$C_R(t) = \frac{\langle h(0)h(t)\rangle}{\langle h(0)h(0)\rangle} \tag{4.13}$$

Here, $h(t)$ is defined as a binary function that equals 1 if a water molecule is within the first solvation shell (determined by the first RDF minimum, typically ~3.5 Å for O(water)–O(water) and ~3.38 Å for B–O(water)) at time t, and 0 otherwise. The residence time τ was then obtained by fitting $C_R(t)$ to a stretched exponential function,

$$C_R(t) \approx e^{-\left(\frac{t}{\tau}\right)^{\beta}} \tag{4.14}$$

where β is the stretching exponent. This metric provides insight into the stability of hydrogen-bonding interactions and their influence on diffusive dynamics. The formulation follows established approaches reported in the literature [177].

Structural properties were characterized using radial distribution functions (RDFs), g(r), which describe the probability of finding a pair of atoms at distance r, offering insights into solvation shells and hydrogen-bond networks. Coordination numbers were calculated by integrating the RDF up to the first minimum, reflecting the average number of neighbors in the first solvation shell. These analyses, combined with MSD and residence time calculations, provide a comprehensive picture of boron's transport and structural behavior.

Diffusion Coefficients

The MSD plots for boron at both concentrations are presented in Figure 4.15. At 0.39 mol/L (Figure 4.15a), the MSD exhibits a linear increase over time, characteristic of Fickian diffusion [178], yielding a diffusion coefficient of 4×10^{-10} m^2/s. At 1.18 mol/L (Figure 4.15b), the MSD slope is shallower, indicating reduced mobility, with a diffusion coefficient of 1.68×10^{-10} m^2/s. The diffusion coefficient of boron in the literature is reported as 1.12×10^{-9} m^2/s [179]. Table 4.8 summarizes these results alongside water's diffusion coefficients. In the 0.39 mol/L solution, water's diffusion coefficient is 2.5×10^{-9} m^2/s, identical to that of pure water, which aligns closely with experimental values (2.3–2.5×10^{-9} m^2/s at 300 K) [180]. At 1.18 mol/L, water's diffusion coefficient decreases to 1.63×10^{-9} m^2/s, reflecting the impact of

higher boron concentration.

Table 4.8: *Diffusion coefficients of boron and hydrogen in boric acid solutions.*

Species	0.39 M Solution	1.18 M Solution
Boron diff. coeff. (m^2/s)	3.7×10^{-10}	1.68×10^{-10}
Hydrogen diff. coeff. (m^2/s)	2.5×10^{-9}	1.63×10^{-9}

Residence Times

Residence times, derived from the $C_R(t)$ correlation functions (equation 4.13) (Figure 4.16), are summarized in Table 4.9. In pure water, the O(water)–O(water) residence time is 1.44 ps with $\beta = 0.60$, indicating rapid water exchange within a heterogeneous hydrogen-bond network. In the 0.39 mol/L boric acid solution, this increases to 1.60 ps ($\beta = 0.59$), and at 1.18 mol/L it rises further to 2.10 ps ($\beta = 0.54$), suggesting slower but still heterogeneous water dynamics due to boron's presence. The B(boric acid)–O(water) residence time is significantly longer: 8.52 ps ($\beta = 0.42$) at 0.39 mol/L and 11.07 ps ($\beta = 0.39$) at 1.18 mol/L, reflecting stronger and more persistent interactions between boric acid and water molecules in the first hydration shell. The relatively low β values (< 1) in all cases indicate a distribution of residence times, where some water molecules exchange rapidly while others remain bound longer; in contrast, if $\beta = 1$, the decay would be purely exponential, corresponding to a single, well-defined residence time without such heterogeneity. Although there is no direct comparison between the residence time of boron and water, the water–water values may vary depending on the simulation methods employed [181], [182].

Table 4.9: *Summary of residence time values*

Property	O(w)–O(w)	B(BA)–O(w)
Res. time in water (ps)	1.44	–
Res. time in BA (0.39 M) (ps)	1.60	8.52
Res. time in BA (1.18 M) (ps)	2.10	11.07

4.4.2 Diffusion coefficient in silica nanopores

This study employs MD simulations to explore the transport behavior of boron within silica nanopores, comparing its diffusion characteristics to those in free aqueous solution. The investigation focuses on how nanoscale confinement influences boron's mobility, the structural modifications induced by nanopore interactions, and the implications for borosilicate glass alteration kinetics. Pores with diameters

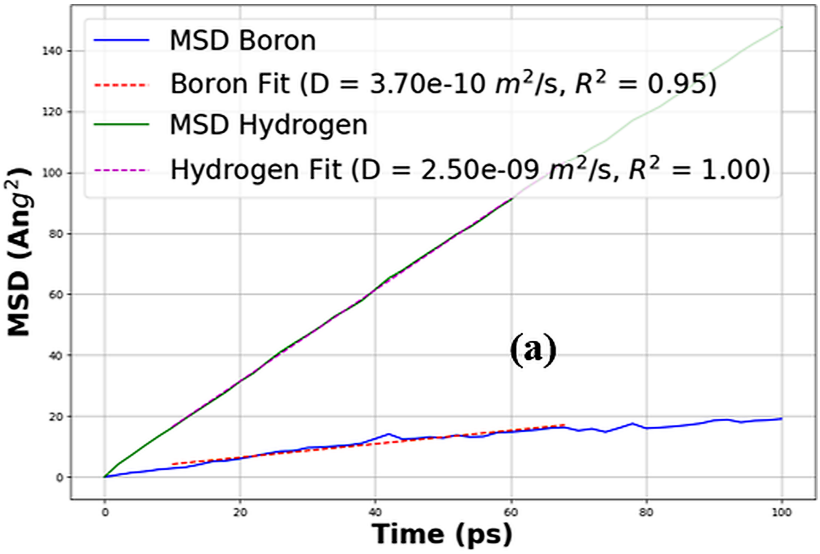

(a) *0.39 mol/L*

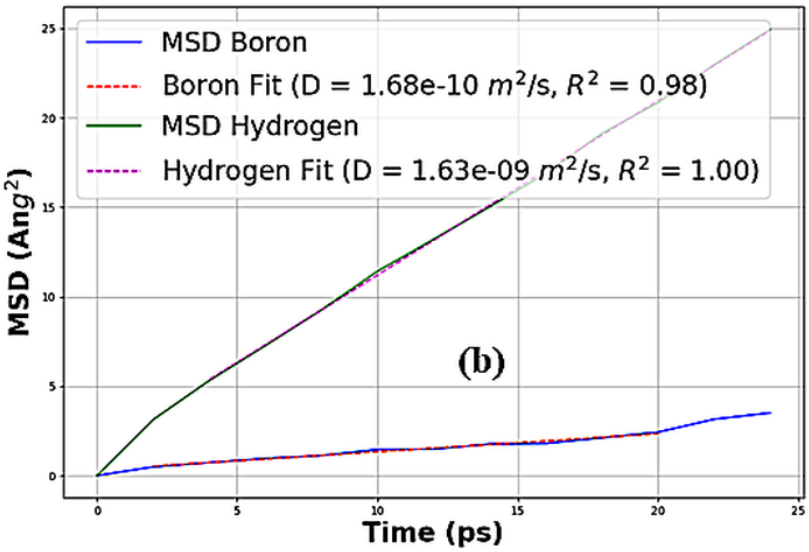

(b) *1.1 mol/L*

Figure 4.15: *Mean square displacement (MSD) of boron and hydrogen atoms in solution as a function of time, obtained from molecular dynamics simulations for two different concentrations: (a) 0.39 mol/L and (b) 1.1 mol/L. The linear increase in MSD with time indicates diffusive behavior, from which the self-diffusion coefficients of boron and hydrogen are estimated.*

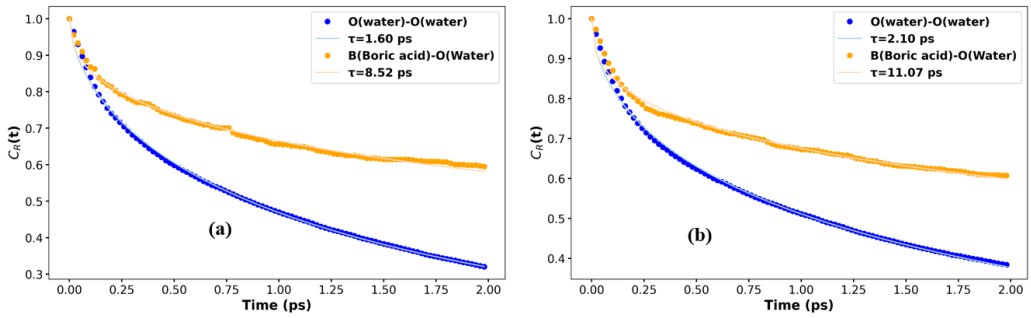

Figure 4.16: *CR(t) as a function of time for O(water)-O(water) and B(Boric acid)-O(water) pair for (a) 0.39 Mol/L (b) 1.18 Mol/L solution*

of 15 Å, 20 Å, and 26 Å were analyzed to assess the effects of pore size and density on diffusion coefficients. All simulations were carried out using **Potential 1**. The boron–silicon (B–Si) interaction was modeled using a purely Coulombic term within the DCRP framework, ensuring accurate electrostatic repulsion at the silica interface. The potential energy curve for the B–Si term is shown in Figure 4.17. These findings offer critical insights into boron's behavior in confined environments to replicate the transport property of the ion in an altered glass.

Preparation of Nanoconfined Structures

The construction of silica nanopore structures was carefully designed to replicate the nanoscale porosity characteristic of gel-like alteration layers in borosilicate glass.

The preparation of the nanoporous structure was done in three steps.

In the first step, the preparation of the silica glass was carried out in multiple stages. Initially, the system was equilibrated at 4000 K for $2{,}000{,}000$ time steps at constant volume and temperature. Next, a thermal quench was performed by reducing the temperature in 100 K increments until reaching 300 K, with equilibration at each step for $100{,}000$ time steps, still at constant volume. The equilibrium volume at 300 K was then established through a $200{,}000$-step NPT MD simulation at 1 bar. Finally, the system was relaxed for $100{,}000$ time steps in the NVE ensemble using the previously determined equilibrium state to yield the modeled glass structure. The initial size of the simulation box was approximately $60 \times 60 \times 100$ Å^3 with $25{,}800$ atoms; the final size of the box was close to that of the initial glass.

The cylindrical nanopores were created by removing atoms within specified radii along the z-axis, yielding cylindrical pores with diameters of 15 Å, 20 Å, and 26 Å. These pore sizes were selected to span a range from strong confinement, where the pore diameter is comparable to boron's hydration shell (~ 5–6 Å), to weaker confinement, where bulk-like behavior might emerge. After removing the atoms, the silica

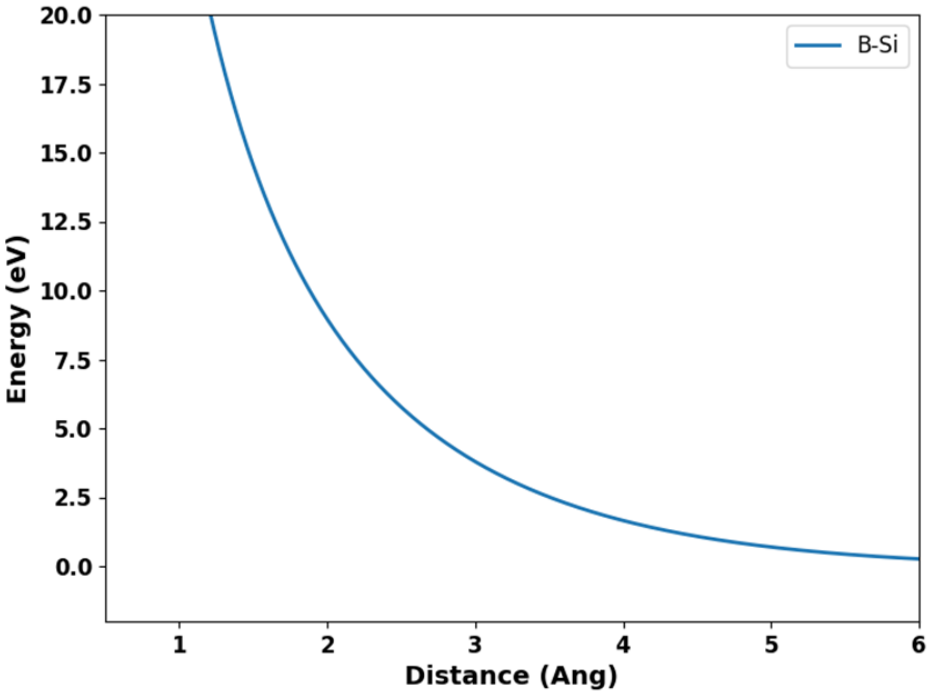

Figure 4.17: *Potential energy for B-Si pairs.*

slabs with pores were stabilized during NVT simulations at 500 K for $1{,}000{,}000$ steps and then again at 300 K for $100{,}000$ steps.

The second step was to prepare in parallel a solution containing 272 $B(OH)_3$ molecules and approximately $12{,}000$ water molecules with the same size of simulation box as that of the silica slab. The number of water molecules was fine-tuned for each pore size to maintain a consistent average density across systems, with slight adjustments to account for pore volume differences. Initial molecular configurations were generated by randomly placing $B(OH)_3$ and water molecules within the pore, enforcing a minimum interatomic distance of 1.9 Å to prevent steric overlaps.

The third step is accompanied by filling nanopores inside the silica slab by merging the solution inside the nanopores. Initially, the distance between the interface and solution is kept to be 2 Å to avoid unphysically high forces near the interface, the visual representation of the preparation of nanopores is depicted in Figure 4.18. We started with an initial higher density to avoid voids near the center of the pores. It is a commonly accepted fact that the density of water is higher near the interface. Achieving a stable and physically realistic density distribution posed a significant challenge due to the non-uniform density profile within the pores which is also observed in the literature [183], [184], [185], [186], [187], [188], [189]. Density was found to be elevated near the silica interface, typically 20–30% higher than at the pore cen-

ter, due to strong interactions between water molecules and surface silanol groups. This interfacial layering, observed in radial density profiles, led to a risk of voids forming near the pore center if the system was initialized with a uniform density of 1.0 g/cm^3. To address this, the initial density was set to an elevated value which stabilized the pore structure by preventing central voids during equilibration. This approach ensured a uniform distribution of molecules across the pore while accommodating the naturally higher density at the interface. This approach is similar to the works of Zhang *et al* [190].

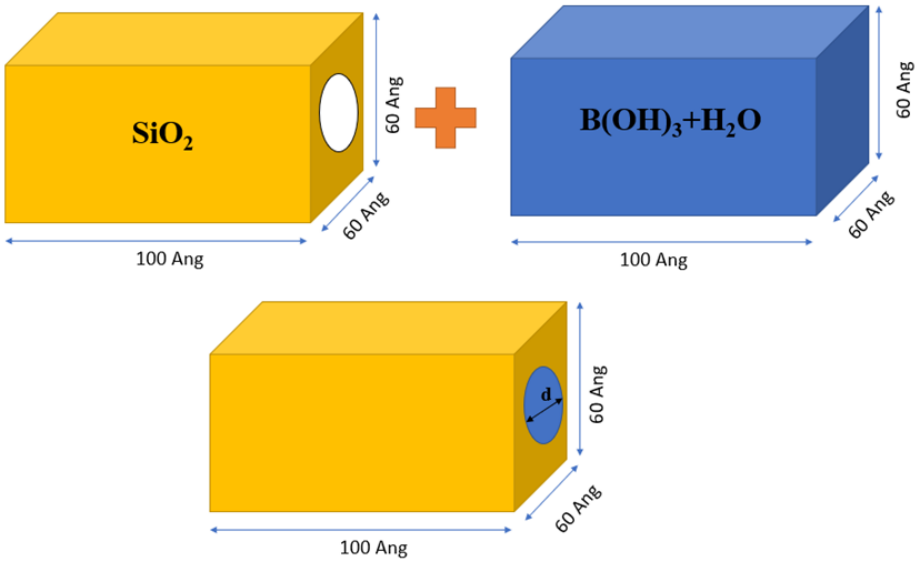

Figure 4.18: *Process of Nanoporous silica preparation*

The system is stabilized using NVT ensemble at 500K for 1,000,000 steps and then under NVT condition again for 300K for 100,000 steps. For calculation of diffusion coefficient, the procedure was same as employed in 4.4.1.

Density Profiles and Spatial Heterogeneity

As mentioned in previous section, radial density profiles, shown in Figure 4.19a, reveal the non-uniform density distribution within the pores. Water density is elevated by 20–30% near the silica interface due to strong hydrogen-bonding interactions with silanol groups, forming a layered structure that extends several angstroms into the pore. In contrast, the density near the pore center is lower, resembling bulk-like water. To prevent voids in the central region, which could destabilize the system, the initial density was set to ~1.3 g/cm^3. Boron atoms preferentially reside near the pore center, avoiding the densely packed interfacial layers, while the hydrogen is attracted towards the interface.

Figure 4.19b illustrates the spatial variation in diffusion coefficients, with the highest mobility at the pore center and a sharp decline near the walls, where water

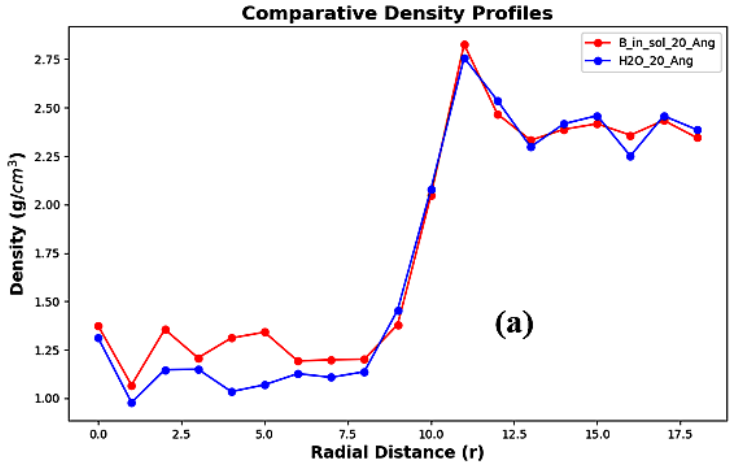

(a) *Density profiles of water confined in 20 Å.*

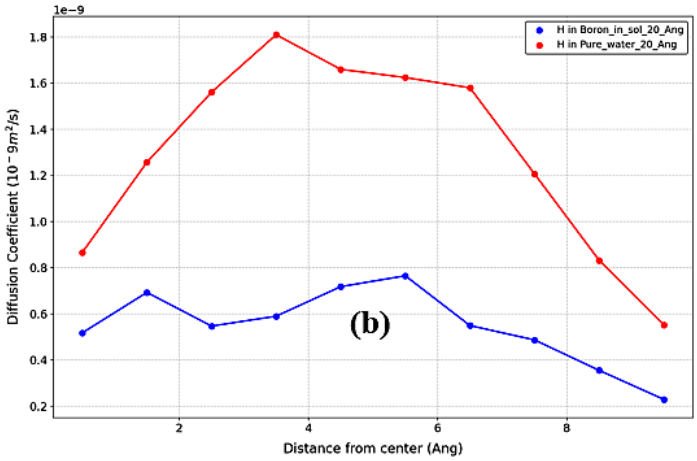

(b) *Diffusion coefficient as a function of distance from the center.*

Figure 4.19: *(a) Density profiles of confined water. (b) Diffusion coefficient as a function of distance from the center.*

is more ordered. Literature, including work by Mahadevan and Garofalini [42], confirms that confined fluids exhibit spatially dependent dynamics due to surface-induced structuring and geometric constraints [42], [130].

Boron Diffusion in Nanopores

Figure 4.20 shows the mean square displacement (MSD) of boron atoms for the three pore sizes considered. In the 15 Å pore, the MSD curve is nearly flat and may indicate strongly constrained motion dominated by frequent interactions with the pore surface. A diffusion coefficient of $1.94 \times 10^{-11}\,\mathrm{m^2\,s^{-1}}$ was estimated from the MSD slope; however, this value should be interpreted with caution. Because the MSD may not reach a clear long-time linear (Fickian) regime within the simulated

timescale, the extracted diffusion coefficient might overestimate the effective long-range translational mobility and instead reflect short-time, localized motion under confinement.

Similar limitations may apply to the 20 Å and 26 Å pores, for which diffusion coefficients of $1.73 \times 10^{-11}\,\mathrm{m^2\,s^{-1}}$ and $2.62 \times 10^{-11}\,\mathrm{m^2\,s^{-1}}$, respectively, were obtained. Although the increase in MSD slope with pore size suggests a progressive relaxation of confinement effects, the boron dynamics may remain partially non-Fickian, even in the largest pore. Consequently, these diffusion coefficients should be regarded as approximate or upper-bound estimates of boron mobility rather than as definitive measures of long-range diffusion.

Overall, the MSD results suggest a qualitative pore-size dependence, with smaller pores imposing stronger constraints on boron motion through steric hindrance and surface interactions. Quantitatively, however, the analysis highlights that diffusion coefficients derived from non-Fickian or short-time MSD behavior may not directly represent macroscopic transport.

The suppression of boron's diffusion is closely tied to the size of its hydration shell. In free solution, radial distribution functions (RDFs) reveal a first hydration shell at 3.38 Å and a second at 5.5 Å (Figure 4.13). In the 15 Å pore, the pore diameter is only slightly larger than the combined extent of these shells (~9 Å), causing significant strain to the hydration structure. This perturbation disrupts the hydrogen-bond network, elevating energetic barriers to diffusion. In larger pores (20 Å and 26 Å), the hydration shell experiences less disruption, allowing boron to regain some mobility, though still constrained compared to bulk conditions. Literature [42], [130] supports this, noting that confinement effects dominate when pore sizes approach molecular dimensions, amplifying viscous drag and surface interactions.

Water Diffusion in Nanopores

Figure 4.21 shows the mean square displacement (MSD) of hydrogen atoms, representing water dynamics, in the nanopore systems containing boron-infused solution. Water's diffusion coefficient also decreases under confinement, though less severely than that of boron. Figure 4.22 presents a comparison between the diffusion coefficients of water in pure water and in boron-containing solution. In the 15 Å pore, water's diffusion coefficient is $2.34 \times 10^{-10}\,\mathrm{m^2/s}$, compared to $6.98 \times 10^{-10}\,\mathrm{m^2/s}$ for pure water under similar confinement. In the 20 Å pore, the value increases to $4.94 \times 10^{-10}\,\mathrm{m^2/s}$, and in the 26 Å pore, it reaches $7.11 \times 10^{-10}\,\mathrm{m^2/s}$. These values remain substantially lower than the bulk water diffusion coefficient of $2.5 \times 10^{-9}\,\mathrm{m^2/s}$, confirming the effect of confinement. However, water's smaller molecular size and simpler hydrogen-bonding network allow greater adaptability compared to boron.

The relative resilience of water's mobility is evident in the diffusion coefficient ra-

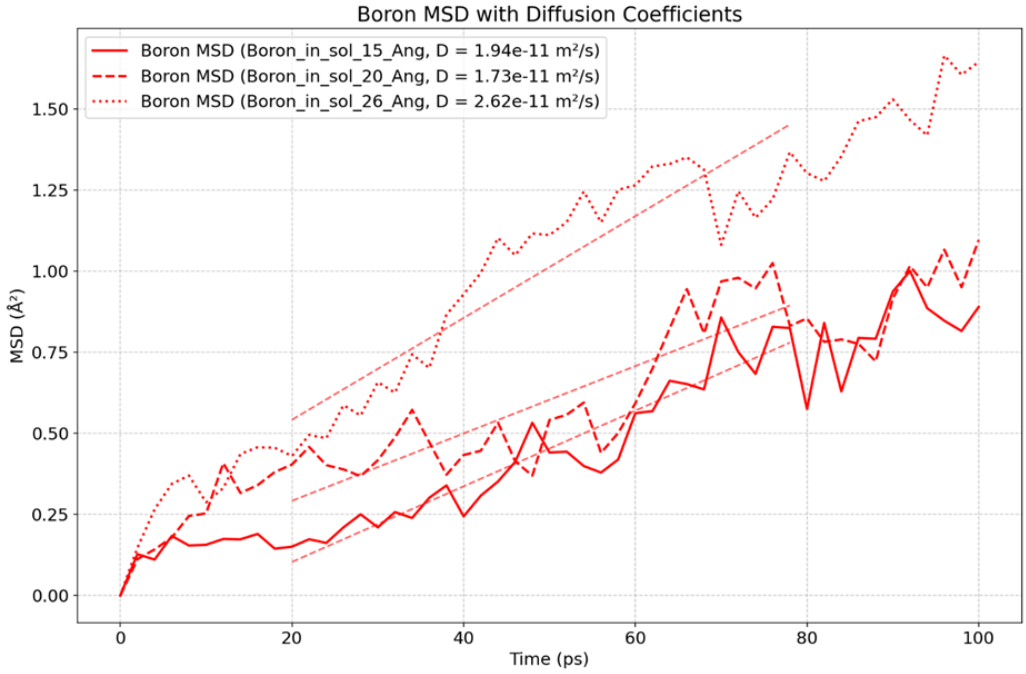

Figure 4.20: *Mean squared displacement (MSD) of boron atoms confined in pores of 15, 20, and 26 Å diameter.*

tios presented in Table 4.10. In the 15 Å pore, water's diffusion in the boron-infused solution is reduced by a factor of 2.98 compared to pure water, while boron's diffusion drops by a factor of approximately 20 relative to its free solution value. This disparity stems from boron's larger effective size, stronger hydrogen bonds, and greater sensitivity to hydration shell disruptions. A study by Risplendi *et al.* indicate that boric acid forms stronger hydrogen bonds with water than water does with itself, explaining boron's pronounced confinement effects [176].

Table 4.10: *Diffusion coefficients of H_2O and boron for various pore sizes.*

Pore size (Å)	**H_2O (pure)** (m^2/s)	**H_2O (B)** (m^2/s)	**D_{Boron}** (m^2/s)	**$D_{H2O}/D_{H2O(B)}$**	**D_B/D_{H2O}**
15	$6.98 \cdot 10^{-10}$	$2.34 \cdot 10^{-10}$	$1.94 \cdot 10^{-11}$	2.98	0.083
20	$1.21 \cdot 10^{-9}$	$4.94 \cdot 10^{-10}$	$1.73 \cdot 10^{-11}$	2.44	0.035
26	$1.69 \cdot 10^{-9}$	$7.11 \cdot 10^{-10}$	$2.62 \cdot 10^{-11}$	2.37	0.033

Effect of Pore Size and Density

The 26 Å pore allows diffusion coefficients to approach bulk values, signaling a transition to weak confinement. In contrast, the 15 Å pore severely restricts motion, with boron's mobility nearly ceasing as the pore diameter approaches the hydration shell size. The elevated interfacial density exacerbates this effect in smaller pores by enhancing steric and viscous drag near the walls. The deliberate use of an initial density of 1.2-1.4 g/cm^3 ensured stability by filling potential voids, but the resulting

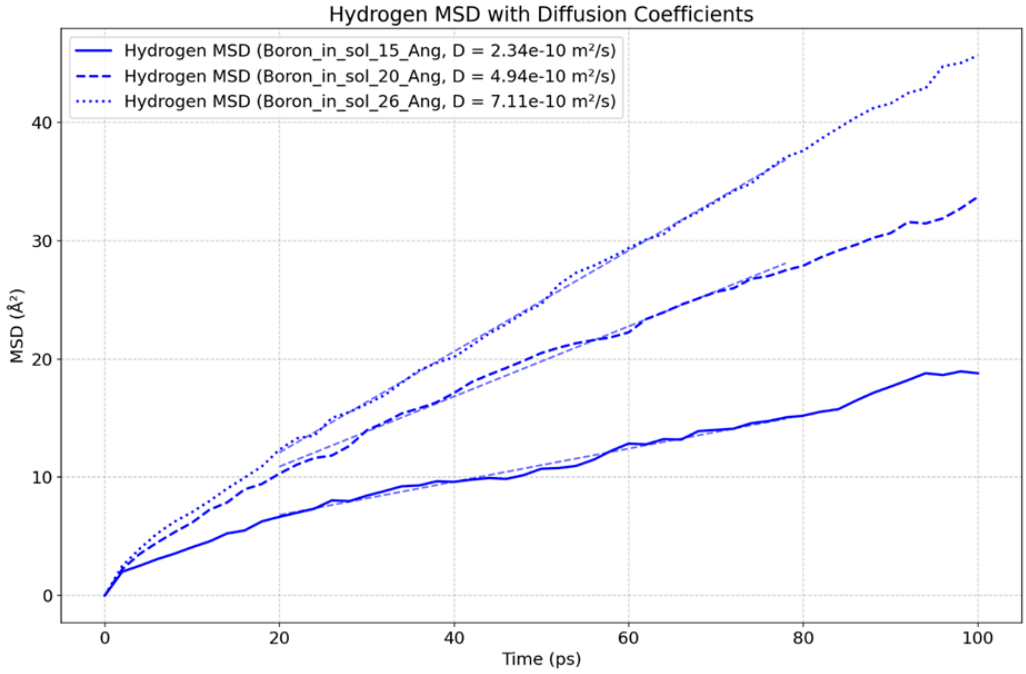

Figure 4.21: *MSD of Hydrogen in nanoconfined boron for pore sizes; 15, 20 and 26 Ang*

20–30% density increase near the interface amplified confinement effects, particularly in the 15 Å pore.

Although density played an important role in controlling the diffusion coefficient, the effect of confinement based on pore size remains the primary driver, with density playing a secondary role.

Comparison with bulk solution

In bulk solution, boron's diffusion coefficient of $0.4 \times 10^{-9}\,\mathrm{m}^2/\mathrm{s}$ reflects its ability to navigate a dynamic hydration shell, with the first and second shells located at 3.38 Å and 5.5 Å, respectively (Figure 4.13). These shells facilitate rapid water exchange and hydrogen-bond reorganization, supporting Fickian diffusion [178]. In contrast, confinement—particularly in the 15 Å pore—compresses the second hydration shell, forcing boron into a constrained coordination environment. This disruption, coupled with transient hydrogen bonds to silanol groups, accounts for the dramatic reduction in diffusion. In larger pores, the hydration shell partially recovers, allowing increased mobility, though still far below bulk values. Experimental studies of confined solutes report similar reductions in mobility when pore sizes approach molecular scales, validating these observations.

Implications for Glass Alteration

The suppression of boron diffusion in nanopores has profound implications for borosilicate glass alteration. In alteration gels, nanoscale porosity restricts the transport of mobile species like boron, leading to local accumulation and potential for-

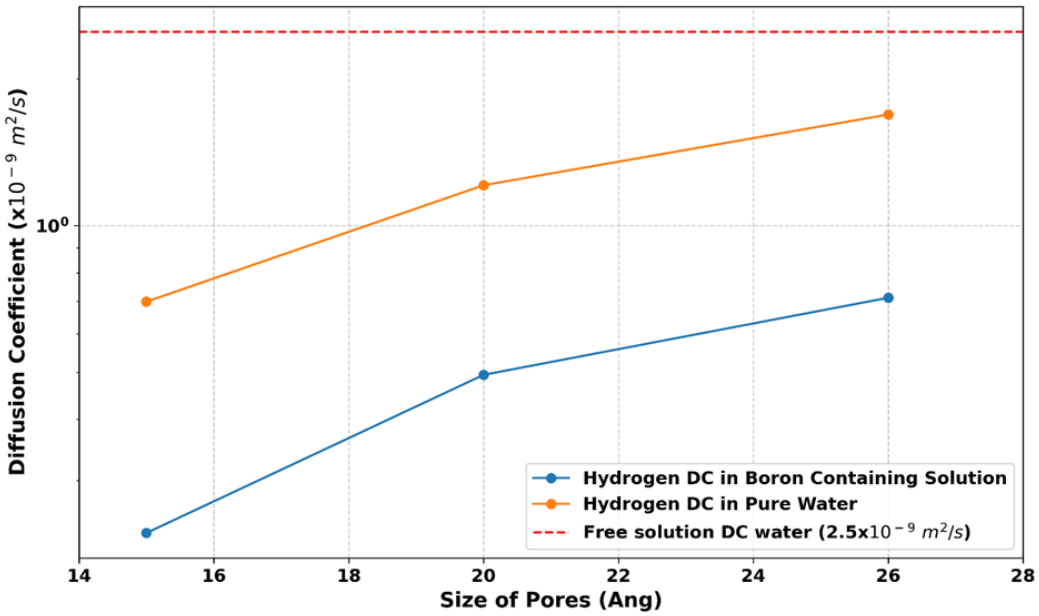

Figure 4.22: *Comparative diffusion coefficient of hydrogen for nanoconfined H2O (orange) and nanoconfined Boron solution*

mation of secondary phases, such as borosilicates. This process reduces effective porosity and permeability, creating a passivating layer that slows dissolution. The simulations suggest that pores smaller than 20 Å are particularly effective at immobilizing boron, supporting the protective gel hypothesis. Boron's greater sensitivity to confinement compared to water indicates it may act as a bottleneck in transport, amplifying its role in gel passivation.

Comparison with Experimental Data

While direct measurements of boron diffusion in silica nanopores are scarce, the simulated trends align with experimental data on related systems. Studies of water diffusion in mesoporous silica report significant suppression for pores below 30 Å, mirroring the current findings. The bulk water diffusion coefficient of $2.5{\times}10^{-9}\,\mathrm{m}^2/\mathrm{s}$ agrees with experimental values ($2.3 - 2.5 \times 10^{-9}\,\mathrm{m}^2/\mathrm{s}$), validating the simulation methodology. The qualitative consistency between simulated and experimental diffusion reductions with decreasing pore size reinforces the reliability of the DCRP potential and simulation protocols.

4.5 Discussion

The findings presented in Sections 4.3 and 4.4 allow us to address three questions concerning the transport properties of boron in aqueous and confined environments, and their relevance to glass alteration kinetics. This section synthesizes our simulation results with theoretical insights, comparisons to previous literature.

What are the transport properties of boron in free solution?

Mechanisms Governing B Diffusion

Boron's diffusion in dilute solution is substantially slower than water's. At 0.39 mol/L, boron diffuses at 3.7×10^{-10} m^2/s, nearly an order of magnitude below water's 2.5×10^{-9} m^2/s. This disparity arises from boron's larger effective size and stronger intermolecular interactions. As $B(OH)_3$, boron maintains a first hydration shell of ~ 3.38 Å and a second shell at ~ 5.5 Å, yielding a hydrodynamic radius greater than water's ~ 2.8 Å O–O distance. Its hydroxyl groups act as both hydrogen-bond donors and acceptors, producing more persistent interactions than water–water bonds and raising the energy barrier for translational motion.

Increasing concentration further hinders mobility. At 1.18 mol/L, boron's diffusion decreases by more than half (1.68×10^{-10} m^2/s), while water's mobility drops by ~35% to 1.63×10^{-9} m^2/s. These reductions reflect the formation of a denser hydrogen-bond network and increased molecular crowding, effects consistent with the broadening of the O–O RDF peak. Transient $B(OH)_3$–$B(OH)_3$ associations may also occur at higher concentrations, further restricting translational motion.

Residence Time Insights

Residence time analysis supports this picture. Water molecules in boron's hydration shell persist for 8.5–11 ps, significantly longer than the 1.4–2.1 ps exchange times in bulk water. The concentration-dependent increase (from 8.52 ps at 0.39 mol/L to 11.07 ps at 1.18 mol/L) highlights the stabilization of boron–water hydrogen bonds in crowded environments. These lifetimes, characterized by stretched exponential decays with $\beta < 1$, indicate heterogeneous dynamics where some water molecules exchange rapidly while others remain bound much longer. Such heterogeneity is consistent with observations in other hydrogen-bonded liquids [181], [182].

Structural Stability and Concentration Effects

Despite reduced mobility, the local structure of $B(OH)_3$ remains stable. The B–O bond length (1.38 Å) and coordination number (~3) are preserved across concentrations, in agreement with DFT and experimental data. This structural stability reinforces the idea that boron's reduced mobility is governed not by geometric distortion, but by its persistent hydration shell and the strengthening of intermolecular interactions at higher concentrations.

Comparison with Experimental Data

The simulated boron diffusivity at 0.39 mol/L (3.7×10^{-10} m^2/s) is lower than the experimental value of $\sim 1.1 \times 10^{-9}$ m^2/s [179], likely reflecting the limitations of the DCRP fixed-charge model in capturing charge redistribution. Water's simulated diffusion (2.5×10^{-9} m^2/s) matches experimental measurements at 300 K [180], validating the methodology. Although absolute values differ for boron, the concentration-dependent trends are consistent with the established link between solute concentra-

tion, solution viscosity, and mobility.

How do these properties change when boron is confined within silica nanopores?

Alterations in Diffusive Mobility

Confinement within silica nanopores severely restricts boron's diffusion, with pore size emerging as the dominant control. In the 15 Å pore, boron's diffusion coefficient drops to $\sim 2 \times 10^{-11}$ m^2/s, nearly two orders of magnitude lower than in free solution. At 20 Å and 26 Å, mobility partially recovers, reaching 1.7×10^{-11} and 2.6×10^{-11} m^2/s, respectively, but remains well below bulk values. This strong suppression indicates that steric hindrance and hydration-shell compression govern boron transport under confinement.

Pore Size Dependence

The confinement effect scales with the overlap between boron's hydration shell and the pore walls. In the 15 Å pore, the hydration shell is strongly compressed, disrupting its natural structure and raising energetic barriers to water exchange. As pore size increases, steric constraints lessen and hydration shells recover bulk-like character, though interfacial effects continue to dampen mobility.

Spatial Heterogeneity

Radial density profiles show that water density near silica walls is elevated by 20–30%, consistent with strong hydrogen bonding to silanol groups [189]. These dense interfacial layers act as viscous barriers to motion, reducing mobility near the pore surface. Boron is therefore localized near the pore center, where steric hindrance is reduced, but still experiences slowed dynamics due to the compressed hydration shell.

Mechanisms of Confinement Effects

The reduction of boron mobility can be attributed to three mechanisms: steric hindrance from pore walls, disruption of hydration-shell dynamics, and viscosity increases associated with interfacial water structuring. Together these factors transform the isotropic diffusion of free solution into an anisotropic, spatially heterogeneous process.

Validation and Literature Consistency

These results align with experimental studies of water transport in mesoporous silica, where pore sizes below 30 Å lead to pronounced diffusion suppression [42], [130]. The stronger sensitivity of boron compared to water reflects its larger hydration shell and stronger hydrogen bonds, in agreement with the findings of Risplendi *et al.*[176] that boric acid forms more persistent hydrogen bonds than water itself.

Can the transport of boron in silica nanopores be linked to the observed slowing of alteration rates?

Residual Alteration Rate and Gel Passivation

The immobilization of boron in nanopores offers a mechanistic explanation for the low residual alteration rates of borosilicate glass. Experimental studies show that nanoporous alteration gel slows dissolution by 2–3 orders of magnitude compared to initial rates [15], [52], [129]. Our simulations indicate that boron's diffusivity in 15–26 Å pores falls by nearly two orders relative to bulk solution, consistent with strong confinement-induced retention within the gel.

Comparison with Experimental Coefficients

Although simulated diffusivities ($\sim 10^{-11}$ m^2/s) remain higher than experimental measurements in gels ($\sim 10^{-21}$ m^2/s), this discrepancy is expected. Simulations employ idealized cylindrical pores, whereas real alteration gels are tortuous, chemically heterogeneous, and subject to progressive pore closure. These features extend diffusion pathways and can ultimately trap boron, forcing transport to proceed via slow solid-state mechanisms. The qualitative agreement—that confinement drastically reduces mobility—remains robust despite quantitative differences.

Coupled Diffusion of Boron and Water

Boron and water transport are strongly coupled. Boron–water residence times (8–11 ps) far exceed water–water lifetimes, stabilizing the hydration shell and slowing solvent dynamics. Conversely, water's dense interfacial layering increases viscous drag, further impeding boron motion. This reciprocal inhibition reduces fluxes of both solute and solvent, reinforcing the passivation of alteration gels.

Transition to Solid-State Diffusion

In the smallest pores, boron's transport approaches a hopping-like mechanism within a rigid hydration shell, more akin to solid-state diffusion than to fluid transport. This transition mirrors the extremely low diffusivities reported for mature alteration gels, where pore connectivity is lost and diffusion pathways collapse [42]. Such conditions account for the persistence of the residual rate phase and the long-term durability of borosilicate glass.

What are the limits of the potential developed?

The DCRP potential successfully reproduces the qualitative suppression of diffusion under confinement but exhibits several limitations. Its fixed-charge nature cannot capture polarization effects central to hydrogen-bond energetics, and the use of purely Coulombic B–Si interactions oversimplifies boron–surface chemistry. The model also assumes idealized cylindrical pores, neglecting the tortuosity, chemical heterogeneity, and evolving connectivity of real gels. Furthermore, the solution is treated as ideal, whereas in real gels the pore solution may be enriched in cations (e.g., Na, Ca), which can significantly limit transport.

Future work should focus on refining force fields with machine learning-based reactive potentials capable of modeling charge transfer and bond formation, as well as

simulating multipore networks that mimic gel morphology. Experimental studies, such as NMR diffusion measurements, would provide critical validation of boron speciation and mobility. Bridging the simulated ($\sim 10^{-11}$ m^2/s) and experimental ($\sim 10^{-21}$ m^2/s) values remains a challenge, but the qualitative agreement strongly supports the mechanistic role of confinement in boron immobilization.

Conclusion

The development of a potential to simulate boron-water interactions within the DCRP framework represents a significant advancement in the simulation of boron in aqueous systems, including in solution confined within silica nanopores, which is the case in the gel layer on altered borosilicate glasses. By employing a force-matching approach based on DFT reference data, this potential enables the execution of large-scale molecular dynamics simulations while maintaining realistic structural fidelity. Its transferability across both bulk aqueous and nanoconfined systems establishes it as a valuable tool for investigating boron behavior over extended timescales.

Despite some limitations in accurately reproducing the immediate local environment surrounding boron, the fitted potentials effectively capture the qualitative behavior of boron in nanoconfined silica, serving as a simplified model for the behavior of boron, an important element in glass, within an alteration gel. This capability is crucial for understanding the role of boron in material degradation and stability under confinement.

Simulations reveal that the mean diffusion coefficient of boron in confined nanopores is at least one order of magnitude lower than that in bulk solution. Furthermore, as the size of the pores approaches that of the hydration shell of the boron atom, the diffusion of boron effectively ceases due to extreme confinement. This confinement is also relevant to the retention of boron in alteration gels, where boron may become trapped within the pores after being released from glass alteration. As the pores become increasingly confined, diffusion through them becomes highly restricted, and the primary mechanism for boron transport shifts to diffusion through the gel skeleton, typically occurring via solid-state diffusion. This hindrance to water molecule transport within the confined environment, where the diffusion of water in boron-infused aqueous solutions is reduced compared to pure water in the same pores, suggests that boron acts as an obstacle.

5 Discussion

Contents

When nuclear glasses undergo aqueous alteration in a confined environment, a microporous silicate gel layer forms [15], exhibiting passivating properties that could reduce the glass alteration rate by several orders of magnitude, transitioning from a rapid initial rate to a low, steady-state residual rate critical for long-term stability of the material. This hydrated, amorphous gel, formed from the glass after release of soluble elements followed by local reorganization or precipitation, serves as a mediating barrier between the pristine glass and the bulk solution. Its evolving properties and morphology—characterized by nanometer-scale pores—partly explain the decreased alteration rate, as the gel reduces fluxes between the pristine glass and the solution through restricted water transport and limited ion mobility. The gel's pore network undergoes maturation over time, where small pores merge into larger ones through hydrolysis and condensation reactions, reducing pore connectivity and minimizing the gel's free energy. Despite advances in modeling and analytical tools [15], [191], there remains a lack of models linking the temporal evolution of gel properties to alteration kinetics, necessitating further investigation into the fundamental mechanisms controlling glass alteration across atomic to macroscopic scales.

Focusing on simple glasses, this work aims to construct a comprehensive, multiscale model of this process by synthesizing insights from a combined approach: integrating macroscopic experimental data, mesoscale Monte Carlo (MC) modeling,

and atomic-scale Molecular Dynamics (MD) simulations. By examining a series of sodium aluminoborosilicate glasses (SBNA1, SBNA4, and SBNA6) with systematically varied alumina content (under pH 9, 90 °C, and a high surface area of glass to solution volume ratio), **we demonstrate that the gel's evolving nanostructure governs the transport of key aqueous species such as H_2O and $B(OH)_3$.** We propose and substantiate a central hypothesis: **the efficacy of the gel as a transport barrier can be directly indexed by the diffusion mechanism of boron, which undergoes a decisive transition from a fast, aqueous-like regime to a slow, solid-state regime as a function of nanoscale pore confinement. This transition is a determinant mechanism of the residual rate and, by extension, the long-term durability of the glass.**

The assertion that the residual rate is controlled by diffusion through the gel layer is not new, but a multi-scale validation of the mechanisms at play remains incomplete. While kinetic models typically implement an apparent diffusion coefficient to capture this effect, the mechanisms underlying this parameter are often not detailed or fully understood. **Our integrated approach provides robust, converging lines of evidence from three distinct scales of analysis. Experiments establish the macroscopic reality and correlations; Monte Carlo simulations bridge the scale gap by modeling the structural evolution of the gel; and Molecular Dynamics reveals the fundamental, atomic-scale physics of transport in the resulting structures.**

At the same time, the multi-scale model highlights significant limitations. The MC framework is intentionally simplified, designed to offer conceptual insights into gel maturation, pore formation, and potential pore channel connectivity rather than replicate the full complexity of glass alteration physics. While it clarifies the link between pore coalescence and transport restriction, it struggles to reproduce the intricate pore morphologies observed in Small-Angle X-ray Scattering (SAXS) or Transmission Electron Microscopy (TEM), limiting direct structural comparisons. Moreover, the treatment of boron is oversimplified, as the model assumes its instantaneous transfer to the bulk solution, thereby neglecting slow diffusion within the gel (estimated at $\sim 10^{-21}$ m^2/s at pH 9 and 90 °C) that governs boron retention and release kinetics. Likewise, the model neglects the chemical and structural complexity of real nuclear glasses and the impact of irradiation (alpha, beta, gamma) on gel properties, such as porosity or reactivity. Environmental variability—such as fluctuating pH or groundwater composition—is also absent, although these factors can strongly affect gel maturation and dissolution. Finally, while this work emphasizes the role of restricted water transport at the gel–glass interface, recent studies indicate that coupled mechanisms—such as the interplay of glass matrix dissolution and ion exchange [192]—may also contribute.

Despite these constraints, the combined experimental–simulation approach provides the first multi-scale validation that residual alteration is governed by nanoscale diffusion through the gel, while also establishing a framework to evaluate additional rate-limiting mechanisms. In doing so, it lays the groundwork for incorporating diffusion mechanisms, complex glass chemistries, and realistic environmental conditions into future predictive models of nuclear glass behavior. Building on this foundation, **our multi-scale model aims to address two central questions:**

1. **How does the glass composition, particularly the aluminum and boron content, affect the formation and reorganization of the passivating gel layer during glass alteration?**
2. **Can the maturation dynamics of the gel layer be correlated with the residual rate?**

5.1 How does the glass composition, particularly the aluminum and boron content, affect the formation and reorganization of the passivating gel layer during glass alteration?

The formation and reorganization of the passivating gel layer in sodium aluminoborosilicate glasses (SBNA1, SBNA4, and SBNA6, with 1, 4, and 6 mol% Al_2O_3, respectively) are critically shaped by the relative contributions of boron and aluminum to the glass structure and to the dynamics of ion transport and exchange during alteration. Boron increases the degree of disorder within the silicate network, thereby enhancing the propensity for rapid restructuring, whereas aluminum has the opposite effect: by increasing the hydrolysis energy of Si–O bonds it stabilizes the network and slows down dissolution, while simultaneously reducing the reformation energy of Si–O bonds, which decreases the rate of gel reorganization [38], [53], [144]. The interplay of these compositional factors determines not only whether a gel forms but also the rate and manner in which it reorganizes into a passivating alteration layer [42], [52].

Effect of composition on pore development: SAXS observations.

Small-Angle X-ray Scattering (SAXS) measurements provide direct insight into how gel porosity develops as a function of composition. For SBNA1, which contains high levels of B and Na but little Al, well-defined pores with an average diameter of approximately 3 nm emerge within only a few days of alteration. These pores remain remarkably stable for at least one year, and the SAXS intensity consistently follows Porod's law [139], [140], indicating a sharp and persistent pore–gel interface.

SBNA4, with intermediate Al content, exhibits a slower trajectory: in the first weeks, the pores are poorly defined, but over the course of one year they gradually sharpen and stabilize around 3 nm. SBNA6, which has the highest Al content, does not reach such a stabilized state. Instead, the gel remains highly porous and interconnected, suggesting that higher levels of Al strongly retard the reorganization process. Taken together, these results show that the final pore sizes of SBNA1 and SBNA4 are comparable, but the kinetics of stabilization differ drastically, emphasizing the decisive role of Al in controlling the mobility of vacancies and the pace of structural rearrangement.

Compositional control of restructuring: Monte Carlo framework.

Monte Carlo simulations reproduce these experimentally observed trends by introducing two key parameters: *wvacan1*, which promotes the long-range redistribution of vacancies and thereby discourages local pore growth, and *wvacan2*, which enhances the local aggregation of vacancies and thus favors pore nucleation and coarsening processes [156]. The balance between these two parameters determines both the characteristic timescale and the outcome of gel restructuring. For a given ratio *wvacan2/wvacan1*, the model consistently predicts the same final pore size, but the rate at which this state is reached depends strongly on the absolute values of the parameters. High *wvacan2* accelerates the restructuring process, yet if *wvacan1* is too low, pores stabilize prematurely at small sizes, producing a fine and relatively immobile pore network. By contrast, higher values of *wvacan1* allow long-range redistribution of vacancies, delaying stabilization but enabling the growth of larger pores.

These findings highlight that gel restructuring is not governed solely by kinetics but by the competition between vacancy migration and pore surface energy. Vacancies tend to redistribute in ways that minimize the energetic cost of maintaining pore surfaces, which results in the progressive disappearance of smaller pores and the gradual growth of larger ones until a stationary state is reached. This correlation between vacancy migration and surface energy provides a coherent framework for rationalizing the observed restructuring behavior, and it offers a promising direction for further exploration in future simulation and experimental studies [42].

Role of Al and B: experimental–simulation correlation.

The convergence of final pore sizes in SBNA1 and SBNA4, despite their different kinetics, can be explained by this MC framework. The higher Al content of SBNA4 reduces vacancy mobility (effectively lowering the value of *wvacan1*), which slows the restructuring process. To reach the same final pore size as SBNA1, the driving force for pore growth, represented by *wvacan2*, must also be reduced. This dual effect implies that aluminum simultaneously lowers vacancy migration and

weakens the influence of pore surface energy on restructuring. Boron, on the other hand, increases structural disorder and thus facilitates rapid gel reorganization [30], [41], [144]. The combined effect may explain why SBNA1 reorganizes quickly but remains chemically unstable, whereas SBNA4 and SBNA6 undergo slower reorganization yet ultimately achieve more passivating gels. Experimentally determined reorganization times illustrate this contrast: approximately 0.4 days for SBNA1, compared with 47 and 134 days for SBNA4 and SBNA6, respectively.

Compositional impact on channel size and transport.

MC simulations further reveal that the matured gel structure contains transport-limiting channels of about 1 nm in diameter, with no evidence for the development of larger pathways. These results are in good agreement with experimental studies on International Simple Glass (ISG), which show hydrated nanopores of approximately 1 nm [58], a size comparable to that of water molecules and boric acid $B(OH)_3$. Dynamic Vapor Sorption (DVS) experiments on the CJ2 system confirm that such microporosity below 2 nm persists over multi-decade timescales, with SAXS analyses demonstrating that the pores remain largely isolated and poorly connected [59]. Reduced pore connectivity is therefore expected to slow the transport of water and solutes across the gel–glass interface, thereby contributing to the passivating effect of the gel.

Compositional effect on chemical maturation: oxygen isotopes.

Physical stabilization of porosity does not necessarily correspond to chemical passivation. ToF-SIMS isotope tracing using $^{18}O/^{16}O$ ratios shows that oxygen exchange occurs not only through open pores but also within the gel network itself, consistent with earlier work [52]. SBNA1, which contains more B and Na than the other studied glasses, displays stronger isotopic exchange than SBNA4 and SBNA6, reflecting its higher free volume and residual chemical reactivity. In all glasses, enrichment peaks of ^{18}O at the gel–glass interface and decrease with time, consistent with progressive chemical reorganization. This indicates that while physical restructuring may stabilize relatively quickly, chemical processes continue on longer timescales, with compositional effects playing a central role in governing the rate of this evolution.

Delayed silicon incorporation in low-Al glass.

Complementary information comes from isotopic tracing of ^{29}Si. For SBNA1, no enrichment was observed after two months of alteration, contrasting with literature reports of earlier Si incorporation in similar systems [53]. At six months, however, significant enrichment was detected, pointing to a delayed onset of Si incorporation into the alteration gel. This result underscores the sensitivity of SBNA1 to small changes in composition and solution chemistry, which can shift the balance between

dissolution–precipitation processes and in-situ reorganization. The delayed incorporation of Si suggests that the gel formed on SBNA1 is less stable and more prone to secondary phase formation, reinforcing the view that Al-rich systems are more resistant to such instabilities [38].

Distinct but coupled compositional effects on physical and chemical maturation.

A key conclusion is that physical and chemical maturation of the gel do not proceed synchronously. SBNA1 rapidly develops a stable pore network but remains chemically reactive for extended periods, as evidenced by both oxygen and silicon isotope tracers. In contrast, SBNA4 and SBNA6 exhibit slower physical restructuring but achieve chemical stabilization more quickly, a behavior that can be attributed to the restraining effect of Al on dissolution and reorganization.

Overall, these findings demonstrate that the alteration gel is a dynamic, composition-dependent structure whose evolution arises from the interplay of three key factors: (i) vacancy migration, which governs the kinetics of physical restructuring; (ii) pore surface energy, which determines stabilization thresholds; and (iii) composition-dependent chemistry, tuned by B, Na, and Al, which controls the timing and extent of reactivity. While Monte Carlo simulations capture the essential physics of vacancy migration and pore coarsening, experimental data provide the additional chemical dimension, highlighting the central role of composition in dictating both the rate and the effectiveness of passivation.

5.2 Can the maturation dynamics of the gel layer be correlated with the residual rate?

Diffusive processes across the gel layer

The residual alteration rate is controlled by transport phenomena through the hydrated gel layer. Three diffusive processes are involved: (1) inward diffusion of water in the gel, (2) penetration of water or hydrated species into the glass network at the gel–glass interface, and (3) outward diffusion of solvated glass components (e.g., B, Na) through the gel layer. Among these, the second—the diffusion of water or hydrated species at the gel–glass interface—appears to be the rate-limiting step. Understanding how the maturation of the gel alters these pathways is essential to explain the residual rate.

Experimental evidence of passivation efficiency

Alteration experiments on the SBNA series illustrate the impact of gel maturation on passivation. SBNA1 undergoes a rapid initial dissolution followed by a sharp rate drop. The gel that develops retains significant amounts of boron ($\sim 15\%$ after 7 days, increasing to 24% after one year), with almost no measurable release of boron

into the bulk solution. This indicates highly passivating properties and is consistent with a residual alteration rate as low as $4.0 \times 10^{-4}\,\mathrm{gm^{-2}d^{-1}}$. Such behavior suggests that passivation in this case is not only linked to the formation of a dense outer layer but also to rapid internal structural reorganization of the gel.

The composition of the glass provides additional insight into these differences. Low-Al glasses such as SBNA1, enriched in B and Na, tend to release Si quickly, which has been associated in previous studies with the precipitation of a dense surface layer [52]. By contrast, higher-Al glasses such as SBNA4 and SBNA6 release Si more slowly, reflecting the network-strengthening effect of alumina. As a result, their gels mature more gradually and are less effective in limiting B and Na release. ToF-SIMS analyses revealed that low-Al_2O_3 glasses reorganize locally without measurable exchange with ^{29}Si from solution. Strikingly, SBNA1 retained boron in the gel after only 7 days from out expeiments which is consistent with early retention in previous studies [53], raising the question of whether the observed rapid passivation is due solely to the outer dense layer or also to deeper diffusive processes within the gel.

In contrast, SBNA4 and SBNA6 exhibit slower maturation ($\tau \approx 47$ and 134 days, respectively). Their gels retain little to no boron ($\sim 5\%$ for SBNA4, negligible for SBNA6), and the residual rates are correspondingly higher: 2.4×10^{-3} and $9.5 \times 10^{-3}\,\mathrm{gm^{-2}d^{-1}}$. Diffusion coefficients of boron in these gels are on the order of $10^{-20}\,\mathrm{m^2/s}$, consistent with slow solid-state diffusion. These observations demonstrate how the efficiency of passivation depends directly on the pace and outcome of gel maturation.

Maturation and pore structure evolution

Monte Carlo simulations provide a structural interpretation of the maturation process. Small pores in the gel progressively merge into larger, less connected ones, reducing interfacial energy until a "pore saturation" state is reached. At this stage, the pore network consists of stable, transport-limiting channels with characteristic diameters of about 10 Å.

This evolution is reflected in the alteration kinetics. In silica-saturated conditions, the residual rate emerges from the combined effect of network dissolution (dominated by Si–O–B bond breaking) and gel densification. As condensation reactions proceed, the gel reorganizes into a denser Si/Al network. Once pore saturation is achieved, water transport toward the hydration front is significantly impeded. The increasingly tortuous pathways in the matured gel slow inward diffusion, establishing the low residual rate.

Molecular-scale mechanisms of nanoconfinement

Tracer experiments combining ^{10}B and ^{18}O highlight the restricted transport through

matured gels. While ^{18}O atoms penetrate to the gel–glass interface, boron species do not, confirming that hydrated $B(OH)_3$ molecules are too large to traverse the narrow pore channels. The estimated boron diffusion coefficient is several orders of magnitude lower than in bulk solution ($\sim 10^{-9}\,\mathrm{m}^2/\mathrm{s}$).

Molecular Dynamics simulations further reveal the physics of nanoconfinement. Using a reactive potential [125], with refined parameters for boron in confined pores, we probed the diffusion of boron and water species in idealized silica nanopores. The results show a sharp non-linear response: in pores larger than 20 Å, $B(OH)_3$ diffuses freely, but below a critical diameter of ~ 15 Å its diffusion coefficient drops by orders of magnitude. This slowdown arises because the hydration shell of $B(OH)_3$ is compressed, and interactions with silanol groups on pore walls immobilize the species through steric hindrance and transient hydrogen bonding.

The ~ 10 Å channels predicted by the Monte Carlo model fall well below this threshold, providing a robust mechanistic explanation for the observed low boron mobility in matured gels. An additional observation is that the presence of boron itself can hinder water transport, suggesting a coupled diffusion process across the gel–glass interface.

Establishing the link to the residual rate

Together, experimental evidence, mesoscopic modeling, and atomistic simulations converge on the following picture: the residual alteration rate is governed by the dynamics of gel maturation. Rapid maturation, as in SBNA1, produces restrictive nanopores that immobilize boron and impede water transport, yielding very low residual rates. Slower maturation, as observed for SBNA4 and SBNA6, leaves more open channels, leading to higher boron mobility and higher residual rates.

Although compositional effects (such as alumina content) influence the pace of gel development, they act primarily by shaping the kinetics of maturation. It is ultimately the restructuring of the pore network, the degree of nanoconfinement, and the accessibility of the gel–glass interface that determine the long-term residual rate of nuclear glass alteration.

Conclusion

The results of this thesis demonstrate that the drastic drop in alteration rate—by three to four orders of magnitude between the initial and residual regimes—can be directly explained by the maturation dynamics of the gel layer. Using the conceptual framework originally proposed by M. Taron [193], we extend and refine the scheme of alteration presented in Figure 5.1. In this adapted version, the progress of this thesis is highlighted by the rectangles, which emphasize the new insights gained.

Specifically, the thesis establishes that:

- **Glass composition (Al and B content) governs gel formation and reorganization.** Low-Al, B-rich glasses (e.g., SBNA1) reorganize quickly and produce restrictive nanopores that immobilize boron, while high-Al glasses (SBNA6) mature more slowly and remain more permeable.
- **Gel maturation is the key control of the residual rate.** Rapid maturation leads to nanoconfinement of aqueous species in narrow channels (~ 10 Å), producing very low residual rates, whereas slower maturation leaves more open networks and higher long-term release.
- **Monte Carlo simulations clarify the maturation mechanism.** They show that maturation is possibly driven by the competition between vacancy migration (which redistributes free volume and delays stabilization) and pore surface energy (which favors the coalescence of small pores into larger, more stable ones).
- **Transport-limiting diffusion emerges from nanoconfinement.** Boron, which diffuses freely in solution, becomes immobilized once pore diameters fall below ~ 15 Å, providing the mechanistic basis for residual passivation.

By combining macroscopic experiments, Monte Carlo modeling, and Molecular Dynamics simulations, this work provides the first **multi-scale validation that the residual rate is governed by nanoscale diffusion through the gel layer.** The integration of these results into the alteration scheme clarifies how composition, pore network restructuring, and nanoconfinement collectively regulate the transition from the initial to the residual regime, thus controlling the long-term durability of nuclear glasses.

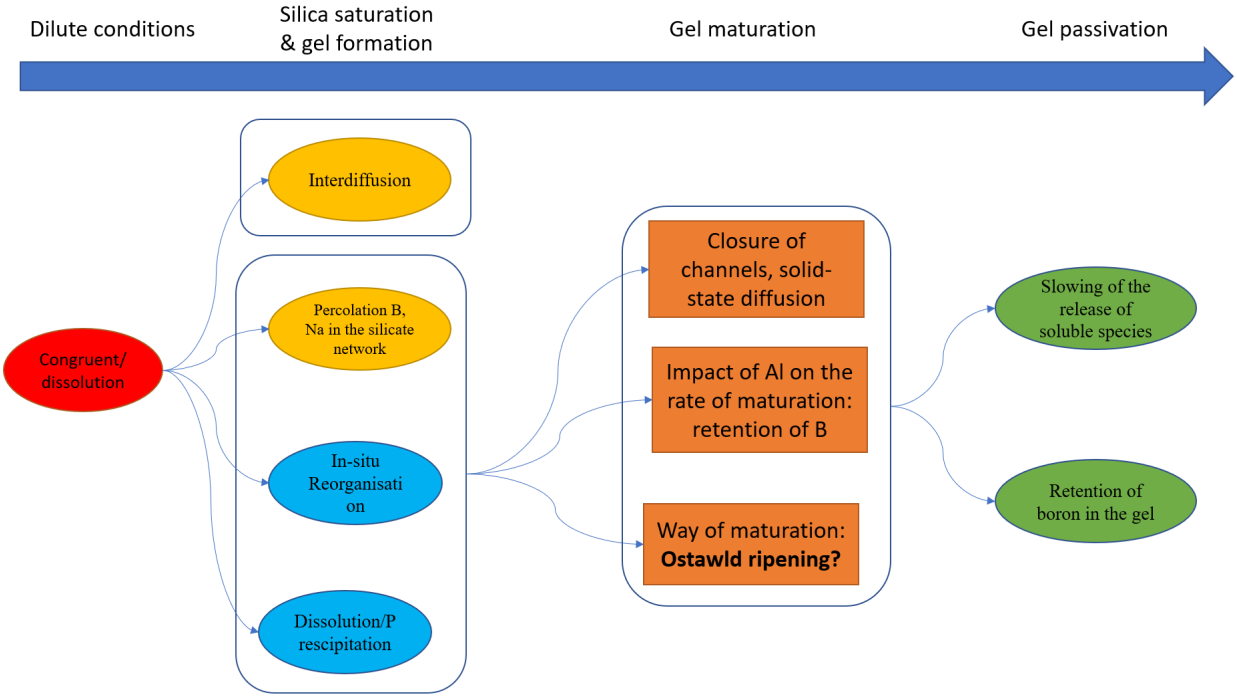

Figure 5.1: *Illustration of various alteration scenarios influenced by composition and the mechanisms governing gel maturation, which regulate the passivation process and control the residual rate. The scheme is based on the original framework of M. Taron [193], with the progress of this thesis highlighted by rectangles.*

5.3 Perspectives

To advance the understanding of the residual alteration rate in nuclear glasses, several improvements to the current Monte Carlo (MC) and Molecular Dynamics (MD) models are proposed to enhance their predictive accuracy and alignment with experimental observations.

5.3.1 Monte Carlo Model Enhancements

The current Monte Carlo (MC) model simplifies boron dynamics by assuming that boron atoms, once released from the glass network via hydrolysis, are instantaneously transferred to the bulk solution. This assumption neglects boron diffusion within the gel layer—a process that is essential for accurately capturing the observed decrease in boron release over time. Furthermore, the gel structures generated by the MC model currently show discrepancies when compared to experimental observations obtained through techniques such as Small-Angle X-ray Scattering (SAXS) and Transmission Electron Microscopy (TEM), particularly in terms of pore size distribution and structural connectivity.

Experimental studies have reported an effective boron diffusion coefficient of approximately 10^{-21} m^2/s at pH 9 and 90 °C within the gel layer, underscoring the

need to incorporate a diffusion mechanism into the MC framework. Integrating such a mechanism, as initially explored by Aertsens and co-workers [145] , would enable a more accurate representation of boron retention and release kinetics. To address the additional computational complexity introduced by this enhancement, it is recommended to accelerate the MC code using GPU parallelization or other optimization techniques. This would allow simulations of larger systems over extended timescales, thereby facilitating a more comprehensive modeling of gel evolution and boron transport that better aligns with experimental data.

In addition, an experimental study could be designed to validate the hypothesis that glasses with low aluminum content exhibit a rougher glass–solution interface at the initial stages of alteration compared to high-aluminum glasses. This experiment could involve altering glass samples under low surface area-to-volume (SA/V) conditions and characterizing the resulting interfaces using Atomic Force Microscopy (AFM).

5.3.2 Molecular Dynamics Simulation Improvements

The MD simulations currently focus on the diffusion coefficient of boron in nanoconfined silica pores, revealing critical insights into its transition from an aqueous-like to a solid-state regime. To broaden the scope, similar nanoconfinement studies can be extended to other key elements in the glass, such as sodium and aluminum, to understand their transport behaviors and interactions within the gel layer. The current Dissociative Charge-Reactive Potentials (DCRP) with fixed charges lead to the formation of under-coordinated anionic species, such as $\{BO_3H_2\}^-$ and $\{BO_3\}^{3-}$, which are not fully representative of the boron local environment. Refining the analytical form of DCRP potentials by incorporating three-body terms would improve accuracy.

Furthermore, developing machine learning potentials offers a transformative opportunity to model complex interactions across multiple environments—boron in solution, within the glass matrix, and at the glass-gel interface. Such a potential would enable a unified description of boron dynamics, capturing the nuanced chemistry and physics at each stage of the alteration process. These enhancements would align MD simulations more closely with experimental diffusion coefficients and provide deeper insights into the atomic-scale mechanisms driving gel passivation.

These improvements aim to bridge the gap between experimental observations and computational predictions, offering a more robust multi-scale model for understanding the long-term durability of nuclear glasses.

A Appendix A

Experimental conditions. In this section we have presented the raw solution data from the Experiment in section 2.2.1. Glass powder from the 40–100 µm fraction was exposed to 50 mL of ultrapure water (18.2 MΩ·cm) with a surface-to-volume ratio of 50 cm^{-1}, while maintaining a pH of 9.0 ± 0.1 using a 10^{-2} M LiOH solution at a temperature of 90°C.

Table A.1: *Extracted dataset for SBNA1: Silicon concentration, normalized loss (NL), and altered layer thickness (Eth).*

Days	Time (h)	S/V	C(Si) (mg/L)	NL(Si) (g/cm^2)	Eth(Si) (nm)
0	0	50.01	0.00	0	0.00
1	24	50.01	437.81	3.10×10^{-5}	125.94
3	72	50.67	394.92	2.80×10^{-5}	113.76
4	96	51.46	436.41	3.08×10^{-5}	125.36
7	168	52.26	475.53	3.35×10^{-5}	136.13
11	264	52.89	451.22	3.19×10^{-5}	129.52
28	672	53.63	470.33	3.31×10^{-5}	134.64
56	1344	54.30	468.12	3.30×10^{-5}	134.06
113	2712	55.09	430.29	3.05×10^{-5}	124.18
185	4440	55.97	446.90	3.16×10^{-5}	128.45
236	5664	56.59	462.17	3.26×10^{-5}	132.33
365	8760	57.29	500.59	3.49×10^{-5}	141.97

Table A.2: *Extracted dataset for SBNA1: Boron concentration, normalized loss (NL), and altered layer thickness (Eth).*

Days	Time (h)	S/V	C(B) (mg/L)	NL(B) (g/cm^2)	Eth(B) (nm)
0	0	50.01	0.00	0	0.00
1	24	50.01	536.14	1.49×10^{-4}	605.59
3	72	50.67	526.44	1.46×10^{-4}	594.63
4	96	51.46	580.28	1.61×10^{-4}	654.52
7	168	52.26	574.34	1.59×10^{-4}	648.01
11	264	52.89	571.68	1.59×10^{-4}	645.13
28	672	53.63	600.86	1.66×10^{-4}	676.27
56	1344	54.30	589.24	1.63×10^{-4}	664.03
113	2712	55.09	599.22	1.66×10^{-4}	674.39
185	4440	55.97	614.47	1.70×10^{-4}	689.98
236	5664	56.59	616.81	1.70×10^{-4}	692.35
365	8760	57.29	633.42	1.74×10^{-4}	708.94

Table A.3: *Extracted dataset for SBNA1: Sodium concentration, normalized loss (NL), and altered layer thickness (Eth).*

Days	Time (h)	S/V	C(Na) (mg/L)	NL(Na) (g/cm^2)	Eth(Na) (nm)
0	0	50.01	0.00	0	0.00
1	24	50.01	847.86	1.32×10^{-4}	535.47
3	72	50.67	831.70	1.29×10^{-4}	525.26
4	96	51.46	918.39	1.43×10^{-4}	579.17
7	168	52.26	887.69	1.38×10^{-4}	560.37
11	264	52.89	907.30	1.41×10^{-4}	572.24
28	672	53.63	950.12	1.47×10^{-4}	597.78
56	1344	54.30	931.45	1.44×10^{-4}	586.78
113	2712	55.09	969.83	1.50×10^{-4}	609.08
185	4440	55.97	986.37	1.52×10^{-4}	618.53
236	5664	56.59	995.41	1.53×10^{-4}	623.64
365	8760	57.29	1061.91	1.63×10^{-4}	660.79

Table A.4: *SBNA4 — Silicon: concentration, normalized loss (NL), and altered layer thickness (Eth).*

Days	Time (h)	S/V	C(Si) (mg/L)	NL(Si) (g/cm^2)	Eth(Si) (nm)
0	0	48.80	0.00	0	0.00
1	24	49.86	39.53	3.75×10^{-4}	13.11
3	72	50.54	40.88	4.38×10^{-4}	14.42
4	96	52.15	45.51	4.38×10^{-4}	15.03
7	168	53.81	45.58	4.73×10^{-4}	15.62
11	264	54.61	44.92	3.44×10^{-4}	16.19
28	672	55.27	49.58	1.70×10^{-4}	16.73
56	1344	56.29	52.42	6.7×10^{-5}	17.26
112	2688	57.02	51.05	2.4×10^{-5}	17.78
169	4056	57.89	57.82	-4.0×10^{-6}	18.28
227	5448	58.89	59.45	5.0×10^{-5}	18.76
298	7152	59.84	63.13	2.0×10^{-5}	19.24
336	8064	60.80	64.08	1.0×10^{-5}	19.70
365	8760	61.81	65.55	-1.0×10^{-5}	20.15

Table A.5: *SBNA4 — Boron: concentration, normalized loss (NL), and altered layer thickness (Eth).*

Days	Time (h)	S/V	C(B) (mg/L)	NL(B) (g/cm^2)	Eth(B) (nm)
0	0	48.80	0.00	0	0.00
1	24	49.86	190.88	1.46×10^{-3}	151.35
3	72	50.54	307.39	1.06×10^{-3}	266.51
4	96	52.15	402.53	1.14×10^{-3}	357.02
7	168	53.81	562.10	1.70×10^{-3}	516.52
11	264	54.61	672.38	9.2×10^{-4}	627.47
28	672	55.27	1135.71	1.13×10^{-3}	1086.13
56	1344	56.29	1537.64	8.6×10^{-4}	1485.22
112	2688	57.02	1836.96	1.08×10^{-3}	1785.91
169	4056	57.89	2228.62	1.41×10^{-3}	2170.80
227	5448	58.89	2397.24	1.31×10^{-3}	2337.79
298	7152	59.84	2573.99	1.38×10^{-3}	2510.85
336	8064	60.80	2467.29	9.8×10^{-4}	2403.20
365	8760	61.81	2443.12	9.6×10^{-4}	2377.58

Table A.6: *SBNA4 — Sodium: concentration, normalized loss (NL), and altered layer thickness (Eth).*

Days	Time (h)	S/V	C(Na) (mg/L)	NL(Na) (g/cm^2)	Eth(Na) (nm)
0	0	48.80	0.00	0	0.00
1	24	49.86	112.80	3.9×10^{-4}	21.73
3	72	50.54	192.84	3.7×10^{-4}	32.48
4	96	52.15	254.09	3.9×10^{-4}	45.70
7	168	53.81	357.52	4.1×10^{-4}	67.83
11	264	54.61	439.78	3.1×10^{-4}	85.89
28	672	55.27	703.48	3.2×10^{-4}	152.60
56	1344	56.29	951.70	3.4×10^{-4}	216.55
112	2688	57.02	1071.27	3.9×10^{-4}	270.13
169	4056	57.89	1275.00	4.4×10^{-4}	341.08
227	5448	58.89	1391.50	5.8×10^{-4}	380.71
298	7152	59.84	1605.56	6.5×10^{-4}	423.12
336	8064	60.80	1604.29	6.8×10^{-4}	418.90
365	8760	61.81	1575.51	7.1×10^{-4}	427.58

Table A.7: *Extracted dataset for SBNA6: Silicon concentration, normalized loss (NL), and altered layer thickness (Eth).*

Days	Time (h)	S/V	C(Si) (mg/L)	NL(Si) (g/cm^2)	Eth(Si) (nm)
0	0	50.92	0.00	0	0.00
1	24	50.92	29.93	2.02×10^{-6}	8.54
3	72	51.45	46.25	3.10×10^{-6}	13.15
7	168	52.06	62.24	4.16×10^{-6}	17.61
14	336	52.68	73.44	4.88×10^{-6}	20.70
28	672	53.21	77.41	5.14×10^{-6}	21.78
56	1344	53.96	82.21	5.45×10^{-6}	23.07
113	2712	54.59	96.45	6.34×10^{-6}	26.86
185	4440	55.20	113.21	7.38×10^{-6}	31.28
236	5664	55.85	124.13	8.05×10^{-6}	34.11
365	8760	56.46	139.33	8.97×10^{-6}	38.03

Table A.8: *Extracted dataset for SBNA6: Boron concentration, normalized loss (NL), and altered layer thickness (Eth).*

Days	Time (h)	S/V	C(B) (mg/L)	NL(B) (g/cm^2)	Eth(B) (nm)
0	0	50.92	0.00	0	0.00
1	24	50.92	23.23	8.54×10^{-6}	36.17
3	72	51.45	47.93	1.75×10^{-5}	74.24
7	168	52.06	94.25	3.42×10^{-5}	144.77
14	336	52.68	163.25	5.87×10^{-5}	248.61
28	672	53.21	246.79	8.81×10^{-5}	373.10
56	1344	53.96	359.24	1.27×10^{-4}	538.32
113	2712	54.59	548.60	1.92×10^{-4}	813.35
185	4440	55.20	737.28	2.56×10^{-4}	1084.38
236	5664	55.85	862.63	2.98×10^{-4}	1262.33
365	8760	56.46	1044.78	3.58×10^{-4}	1518.15

Table A.9: *Extracted dataset for SBNA6: Sodium concentration, normalized loss (NL), and altered layer thickness (Eth).*

Days	Time (h)	S/V	C(Na) (mg/L)	NL(Na) (g/cm^2)	Eth(Na) (nm)
0	0	50.92	0.00	0	0.00
1	24	50.92	19.04	4.63×10^{-6}	19.62
3	72	51.45	34.87	8.44×10^{-6}	35.75
7	168	52.06	65.26	1.57×10^{-5}	66.38
14	336	52.68	116.61	2.77×10^{-5}	117.51
28	672	53.21	150.10	3.55×10^{-5}	150.53
56	1344	53.96	222.80	5.22×10^{-5}	221.21
113	2712	54.59	352.78	8.17×10^{-5}	346.12
185	4440	55.20	473.25	1.09×10^{-4}	460.63
236	5664	55.85	555.29	1.27×10^{-4}	537.69
365	8760	56.46	688.97	1.56×10^{-4}	661.91

B Appendix B

X-ray diffraction experiments were performed at the ESRF (Grenoble) on the ID15A beamline [194], [195] to investigate the structure of aqueous boric acid solutions at different concentrations. Liquid samples consisted of either pure H_2O or $B(OH)_3$ dissolved in H_2O at molarities of 1 M. Diffraction patterns were collected under identical experimental conditions, with additional reference measurements on empty capillaries and background glass.

The raw scattering intensities were corrected, normalized, and converted into total structure factors using the GUDRUN software package [196]. This procedure removes background contributions, absorption effects, and multiple scattering, yielding structure factors suitable for direct comparison with simulations.

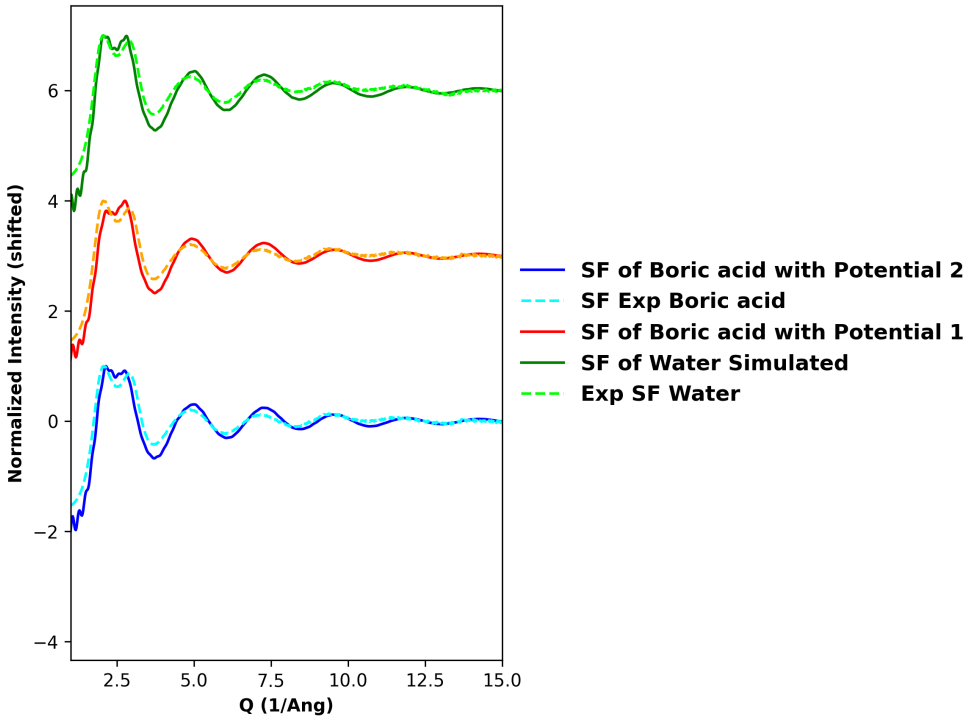

Figure B.1: *Structure factors (SF) of aqueous 1M boric acid solution, compared with pure water. Experimental scattering data were collected at the ESRF ID15A beamline and processed using the GUDRUN software to obtain normalized structure factors. Simulated SF curves (solid lines) obtained with two different interaction potentials are compared with the experimental measurements (dashed lines). Intensities are normalized and vertically shifted for clarity.*

Figure B.1 shows the processed experimental structure factors of boric acid so-

lutions alongside molecular dynamics simulations performed with two different interaction potentials (Potential 1 and Potential 2) mentioned in Section 4.3. The simulated structures of boric acid used for these calculations are the same as those described in Section 4.4.1. The DCRP water model reproduces the experimental water structure factor across the full Q range with accurate peak positions and amplitudes, validating the validity of DCRP potential parameters from literature. For boric acid, both potentials (Potential 1 and Potential 2) place the main peaks correctly, but **Potential 2** (blue) tracks the experimental amplitudes and the damping of oscillations better especially the first-peak height. **Potential 1** (red) shows larger deviations, with a slightly mis-scaled first peak and over/under-shoots in the mid-Q oscillations. At high Q, both simulations approach the experimental envelope. Overall, Potential 2 provides the better quantitative match for $B(OH)_3$ in water.

The good agreement between experiment and simulation confirms that the chosen potentials reproduce the main structural features of boric acid in water.

Bibliography

[1] I. A. E. Agency, *Classification of radioactive waste*, 2009. [Online]. Available: https://www-pub.iaea.org/MTCD/Publications/PDF/Pub1419_web.pdf

[2] Andra, *National inventory of radioactive materials and waste*, 2018. [Online]. Available: https://international.andra.fr/sites/international/files/2019-03/Andra-Synthese-2018_EN_relu_HD.pdf

[3] C. L. Thorpe et al., "Forty years of durability assessment of nuclear waste glass by standard methods," *npj Mater Degrad*, vol. 5, no. 1, pp. 1–28, Dec. 20, 2021, ISSN: 2397-2106. DOI: 10.1038/s41529-021-00210-4 [Online]. Available: https://www.nature.com/articles/s41529-021-00210-4

[4] C. M. Jantzen, "6 - historical development of glass and ceramic waste forms for high level radioactive wastes," in *Handbook of Advanced Radioactive Waste Conditioning Technologies*, ser. Woodhead Publishing Series in Energy, M. I. Ojovan, Ed., Woodhead Publishing, Jan. 1, 2011, pp. 159–172, ISBN: 978-1-84569-626-9. DOI: 10.1533/9780857090959.1.159 [Online]. Available: https://www.sciencedirect.com/science/article/pii/B9781845696269500067

[5] C. M. Jantzen, W. E. Lee, and M. I. Ojovan, "6 - radioactive waste (RAW) conditioning, immobilization, and encapsulation processes and technologies: Overview and advances," in *Radioactive Waste Management and Contaminated Site Clean-Up*, ser. Woodhead Publishing Series in Energy, W. E. Lee, M. I. Ojovan, and C. M. Jantzen, Eds., Woodhead Publishing, Jan. 1, 2013, pp. 171–272, ISBN: 978-0-85709-435-3. DOI: 10.1533/9780857097446.1.171 [Online]. Available: https://www.sciencedirect.com/science/article/pii/B9780857094353500069

[6] C. M. Jantzen, "9 - development of glass matrices for high level radioactive wastes," in *Handbook of Advanced Radioactive Waste Conditioning Technologies*, ser. Woodhead Publishing Series in Energy, M. I. Ojovan, Ed., Woodhead Publishing, Jan. 1, 2011, pp. 230–292, ISBN: 978-1-84569-626-9. DOI: 10.1533/9780857090959.2.230 [Online]. Available: https://www.sciencedirect.com/science/article/pii/B9781845696269500092

[7] C. Poinssot and S. Gin, "Long-term behavior science: The cornerstone approach for reliably assessing the long-term performance of nuclear waste," *Journal of Nuclear Materials*, vol. 420, no. 1, pp. 182–192, Jan. 1, 2012, ISSN: 0022-3115. DOI: 10.1016/j.jnucmat.2011.09.012 Accessed: Sep. 8, 2025.

[Online]. Available: https://www.sciencedirect.com/science/article/pii/S0022311511008476

[8] S. Gin, P. Jollivet, M. Tribet, S. Peuget, and S. Schuller, "Radionuclides containment in nuclear glasses: An overview," *Radiochimica Acta*, vol. 105, no. 11, pp. 927–959, Nov. 1, 2017, ISSN: 2193-3405. DOI: 10.1515/ract-2016-2658 [Online]. Available: https://www.degruyter.com/document/doi/10.1515/ract-2016-2658/html

[9] O. Pinet et al., "Glass ceramic for the vitrification of high level waste with a high molybdenum content," *Journal of Nuclear Materials*, vol. 519, pp. 121–127, Jun. 1, 2019, ISSN: 0022-3115. DOI: 10.1016/j.jnucmat.2019.03.041 Accessed: Sep. 25, 2025. [Online]. Available: https://www.sciencedirect.com/science/article/pii/S0022311518315885

[10] P. Frugier, C. Martin, I. Ribet, T. Advocat, and S. Gin, "The effect of composition on the leaching of three nuclear waste glasses: R7t7, AVM and VRZ," *Journal of Nuclear Materials*, vol. 346, no. 2, pp. 194–207, Nov. 15, 2005, ISSN: 0022-3115. DOI: 10.1016/j.jnucmat.2005.06.023 [Online]. Available: https://www.sciencedirect.com/science/article/pii/S0022311505002941

[11] E. Vernaz, S. Gin, and C. Veyer, "Waste glass," in *Comprehensive Nuclear Materials*, R. J. M. Konings, Ed., vol. 5, Amsterdam: Elsevier, 2012, pp. 451–483.

[12] Andra, *All you need to know about radioactive waste management*, Aug. 2021. [Online]. Available: https://international.andra.fr/sites/international/files/2021-11/Andra-MAJ_Plaquette_institutionnelle-19_08Aout_EN_LQP.pdf

[13] S. Gin et al., "An international initiative on long-term behavior of high-level nuclear waste glass," *Materials Today*, vol. 16, no. 6, pp. 243–248, Jun. 1, 2013, ISSN: 1369-7021. DOI: 10.1016/j.mattod.2013.06.008 [Online]. Available: https://www.sciencedirect.com/science/article/pii/S1369702113001995

[14] J. D. Vienna, J. Ryan, S. Gin, and Y. Inagaki, "Current understanding and remaining challenges in modeling long-term degradation of borosilicate nuclear waste glasses," *INTERNATIONAL JOURNAL OF APPLIED GLASS SCIENCE*, vol. 4, no. 4, pp. 283–294, 2013, ISSN: 2041-1286. DOI: 10.1111/ijag.12050

[15] S. Gin, J.-M. Delaye, F. Angeli, and S. Schuller, "Aqueous alteration of silicate glass: State of knowledge and perspectives," *npj Mater Degrad*, vol. 5, no. 1, pp. 1–20, Aug. 13, 2021, ISSN: 2397-2106. DOI: 10.1038/s41529-021-00190-5

[Online]. Available: https://www.nature.com/articles/s41529-021-00190-5

[16] S. Gin et al., "Insights into the mechanisms controlling the residual corrosion rate of borosilicate glasses," *npj Mater Degrad*, vol. 4, no. 1, pp. 1–9, Dec. 11, 2020, ISSN: 2397-2106. DOI: 10.1038/s41529-020-00145-2 [Online]. Available: https://www.nature.com/articles/s41529-020-00145-2

[17] J. E. Shelby, *Introduction to Glass Science and Technology*, Second. Cambridge, UK: The Royal Society of Chemistry, 2005, ISBN: 0-85404-639-9.

[18] S. Narayanasamy et al., "Influence of composition of nuclear waste glasses on vapor phase hydration," *Journal of Nuclear Materials*, vol. 525, pp. 53–71, Nov. 1, 2019, ISSN: 0022-3115. DOI: 10.1016/j.jnucmat.2019.07.015 [Online]. Available: https://www.sciencedirect.com/science/article/pii/S0022311519303976

[19] R. Zanini, G. Franceschin, E. Cattaruzza, and A. Traviglia, "A review of glass corrosion: The unique contribution of studying ancient glass to validate glass alteration models," *npj Mater Degrad*, vol. 7, no. 1, p. 38, May 20, 2023, ISSN: 2397-2106. DOI: 10.1038/s41529-023-00355-4 [Online]. Available: https://www.nature.com/articles/s41529-023-00355-4

[20] A. Quintas, D. Caurant, O. Majérus, T. Charpentier, and J. .-. Dussossoy, "Effect of compositional variations on charge compensation of AlO4 and BO4 entities and on crystallization tendency of a rare-earth-rich aluminoborosilicate glass," *Materials Research Bulletin*, vol. 44, no. 9, pp. 1895–1898, Sep. 1, 2009, ISSN: 0025-5408. DOI: 10.1016/j.materresbull.2009.05.009 [Online]. Available: https://www.sciencedirect.com/science/article/pii/S0025540809001512

[21] Y. H. Yun and P. J. Bray, "Nuclear magnetic resonance studies of the glasses in the system na2o b2o3 SiO2," *Journal of Non-Crystalline Solids*, vol. 27, no. 3, pp. 363–380, Mar. 1, 1978, ISSN: 0022-3093. DOI: 10.1016/0022-3093(78)90020-0 [Online]. Available: https://www.sciencedirect.com/science/article/pii/0022309378900200

[22] W. J. Dell, P. J. Bray, and S. Z. Xiao, "11b NMR studies and structural modeling of na2o b2o3 SiO2 glasses of high soda content," *Journal of Non-Crystalline Solids*, vol. 58, no. 1, pp. 1–16, Oct. 1, 1983, ISSN: 0022-3093. DOI: 10.1016/0022-3093(83)90097-2 [Online]. Available: https://www.sciencedirect.com/science/article/pii/0022309383900972

[23] L. Deng and J. Du, "Borosilicate and boroaluminosilicate glasses," in *Atomistic Simulations of Glasses*, John Wiley & Sons, Ltd, 2022, pp. 224–260, ISBN: 978-1-118-93907-9. DOI: 10.1002/9781118939079.ch8 [Online]. Available: https://onlinelibrary.wiley.com/doi/abs/10.1002/9781118939079.ch8

[24] D. Manara, A. Grandjean, and D. R. Neuville, "Advances in understanding the structure of borosilicate glasses: A raman spectroscopy study," *American Mineralogist*, vol. 94, no. 5, pp. 777–784, May 1, 2009, ISSN: 1945-3027. DOI: 10.2138/am.2009.3027 [Online]. Available: https://www.degruyterbrill.com/document/doi/10.2138/am.2009.3027/html

[25] L.-S. Du and J. F. Stebbins, "Network connectivity in aluminoborosilicate glasses: A high-resolution 11b, 27al and 17o NMR study," *Journal of Non-Crystalline Solids*, vol. 351, no. 43, pp. 3508–3520, Nov. 1, 2005, ISSN: 0022-3093. DOI: 10.1016/j.jnoncrysol.2005.08.033 [Online]. Available: https://www.sciencedirect.com/science/article/pii/S0022309305006897

[26] S. Gin, X. Beaudoux, F. Angéli, C. Jégou, and N. Godon, "Effect of composition on the short-term and long-term dissolution rates of ten borosilicate glasses of increasing complexity from 3 to 30 oxides," *Journal of Non-Crystalline Solids*, vol. 358, no. 18, pp. 2559–2570, Sep. 15, 2012, ISSN: 0022-3093. DOI: 10.1016/j.jnoncrysol.2012.05.024 [Online]. Available: https://www.sciencedirect.com/science/article/pii/S0022309312002748

[27] W. L. Ebert and J. K. Bates, "A comparison of glass reaction at high and low glass surface/solution volume," *Nuclear Technology*, vol. 104, no. 3, pp. 372–384, 1993. DOI: 10.13182/NT93-A34898

[28] S. Ribet and S. Gin, "Role of neoformed phases on the mechanisms controlling the resumption of SON68 glass alteration in alkaline media," *Journal of Nuclear Materials*, vol. 324, no. 2, pp. 152–164, 2004. DOI: 10.1016/j.jnucmat.2003.09.010

[29] M. Fournier, P. Frugier, and S. Gin, "Resumption of alteration at high temperature and pH: Rates measurements and comparison with initial rates," *Procedia Materials Science*, 2nd International Summer School on Nuclear Glass Wasteform: Structure, Properties and Long-Term Behavior, SumGLASS 2013, vol. 7, pp. 202–208, Jan. 1, 2014, ISSN: 2211-8128. DOI: 10.1016/j.mspro.2014.10.026 [Online]. Available: https://www.sciencedirect.com/science/article/pii/S2211812814010694

[30] M. Taron, S. Gin, H. Kaya, J.-M. Delaye, and S. H. Kim, "Impact of b and al on the initial and residual dissolution rate of alumino-boro-silicate glasses. part II: Gel properties," *npj Mater Degrad*, vol. 9, no. 1, pp. 1–12, May 22, 2025, ISSN: 2397-2106. DOI: 10.1038/s41529-025-00576-9 [Online]. Available: https://www.nature.com/articles/s41529-025-00576-9

[31] P. Frugier et al., "SON68 nuclear glass dissolution kinetics: Current state of knowledge and basis of the new GRAAL model," *Journal of Nuclear Materials*, vol. 380, no. 1, pp. 8–21, Oct. 15, 2008, ISSN: 0022-3115. DOI: 10.1016/j.jnucmat.2008.06.044 [Online]. Available: https://www.sciencedirect.com/science/article/pii/S0022311508003668

[32] S. Gin, P. Jollivet, M. Fournier, F. Angeli, P. Frugier, and T. Charpentier, "Origin and consequences of silicate glass passivation by surface layers," *Nature communications*, vol. 6, p. 6360, Feb. 19, 2015, ISSN: 2041-1723. DOI: 10.1038/ncomms7360

[33] J. D. Vienna, J. J. Neeway, J. V. Ryan, and S. N. Kerisit, "Impacts of glass composition, pH, and temperature on glass forward dissolution rate," *npj Mater Degrad*, vol. 2, no. 1, pp. 1–12, Aug. 6, 2018, ISSN: 2397-2106. DOI: 10.1038/s41529-018-0042-5 [Online]. Available: https://www.nature.com/articles/s41529-018-0042-5

[34] J. J. Neeway et al., "Ion-exchange interdiffusion model with potential application to long-term nuclear waste glass performance," *J. Phys. Chem. C*, vol. 120, no. 17, pp. 9374–9384, May 5, 2016, ISSN: 1932-7447. DOI: 10.1021/acs.jpcc.6b03681 [Online]. Available: https://doi.org/10.1021/acs.jpcc.6b03681

[35] D. Strachan, "Glass dissolution as a function of pH and its implications for understanding mechanisms and future experiments," *Geochimica et Cosmochimica Acta*, vol. 219, pp. 111–123, Dec. 15, 2017, ISSN: 0016-7037. DOI: 10.1016/j.gca.2017.09.008 [Online]. Available: https://www.sciencedirect.com/science/article/pii/S001670371730563X

[36] S. Gin et al., "The controversial role of inter-diffusion in glass alteration," *Chemical Geology*, vol. 440, pp. 115–123, Nov. 15, 2016, ISSN: 0009-2541. DOI: 10.1016/j.chemgeo.2016.07.014 [Online]. Available: https://www.sciencedirect.com/science/article/pii/S000925411630345X

[37] D. Caurant, P. Loiseau, O. Majérus, V. Aubin-Chevaldonnet, I. Bardez, and A. Quintas, *Glasses, Glass-Ceramics and Ceramics for Immobilization of Highly Radioactive Nuclear Wastes*. Nova Science Publishers, Inc., 2007, ISBN: 978-1-60456-174-6.

[38] K. Damodaran, J.-M. Delaye, A. G. Kalinichev, and S. Gin, "Deciphering the non-linear impact of al on chemical durability of silicate glass," *Acta Materialia*, vol. 225, p. 117 478, Feb. 15, 2022, ISSN: 1359-6454. DOI: 10.1016/j.actamat.2021.117478 [Online]. Available: https://www.sciencedirect.com/science/article/pii/S1359645421008570

[39] J. T. Reiser et al., "Effects of al:si and (al plus na):si ratios on the static corrosion of sodium-boroaluminosilicate glasses," *INTERNATIONAL JOURNAL OF APPLIED GLASS SCIENCE*, vol. 13, no. 1, pp. 94–111, Jan. 2022, ISSN: 2041-1286. DOI: 10.1111/ijag.16109

[40] J. D. Vienna and J. Crum V, "Non-linear effects of alumina concentration on product consistency test response of waste glasses," *JOURNAL OF NUCLEAR MATERIALS*, vol. 511, pp. 396–405, 2018, ISSN: 0022-3115. DOI: 10.1016/j.jnucmat.2018.09.040

[41] M. Taron, S. Gin, and J.-M. Delaye, "Impact of b and al on the initial and residual dissolution rate of alumino-borosilicate glasses. part i: Kinetic data," *npj Mater Degrad*, vol. 9, no. 1, pp. 1–9, Mar. 27, 2025, ISSN: 2397-2106. DOI: 10.1038/s41529-025-00577-8 [Online]. Available: https://www.nature.com/articles/s41529-025-00577-8

[42] S. Gin et al., "Dynamics of self-reorganization explains passivation of silicate glasses," *NATURE COMMUNICATIONS*, vol. 9, 2018, ISSN: 2041-1723. DOI: 10.1038/s41467-018-04511-2

[43] D. Rebiscoul, P. Frugier, S. Gin, and A. Ayral, "Protective properties and dissolution ability of the gel formed during nuclear glass alteration," *Journal of Nuclear Materials*, vol. 342, no. 1, pp. 26–34, Jun. 30, 2005, ISSN: 0022-3115. DOI: 10.1016/j.jnucmat.2005.03.018 [Online]. Available: https://www.sciencedirect.com/science/article/pii/S0022311505001364

[44] S. Mercado-Depierre, F. Angeli, F. Frizon, and S. Gin, "Antagonist effects of calcium on borosilicate glass alteration," *Journal of Nuclear Materials*, vol. 441, no. 1, pp. 402–410, Oct. 1, 2013, ISSN: 0022-3115. DOI: 10.1016/j.jnucmat.2013.06.023 [Online]. Available: https://www.sciencedirect.com/science/article/pii/S0022311513008477

[45] D. Rebiscoul et al., "Morphological evolution of alteration layers formed during nuclear glass alteration: New evidence of a gel as a diffusive barrier," *Journal of Nuclear Materials*, vol. 326, no. 1, pp. 9–18, 2004, ISSN: 0022-3115. DOI: https://doi.org/10.1016/j.jnucmat.2003.10.015

[46] C. Cailleteau et al., "Insight into silicate-glass corrosion mechanisms," *Nature Mater*, vol. 7, no. 12, pp. 978–983, Dec. 2008, ISSN: 1476-4660. DOI: 10.1038/nmat2301 [Online]. Available: https://www.nature.com/articles/nmat2301

[47] R. H. DOREMUS, "INTERDIFFUSION OF HYDROGEN AND ALKALI IONS IN a GLASS SURFACE," in D. E. B. T. .-. G. S. DAY, Ed., Elsevier, 1975, pp. 137–144, ISBN: 978-0-7204-0419-7.

[48] W. A. Lanford, K. Davis, P. Lamarche, T. Laursen, R. Groleau, and R. H. Doremus, "Hydration of soda-lime glass," *Journal of Non-Crystalline Solids*, vol. 33, no. 2, pp. 249–266, Jun. 1, 1979, ISSN: 0022-3093. DOI: 10.1016/0022-3093(79)90053-X [Online]. Available: https://www.sciencedirect.com/science/article/pii/002230937990053X

[49] R. Hellmann et al., "Nanometre-scale evidence for interfacial dissolution-reprecipitation control of silicate glass corrosion," *NATURE MATERIALS*, vol. 14, no. 3, pp. 307–311, Mar. 2015, ISSN: 1476-1122. DOI: 10.1038/nmat4172

[50] T. Geisler et al., "The mechanism of borosilicate glass corrosion revisited," *GEOCHIMICA ET COSMOCHIMICA ACTA*, vol. 158, pp. 112–129, 2015, ISSN: 0016-7037. DOI: 10.1016/j.gca.2015.02.039

[51] S. Gin et al., "Atom-probe tomography, TEM and ToF-SIMS study of borosilicate glass alteration rim: A multiscale approach to investigating rate-limiting mechanisms," *Geochimica et Cosmochimica Acta*, vol. 202, 2017, ISSN: 00167037. DOI: 10.1016/j.gca.2016.12.029

[52] S. Gin et al., "A general mechanism for gel layer formation on borosilicate glass under aqueous corrosion," *J. Phys. Chem. C*, vol. 124, no. 9, pp. 5132–5144, Mar. 5, 2020, ISSN: 1932-7447. DOI: 10.1021/acs.jpcc.9b10491 [Online]. Available: https://doi.org/10.1021/acs.jpcc.9b10491

[53] K. Damodaran, S. Gin, S. Narayanasamy, and J.-M. Delaye, "On the effect of al on alumino-borosilicate glass chemical durability," *npj Mater Degrad*, vol. 7, no. 1, pp. 1–9, May 30, 2023, ISSN: 2397-2106. DOI: 10.1038/s41529-023-00364-3 [Online]. Available: https://www.nature.com/articles/s41529-023-00364-3

[54] S. Gin et al., "The fate of silicon during glass corrosion under alkaline conditions: A mechanistic and kinetic study with the international simple glass," *GEOCHIMICA ET COSMOCHIMICA ACTA*, vol. 151, pp. 68–85, 2015, ISSN: 0016-7037. DOI: 10.1016/j.gca.2014.12.009

[55] O. Deruelle, O. Spalla, P. Barboux, and J. Lambard, "Growth and ripening of porous layers in water altered glasses," *Journal of Non-Crystalline Solids*, vol. 261, no. 1, pp. 237–251, 2000, ISSN: 0022-3093. DOI: https://doi.org/10.1016/S0022-3093(99)00587-6

[56] C. e. Cailleteau, F. Devreux, O. Spalla, F. e. e. Angeli, and S. e. Gin, "Why do certain glasses with a high dissolution rate undergo a low degree of corrosion?" *The Journal of Physical Chemistry C*, vol. 115, no. 13, pp. 5846–5855, Apr. 7, 2011, ISSN: 1932-7447. DOI: 10.1021/jp111458f

[57] P. Jollivet, F. Angeli, C. Cailleteau, F. Devreux, P. Frugier, and S. Gin, "Investigation of gel porosity clogging during glass leaching," *JOURNAL OF NON-CRYSTALLINE SOLIDS*, vol. 354, no. 45, pp. 4952–4958, Nov. 2008, ISSN: 0022-3093. DOI: 10.1016/j.jnoncrysol.2008.07.023

[58] M. Collin et al., "Structure of international simple glass and properties of passivating layer formed in circumneutral pH conditions," *npj Materials Degradation*, vol. 2, no. 1, p. 4, 2018, ISSN: 2397-2106. DOI: 10.1038/s41529-017-0025-y

[59] S. Narayanasamy et al., "Aqueous alteration of a borosilicate glass from 7 days to 27 years: Insights into the role of gel maturation on glass alteration kinetics," *npj Materials Degradation(Manuscript accepted for publication)*,

[60] J. M. Rimsza, T. S. Mahadevan, L. Deng, and J. Du, "Simulations of glass–water interactions," in *Atomistic Simulations of Glasses*, John Wiley & Sons, Ltd, 2022, pp. 490–521, ISBN: 978-1-118-93907-9. DOI: 10.1002/9781118939079.ch15 [Online]. Available: https://onlinelibrary.wiley.com/doi/abs/10.1002/9781118939079.ch15

[61] B. M. Lowe, C.-K. Skylaris, and N. G. Green, "Acid-base dissociation mechanisms and energetics at the silica–water interface: An activationless process," *Journal of Colloid and Interface Science*, vol. 451, pp. 231–244, Aug. 1, 2015, ISSN: 0021-9797. DOI: 10.1016/j.jcis.2015.01.094 [Online]. Available: https://www.sciencedirect.com/science/article/pii/S0021979715003240

[62] J. M. Rimsza and J. Du, "Interfacial structure and evolution of the water–silica gel system by reactive force-field-based molecular dynamics simulations," *J. Phys. Chem. C*, vol. 121, no. 21, pp. 11 534–11 543, Jun. 1, 2017, ISSN: 1932-7447. DOI: 10.1021/acs.jpcc.7b02734 [Online]. Available: https://doi.org/10.1021/acs.jpcc.7b02734

[63] A. Pelmenschikov, H. Strandh, L. G. M. Pettersson, and J. Leszczynski, "Lattice resistance to hydrolysis of si-o-si bonds of silicate minerals: Ab initio calculations of a single water attack onto the (001) and (111) beta-cristobalite surfaces," *JOURNAL OF PHYSICAL CHEMISTRY B*, vol. 104, no. 24, pp. 5779–5783, 2000, ISSN: 1520-6106. DOI: 10.1021/jp994097r

[64] Y. Ma, A. S. Foster, and R. M. Nieminen, "Reactions and clustering of water with silica surface," *J. Chem. Phys.*, vol. 122, no. 14, Apr. 8, 2005, ISSN: 0021-9606. DOI: 10.1063/1.1878652 [Online]. Available: https://pubs.aip.org/aip/jcp/article/122/14/144709/914332/Reactions-and-clustering-of-water-with-silica

[65] L. J. Criscenti, J. D. Kubicki, and S. L. Brantley, "Silicate glass and mineral dissolution: Calculated reaction paths and activation energies for hydrolysis of a q3 si by h3o+ using ab initio methods," *J Phys Chem A*, vol. 110, no. 1, pp. 198–206, Jan. 12, 2006, ISSN: 1089-5639. DOI: 10.1021/jp044360a

[66] T. T. Trinh, A. P. J. Jansen, and R. A. v. Santen, "Mechanism of oligomerization reactions of silica," *J Phys Chem B*, vol. 110, no. 46, pp. 23 099–23 106, Nov. 23, 2006, ISSN: 1520-6106. DOI: 10.1021/jp063670l

[67] P. Masini and M. Bernasconi, "Ab initio simulations of hydroxylation and dehydroxylation reactions at surfaces: Amorphous silica and brucite," *J. Phys.: Condens. Matter*, vol. 14, no. 16, p. 4133, Apr. 2002, ISSN: 0953-8984. DOI: 10.1088/0953-8984/14/16/306 [Online]. Available: https://dx.doi.org/10.1088/0953-8984/14/16/306

[68] A. V. Bandura, J. D. Kubicki, and J. O. Sofo, "Periodic density functional theory study of water adsorption on the α-quartz (101) surface," *J. Phys. Chem. C*, vol. 115, no. 13, pp. 5756–5766, Apr. 7, 2011, ISSN: 1932-7447. DOI: 10.1021/jp1106636 [Online]. Available: https://doi.org/10.1021/jp1106636

[69] A. Rimola and P. Ugliengo, "A quantum mechanical study of the reactivity of (SiO)2-defective silica surfaces," *J. Chem. Phys.*, vol. 128, no. 20, May 28, 2008, ISSN: 0021-9606. DOI: 10.1063/1.2929827 [Online]. Available: https://pubs.aip.org/aip/jcp/article/128/20/204702/1003516/A-quantum-mechanical-study-of-the-reactivity-of

[70] X. Wei, D. Zhang, and C. Liu, "A DFT study on the hydrolysis stabilities of silica molecular chains and rings based on the two-membered rings," *Journal of Molecular Structure: THEOCHEM*, vol. 859, no. 1, pp. 1–6, Jun. 30, 2008, ISSN: 0166-1280. DOI: 10.1016/j.theochem.2008.02.020 [Online]. Available: https://www.sciencedirect.com/science/article/pii/S0166128008001115

[71] I. G. Batyrev, B. Tuttle, D. M. Fleetwood, R. D. Schrimpf, L. Tsetseris, and S. T. Pantelides, "Reactions of water molecules in silica-based network glasses," *Phys. Rev. Lett.*, vol. 100, no. 10, p. 105 503, Mar. 13, 2008. DOI: 10.1103/PhysRevLett.100.105503 [Online]. Available: https://link.aps.org/doi/10.1103/PhysRevLett.100.105503

[72] J. D. Kubicki and D. Sykes, "Molecular orbital calculations on the vibrational spectra of q3 t-(OH) species and the hydrolysis of a three-membered aluminosilicate ring," *Geochimica et Cosmochimica Acta*, vol. 59, no. 23, pp. 4791–4797, Dec. 1, 1995, ISSN: 0016-7037. DOI: 10.1016/0016-7037(95)00325-8 [Online]. Available: https://www.sciencedirect.com/science/article/pii/0016703795003258

[73] L. J. Criscenti, S. L. Brantley, K. T. Mueller, N. Tsomaia, and J. D. Kubicki, "Theoretical and 27al CPMAS NMR investigation of aluminum coordination changes during aluminosilicate dissolution," *Geochimica et Cosmochimica Acta*, vol. 69, no. 9, pp. 2205–2220, May 1, 2005, ISSN: 0016-7037. DOI: 10.1016/j.gca.2004.10.020 [Online]. Available: https://www.sciencedirect.com/science/article/pii/S0016703704008312

[74] F. Bouyer, G. Geneste, S. Ispas, W. Kob, and P. Ganster, "Water solubility in calcium aluminosilicate glasses investigated by first principles techniques," *Journal of Solid State Chemistry*, vol. 183, no. 12, pp. 2786–2796, Dec. 1, 2010, ISSN: 0022-4596. DOI: 10.1016/j.jssc.2010.08.031 [Online]. Available: https://www.sciencedirect.com/science/article/pii/S0022459610003658

[75] P. Zapol, H. He, K. D. Kwon, and L. J. Criscenti, "First-principles study of hydrolysis reaction barriers in a sodium borosilicate glass," *International Journal of Applied Glass Science*, vol. 4, no. 4, pp. 395–407, 2013, ISSN: 2041-1294. DOI: 10.1111/ijag.12052 [Online]. Available: https://onlinelibrary.wiley.com/doi/abs/10.1111/ijag.12052

[76] Y. Xiao and A. C. Lasaga, "Ab initio quantum mechanical studies of the kinetics and mechanisms of silicate dissolution: H+(h3o+) catalysis," *Geochimica et Cosmochimica Acta*, vol. 58, no. 24, pp. 5379–5400, Dec. 1, 1994, ISSN: 0016-7037. DOI: 10.1016/0016-7037(94)90237-2 [Online]. Available: https://www.sciencedirect.com/science/article/pii/0016703794902372

[77] G. Geneste, F. Bouyer, and S. Gin, "Hydrogen–sodium interdiffusion in borosilicate glasses investigated from first principles," *Journal of Non-Crystalline Solids*, vol. 352, no. 28, pp. 3147–3152, Aug. 15, 2006, ISSN: 0022-3093. DOI: 10.1016/j.jnoncrysol.2006.04.023 [Online]. Available: https://www.sciencedirect.com/science/article/pii/S0022309306005850

[78] A. Tilocca and A. N. Cormack, "Exploring the surface of bioactive glasses: Water adsorption and reactivity," *J. Phys. Chem. C*, vol. 112, no. 31, pp. 11 936–11 945, Aug. 1, 2008, ISSN: 1932-7447. DOI: 10.1021/jp803541j [Online]. Available: https://doi.org/10.1021/jp803541j

[79] E. Berardo, A. Pedone, P. Ugliengo, and M. Corno, "DFT modeling of 45s5 and 77s soda-lime phospho-silicate glass surfaces: Clues on different bioactivity mechanism," *Langmuir*, vol. 29, no. 19, pp. 5749–5759, May 14, 2013, ISSN: 0743-7463. DOI: 10.1021/la304795w [Online]. Available: https://doi.org/10.1021/la304795w

[80] S. Nangia and B. J. Garrison, "Reaction rates and dissolution mechanisms of quartz as a function of pH," *J Phys Chem A*, vol. 112, no. 10, pp. 2027–2033, Mar. 13, 2008, ISSN: 1520-5215. DOI: 10.1021/jp076243w

[81] D. W. Heermann, *Computer Simulation Methods in Theoretical Physics*. Berlin, Heidelberg: Springer, 1990, ISBN: 978-3-540-52210-2 978-3-642-75448-7. DOI: 10.1007/978-3-642-75448-7 [Online]. Available: http://link.springer.com/10.1007/978-3-642-75448-7

[82] A. Pedone, M. Bertani, L. Brugnoli, and A. Pallini, "Interatomic potentials for oxide glasses: Past, present, and future," *Journal of Non-Crystalline Solids: X*, vol. 15, p. 100 115, Sep. 1, 2022, ISSN: 2590-1591. DOI: 10.1016/j.nocx.2022.100115 [Online]. Available: https://www.sciencedirect.com/science/article/pii/S2590159122000358

[83] L. V. Woodcock, C. A. Angell, and P. Cheeseman, "Molecular dynamics studies of the vitreous state: Simple ionic systems and silica," *The Journal of Chemical Physics*, vol. 65, no. 4, pp. 1565–1577, Aug. 15, 1976, ISSN: 0021-9606. DOI: 10.1063/1.433213 [Online]. Available: https://doi.org/10.1063/1.433213

[84] T. F. Soules, "Molecular dynamic calculations of glass structure and diffusion in glass," *Journal of Non-Crystalline Solids*, Proceedings of the Sixth University Conference on Glass Science, vol. 49, no. 1, pp. 29–52, May 1, 1982, ISSN: 0022-3093. DOI: 10.1016/0022-3093(82)90107-7 [Online]. Available: https://www.sciencedirect.com/science/article/pii/0022309382901077

[85] B. P. Feuston and S. H. Garofalini, "Empirical three-body potential for vitreous silica," *The Journal of Chemical Physics*, vol. 89, no. 9, pp. 5818–5824, Nov. 1, 1988, ISSN: 0021-9606. DOI: 10.1063/1.455531 [Online]. Available: https://doi.org/10.1063/1.455531

[86] R. G. Newell, B. P. Feuston, and S. H. Garofalini, "The structure of sodium trisilicate glass via molecular dynamics employing three-body potentials," *Journal of Materials Research*, vol. 4, no. 2, pp. 434–439, Mar. 1, 1989, ISSN: 2044-5326. DOI: 10.1557/JMR.1989.0434 [Online]. Available: https://doi.org/10.1557/JMR.1989.0434

[87] Y. Onodera et al., "Origin of the mixed alkali effect in silicate glass," *NPG Asia Mater*, vol. 11, no. 1, pp. 1–11, Dec. 6, 2019, ISSN: 1884-4057. DOI: 10.1038/s41427-019-0180-4 [Online]. Available: https://www.nature.com/articles/s41427-019-0180-4

[88] S. Tsuneyuki, M. Tsukada, H. Aoki, and Y. Matsui, "First-principles interatomic potential of silica applied to molecular dynamics," *Phys. Rev. Lett.*, vol. 61, no. 7, pp. 869–872, Aug. 15, 1988. DOI: 10.1103/PhysRevLett.61.869 [Online]. Available: https://link.aps.org/doi/10.1103/PhysRevLett.61.869

[89] B. W. H. van Beest, G. J. Kramer, and R. A. van Santen, "Force fields for silicas and aluminophosphates based on ab initio calculations," *Phys. Rev. Lett.*, vol. 64, no. 16, pp. 1955–1958, Apr. 16, 1990. DOI: 10.1103/PhysRevLett.64.1955 [Online]. Available: https://link.aps.org/doi/10.1103/PhysRevLett.64.1955

[90] A. Pedone, G. Malavasi, M. C. Menziani, A. N. Cormack, and U. Segre, "A new self-consistent empirical interatomic potential model for oxides, silicates, and silica-based glasses," *J. Phys. Chem. B*, vol. 110, no. 24, pp. 11 780–11 795, Jun. 1, 2006, ISSN: 1520-6106. DOI: 10.1021/jp0611018 [Online]. Available: https://doi.org/10.1021/jp0611018

[91] S. Sundararaman, L. Huang, S. Ispas, and W. Kob, "New optimization scheme to obtain interaction potentials for oxide glasses," *The Journal of Chemical Physics*, vol. 148, no. 19, p. 194 504, May 21, 2018, ISSN: 0021-9606. DOI: 10.1063/1.5023707 [Online]. Available: https://doi.org/10.1063/1.5023707

[92] S. Sundararaman, L. Huang, S. Ispas, and W. Kob, "New interaction potentials for alkali and alkaline-earth aluminosilicate glasses," *The Journal of Chemical Physics*, vol. 150, no. 15, p. 154 505, Apr. 19, 2019, ISSN: 0021-9606. DOI: 10.1063/1.5079663 [Online]. Available: https://doi.org/10.1063/1.5079663

[93] D. J. Price and C. L. Brooks, "A modified TIP3p water potential for simulation with ewald summation," *J. Chem. Phys.*, vol. 121, no. 20, pp. 10 096–10 103, Nov. 22, 2004, ISSN: 0021-9606. DOI: 10.1063/1.1808117 [Online]. Available:

https://pubs.aip.org/aip/jcp/article/121/20/10096/532393/A-modified-TIP3P-water-potential-for-simulation

[94] C. D. Berweger, W. F. van Gunsteren, and F. Müller-Plathe, "Force field parametrization by weak coupling. re-engineering SPC water," *Chemical Physics Letters*, vol. 232, no. 5, pp. 429–436, Jan. 27, 1995, ISSN: 0009-2614. DOI: 10.1016/0009-2614(94)01391-8 [Online]. Available: https://www.sciencedirect.com/science/article/pii/0009261494013918

[95] L. A. Belyaeva and G. F. Schneider, "Wettability of graphene," *Surface Science Reports*, vol. 75, no. 2, p. 100 482, May 1, 2020, ISSN: 0167-5729. DOI: 10.1016/j.surfrep.2020.100482 [Online]. Available: https://www.sciencedirect.com/science/article/pii/S0167572920300030

[96] E. Pafong, J. Geske, and B. Drossel, "On the influence of the intermolecular potential on the wetting properties of water on silica surfaces," *The Journal of Chemical Physics*, vol. 145, no. 11, p. 114 901, Sep. 16, 2016, ISSN: 0021-9606. DOI: 10.1063/1.4962516 [Online]. Available: https://doi.org/10.1063/1.4962516

[97] R. T. Cygan, J.-J. Liang, and A. G. Kalinichev, "Molecular models of hydroxide, oxyhydroxide, and clay phases and the development of a general force field," *J. Phys. Chem. B*, vol. 108, no. 4, pp. 1255–1266, Jan. 1, 2004, ISSN: 1520-6106. DOI: 10.1021/jp0363287 [Online]. Available: https://doi.org/10.1021/jp0363287

[98] I. C. Bourg and C. I. Steefel, "Molecular dynamics simulations of water structure and diffusion in silica nanopores," *J. Phys. Chem. C*, vol. 116, no. 21, pp. 11 556–11 564, May 31, 2012, ISSN: 1932-7447. DOI: 10.1021/jp301299a [Online]. Available: https://doi.org/10.1021/jp301299a

[99] R. Shahsavari, R. J.-M. Pellenq, and F.-J. Ulm, "Empirical force fields for complex hydrated calcio-silicate layered materials," *Phys. Chem. Chem. Phys.*, vol. 13, no. 3, pp. 1002–1011, Dec. 22, 2010, ISSN: 1463-9084. DOI: 10.1039/C0CP00516A [Online]. Available: https://pubs.rsc.org/en/content/articlelanding/2011/cp/c0cp00516a

[100] D. Hou, C. Lu, T. Zhao, P. Zhang, and Q. Ding, "Structural, dynamic and mechanical evolution of water confined in the nanopores of disordered calcium silicate sheets," *Microfluid Nanofluid*, vol. 19, no. 6, pp. 1309–1323, Dec. 1, 2015, ISSN: 1613-4990. DOI: 10.1007/s10404-015-1646-5 [Online]. Available: https://doi.org/10.1007/s10404-015-1646-5

[101] P. A. Madden and M. Wilson, "'covalent' effects in 'ionic' systems," *Chem. Soc. Rev.*, vol. 25, no. 5, pp. 339–350, Jan. 1, 1996, ISSN: 1460-4744. DOI: 10.1039/CS9962500339 [Online]. Available: https://pubs.rsc.org/en/content/articlelanding/1996/cs/cs9962500339

[102] A. Aguado and P. A. Madden, "Oxide potentials from ab initio molecular dynamics: An assessment of their transferability," *J. Chem. Phys.*, vol. 118, no. 13, pp. 5718–5728, Apr. 2003, ISSN: 0021-9606. DOI: 10.1063/1.1556073 [Online]. Available: https://aip.scitation.org/doi/10.1063/1.1556073

[103] S. Jahn, P. A. Madden, and M. Wilson, "Transferable interaction model for al2o3," *Phys. Rev. B*, vol. 74, no. 2, p. 024 112, Jul. 24, 2006. DOI: 10.1103/PhysRevB.74.024112 [Online]. Available: https://link.aps.org/doi/10.1103/PhysRevB.74.024112

[104] M. Salanne and P. A. Madden, "Polarization effects in ionic solids and melts," *Molecular Physics*, vol. 109, no. 19, pp. 2299–2315, Oct. 10, 2011, ISSN: 0026-8976. DOI: 10.1080/00268976.2011.617523 [Online]. Available: https://doi.org/10.1080/00268976.2011.617523

[105] M. Salanne, B. Rotenberg, S. Jahn, R. Vuilleumier, C. Simon, and P. A. Madden, "Including many-body effects in models for ionic liquids," *Theor Chem Acc*, vol. 131, no. 3, p. 1143, Feb. 17, 2012, ISSN: 1432-2234. DOI: 10.1007/s00214-012-1143-9 [Online]. Available: https://doi.org/10.1007/s00214-012-1143-9

[106] F. Pacaud, J.-M. Delaye, T. Charpentier, L. Cormier, and M. Salanne, "Structural study of na2o-b2o3-SiO2 glasses from molecular simulations using a polarizable force field," *Journal of Chemical Physics*, vol. 147, no. 16, 2017, ISSN: 0021-9606. DOI: 10.1063/1.4992799

[107] S. Tazi, J. J. Molina, B. Rotenberg, P. Turq, R. Vuilleumier, and M. Salanne, "A transferable ab initio based force field for aqueous ions," *J. Chem. Phys.*, vol. 136, no. 11, p. 114 507, Mar. 21, 2012, ISSN: 0021-9606. DOI: 10.1063/1.3692965 [Online]. Available: https://aip.scitation.org/doi/10.1063/1.3692965

[108] J. J. Molina et al., "Ions in solutions: Determining their polarizabilities from first-principles," *J. Chem. Phys.*, vol. 134, no. 1, p. 014 511, Jan. 7, 2011, ISSN: 0021-9606. DOI: 10.1063/1.3518101 [Online]. Available: https://aip.scitation.org/doi/full/10.1063/1.3518101

[109] P. Jungwirth and D. J. Tobias, "Specific ion effects at the air/water interface," *Chem. Rev.*, vol. 106, no. 4, pp. 1259–1281, Apr. 1, 2006, ISSN: 0009-2665. DOI: 10.1021/cr0403741 [Online]. Available: https://doi.org/10.1021/cr0403741

[110] S. Tesson et al., "Classical polarizable force field to study hydrated charged clays and zeolites," *J. Phys. Chem. C*, vol. 122, no. 43, pp. 24 690–24 704, Nov. 1, 2018, ISSN: 1932-7447. DOI: 10.1021/acs.jpcc.8b06230 [Online]. Available: https://doi.org/10.1021/acs.jpcc.8b06230

[111] L. X. Dang and T.-M. Chang, "Molecular dynamics study of water clusters, liquid, and liquid–vapor interface of water with many-body potentials," *J. Chem. Phys.*, vol. 106, no. 19, pp. 8149–8159, May 15, 1997, ISSN: 0021-9606. DOI: 10.1063/1.473820 [Online]. Available: https://aip.scitation.org/doi/10.1063/1.473820

[112] P. M. Agrawal, L. M. Raff, M. T. Hagan, and R. Komanduri, "Molecular dynamics investigations of the dissociation of SiO2 on an ab initio potential energy surface obtained using neural network methods," *The Journal of Chemical Physics*, vol. 124, no. 13, p. 134 306, Apr. 7, 2006, ISSN: 0021-9606. DOI: 10.1063/1.2185638 [Online]. Available: https://doi.org/10.1063/1.2185638

[113] T. Morawietz, A. Singraber, C. Dellago, and J. Behler, "How van der waals interactions determine the unique properties of water," *Proceedings of the National Academy of Sciences*, vol. 113, no. 30, pp. 8368–8373, Jul. 26, 2016. DOI: 10.1073/pnas.1602375113 [Online]. Available: https://www.pnas.org/doi/10.1073/pnas.1602375113

[114] K. Chenoweth, A. C. T. van Duin, and W. A. Goddard, "ReaxFF reactive force field for molecular dynamics simulations of hydrocarbon oxidation," *J. Phys. Chem. A*, vol. 112, no. 5, pp. 1040–1053, Feb. 1, 2008, ISSN: 1089-5639. DOI: 10.1021/jp709896w [Online]. Available: https://doi.org/10.1021/jp709896w

[115] A. C. T. van Duin, S. Dasgupta, F. Lorant, and W. A. Goddard, "ReaxFF: A reactive force field for hydrocarbons," *J. Phys. Chem. A*, vol. 105, no. 41, pp. 9396–9409, Oct. 1, 2001, ISSN: 1089-5639. DOI: 10.1021/jp004368u [Online]. Available: https://doi.org/10.1021/jp004368u

[116] H. R. Larsson, A. C. T. van Duin, and B. Hartke, "Global optimization of parameters in the reactive force field ReaxFF for SiOH," *J Comput Chem*, vol. 34, no. 25, pp. 2178–2189, Sep. 30, 2013, ISSN: 1096-987X. DOI: 10.1002/jcc.23382

[117] J. Yeon and A. C. Van Duin, "ReaxFF molecular dynamics simulations of hydroxylation kinetics for amorphous and nano-silica structure, and its relations with atomic strain energy," *Journal of Physical Chemistry C*, vol. 120, no. 1, pp. 305–317, Jan. 21, 2016, ISSN: 1932-7447. DOI: 10.1021/acs.jpcc.5b09784 [Online]. Available: http://www.scopus.com/inward/record.url?scp=84954449905&partnerID=8YFLogxK

[118] T. P. Senftle et al., "The ReaxFF reactive force-field: Development, applications and future directions," *npj Comput Mater*, vol. 2, no. 1, pp. 1–14, Mar. 4, 2016, ISSN: 2057-3960. DOI: 10.1038/npjcompumats.2015.11 [Online]. Available: https://www.nature.com/articles/npjcompumats201511

[119] "Copyright," in *An Introduction to Nuclear Waste Immobilisation (Third Edition)*, M. I. Ojovan, W. E. Lee, and S. N. Kalmykov, Eds., Elsevier, Jan. 1, 2019, p. iv, ISBN: 978-0-08-102702-8. DOI: 10.1016/B978-0-08-102702-8.00027-3 [Online]. Available: https://www.sciencedirect.com/science/article/pii/B9780081027028000273

[120] T. S. Mahadevan and J. Du, "Hydration and reaction mechanisms on sodium silicate glass surfaces from molecular dynamics simulations with reactive force fields," *Journal of the American Ceramic Society*, vol. 103, no. 6, pp. 3676–3690, 2020, ISSN: 1551-2916. DOI: 10.1111/jace.17059 [Online]. Available: https://onlinelibrary.wiley.com/doi/abs/10.1111/jace.17059

[121] T. S. Mahadevan and J. Du, "Atomic and micro-structure features of nanoporous aluminosilicate glasses from reactive molecular dynamics simulations," *Journal of the American Ceramic Society*, vol. 104, no. 1, pp. 229–242, 2021, ISSN: 1551-2916. DOI: 10.1111/jace.17465 [Online]. Available: https://onlinelibrary.wiley.com/doi/abs/10.1111/jace.17465

[122] J. Yu, S. B. Sinnott, and S. R. Phillpot, "Charge optimized many-body potential for the $\mathrm{si} {\mathrm{SiO}}_{2}$ system," *Phys. Rev. B*, vol. 75, no. 8, p. 085 311, Feb. 9, 2007. DOI: 10.1103/PhysRevB.75.085311 [Online]. Available: https://link.aps.org/doi/10.1103/PhysRevB.75.085311

[123] J. M. Rimsza, J. Yeon, A. C. T. van Duin, and J. Du, "Water interactions with nanoporous silica: Comparison of ReaxFF and ab initio based molecular dynamics simulations," *J. Phys. Chem. C*, vol. 120, no. 43, pp. 24 803–24 816, Nov. 3, 2016, ISSN: 1932-7447. DOI: 10.1021/acs.jpcc.6b07939 [Online]. Available: https://doi.org/10.1021/acs.jpcc.6b07939

[124] S. H. Hahn et al., "Development of a ReaxFF reactive force field for NaSiO x/water systems and its application to sodium and proton self-diffusion," *Journal of Physical Chemistry C*, vol. 122, no. 34, pp. 19 613–19 624, Aug. 30, 2018, ISSN: 1932-7447. DOI: 10.1021/acs.jpcc.8b05852 [Online]. Available: http://www.scopus.com/inward/record.url?scp=85052296045&partnerID=8YFLogxK

[125] T. S. Mahadevan and S. H. Garofalini, "Dissociative water potential for molecular dynamics simulations," *J. Phys. Chem. B*, vol. 111, no. 30, pp. 8919–8927, Aug. 1, 2007, ISSN: 1520-6106. DOI: 10.1021/jp072530o [Online]. Available: https://doi.org/10.1021/jp072530o

[126] T. S. Mahadevan, W. Sun, and J. Du, "Development of water reactive potentials for sodium silicate glasses," *J. Phys. Chem. B*, vol. 123, no. 20, pp. 4452–4461, May 23, 2019, ISSN: 1520-6106, 1520-5207. DOI: 10.1021/acs.jpcb.9b02216 [Online]. Available: https://pubs.acs.org/doi/10.1021/acs.jpcb.9b02216

[127] M. Kagan, G. K. Lockwood, and S. H. Garofalini, "Reactive simulations of the activation barrier to dissolution of amorphous silica in water," *PHYSICAL CHEMISTRY CHEMICAL PHYSICS*, vol. 16, no. 20, pp. 9294–9301, 2014, ISSN: 1463-9076. DOI: 10.1039/c4cp00030g

[128] H. Jabraoui, S. Gin, T. Charpentier, R. Pollet, and J.-M. Delaye, "Leaching and reactivity at the sodium aluminosilicate glass-water interface: Insights from a ReaxFF molecular dynamics," *JOURNAL OF PHYSICAL CHEMISTRY C*, vol. 125, no. 49, pp. 27 170–27 184, 2021, ISSN: 1932-7447. DOI: 10.1021/acs.jpcc.1c07266

[129] J. M. Rimsza and J. Du, "Nanoporous silica gel structures and evolution from reactive force field-based molecular dynamics simulations," *npj Mater Degrad*, vol. 2, no. 1, pp. 1–10, Jul. 24, 2018, ISSN: 2397-2106. DOI: 10.1038/s41529-018-0039-0 [Online]. Available: https://www.nature.com/articles/s41529-018-0039-0

[130] M. Collin, S. Gin, B. Dazas, T. Mahadevan, J. Du, and I. C. Bourg, "Molecular dynamics simulations of water structure and diffusion in a 1 nm diameter silica nanopore as a function of surface charge and alkali metal counterion identity," *J. Phys. Chem. C*, vol. 122, no. 31, pp. 17 764–17 776, Aug. 9, 2018, ISSN: 1932-7447. DOI: 10.1021/acs.jpcc.8b03902 [Online]. Available: https://doi.org/10.1021/acs.jpcc.8b03902

[131] M. Collin, M. Fournier, T. Charpentier, M. Moskura, and S. Gin, "Impact of alkali on the passivation of silicate glass," *npj Materials Degradation*, vol. 2, no. 1, p. 16, 2018, ISSN: 2397-2106. DOI: 10.1038/s41529-018-0036-3

[132] M. Tribet et al., "New insights about the importance of the alteration layer/glass interface," *The Journal of Physical Chemistry C*, vol. 124, no. 18, pp. 10 032–10 044, May 7, 2020, ISSN: 1932-7447. DOI: 10.1021/acs.jpcc.0c02121

[133] A. Fluegel, "Global model for calculating room-temperature glass density from the composition," *Journal of the American Ceramic Society*, vol. 90, no. 8, pp. 2622–2625, 2007, ISSN: 1551-2916. DOI: 10.1111/j.1551-2916.2007.01751.x [Online]. Available: https://onlinelibrary.wiley.com/doi/abs/10.1111/j.1551-2916.2007.01751.x

[134] F. Angeli, T. Charpentier, D. De Ligny, and C. Cailleteau, "Boron speciation in soda-lime borosilicate glasses containing zirconium," *Journal of the American Ceramic Society*, vol. 93, no. 9, pp. 2693–2704, 2010, ISSN: 1551-2916. DOI: 10.1111/j.1551-2916.2010.03771.x [Online]. Available: https://onlinelibrary.wiley.com/doi/abs/10.1111/j.1551-2916.2010.03771.x

[135] J. Hopf et al., "Glass–water interaction: Effect of high-valence cations on glass structure and chemical durability," *Geochimica et Cosmochimica Acta*, vol. 181, pp. 54–71, May 15, 2016, ISSN: 0016-7037. DOI: 10.1016/j.gca.2016.02.023 [Online]. Available: https://www.sciencedirect.com/science/article/pii/S0016703716300692

[136] M. Collin, S. Gin, P. Jollivet, L. Dupuy, V. Dauvois, and L. Duffours, "ToF-SIMS depth profiling of altered glass," *npj Mater Degrad*, vol. 3, no. 1, pp. 1–10, Apr. 2, 2019, ISSN: 2397-2106. DOI: 10.1038/s41529-019-0076-3 [Online]. Available: https://www.nature.com/articles/s41529-019-0076-3

[137] "X-ray mass attenuation coefficients. "[Online]. Available: https://physics.nist.gov/PhysRefData/XrayMassCoef/tab3.html

[138] A. Ledieu, F. Devreux, and P. Barboux, "The role of aluminium in the durability of alumino-borosilicate glasses," *Physics and Chemistry of Glasses*, vol. 46, no. 1, pp. 12–20, Feb. 1, 2005.

[139] E. Walenta, "Small angle x-ray scattering. von o. GLATTER und o. KRATKY. london: Academic press inc. ltd. 1982. ISBN 0-12-286280-5. x, 515 seiten, geb. £ 43,60; US $ 81.00," *Acta Polymerica*, vol. 36, no. 5, pp. 296–296, 1985, ISSN: 1521-4044. DOI: 10.1002/actp.1985.010360520 [Online]. Available: https://onlinelibrary.wiley.com/doi/abs/10.1002/actp.1985.010360520

[140] L. Sicard, O. Spalla, and P. Barboux, "Study of the kinetics of glass alteration by small-angle x-ray scattering," *J. Phys. Chem. B*, vol. 108, no. 23, pp. 7702–7708, Jun. 1, 2004, ISSN: 1520-6106. DOI: 10.1021/jp049727q [Online]. Available: https://doi.org/10.1021/jp049727q

[141] H.-P. Boehm, "The chemistry of silica. solubility, polymerization, colloid and surface properties, and biochemistry. von r. k. iler. john wiley and sons, chichester 1979. XXIV, 886 s., geb. £39.50," *Angewandte Chemie*, vol. 92, no. 4, pp. 328–328, 1980, ISSN: 1521-3757. DOI: 10.1002/ange.19800920433 [Online]. Available: https://onlinelibrary.wiley.com/doi/abs/10.1002/ange.19800920433

[142] A. Ledieu, F. Devreux, P. Barboux, and Y. Minet, "Contribution of monte carlo modeling to understanding the alteration of nuclear glasses by water," *NUCLEAR SCIENCE AND ENGINEERING*, vol. 153, no. 3, pp. 285–300, 2006, ISSN: 0029-5639. DOI: 10.13182/NSE06-A2614

[143] C. Cailleteau, C. Weigel, A. Ledieu, P. Barboux, and F. Devreux, "On the effect of glass composition in the dissolution of glasses by water," *Journal of Non-Crystalline Solids*, Physics of Non-Crystalline Solids 11, vol. 354, no. 2, pp. 117–123, Jan. 15, 2008, ISSN: 0022-3093. DOI: 10.1016/j.jnoncrysol.2007.07.063 [Online]. Available: https://www.sciencedirect.com/science/article/pii/S0022309307010332

[144] X. Lu, M. Ren, L. Deng, C. J. Benmore, and J. Du, "Structural features of ISG borosilicate nuclear waste glasses revealed from high-energy x-ray diffraction and molecular dynamics simulations," *Journal of Nuclear Materials*, vol. 515, pp. 284–293, Mar. 1, 2019, ISSN: 0022-3115. DOI: 10.1016/j.jnucmat.2018.12.041 [Online]. Available: https://www.sciencedirect.com/science/article/pii/S0022311518311620

[145] M. Aertsens and P. VanIseghem, "Modelling glass dissolution with a monte carlo technique," in *SCIENTIFIC BASIS FOR NUCLEAR WASTE MANAGEMENT XIX*, W. M. Murphy and D. A. Knecht, Eds., ser. MATERIALS RESEARCH SOCIETY SYMPOSIUM PROCEEDINGS, vol. 412, 1996, pp. 271–278, ISBN: 1-55899-315-0.

[146] A. Ledieu, F. Devreux, and P. Barboux, "Monte carlo simulations of borosilicate glass corrosion: Predictions for morphology and kinetics," *Journal of Non-Crystalline Solids*, Physics of Non-Crystalline Solids 10, vol. 345-346, pp. 715–719, Oct. 15, 2004, ISSN: 0022-3093. DOI: 10.1016/j.jnoncrysol.2004.08.152 [Online]. Available: https://www.sciencedirect.com/science/article/pii/S0022309304007525

[147] S. Kerisit, J. V. Ryan, and E. M. Pierce, "Monte carlo simulations of the corrosion of aluminoborosilicate glasses," *Journal of Non-Crystalline Solids*, vol. 378, pp. 273–281, Oct. 15, 2013, ISSN: 0022-3093. DOI: 10.1016/j.jnoncrysol.2013.07.014 [Online]. Available: https://www.sciencedirect.com/science/article/pii/S002230931300392X

[148] M. Aertsens and D. Ghaleb, "New techniques for modelling glass dissolution," *Journal of Nuclear Materials*, Glass in its Disposal Environment, vol. 298, no. 1, pp. 37–46, Sep. 1, 2001, ISSN: 0022-3115. DOI: 10.1016/S0022-3115(01)00575-X [Online]. Available: https://www.sciencedirect.com/science/article/pii/S002231150100575X

[149] F. Devreux, A. Ledieu, P. Barboux, and Y. Minet, "Leaching of borosilicate glasses. II. model and monte-carlo simulations," *Journal of Non-Crystalline Solids*, vol. 343, no. 1, pp. 13–25, Sep. 1, 2004, ISSN: 0022-3093. DOI: 10.1016/j.jnoncrysol.2004.06.007 [Online]. Available: https://www.sciencedirect.com/science/article/pii/S0022309304004363

[150] M. Arab, C. Cailleteau, F. Angeli, F. Devreux, L. Girard, and O. Spalla, "Aqueous alteration of five-oxide silicate glasses: Experimental approach and monte carlo modeling," *Journal of Non-Crystalline Solids*, vol. 354, no. 2, pp. 155–161, 2008, ISSN: 0022-3093. DOI: https://doi.org/10.1016/j.jnoncrysol.2007.06.095

[151] S. Kerisit, E. M. Pierce, and J. V. Ryan, "Monte carlo simulations of coupled diffusion and surface reactions during the aqueous corrosion of borosilicate glasses," *Journal of Non-Crystalline Solids*, vol. 408, pp. 142–149, Jan. 15, 2015, ISSN: 0022-3093. DOI: 10.1016/j.jnoncrysol.2014.07.020 [Online]. Available: https://www.sciencedirect.com/science/article/pii/S0022309314003329

[152] S. Kerisit and E. M. Pierce, "Monte carlo simulations of the dissolution of borosilicate glasses in near-equilibrium conditions," *Journal of Non-Crystalline Solids*, vol. 358, no. 10, pp. 1324–1332, May 15, 2012, ISSN: 0022-3093. DOI: 10.1016/j.jnoncrysol.2012.03.003 [Online]. Available: https://www.sciencedirect.com/science/article/pii/S002230931200155X

[153] S. Kerisit and E. M. Pierce, "Monte carlo simulations of the dissolution of borosilicate and aluminoborosilicate glasses in dilute aqueous solutions," *Geochimica et Cosmochimica Acta*, vol. 75, no. 18, pp. 5296–5309, Sep. 15, 2011, ISSN: 0016-7037. DOI: 10.1016/j.gca.2011.06.036 [Online]. Available: https://www.sciencedirect.com/science/article/pii/S0016703711003747

[154] A. Jan, J.-M. Delaye, S. Gin, and S. Kerisit, "Molecular dynamics simulation of ballistic effects in simplified nuclear waste glasses," *Journal of Non-Crystalline Solids*, vol. 505, pp. 188–201, Feb. 1, 2019, ISSN: 0022-3093. DOI: 10.1016/j.jnoncrysol.2018.11.021 [Online]. Available: https://www.sciencedirect.com/science/article/pii/S0022309318306768

[155] S. Mougnaud et al., "Heavy ion radiation ageing impact on long-term glass alteration behavior," *Journal of Nuclear Materials*, vol. 510, pp. 168–177, Nov. 1, 2018, ISSN: 0022-3115. DOI: 10.1016/j.jnucmat.2018.07.046 [Online]. Available: https://www.sciencedirect.com/science/article/pii/S0022311518304938

[156] J.-M. Delaye, S. Tiwari, E. Brun, P. C. M. Fossati, and S. Gin, "Advanced monte carlo method for simulating glass alteration: Application to aluminoborosilicate glasses," *Journal of the American Ceramic Society*, vol. n/a, e20167, n/a, ISSN: 1551-2916. DOI: 10.1111/jace.20167 [Online]. Available: https://onlinelibrary.wiley.com/doi/abs/10.1111/jace.20167

[157] D. Caurant, A. Quintas, O. Majérus, T. Charpentier, and I. Bardez, "Structural role and distribution of alkali and alkaline-earth cations in rare earth-rich aluminoborosilicate glasses," *Advanced Materials Research*, vol. 39-40, pp. 19–24, 2008, ISSN: 1662-8985. DOI: 10.4028/www.scientific.net/AMR.39-40.19 [Online]. Available: https://www.scientific.net/AMR.39-40.19

[158] R. L. Martin, B. Smit, and M. Haranczyk, "Addressing challenges of identifying geometrically diverse sets of crystalline porous materials," *J. Chem. Inf. Model.*, vol. 52, no. 2, pp. 308–318, Feb. 27, 2012, ISSN: 1549-9596. DOI: 10.1021/ci200386x [Online]. Available: https://doi.org/10.1021/ci200386x

[159] R. L. Martin and M. Haranczyk, "Construction and characterization of structure models of crystalline porous polymers," *Crystal Growth & Design*, vol. 14, no. 5, pp. 2431–2440, May 7, 2014, ISSN: 1528-7483. DOI: 10.1021/cg500158c [Online]. Available: https://doi.org/10.1021/cg500158c

[160] M. Pinheiro, R. L. Martin, C. H. Rycroft, A. Jones, E. Iglesia, and M. Haranczyk, "Characterization and comparison of pore landscapes in crystalline porous materials," *Journal of Molecular Graphics and Modelling*, vol. 44, pp. 208–219, Jul. 1, 2013, ISSN: 1093-3263. DOI: 10.1016/j.jmgm.2013.05.007 [Online]. Available: https://www.sciencedirect.com/science/article/pii/S109332631300096X

[161] M. Pinheiro, R. L. Martin, C. H. Rycroft, and M. Haranczyk, "High accuracy geometric analysis of crystalline porous materials," *CrystEngComm*, vol. 15, no. 37, pp. 7531–7538, Sep. 5, 2013, ISSN: 1466-8033. DOI: 10.1039/C3CE41057A [Online]. Available: https://pubs.rsc.org/en/content/articlelanding/2013/ce/c3ce41057a

[162] J. T. Reiser et al., "Comparative structural investigations of nuclear waste glass alteration layers and sol-gel synthesized aerogels," *npj Mater Degrad*, vol. 4, no. 1, pp. 1–9, Feb. 21, 2020, ISSN: 2397-2106. DOI: 10.1038/s41529-020-0109-y [Online]. Available: https://www.nature.com/articles/s41529-020-0109-y

[163] J. Du and J. M. Rimsza, "Atomistic computer simulations of water interactions and dissolution of inorganic glasses," *npj Mater Degrad*, vol. 1, no. 1, pp. 1–12, Nov. 13, 2017, ISSN: 2397-2106. DOI: 10.1038/s41529-017-0017-y [Online]. Available: https://www.nature.com/articles/s41529-017-0017-y

[164] B. Guillot and Y. Guissani, "How to build a better pair potential for water," *J. Chem. Phys.*, vol. 114, no. 15, pp. 6720–6733, Apr. 15, 2001, ISSN: 0021-9606. DOI: 10.1063/1.1356002 [Online]. Available: https://aip.scitation.org/doi/10.1063/1.1356002

[165] T. Mahadevan, A. Baroni, M. Taron, S. Gin, J. Du, and J.-M. Delaye, "Development of potentials for molecular dynamics simulations of dry and hydrated calcium aluminosilicate glasses by force matching and refinement," *Journal of Non-Crystalline Solids*, vol. 592, p. 121 746, Sep. 15, 2022, ISSN: 0022-3093. DOI: 10.1016/j.jnoncrysol.2022.121746 [Online]. Available: https://www.sciencedirect.com/science/article/pii/S0022309322003453

[166] J. Hutter, M. Iannuzzi, F. Schiffmann, and J. VandeVondele, "Cp2k: Atomistic simulations of condensed matter systems," *WIREs Computational Molecular Science*, vol. 4, no. 1, pp. 15–25, 2014, ISSN: 1759-0884. DOI: 10.1002/wcms.1159 [Online]. Available: https://onlinelibrary.wiley.com/doi/abs/10.1002/wcms.1159

[167] W.-L. Li, K. Chen, E. Rossomme, M. Head-Gordon, and T. Head-Gordon, "Optimized pseudopotentials and basis sets for semiempirical density functional theory for electrocatalysis applications," *J. Phys. Chem. Lett.*, vol. 12, no. 42, pp. 10 304–10 309, Oct. 28, 2021, ISSN: 1948-7185, 1948-7185. DOI: 10.1021/acs.jpclett.1c02918 [Online]. Available: https://pubs.acs.org/doi/10.1021/acs.jpclett.1c02918

[168] J. P. Perdew, K. Burke, and M. Ernzerhof, "Generalized gradient approximation made simple," *Phys. Rev. Lett.*, vol. 77, no. 18, pp. 3865–3868, Oct. 28, 1996. DOI: 10.1103/PhysRevLett.77.3865 [Online]. Available: https://link.aps.org/doi/10.1103/PhysRevLett.77.3865

[169] D. Marrocchelli, M. Salanne, P. A. Madden, C. Simon, and P. Turq, "The construction of a reliable potential for GeO2 from first-principles," *Molecular Physics*, vol. 107, no. 4, pp. 443–452, Feb. 20, 2009, ISSN: 0026-8976, 1362-3028. DOI: 10.1080/00268970902845347 arXiv: 1001.1843[cond-mat]. [Online]. Available: http://arxiv.org/abs/1001.1843

[170] B. Stevensson, Y. Yu, and M. Edén, "Structure–composition trends in multicomponent borosilicate-based glasses deduced from molecular dynamics simulations with improved b–o and p–o force fields," *Phys. Chem. Chem. Phys.*, vol. 20, no. 12, pp. 8192–8209, Mar. 21, 2018, ISSN: 1463-9084. DOI: 10.1039/C7CP08593A [Online]. Available: https://pubs.rsc.org/en/content/articlelanding/2018/cp/c7cp08593a

[171] "Minuit - a system for function minimization and analysis of the parameter errors and correlations," *Computer Physics Communications*, vol. 10, no. 6, pp. 343–367, Dec. 1, 1975, ISSN: 0010-4655. DOI: 10.1016/0010-4655(75)90039-9 [Online]. Available: https://www.sciencedirect.com/science/article/pii/0010465575900399

[172] W. G. Hoover, "Canonical dynamics: Equilibrium phase-space distributions," *Phys. Rev. A*, vol. 31, no. 3, pp. 1695–1697, Mar. 1, 1985. DOI: 10.1103/PhysRevA.31.1695 [Online]. Available: https://link.aps.org/doi/10.1103/PhysRevA.31.1695

[173] S. Nosé, "A unified formulation of the constant temperature molecular dynamics methods," *The Journal of Chemical Physics*, vol. 81, no. 1, pp. 511–519, Jul. 1, 1984, ISSN: 0021-9606. DOI: 10.1063/1.447334 [Online]. Available: https://doi.org/10.1063/1.447334

[174] M. E. Tuckerman, J. Alejandre, R. López-Rendón, A. L. Jochim, and G. J. Martyna, "A liouville-operator derived measure-preserving integrator for molecular dynamics simulations in the isothermal–isobaric ensemble," *J. Phys. A: Math. Gen.*, vol. 39, no. 19, p. 5629, Apr. 2006, ISSN: 0305-4470. DOI: 10.1088/0305-4470/39/19/S18 [Online]. Available: https://dx.doi.org/10.1088/0305-4470/39/19/S18

[175] G. J. Martyna, M. L. Klein, and M. Tuckerman, "Nosé–hoover chains: The canonical ensemble via continuous dynamics," *The Journal of Chemical Physics*, vol. 97, no. 4, pp. 2635–2643, Aug. 15, 1992, ISSN: 0021-9606. DOI: 10.1063/1.463940 [Online]. Available: https://doi.org/10.1063/1.463940

[176] F. Risplendi, F. Raffone, L.-C. Lin, J. C. Grossman, and G. Cicero, "Fundamental insights on hydration environment of boric acid and its role in separation from saline water," *J. Phys. Chem. C*, vol. 124, no. 2, pp. 1438–1445, Jan. 16, 2020, ISSN: 1932-7447. DOI: 10.1021/acs.jpcc.9b10065 [Online]. Available: https://doi.org/10.1021/acs.jpcc.9b10065

[177] B. S. Mallik and A. Chandra, "Hydrogen bond and residence dynamics of ion–water and water–water pairs in supercritical aqueous ionic solutions: Dependence on ion size and density," *The Journal of Chemical Physics*, vol. 125, no. 23, p. 234 502, Dec. 18, 2006, ISSN: 0021-9606. DOI: 10.1063/1.2403867 [Online]. Available: https://doi.org/10.1063/1.2403867

[178] D. T. Gillespie and E. Seitaridou, "1 the fickian theory of diffusion," in *Simple Brownian Diffusion: An Introduction to the Standard Theoretical Models*, D. T. Gillespie and E. Seitaridou, Eds., Oxford University Press, Oct. 25, 2012, p. 0, ISBN: 978-0-19-966450-4. DOI: 10.1093/acprof:oso/9780199664504.003.0001 [Online]. Available: https://doi.org/10.1093/acprof:oso/9780199664504.003.0001

[179] J. E. Mackin, "The free-solution diffusion coefficient of boron: Influence of dissolved organic matter," *Marine Chemistry*, vol. 20, no. 2, pp. 131–140, Nov. 1, 1986, ISSN: 0304-4203. DOI: 10.1016/0304-4203(86)90035-6 [Online]. Available: https://www.sciencedirect.com/science/article/pii/0304420386900356

[180] M. Holz, S. R. Heil, and A. Sacco, "Temperature-dependent self-diffusion coefficients of water and six selected molecular liquids for calibration in accurate 1h NMR PFG measurements," *Phys. Chem. Chem. Phys.*, vol. 2, no. 20, pp. 4740–4742, Jan. 1, 2000, ISSN: 1463-9084. DOI: 10.1039/B005319H [Online]. Available: https://pubs.rsc.org/en/content/articlelanding/2000/cp/b005319h

[181] J. Liu, X. He, J. Z. H. Zhang, and L.-W. Qi, "Hydrogen-bond structure dynamics in bulk water: Insights from ab initio simulations with coupled cluster theory," *Chemical Science*, vol. 9, no. 8, pp. 2065–2073, 2018. DOI: 10.1039/C7SC04205A [Online]. Available: https://pubs.rsc.org/en/content/articlelanding/2018/sc/c7sc04205a

[182] M. C. Morón, D. Prada-Gracia, and F. Falo, "Macro and nano scale modelling of water–water interactions at ambient and low temperature: Relaxation and residence times," *Phys. Chem. Chem. Phys.*, vol. 18, no. 14, pp. 9377–9387, Mar. 30, 2016, ISSN: 1463-9084. DOI: 10.1039/C5CP06791J [Online]. Available: https://pubs.rsc.org/en/content/articlelanding/2016/cp/c5cp06791j

[183] S. Xu, G. W. Scherer, T. S. Mahadevan, and S. H. Garofalini, "Thermal expansion of confined water," *Langmuir*, vol. 25, no. 9, pp. 5076–5083, May 5, 2009, ISSN: 0743-7463. DOI: 10.1021/la804061p [Online]. Available: https://doi.org/10.1021/la804061p

[184] P. Gallo, M. A. Ricci, and M. Rovere, "Layer analysis of the structure of water confined in vycor glass," *The Journal of Chemical Physics*, vol. 116, no. 1, pp. 342–346, Jan. 1, 2002, ISSN: 0021-9606. DOI: 10.1063/1.1423662 [Online]. Available: https://doi.org/10.1063/1.1423662

[185] "Modifications of the hydrogen bond network of liquid water in a cylindrical SiO2 pore," *Journal of Molecular Liquids*, vol. 85, no. 1, pp. 127–137, Apr. 1, 2000, ISSN: 0167-7322. DOI: 10.1016/S0167-7322(99)00169-5 [Online]. Available: https://www.sciencedirect.com/science/article/pii/S0167732299001695

[186] N. Giovambattista, P. J. Rossky, and P. G. Debenedetti, "Effect of temperature on the structure and phase behavior of water confined by hydrophobic, hydrophilic, and heterogeneous surfaces," *J. Phys. Chem. B*, vol. 113, no. 42, pp. 13 723–13 734, Oct. 22, 2009, ISSN: 1520-6106. DOI: 10.1021/jp9018266 [Online]. Available: https://doi.org/10.1021/jp9018266

[187] S. H. Lee and P. J. Rossky, "A comparison of the structure and dynamics of liquid water at hydrophobic and hydrophilic surfaces—a molecular dynamics simulation study," *The Journal of Chemical Physics*, vol. 100, no. 4, pp. 3334–3345, Feb. 15, 1994, ISSN: 0021-9606. DOI: 10.1063/1.466425 [Online]. Available: https://doi.org/10.1063/1.466425

[188] A. J. Patel, P. Varilly, and D. Chandler, "Fluctuations of water near extended hydrophobic and hydrophilic surfaces," *J Phys Chem B*, vol. 114, no. 4, pp. 1632–1637, Feb. 4, 2010, ISSN: 1520-5207. DOI: 10.1021/jp909048f

[189] E. de la Llave, V. Molinero, and D. A. Scherlis, "Water filling of hydrophilic nanopores," *The Journal of Chemical Physics*, vol. 133, no. 3, p. 034 513, Jul. 21, 2010, ISSN: 0021-9606. DOI: 10.1063/1.3462964 [Online]. Available: https://doi.org/10.1063/1.3462964

[190] Q. Zhang, K.-Y. Chan, and N. Quirke, "Molecular dynamics simulation of water confined in a nanopore of amorphous silica," *Molecular Simulation*, Dec. 1, 2009. DOI: 10.1080/08927020903116029 [Online]. Available: https://www.tandfonline.com/doi/abs/10.1080/08927020903116029

[191] G. S. Frankel et al., "Recent advances in corrosion science applicable to disposal of high-level nuclear waste," *Chemical Reviews*, 2021, ISSN: 15206890. DOI: 10.1021/acs.chemrev.0c00990

[192] D. Strachan et al., "On the dissolution of a borosilicate glass with the use of isotopic tracing – insights into the mechanism for the long-term dissolution rate," *Geochimica et Cosmochimica Acta*, vol. 318, pp. 213–229, Feb. 1, 2022, ISSN: 0016-7037. DOI: 10.1016/j.gca.2021.12.004 [Online]. Available: https://www.sciencedirect.com/science/article/pii/S0016703721006980

[193] M. Taron, "Simulation à l'échelle nanoscopique du transport réactif : Application à la dissolution des verres nucléaires," *PhD Thesis*, 2022.

[194] G. B. M. Vaughan et al., "ID15a at the ESRF – a beamline for high speed operando x-ray diffraction, diffraction tomography and total scattering," *J Synchrotron Rad*, vol. 27, no. 2, pp. 515–528, Mar. 1, 2020, Publisher: International Union of Crystallography, ISSN: 1600-5775. DOI: 10.1107/S1600577519016813 Accessed: Oct. 1, 2025. [Online]. Available: https://journals.iucr.org/s/issues/2020/02/00/il5045/

[195] G. B. M. Vaughan, S. Checchia, and M. Di Michiel, "Characterization and calibration of DECTRIS PILATUS3 x CdTe 2m high-z hybrid pixel detector for high-precision powder diffraction measurements," *J Appl Cryst*, vol. 58, no. 1, pp. 76–86, Feb. 1, 2025, Publisher: International Union of Crystallography, ISSN: 1600-5767. DOI: 10.1107/S1600576724010033 Accessed: Oct. 1, 2025. [Online]. Available: https://journals.iucr.org/j/issues/2025/01/00/te5142/

[196] A. K. Soper, *Gudrun manual*, Accessed: October 9, 2025, ISIS Facility, Rutherford Appleton Laboratory, Chilton, Didcot, UK, 2006. [Online]. Available: http://wwwisis2.isis.rl.ac.uk/Disordered/Manuals/gudrun/Gudrun_manual_2006.pdf